Dynamic modelling of local fuel desorption and retention in the wall of nuclear fusion reactors for auto-consistent plasma-wall interaction simulations.

Julien Denis

DOCTORAL THESIS

Aix-Marseille University

Doctoral School: *Sciences pour l'Ingénieur : Mécanique, Physique, Micro et Nanoélectronique*

Speciality: **Mécanique et Physique des Fluides**

Dynamic modelling of local fuel desorption and retention in the wall of nuclear fusion reactors for auto-consistent plasma-wall interaction simulations.

Presented by:

Julien DENIS

Board of examiners for the public PhD defense on the 17th of December 2019:

Pr. Christian THEILER	Reviewer	SPC, EPFL
Pr. Khaled HASSOUNI	Reviewer	LSPM, Université Paris 13
Pr. Charlotte BECQUART	Examiner	UMET, Université de Lille
Dr. Sabina MARKELJ	Examiner	F2, Jožef Stefan Institut
Dr. Bernard PÉGOURIÉ	Examiner	IRFM, CEA
Dr. Guido CIRAOLO	PhD director	IRFM, CEA
Dr. Eric SERRE	PhD co-director	M2P2, CNRS
Dr. Jérôme BUCALOSSI	PhD supervisor	IRFM, CEA
Dr. Sebastijan BREZINSEK	Invited	IEK, FZJ

Laboratory:

Institut de **R**echerche sur la **F**usion par confinement **M**agnétique

CEA – Cadarache, 13108 Saint-Paul-lez-Durance, France

Thèse de doctorat

Université d'Aix-Marseille

École doctorale : *Sciences pour l'Ingénieur : Mécanique, Physique, Micro et Nanoélectronique*

Spécialité : **Mécanique et Physique des Fluides**

Modélisation dynamique de la désorption et de la rétention locales de combustible dans la paroi des réacteurs à fusion nucléaire.

Présentée par :

Julien DENIS

Thèse soutenue publiquement le 17 Décembre 2019 devant le jury composé de :

Pr. Christian Theiler	Rapporteur	SPC, EPFL
Pr. Khaled Hassouni	Rapporteur	LSPM, Université Paris 13
Pr. Charlotte Becquart	Examinateur	UMET, Université de Lille
Dr. Sabina Markelj	Examinateur	F2, Jožef Stefan Institut
Dr. Bernard Pégourié	Examinateur	IRFM, CEA
Dr. Guido Ciraolo	Directeur de thèse	IRFM, CEA
Dr. Eric Serre	Co-directeur de thèse	M2P2, CNRS
Dr. Jérôme Bucalossi	Encadrant de thèse	IRFM, CEA
Dr. Sebastijan Brezinsek	Invité	IEK, FZJ

Laboratoire :

Institut de **R**echerche sur la **F**usion par confinement **M**agnétique

CEA – Cadarache, 13108 Saint-Paul-lez-Durance, France

À ma maman, à mes grands-parents.

Remerciements

Je viens de mettre enfin LE point final à cette oeuvre de la physique, qui ne méritera certainement pas un Prix Nobel, mais dans laquelle j'ai jeté toutes mes forces. Avant de tourner une page définitive sur ces années de thésard, je me dois d'écrire l'ultime section de ce manuscrit, sans nul doute la plus importante. Car en effet cette oeuvre n'existerait pas sans le soutien des personnes qui m'ont entouré pendant cette thèse.

En premier lieu, je voudrais remercier mon directeur de thèse Guido Ciraolo et mon encadrant Jérôme Bucalossi de m'avoir accompagné au cours de ce doctorat. Le chemin a été long et semé d'embûches et je retiens qu'à aucun moment vous ne m'avez laissé tomber. Je remercie également mon co-directeur de thèse Eric Serre pour m'avoir fait découvrir la collaboration européenne au sein d'EUROfusion ainsi que pour son aide précieuse dans la dernière ligne droite de l'écriture de ce rapport. Enfin j'exprime ma gratitude envers la personne qui m'a tendu la main, et qui ne l'a pas lâchée jusqu'au bout, à savoir Bernard Pégourié. Il mérite incontestablement sa place dans l'encadrement de cette thèse.

Je souhaite également exprimer ma reconnaissance envers Pr. Christian Theiler et Pr. Khaled Hassouni pour avoir accepté le challenge d'examiner ce rapport qui, à première vue, peut faire peur. Je remercie aussi Pr. Charlotte Becquart et Dr. Sabina Markelj d'être venues à ma soutenance, parfois de très loin. Je remercie ce jury de thèse au complet pour leurs nombreux commentaires et questions qu'ils ont exprimés pendant les presque trois heures de soutenance et qui montrent l'intérêt qu'ils ont eu pour mon travail. J'en profite aussi pour remercier Dr. Sebastijan Brezinsek de l'intérêt qu'il a porté à ce travail.

Cette thèse, mêlant différentes physiques, n'aurait pu se faire sans l'aide d'experts dans chaque thématique abordée. Je remercie chaleureusement Etienne Hodille de m'avoir tout appris de la physique de l'interaction hydrogène-matériau et de m'avoir confié son joujou. Je remercie également Jonathan Gaspar, le spécialiste de l'équation de la chaleur, pour sa disponibilité et son aide toujours bienveillante.

Je souhaiterais également remercier tous mes collègues du Groupe Divertor et Interaction Plasma-Paroi, à savoir Hugo Bufferand, Pascal Devynck, Olivier Meyer, Nicolas Fedorczak, Patrick Tamain, Christian Grisolia, Jamie Gunn, Jean-Yves Pascal ainsi que

Philippe Gendrih d'avoir partagé ces années dédiées à la science. J'ai une pensée toute particulière pour mes deux collègues du fond du couloir : Pascale Monier-Garbet, que je remercie de nous avoir rappelé chaque jour et à juste titre que l'important est ce qui se passe expérimentalement dans le tokamak, ainsi que Stéphane Vartanian que je remercie pour son soutien sans faille, son humanité et surtout pour m'avoir poussé à m'auto-former au standard téléphonique. Je remercie aussi Yannick Marandet, Thierry Loarer et Jean-Laurent Gardarein pour le temps qu'ils m'ont dédié et pour nos échanges qui ont toujours été très enrichissants.

Quisiera darle las gracias al profesor Francisco Castejón y al profesor Antonio Rivera por haberme transmitido el virus de la Fusión Nuclear.

Une thèse est un parcours dans les méandres de la physique, mais aussi dans ceux de l'administration. Heureusement les anges gardiennes que sont Valérie Icard, Nathalie Borio, Laurence Azcona et Nathalie Bihan ont veillé sur moi. Je les en remercie. Je remercie également Frédéric Imbeaux et Isabelle Porchy pour leur aide et leur sincérité dans les moments difficiles que j'ai eu à traverser. Je remercie aussi Sandrine Garnier pour son écoute et son aide. J'ai une pensée toute particulière pour Pascal Campion, que je remercie pour son humanité, sa bienveillance et sa disponibilité. Je remercie également Géraldine Callier pour son aide à chaque début d'année universitaire. A travers ces personnes je souhaite exprimer ma gratitude envers l'Institut de Recherche sur la Fusion par confinement Magnétique, le CEA Cadarache, la Région Provence Alpes Côte d'Azur et l'École Doctorale 353 de l'université d'Aix-Marseille pour m'avoir donné l'opportunité de faire cette thèse et de la terminer dans les meilleurs conditions possibles.

Ces années de doctorat ont été riches en émotions et en très belles rencontres. J'ai eu notamment l'honneur de rencontrer le meilleur de ce que fait l'Italie ! Je veux bien entendu parler d'Alberto, de Matteo et de Davide. En plus d'être de grands scientifiques, vous êtes de très belles personnes. Ce travail existe en grande partie grâce à votre soutien sans faille et votre amitié. Merci !
J'adresse un grand merci à mes compagnons de route du 508, Phoenix, Federico, Raffaele, Adrien, Giacomo, Karol, Achille, Julio et Giorgio pour leur bonne humeur et leur goût pour le café de qualité. J'ai été heureux tous les jours de me lever à 6h30 pour aller travailler à vos côtés ! Je remercie mes compagnons de déjeuner à la cantine et de soirées aixoises enivrées, et dont le seul défaut commun est de ne pas avoir eu leur bureau au premier étage du 508, à savoir Camille B, captain Nicolas, Peter, Axel, Samuele, Elisabetta, Cristian, Camille G, Sarah, Nicolas B, Guillaume U, Anastasia, Damien, Guillaume B, Juan, William ainsi que les plus anciens Didier, Jorge, Hugo, L'eau Rend, Olivier, Jae Heon, captain Alexandre, TC, Romain, Laurent C, Damien et Claudia. Un grand merci aux membres de l'équipe de Pomone que je n'ai pas encore cités et qui nous ont accueillis tant de fois pour des soirées souvent mémorables !

Cette thèse n'aurait pu aboutir sans le soutien des amis avec un grand A. Je pense

notamment à la team des Turgaliens, qui m'a donné la cefor de Paname et de Limoges à savoir Etienne, Fredo, Marta, Yoann, Antonia, Agathe, Pierre, Marion et Loic. De même j'ai une pensée pour la team Madrid, Elsa, Fabien et MBG, qui m'a toujours soutenu et qui m'a montré que la vie continuait. Je remercie les gadzs d'avoir toujours été là notamment Mal&, toute la fam's 123 ainsi que Pedro et Duff. Je pense également à mes potes de Calmette, Tinmar, Antoine et David ainsi qu'à celui qui a ouvert la voie des tennismen-docteur David K.

I would like also to thank Nimesh and his wonderful family for welcoming me in Rickmansworth and for making me discover the Indian tea.

En écrivant ces quelques lignes j'ai également une pensée affective pour les amies et collègues de ma Maman que je remercie pour leur présence et leur soutien.

Je pense aussi à ma belle famille qui m'a pardonné l'enlèvement de leur fille/soeur et qui a toujours été à mes côtés au cours de ces longues années.

Je remercie bien entendu ma famille avec un grand F, cousins, cousines et mon oncle pour leur soutien sans faille. Je suis fier de faire partie des leurs. Je remercie Marion et Cyrille pour avoir souvent fait les kilomètres séparant Aurillac et Aix pour me soutenir et me remotiver. J'ai une pensée très émue pour ma ptite tatie qui a affronté toutes ces épreuves avec moi.

Je remercie ma Marion, celle qui me soutient de jour comme de nuit (apparemment) depuis tant d'années.

Enfin je remercie du fond du coeur ma Maman, mon Papy et ma Mamie qui ont veillé sur moi de là-haut et à qui je dédie cette thèse.

Abstract

In all plasma devices, from the simplest neon tube to the most advanced nuclear fusion reactor, a constant exchange of particle develops between the plasma and the wall: the ions are driven by the pressure gradient to the wall where they recombine, interact with the material and can be subsequently reemitted into the plasma in both atomic form (reflection) and molecular form (desorption). This interesting phenomenon, referred to as recycling, is of critical interest for nuclear fusion reactors such as tokamaks. Indeed, once the plasma is established, particle recycling on the wall represents the main particle source for the plasma. Under steady-state conditions, the ratio between the external gas throughput and the total recycling flux is estimated around 10 % in present day tokamaks and is expected around 1 % in next-generation reactors like ITER. A complete understanding of the recycling phenomenon is therefore essential to ensure a reliable plasma density control, which has proven to be a critical issue for long-term operation of those reactors. Indeed, the wall materials can pump and store a tremendous amount of fuel (fuel retention) which may, under some conditions, be released back into the reactor vacuum chamber. As a consequence, the recycling strongly depends on the interaction between the fuel (hydrogen) and the plasma facing materials. Moreover, the impact of recycling on reactor performance was highlighted at the JET tokamak with the change from a carbon wall (JET-C) to the beryllium – tungsten ITER-like Wall (JET-ILW). The change in the recycling process between both wall configurations has been pointed out as a possible explanation for the degraded confinement in high confinement mode observed in JET-ILW w.r.t. the one observed in JET-C. However, the in-situ experimental study of the recycling process and of its potential consequences remains challenging. Modelling can assist in the understanding of these phenomena.
Among the numerical tools that scientists have in their hands, the so-called edge-plasma transport codes present the most-advanced description of the plasma-wall interaction. However, the description of recycling remains partial: atomic reflection is already handled, often through tabulated numerical results, while molecular desorption is set ad-hoc by the code user. This PhD focuses on the development of an extension of the SolEdge2D-EIRENE transport code, named D-WEE, whose goal is to model the dynamics of thermal desorption of hydrogen isotopes from the surface of plasma facing materials. To achieve this purpose, D-WEE models hydrogen isotopes implantation, transport by diffusion and retention in those materials in the entire reactor vacuum chamber. The diffusion and retention of hydrogen are strongly dependent on the material temperature. D-WEE also treats the thermal dynamics of plasma facing components. Despite the undertaken efforts,

some numerical difficulties related to the temperature model dampen the hopes of auto-consistent plasma-wall simulations (with feedback of D-WEE on SolEdge2D-EIRENE) in the time-scale of this PhD.
However, before launching such auto-consistent simulations, D-WEE has to be initialised to ensure a realistic wall behaviour in terms of dynamics (pumping or fuelling areas) and fuel reservoir (inventory/retention). A methodology based on modelling is introduced to perform such initialisation. A synthetic plasma pulse is built from consecutive SolEdge2D-EIRENE simulations. This synthetic pulse is used as a plasma background for the D-WEE module. A sequence of plasma pulses is simulated with D-WEE to model a tokamak operation. This simulation enables to extract at a desired time during a pulse the local fuel inventory and the local desorption flux density which could be used as initial condition for coupled plasma-wall simulations. In this PhD, this methodology is applied to a JET tokamak discharge. D-WEE requires input parameters to define the interaction between hydrogen and the considered material (diffusion coefficient, trapping parameters, etc.). The analysis of the literature of hydrogen/material interaction models and of the available parameters have shown that the description of the hydrogen — beryllium interaction was incomplete and must be improved. A simulation under the beryllium – tungsten ILW configuration cannot be envisaged presently. A full tungsten wall configuration (in terms of diffusion and trapping of hydrogen) was therefore considered in the simulation. This simulation must be seen as a proof of principle of the suggested methodology. Nonetheless, the simulated wall dynamics during the consecutive pulses is studied, reveling some interesting behaviours that could impact the reactor operation and performance. To assess the relevance of the wall dynamics obtained in the simulation, a confrontation to post-pulse experimental pressure measurement is performed. Such confrontation reveals a qualitative agreement between the temporal pressure drop obtained in the simulation (with a $t^{-0.8}$ trend) and the one observed experimentally under ILW configuration. The retention rate during the discharge is also studied and reproduces qualitatively the experimental trends.

Résumé substantiel

Dans tout dispositif plasma, du très basique tube néon au plus complexe des réacteurs à fusion nucléaire, un échange constant de particules se développe entre le plasma et la paroi : les ions sont transportés par le gradient de pression à la paroi où ils se recombinent, interagissent avec le matériau et peuvent par la suite être renvoyés dans le plasma sous forme d'atomes (réflexion) ou de molécules (désorption). Ce phénomène intriguant, souvent appelé recyclage, présente un intérêt crucial pour les réacteurs à fusion nucléaire tels que les tokamaks. En effet, une fois le plasma établi, le recyclage des particules représente la principale source de particules pour le plasma. A l'état stationnaire, le ratio entre l'injection externe de gaz et le flux total de recyclage est estimé à environ 10 % dans les tokamaks actuels et est attendu aux alentours de 1 % dans les réacteurs de prochaine génération tels qu'ITER. Une connaissance complète du recyclage est donc essentielle pour assurer un contrôle fiable de la densité plasma, contrôle qui s'est avéré par le passé être un enjeu majeur pendant les opérations longue durée des tokamaks. En effet, les matériaux composant le mur peuvent pomper et stocker une quantité considérable de combustible (phénomène de rétention) qui peut, sous certaines conditions, être libérée dans la chambre à vide du réacteur. Le recyclage dépend donc fortement de l'interaction entre le combustible, à savoir les isotopes de l'hydrogène (IH), et les matériaux composant le mur. De plus, l'impact du recyclage sur les performances du réacteur a été mis en lumière dans le tokamak JET suite au changement du mur d'une configuration carbon (JET-C) à une configuration béryllium – tungstène similaire à celle prévue dans ITER connue sous le nom d'ITER-like Wall (JET-ILW). Le changement du processus de recyclage entre les deux configurations a été pointé du doigt comme une explication possible de la dégradation du confinement observé en mode H (mode d'opération dit à haut confinement, défini par rapport au mode à faible confinement appelé mode L) sur JET-ILW par rapport à celui observé sur JET-C. En effet, des phénomènes intrigants, possiblement liés au recyclage, ont été observés dans le JET-ILW durant des évènements transitoires forts caractéristiques de ce mode H, appelés Mode Localisé de Bord (MLB), ainsi que dans la phase entre ces MLBs. Cependant, les études in-situ du recyclage et de ses potentielles conséquences sur l'opération du réacteur demeurent complexes. La modélisation numérique peut faciliter la compréhension de ce phénomène. Parmi les outils numériques à la disposition des scientifiques, les codes de transport de plasma de bord présentent la description la plus avancée de l'interaction plasma-paroi. Toutefois, la description du recyclage dans ces codes reste partielle : la réflexion atomique est déjà traitée, souvent à partir de résultats numériques compilés, tandis que la désorption

moléculaire est fixée de manière ad-hoc par l'utilisateur. Cette thèse de doctorat se concentre donc sur le développement d'une extension au code de transport de plasma de bord SolEdge-EIRENE, dénommée D-WEE, dont l'objectif est de modéliser la dynamique de la rétention des IHs dans les matériaux et de la désorption thermique de ces IHs de la surface des matériaux afin d'en étudier son effet potentiel sur l'opération du réacteur et sur sa performance. Le but ultime de cet effort de modélisation est de simuler un évènement MLB suivi de la phase consécutive inter-MLB pour étudier l'effet potentiel de l'interaction IH–matériau dans la réduction de la performance observée dans le JET-ILW. Le module D-WEE a été développé avec cette perspective.

Le module D-WEE, qui est présenté de manière exhaustive dans le chapitre 2 de cette thèse, est composé de deux codes internes : MHIMS et WEE-temp.
MHIMS décrit l'interaction entre les IHs et les matériaux composant le mur par l'intermédiaire du système d'équations dit de Réaction-Diffusion. Il simule l'implantation des ions et des atomes d'IH, leur diffusion et leur piégeage dans les défauts du matériau, ainsi que leur éventuelle désorption de la surface des matériaux dans la chambre du réacteur. MHIMS a été fortement amélioré d'un point de vue numérique pour diminuer son temps de calcul tout en préservant sa précision. Il est maintenant capable de simuler la chambre à vide complète des réacteurs de fusion en tenant compte des différents matériaux qui la compose, sous réserve d'une paramétrisation adéquate du modèle pour les matériaux considérés. A l'heure actuelle, la version de MHIMS utilisée dans le module D-WEE ne tient pas en compte des processus d'interaction de l'IH avec la surface des matériaux. Les modèles disponibles dans la littérature pour traiter ces processus ainsi que les paramètres nécessaires dans ces modèles ont montré des inconsistances dans des conditions d'implantation typiques des tokamaks, inconsistances qui pourraient amener à une surestimation du pompage de l'IH par le mur. La modélisation de l'interaction IH–béryllium requière le traitement de ces processus de surface car près de 75 % de l'inventaire total en combustible observé dans le béryllium est possiblement adsorbé à la surface de cavités interconnectées au sein de la zone d'implantation. De plus, un changement manifeste de l'interaction IH–béryllium avec la température du matériau durant l'implantation a été observé expérimentalement dans la littérature. Ce changement de mécanisme de rétention a été montré par Reinelt et al. : les spectres de spectrométrie de masse de thermodésorption obtenus après implantation de deutérium dans du béryllium à 320 K (approximativement la température de base du béryllium dans la première paroi d'ITER) et à 530 K (approximativement la température de base du béryllium dans la première paroi du JET-ILW) montrent des structures très différentes. Aucun effort de modélisation n'a été entrepris dans la communauté de fusion pour simuler et comprendre ce changement d'interaction. En conséquence, les connaissances actuelles ne permettent pas de modéliser l'interaction IH–béryllium. Pour l'interaction IH–tungstène, la paramétrisation de MHIMS proposée par Hodille et al. a été sélectionnée. Cette paramétrisation a été obtenue par reproduction avec MHIMS de l'expérience d'implantation suivie de l'analyse par spectrométrie de masse de thermodésorption effectuées par Ogorodnikova et al.. La solidité de cette paramétrisation a été confirmée par des simulations et des con-

frontations supplémentaires aux expériences. Avec ce jeu de paramètres, Hodille et al. ont été capables de reproduire avec un bon accord l'évolution temporelle de la rétention du deutérium avec la fluence mesurée par Ogorodnikova et al. sur trois ordres de grandeur de fluence de deutérium pour deux températures d'implantation. De plus, ces paramètres ont permis de reproduire l'évolution expérimentale de la rétention de deutérium avec la température d'implantation obtenue par Tian et al. pour des conditions d'implantation similaires à celles trouvées dans des réacteurs à fusion.
Enfin, les processus de diffusion, piégeage et dépiégeage de l'IH simulés par MHIMS sont des processus thermiquement activés. Un modèle thermique est donc nécessaire pour compléter la description de la dynamique du mur. Le code WEE-temp calcule le profil de température dans la profondeur du matériau de surface (correspond à la zone simulée par MHIMS) des composants formant la chambre à vide des réacteurs (appelés Composant Face au Plasma, CFP). WEE-temp peut simuler les CFPs activement-refroidis ainsi que les CFPs à refroidissement inertiel, en supposant une géométrie simplifiée en forme de bloc composé d'une superposition de couches de matériaux. Le calcul de température peut être effectué aussi bien à l'état stationnaire que pendant des forts transitoires de flux de chaleur tels que les MLBs. Dans la perspectives des tokamaks WEST et ITER, une attention particulière a été portée à la modélisation des CFPs activement-refroidis. Des ajustements du modèle ont été proposés pour reproduire le comportement thermique réel de ces CFPs. Pour les CFPs inertiels, un ajustement du modèle a été suggéré afin de reproduire le refroidissement entre décharges de ces CFPs (dû à la dissipation thermique de la chaleur dans la structure du tokamak) tout en préservant leur comportement inertiel durant les décharges.

Cependant, avant de lancer des simulations auto-consistantes avec rétroaction de D-WEE sur SolEdge2D-EIRENE, D-WEE doit être initialisé pour assurer un comportement réaliste du mur s'agissant de la dynamique (zones de pompage ou d'injection d'hydrogène) et du réservoir d'IHs (inventaire/rétention d'IHs). Une méthodologie en quatre étapes basée sur la modélisation est introduite dans le chapitre 2 pour procéder à cette initialisation et mener vers la modélisation d'un évènement MLB. Dans l'étape 1, une décharge plasma synthétique est construite à partir de simulations SolEdge2D-EIRENE consécutives. Cette décharge synthétique est utilisée en tant qu'entrée fixe du module D-WEE. Puis une séquence de décharges plasma est simulée avec D-WEE pour modéliser l'opération d'un tokamak (étape 2). Cette simulation permet d'extraire au temps désiré l'inventaire local en hydrogène ainsi que la densité de flux de désorption locale qui peuvent être utilisés comme condition initiale pour les simulations auto-consistantes susmentionnées. Une fois le mur initialisé, l'étape 3 peut être lancée. Cette étape consiste en un redémarrage de la simulation SolEdge2D-EIRENE de l'étape 1 en mode auto-consistant et a pour but de calculer un nouveau plasma stationnaire avec SolEdge2D-EIRENE dû à la modification du recyclage introduit par la rétroaction de D-WEE. Enfin, l'étape 4 correspond à la modélisation d'un évènement MLB suivi de la phase consécutive inter-MLB. Malgré les efforts consentis, des difficultés numériques liées au modèle de température ont éteint les espoirs de simulation auto-consistante de la dynamique plasma-paroi avec

rétroaction de D-WEE sur SolEdge2D-EIRENE, i.e. les étapes 3 et 4 de la méthodologie introduite dans cette thèse. Ces étapes seront abordées dans des travaux ultérieurs. Cependant, l'initialisation du mur, à savoir les étapes 1 et 2 de la méthodologie, peuvent être réalisées. Ces deux étapes ont fait l'objet des chapitres 3 et 4 de la thèse.

L'étape 1 de cette méthodologie est appliquée dans le chapitre 3 : les deux phases stationnaires (phase mode H et phase mode L) d'une décharge en pur deutérium du tokamak JET sont simulées avec le code de plasma de bord SolEdge2D-EIRENE. Les résultats des simulations sont confrontés aux mesures expérimentales disponibles pour la décharge en question. Les profils du courant de saturation J_{sat} au niveau du divertor obtenus dans les deux simulations sont consistants avec les profils expérimentaux des sondes de Langmuir sauf pour la phase mode H pour laquelle le profil expérimental au niveau du divertor interne est supérieur. Il en résulte une bonne estimation des flux incidents d'ion sur le divertor, et donc de la fluence ionique intégrée déposée durant la phase de courant constant de la décharge. Cependant, aucune conclusion ne peut être tirée sur les densités de flux d'implantation et sur les énergies d'impact durant l'expérience en raison de l'absence d'estimation de T_e à partir des données des sondes de Langmuir. Ces deux phases plasma, qui sont supposées être représentatives de la décharge plasma complète, peuvent ensuite être utilisées comme fonds plasma pour des simulations avec le code D-WEE.

Dans le chapitre 4, l'étape 2 de la méthodologie introduite dans cette thèse est effectuée. Une séquence de décharges plasma est simulée avec D-WEE pour initialiser le mur au niveau de la densité de flux de désorption d'IHs, de l'inventaire local d'IHs et de la température du mur. Cette simulation a été effectuée pour le tokamak JET en considérant un mur complet (divertor et première paroi) en tungstène à cause du manque de modèle et de paramétrisation pour l'interaction IH–béryllium mentionnée précédemment. A ce stade, quatre décharges consécutives suivies de 30 min de temps de repos ont été simulées. Les décharges sont reconstruites à partir des résultats des simulations SolEdge2D-EIRENE présentées dans le chapitre 3. Une reproductibilité des troisième et quatrième décharges est observée au niveau de l'excursion de température et de la rétention dynamique (amplitude et dynamique). On peut donc conclure que la rétention dynamique du mur a été initialisée. Par conséquent, l'état local du mur peut être extrait de cette simulation, comme par exemple à la fin de la phase mode H de la quatrième décharge. Cet état du mur peut être considéré comme condition initiale pour des simulations couplées plasma-mur avec rétroaction de D-WEE sur SolEdge2D-EIRENE. Ces simulations seront effectuées dans un travail futur.

La dynamique du mur simulée pendant la séquence de décharges a également été étudiée dans le chapitre 4 de cette thèse. Les résultats de simulations ont montré que D-WEE est capable de reproduire qualitativement la décroissance du taux de rétention expérimentalement observée dans JET-ILW pendant les décharges plasma (un flux de rétention de l'ordre de 10^{21} D.s^{-1} qui décroît en quelques secondes). L'étude du flux de rétention pendant les décharges et entre les décharges a montré que les pièges responsables de la

rétention dynamique sont le piège 1 (avec une énergie de dépiégeage $E_{dt,1} = 0.85$ eV) dans le divertor et le piège 3 (avec une énergie de dépiégeage $E_{dt,3} = 1.5$ eV) dans la première paroi. Cette différence de pièges impliqués dans la rétention dynamique est due a la différence de température de base des deux zones (50 – 70 °C pour le divertor, 200 °C pour la première paroi). A la fin de la phase mode H, le flux de rétention est dû à la diffusion et au piégeage du deutérium dans la profondeur des matériaux. Il est dominé par la rétention dans le piège 3 dans la première paroi en raison de la grande densité de ce piège et de la grande surface d'exposition de la première paroi (134 m^2 pour la première paroi, 40 m^2 pour le divertor). Une confrontation de la simulation avec les mesures expérimentales de pression entre décharges a révélé un accord qualitatif entre la chute de pression calculée par D-WEE (avec une tendance en $t^{-0.74}$) et la chute de pression expérimentale (avec une tendance en $t^{-0.89}$). Cependant, la quantité de deutérium désorbée entre décharges (et donc le réservoir de rétention dynamique) est clairement sous-estimée dans la simulation (1.3×10^{22} deutérium de différence entre la simulation et l'expérience 13 min après la fin de la décharge). Cette différence est très certainement liée à la considération d'une première paroi en tungstène dans la simulation. Néanmoins, l'inventaire dans le piège 3 du tungstène de la première paroi à la fin de la quatrième décharge est assez grand pour entraîner une telle quantité de particules dégazées entre décharges ce qui indique que la dynamique de ce piège est incorrecte, probablement due à une énergie de dépiégeage trop grande. On peut donc supposer que le béryllium dans la première paroi du JET-ILW possède un ou des pièges avec une énergie de dépiégeage inférieure à celle du piège 3. Toutefois, la simulation montre que D-WEE est capable de reproduire qualitativement des tendances expérimentales (ordre de grandeur du flux de retention pendant les décharges et évolution temporelle du dégazage post-décharge) si les paramètres corrects de piégeage et les conditions d'implantation globales (distributions de densité de flux d'implantation, d'énergie d'impact, etc.) sont considérés. Elle suggère également que la rétention dynamique peut être liée au béryllium de la première paroi dans le réacteur JET-ILW. Cette suggestion est conforme avec les observations expérimentales qui ont montré la haute capacité de stockage de IHs du béryllium dans la zone d'implantation (avec une densité en IHs jusqu'à 35 at.% de béryllium, un facteur ~ 4 supérieur à la capacité du tungstène considéré dans cette thèse). De plus, le fait que des flux de rétention similaires pendant les décharges ($\sim 10^{21}$ s^{-1}) aient été observés dans le JET avec des limiteurs en béryllium dans les années 90 et dans le JET-ILW renforce notre conviction que le béryllium de la première paroi est responsable du pompage de l'hydrogène pendant les décharges dans le tokamak JET-ILW. Cependant, si cela est confirmé, on peut se demander si la première paroi du JET-ILW est représentatif de la première paroi du tokamak ITER au niveau du pompage. En effet, la température de base de la première paroi du JET-ILW est de 473 K (200 °C) tandis que la première paroi d'ITER aura une température de base de 343 K (70 °C à cause du refroidissement actif). Des résultats publiés par Reinelt et al. ont montré un changement de l'interaction IH–béryllium selon la température d'exposition et suggère que la première paroi d'ITER ne va pas se comporter comme celle du JET-ILW en particulier durant la phase de démarrage des décharges. Des expériences dans le JET-ILW avec la température de la première paroi

similaire à celle du fluide caloporteur de la première paroi d'ITER pourraient fournir une réponse à cette question. Des simulations de décharge avec une première paroi en béryllium dans D-WEE et une confrontation de ces simulations avec les mesures de pression post-décharge (comme illustrée dans cette thèse) pourraient fournir une indication du ou des pièges responsables du fort pompage observé dans le JET-ILW. Cependant, ceci requière un vaste travail théorique afin de développer un modèle capable de correctement décrire l'interaction IH–béryllium à différentes températures d'exposition.

Enfin, dans le chapitre 4, l'analyse des résultats de simulation de la quatrième décharge est effectuée. Cette analyse a montré des dynamiques de rétention des pièges (pompage et injection de D) liées à la variation de température du mur ainsi qu'à la variation des conditions d'implantation. Ces dynamiques ont été expliquées via le taux de remplissage maximal des pièges définis ci-dessous :

$$
\begin{aligned}
R_{eq,i}^{MAX} &= \frac{n_{t,i}^{MAX}(x)}{n_i(x)} \\
R_{eq,i}^{MAX} &= \frac{1}{1 + \dfrac{\nu_{dt,i}(T)\lambda^2 n_{IS}}{\Gamma_{imp}^{i+} X_{imp}^{i+} + \Gamma_{imp}^{at} X_{imp}^{at}}} \\
R_{eq,i}^{MAX} &= \frac{1}{1 + \dfrac{\nu_{dt,i}(T)}{\nu_t^{MAX}}}
\end{aligned}
$$

où $n_{t,i}^{MAX}$ est la densité maximale de IHs piégés dans le piège de type i [m^{-3}], n_i est la densité de pièges de type i [m^{-3}], x est la profondeur du matériau [m], $\nu_{dt,i}$ est la fréquence de dépiégeage du piège de type i [s^{-1}], T est la température du matériau [K], λ est la distance entre deux sites interstitiels pour les IHs [m], n_{IS} est la densité de ces sites interstitiels [m^{-3}], Γ_{imp}^{i+} et Γ_{imp}^{at} sont respectivement les densités de flux d'implantation des ions et des atomes [$m^{-2}.s^{-1}$], X_{imp}^{i+} et X_{imp}^{at} sont respectivement les profondeurs d'implantation moyennes des ions et des atomes [m]. Le paramètre $R_{eq,i}^{MAX}$ indique l'inventaire d'équilibre des pièges, et donc l'inventaire total en IHs d'équilibre qui se forme dans le matériau pendant l'opération plasma pour une température du matériau et des conditions d'implantation constantes. Ce paramètre donne une indication de la dynamique de rétention qui se produit pendant l'opération plasma. Quand $R_{eq,i}^{MAX}$ augmente, le piège i va se remplir en IHs entraînant une effet de pompage de IHs par le mur vis à vis du plasma, alors que quand $R_{eq,i}^{MAX}$ diminue, le piège i va libérer des IHs entraînant une injection de IHs dans le plasma. Cependant, il est rappelé que l'amplitude de ces dynamiques ainsi que leur vitesse sont fortement dépendantes de la densité de piège. Seules des simulations avec D-WEE peuvent donner une idée de ces deux quantités. L'expression de $R_{eq,i}^{MAX}$ montre un rapport entre la fréquence de dépiégeage du piège considéré $\nu_{dt,i}$, qui dépend de la température du matériau pendant la décharge (l'énergie de dépiégeage étant fixe et dépendant du piège), et la fréquence maximale de piégeage ν_t^{MAX}, qui dépend seulement des conditions d'implantation (densités de flux et

profondeurs moyenne d'implantation).
La dynamique de rétention résultant d'une variation de la température du matériau pour des conditions d'implantation constantes est donc résumée dans le tableau ci-dessous :

A conditions d'implantation constantes	$\nearrow T$	$\searrow T$
Fréquence de dépiégeage $\nu_{dt,i}(T)$ [s^{-1}]	$\nearrow$	$\searrow$
Taux de remplissage des pièges $R_{eq,i}^{MAX}$	$\searrow$	$\nearrow$
Inventaire intégré des pièges $Inv_{t,i}$ [IH.m^{-2}]	$\searrow$	$\nearrow$
Dynamique de rétention	Injection	Pompage

Table 5.1: Dynamique de rétention en fonction de la température du matériau à conditions d'implantation constantes (densité de flux d'implantation, énergie d'impact et angle d'incidence).

L'injection de deutérium dans la chambre à vide depuis le mur à conditions d'implantation constantes est observée dans la simulation de séquence de décharges au voisinage des deux points d'impact du plasma au niveau du divertor pendant le mode H : la haute température de surface atteinte à la fin de cette phase entraîne un dépiégeage du deutérium depuis les pièges à basse énergie. Durant la phase mode L, la baisse de la température de surface aux mêmes endroits entraîne une baisse de la fréquence de dépiégeage des pièges qui provoque une augmentation de l'inventaire local et donc un effet de pompage de deutérium par le mur.
La dynamique de rétention résultant d'une variation des conditions d'implantation à température fixe du matériau est également résumée dans le tableau ci-dessous :

A température constante	$\nearrow (\Gamma_{imp}^{i+} X_{imp}^{i+} + \Gamma_{imp}^{at} X_{imp}^{at})$	$\searrow (\Gamma_{imp}^{i+} X_{imp}^{i+} + \Gamma_{imp}^{at} X_{imp}^{at})$
Fréquence maximale de piégeage ν_t^{MAX} [s^{-1}]	$\nearrow$	$\searrow$
Taux de remplissage des pièges $R_{eq,i}^{MAX}$	$\nearrow$	$\searrow$
Inventaire intégré des pièges $Inv_{t,i}$ [IH.m^{-2}]	$\nearrow$	$\searrow$
Dynamique de rétention	Pompage	Injection

Table 5.2: Dynamique de rétention en fonction des conditions d'implantation à température du matériau constante.

Une telle dynamique de rétention est également observée dans les simulations de D-WEE présentées dans cette thèse. Une émission de deutérium dans la chambre à vide depuis la première paroi est observée après la transition entre la phase mode H et la phase mode L alors que la variation de température dans cette zone du réacteur est très faible durant toute la décharge. Cette émission de deutérium est attribuée à une baisse de l'énergie d'impact des ions et des atomes entre les deux phases (d'un facteur 1.7 à 2.8) ce qui induit une diminution de la profondeur moyenne d'implantation et par conséquent une diminution du taux de remplissage des pièges $R_{eq,i}^{MAX}$.
Les deux tableaux précédents peuvent nous donner une idée de la dynamique de mur pendant les MLBs. Durant de tels évènements, la densité de flux de chaleur augmente brusquement, entraînant une variation rapide de la température de surface (par exemple

jusqu'à $\sim$ +100 °C au point d'impact externe dans JET-ILW). Cette augmentation de température entraîne une hausse de la fréquence de dépiégeage des pièges. Selon le premier tableau, l'inventaire en IHs des pièges peut se réduire entraînant une injection de IHs dans le plasma. Ce phénomène pourrait expliquer la forte émission de photons D_α observée sur la tuile 1 du JET-ILW après des évènements MLB : l'augmentation de la température de surface entraîne une désorption de deutérium depuis les dépôts de béryllium situés sur cette tuile. Cependant, les MLBs induisent également une forte augmentation de la densité de flux d'implantation des ions Γ_{imp}^{i+} d'un facteur ~ 5 et une forte augmentation de l'énergie d'impact des ions E_{imp}^{i+} de ~ 100 eV à l'état stationnaire jusqu'à ~ 1 keV pendant les MLBs. Cette augmentation de l'énergie d'impact induit une source d'implantation des ions plus profonde, i.e. une augmentation de la profondeur d'implantation moyenne X_{imp}^{i+} d'un facteur ~ 4 dans le tungstène à un facteur ~ 8 dans le béryllium selon le code d'implantation SRIM. Par conséquent, le produit $\Gamma_{imp}^{i+} X_{imp}^{i+}$ peut augmenter d'un facteur 20 à 40 durant les MLBs. La fréquence de piégeage maximale ν_t^{MAX} augmente du même facteur ce qui pourrait entraîner un remplissage transitoire des pièges si l'augmentation de la température de surface reste modérée (cf. second tableau). Les particules piégées pendant les MLBs sont ensuite réémises dans le plasma pendant la phase inter-MLB quand les conditions stationnaires du plasma sont retrouvées. Le taux de réémission dépend de la fréquence de dépiégeage des pièges remplis dynamiquement. Ce taux pourrait causer un retard dans la reconstruction du piédestal de densité, retard observé dans le JET-ILW, et donc impacter directement la performance du réacteur. Cette hypothèse pourrait être testée expérimentalement en augmentant la température de base du divertor du JET-ILW, ce qui entraînerait une augmentation de la fréquence de dépiégeage des pièges durant la décharge. Ainsi, l'effet de pompage du mur pendant les MLBs serait diminué et la reconstruction du piédestal possiblement accélérée.

"This report, by its very length, defends itself against the risk of being read."
Winston CHURCHILL

Contents

List of Acronyms

Be	Beryllium
B.C.	Boundary Condition
BCC	Body-Centered Cubic
BDF	Backward Differentiation Formula
BTIS	Basal-Tetrahedral Interstitial Site
CAD	Computer Assisted Drawing
CFC	Carbon Fiber Composite
D	Deuterium
DFT	Density Functional Theory
D-WEE	Desorption from Wall ElemEnts module
ELM	Edge Localised Mode
FEM	Finite Element Methods
GIM	Gas Introduction Module
HCP	Hexagonal Close-Packed
HI	Hydrogen Isotope
H-mode	High confinement mode
HRTS	High Resolution Thomson Scattering diagnostic
ICRH	Ion Cyclotron Resonance Heating
ITER	"The Way" in Latin
JET	Joint European Torus
JET-C	Joint European Torus - Carbon
JET-ILW	Joint European Torus - ITER-Like Wall
JPN	JET Pulse Number
KMC	Kinetic Monte-Carlo
LHS	Left-Hand Side
L-mode	Low confinement mode
LP	Langmuir Probe

MHIMS	Migration of Hydrogen Isotopes in Materials code
MPSE	Magnetic Pre-Sheath Entrance
NBI	Neutral Beam Injection
NRA	Nuclear Reaction Analysis
OIS	Octahedral Interstitial Site
OMP	Outer MidPlane
PCBe	PolyCrystalline beryllium
PCW	PolyCrystalline tungsten
PFC	Plasma Facing Component
PFR	Private Flux Region
R-D equations	Reaction-Diffusion equations
RHS	Right-Hand Side
SIMS	Secondary Ion Mass Spectrometry
SOL	Scrape-Off Layer
SRIM	Stopping and Range of Ions in Matter code
T	Tritium
TIS	Tetrahedral Interstitial Site
TRIM	TRansport of Ions in Matter code
VDE	Vertical Displacement Event
VV	Vacuum Vessel
W	Tungsten
WEE-temp	Wall ElemEnts temperature code
WEST	Tungsten Environment in Steady-state Tokamak

Chapter 1

Fuel recycling at the boundary of nuclear fusion reactors.

Contents

1 Magnetic fusion reactors and the plasma-wall interaction.

In the required carbon-free energy mix of the future, which will be predominantly based on intermittent renewable energies, a baseload electricity supply is required. Nuclear fusion is one of the most promising options for generating such electricity on demand. The advantages of nuclear fusion are numerous: high energy efficiency of fusion fuel, abundant fuel reserves, inherent safety features, no production of greenhouse gases and no long-lived radioactive waste.
Nuclear fusion is the combination of light atomic nuclei to form a heavier nucleus and a net release of energy. Since the two reactant nuclei are positively charged, they repel each other due to the Coulomb force. To overcome this repulsion, the reactants must acquire a sufficient kinetic energy: the matter must be heated to a very high temperature. The fusion reaction with the highest cross section at the lowest temperature involves two isotopes of hydrogen, i.e. deuterium (D) and tritium (T):

$$ {}^{2}_{1}\mathrm{D} + {}^{3}_{1}\mathrm{T} \rightarrow {}^{1}_{0}\mathrm{n}\ (14.1\ \mathrm{MeV}) + {}^{4}_{2}\mathrm{He}\ (3.5\ \mathrm{MeV}) \tag{1.1} $$

To achieve a net energy production with D–T fusion reactions, a certain amount of D and T (fuel density n) must be brought at a sufficient temperature (T) during a certain time, i.e. the fuel must be confined, to allow the reactions to happen (the energy confinement time τ_E). This condition is expressed by a useful figure of merit: the *triple product* $nT\tau_E$. The value of the triple product to reach ignition of a fusion reactor, a self-sustaining condition in which the energy sinks of the reactor are counterbalanced by the energy source carried by the charged products of the fusion reaction (E_{ch}, carried by ${}^{4}_{2}\mathrm{He}$ in the case of the D–T reaction), is [1]:

$$ nT\tau_E \geq \frac{12}{\langle \sigma v \rangle} \frac{T^2}{E_{ch}}\ \mathrm{m}^{-3}.\mathrm{keV.s} \tag{1.2} $$

where $\langle \sigma v \rangle$ is the reaction rate coefficient of D–T fusion [$\mathrm{m}^3.\mathrm{s}^{-1}$]. For the D–T reaction, the minimum of the triple product occurs at $T = 14$ keV which corresponds approximatively to a value of $nT\tau_E \geq 3 \times 10^{21}\ \mathrm{m}^{-3}.\mathrm{keV.s}$ [1].
At these temperatures, well above typical ionisation energies (13.6 eV in the hydrogen case), the fusion reactants exist in a plasma state. Magnetic confinement exploits the charged nature of the plasma particles to confine them using a magnetic field. Indeed, charged particles in a magnetic field travel along the magnetic field lines while gyrating in the plane transversal to them. Among all the magnetic fusion reactors, the one that has given the highest level of performance (highest τ_E) is the so-called *tokamak*. Tokamaks are torus machines that generate bended magnetic field lines so that the particles follow closed trajectories as seen in figure 1.1. The confinement of the plasma in the direction of the torus axis is achieved by generating a toroidal magnetic field thanks to toroidal field coils. To avoid plasma drifts that cause particle losses, a poloidal magnetic field is generated by an electrical current driven in the plasma in the toroidal direction. This electrical current

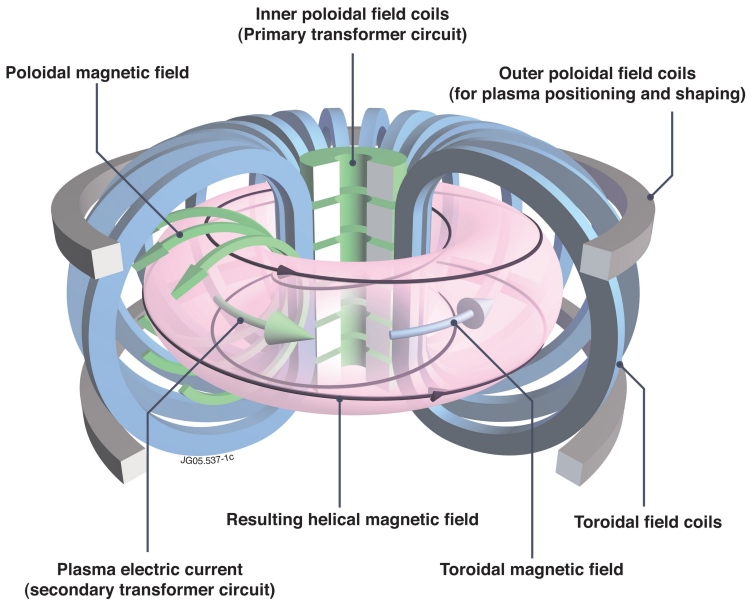

Figure 1.1: Sketch of a tokamak. The toroidal field coils and the plasma electric current create a helical magnetic field around flux surfaces. The plasma charged particles follow this magnetic field describing helical trajectories. Picture taken from reference [2].

is created by the inner poloidal field coils through a transformer action. The combination of the poloidal and toroidal magnetic fields generates a helical magnetic field. The charged particles of the plasma flow around the torus along closed helical magnetic field lines and are confined. These helical field lines wrap around closed surfaces that are called magnetic flux surfaces. Additional poloidal field coils can be used to shape and position the plasma. The heating system generates through different mechanisms (ohmic heating, neutral-beam injection, radio-frequency heating) the very high temperatures required at the centre of the poloidal cross-section of the torus to trigger fusion reactions.

However, the confinement provided by the magnetic fields is not perfect[1]. Turbulence phenomena create a transport of particle and energy transverse to the magnetic fields (often referred to as *anomalous transport*). This net flow of particles and heat reaches a region where the magnetic field lines intercept the wall of the reactor and therefore are opened. In this region, particles and heat flow along the open magnetic field lines and reach the wall surfaces: particles are deconfined. Moreover, in front of the wall an electrostatic sheath arises, the so-called Debye sheath, in which an electrostatic potential further accelerates the ions into the material surfaces. Thus a high flux of energetic particles flows into the wall and can cause severe damages to the plasma facing materials like erosion or bulk damages. Ions interact with the wall and neutralise through recombination: the wall acts as a sink of plasma. However, the wall is not necessarily a mass sink. Indeed the particles can subsequently be re-emitted as neutrals into the vacuum

[1]The confinement in fusion reactors must not be perfect. Indeed, the energy must be collected for electricity generation and the fusion ashes ($^4_2$He in the case of the D–T reaction) must be exhausted for maintaining the discharge.

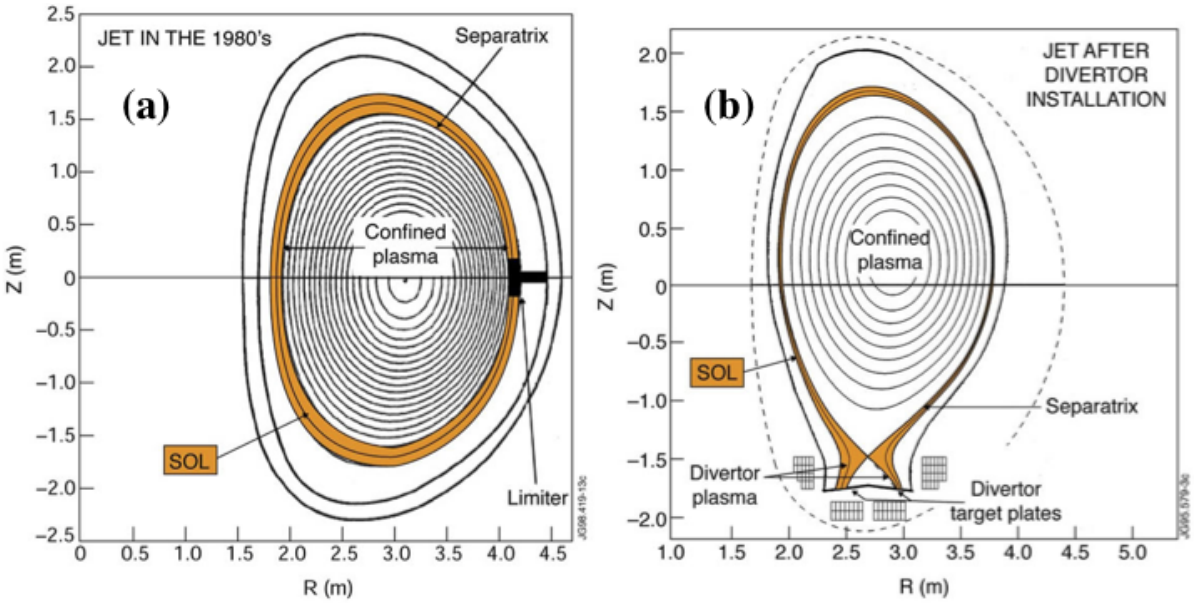

Figure 1.2: Limiter (a) and divertor (b) configurations. The region of the reactor with closed field lines is called the core while the region with open field lines is called the SOL. The core and the SOL are delimited by the separatrix. Picture taken from reference [3].

vessel where they can be ionised again. This back-and-forth of the particles between the plasma and the wall is called *recycling* and is the subject of this PhD. Recycling is part of a variety of processes involving the plasma and the wall which are collectively known as *plasma-wall interaction*.

The confined region, where the magnetic field lines are closed, is called the *core region*, while the unconfined region, where the magnetic field lines are opened, is called the *Scrape-Off Layer* (SOL). The core region and the SOL are delimited by the last closed flux surface also called *separatrix* (cf. figure 1.2). The intersections of the separatrix with the wall are called *strike-points*. Some Plasma Facing Components (PFC) are especially designed to receive the high plasma flux. The limiter is a component extending inside the SOL, effectively limiting the contact between the plasma and the rest of the vacuum vessel (cf. figure 1.2.a). However, material eroded from the limiter can enter directly into the core region, degrading plasma performance through radiation and dilution. As a workaround, scientists and engineers have developed the divertor. The divertor consists in altering the magnetic topology of the torus to move the plasma-wall interaction away from the core region. The plasma flow is diverted towards dedicated PFCs called divertor targets (cf. figure 1.2.b). In this magnetic configuration, the separatrix intersects at a region of zero poloidal magnetic field known as the *X-point*. The zone below the X-point and between the two strike-points is called the *Private Flux Region* (PFR). The divertor is often closed with baffles which confine the recycled neutrals and entail a higher neutral pressure effectively increasing the pumping of fuel, fusion ashes and eroded particles.

2 The ITER and JET ITER-Like Wall projects.

The most ambitious project in the nuclear fusion domain is the ITER project. ITER ("The Way" in Latin) will be the biggest tokamak ever built and aims to demonstrate the viability of nuclear fusion as an energy source. This project was launched in 2006 by a consortium of seven members: the European Union, China, India, Japan, Russia, South Korea and the United States. Its construction began in 2010 in the South of France and was half completed in November 2017. The first plasma operation is expected for the end of 2025. The goals of ITER are to reach for the first time the breakeven (when the heat produced by the fusion reactions is equal to the heat injected in the plasma by external means, i.e. a power gain $Q = 1$) and to produce 500 MW of fusion power for 50 MW of injected heating power ($Q = 10$) during long pulse operations of 400 to 600 s.

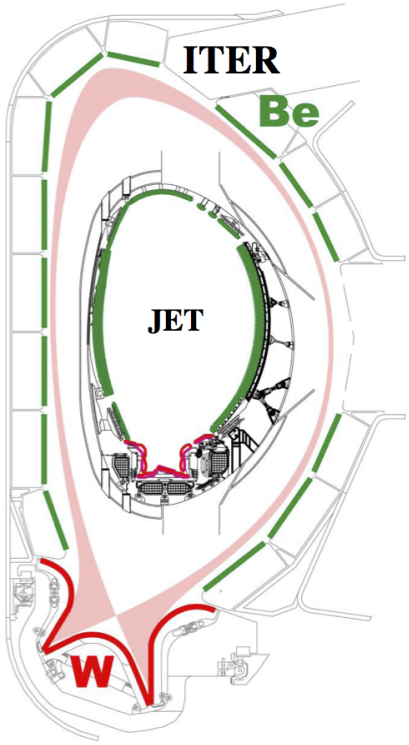

Figure 1.3: Poloidal cross-section of the ITER tokamak. The ITER wall is made of tungsten in the divertor (red) and of beryllium in the first-wall (green). The JET ITER-Like Wall operates with the same material combination as ITER. Picture taken from reference [4].

ITER will have a major radius of 6.2 m with a D-shaped vacuum vessel representing a plasma volume of 840 m^3. Its wall will be made of PFCs which will be actively-cooled with water (with inlet temperature of 70 °C) to exhaust the heat produced by the nuclear fusion reactions as well as the heat injected through the external heating systems. The PFCs will have two different surface materials depending on their location in the vacuum vessel: the divertor will be made of the so-called monoblocks with massive tungsten (W) as surface material (in red in figure 1.3) [5] while the blanket modules in the first-wall

will have massive beryllium (Be, in green in figure 1.3) [6]. W has been selected in the divertor for its low sputtering yield, its low retention of hydrogen isotopes and its high melting temperature [7]. However, due to its high atomic number, W induces excessive radiation losses in the plasma core. It is therefore crucial to limit the sputtering source of W at the divertor targets. Be has been chosen as surface material for the first-wall due its low atomic number (hence inducing lower radiation losses), its ability to remove oxygen from the plasma through chemical gettering and its ability to pump hydrogen almost continuously during short discharges [7].

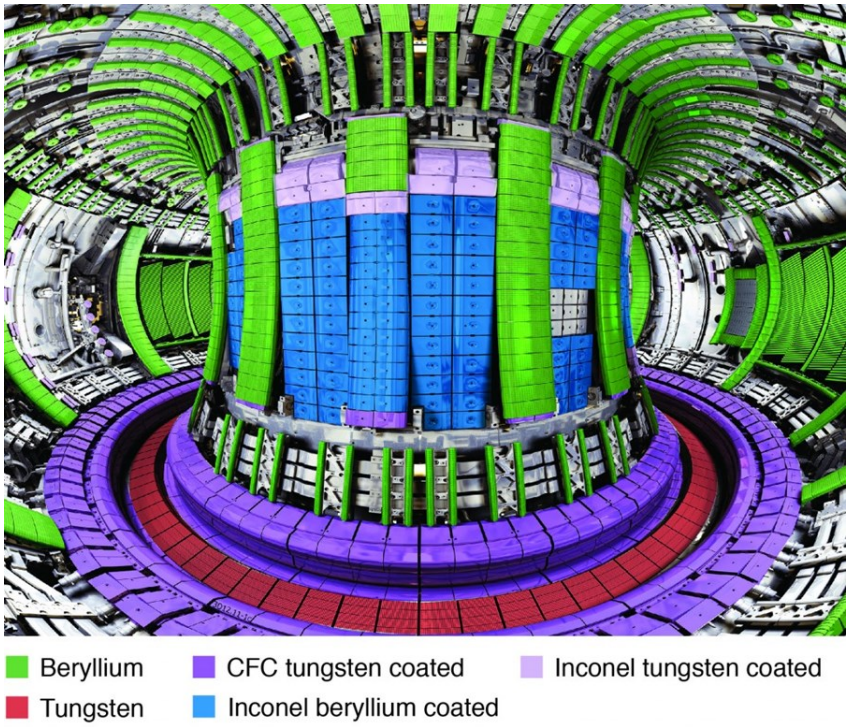

Figure 1.4: Vacuum vessel of the JET ITER-Like Wall tokamak. The different plasma facing materials composing the wall are indicated with colors. Picture taken from reference [8].

The largest tokamak in operation, the Joint European Torus (JET), holds the current world record for controlled fusion power. In 1997, JET produced 16 MW of fusion power for 24 MW of injected power ($Q = 0.67$). JET is smaller than ITER in all dimensions (cf. figure 1.3, major radius of 3 m, plasma volume of $\sim$ 100 m^3). In the period 2009-2011, JET underwent an upgrade from a full carbon wall (JET-C) with all PFCs made of Carbon Fiber Composite (CFC) to a full metallic wall with the ITER material combination. This new wall configuration, called ITER-Like Wall (ILW) is composed of massive W in the outer horizontal target plate in the divertor, W-coated CFC tiles elsewhere in the divertor, massive Be and Be-coated inconel tiles in the first-wall (cf. figure 1.4). The JET-ILW PFCs are inertially-cooled. The vacuum vessel is embedded in an interspace gas baking system which maintains a base temperature of 50 °C in the divertor and of 200 °C in the first-wall. The JET-ILW tokamak provides an ideal test bed in view of the ITER operation and has already achieved its primary goals

of demonstrating plasma compatibility with the W/Be wall and the overall reduction in fuel retention. The work presented in this PhD focuses on the JET-ILW tokamak.

3 Fuel recycling at the wall.

The physical processes involved in the recycling of the fuel (hydrogen isotopes, HI) on the plasma facing materials of nuclear fusion reactors is displayed in figure 1.5.

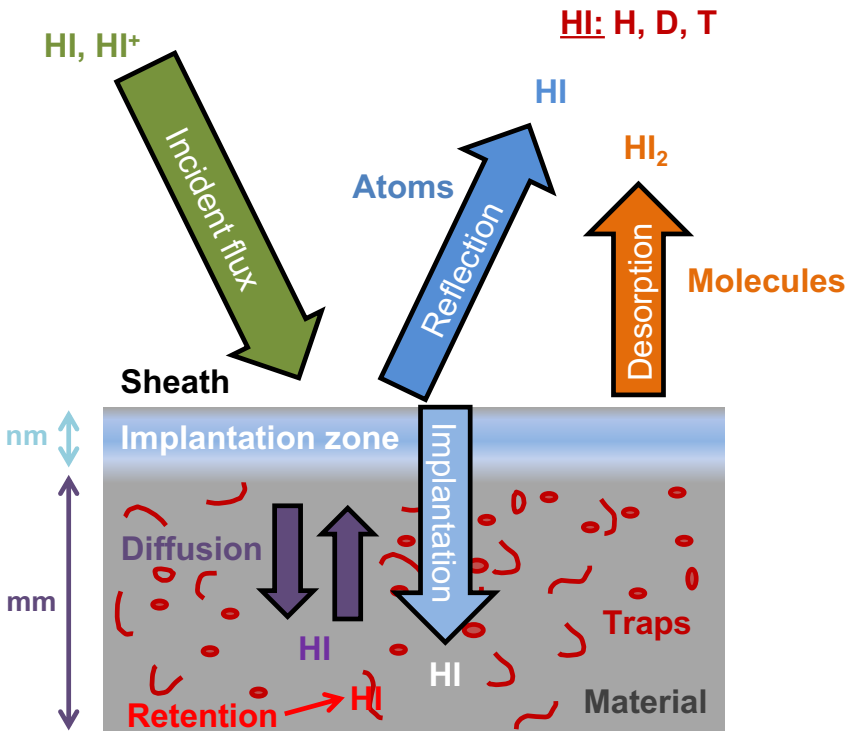

Figure 1.5: Sketch of the physical processes involved in the interaction between the hydrogen isotopes (HI) and the plasma facing materials of nuclear fusion reactors.

First, materials in reactors are exposed to extremely high fluxes of particles, with flux densities ranging from 10^{18} $m^{-2}.s^{-1}$ up to 10^{24} $m^{-2}.s^{-1}$ depending on their location and the SOL plasma conditions. Those particles are both in the form of ions and atoms. The incident ions are accelerated by the sheath potential which increases their kinetic energy. Ions can therefore reach impact energies from 10 eV up to 500 eV depending on the SOL plasma conditions. Under highly energetic transient events, this impact energy can even exceed 1 keV. Incident atoms resulting from charge exchange processes occurring in the plasma can also impact materials. The charge exchange atoms can originate from both the SOL plasma and the core plasma leading to a broad distribution of impact energy. The proximity of the neutral sources (wall) to the low temperature plasma in the SOL leads to a dominating low energy part (< 100 eV).

Such energetic incident particles (green arrow in figure 1.5) penetrate inside the material and experience collisions with the material atoms, dissipating their kinetic energy (as well as the recombination energy for ions). A part of this particles are reflected back to the plasma in the form of atoms (dark blue arrow in figure 1.5). The reflected atoms carry a part of their initial kinetic energy and represent a recycling source of hot particles for the plasma.
The HI particles that are not reflected implant inside the material and thermalise (light blue arrow in figure 1.5), in a zone of several tenths of nanometers depth called the implantation zone. Due to the inhomogeneity of the implantation source, a density gradient builds up in the material with a maximum density at a range of few nanometers. This gradient induces a transport of HI by diffusion in the direction of the surface and in the direction of the depth of the material (purple arrows in figure 1.5). During their randow walk, HIs may encounter traps that will retain them. They can escape from these traps if their kinetic energy is sufficient. The higher the material temperature is, the quicker they can escape from traps.
Traps are lattice defects of the material which have the capacity to retain HI atoms or other plasma species leading to a slowing down of the HI diffusion. The trapping of HI leads to the so-called retention process. Traps are created during the manufacturing of the material (intrinsic traps like grain boundaries or dislocations) or during plasma irradiation (plasma-induced traps like vacancies or bubbles). Traps can be divided into two groups according to their capacity to retain HI: the saturable traps that can accommodate a limited number of HI atoms (e.g. vacancies, dislocations, impurity atoms, etc.) and unsaturable traps that can accommodate an unlimited amount of HI often in the forms of molecules (e.g. bubbles). A sketch of various lattice defects of crystal are shown in figure 1.6.
The HI atoms can eventually reach the rear surface of the PFCs leading to the process called permeation. They can also reach the front surface of the material, recombine with a counterpart to form a HI molecule which can desorb into the plasma. This process is called desorption or outgassing (orange arrow in figure 1.5). These desorbed molecules, which have a kinetic energy on the order of the material thermal energy, induce a second recycling source of cold particles for the plasma.
All the processes described above are involved in the dynamics of the recycling phenomenon. Now, one will introduce some quantities that describe the local recycling situation at the wall surface and which will be used throughout this PhD. First, the reflection process is often characterised through the reflection coefficient, which is the ratio between the averaged total number of reflected particles per incident particles. Reflection of particle is a quick process ($< 10^{-12}$ s) and thus the reflection coefficient can be expressed in terms of flux ratio. It is defined for a given type of incident fuel particles j (either ions or atoms) on a given material:

$$R_n^j(E_{imp}^j, \alpha_{imp}^j) = \frac{\Gamma_{ref}^j}{\Gamma_{inc}^j} \tag{1.3}$$

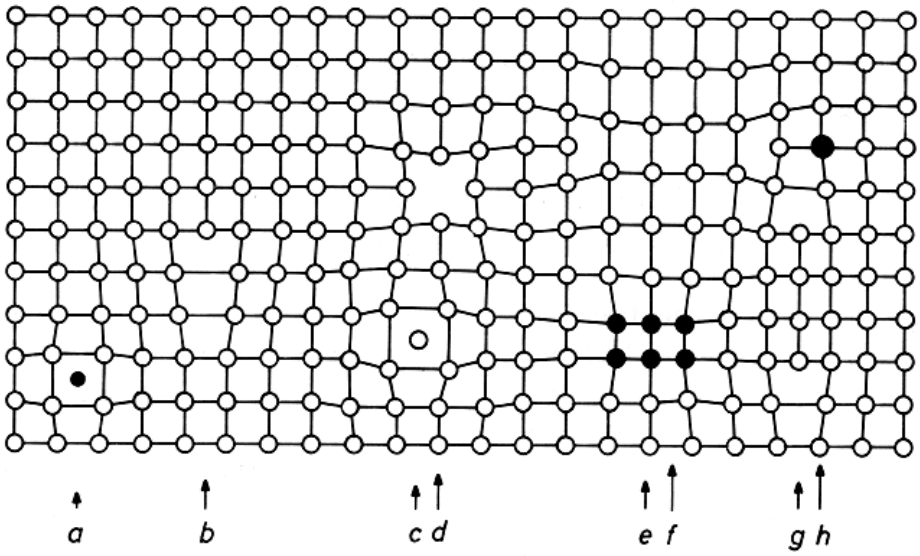

Figure 1.6: Sketch of various crystal lattice defects. Picture taken from reference [9].

where Γ^j_{ref} is its reflected flux density [HI.m^{-2}.s^{-1}] and Γ^j_{inc} its incident flux density [HI.m^{-2}.s^{-1}]. The reflection coefficient is function of the impact energy of the particles E^j_{imp} [eV] and of their angle of incidence of α^j_{imp} [°]. The latter is defined in this PhD as the angle between the velocity vector of the incident particles and the material surface [10]. Consequently, for a normal incidence, α^j_{imp} is equal to 90°. The values of this coefficient as a function of the parameters of incidence are obtained experimentally in ion beam experiments with, for example, a time of flight detector [11]. Monte-Carlo codes like TRIM (TRansport of Ions in Matter) [12] can also give the values of this coefficient through simulations of the particle collisions with the material (under the binary collision approximation) and of the flight path of the reflected particles.
It is also convenient to compare the implantation and the desorption processes through the *molecular recycling coefficient* R_m defined as follows:

$$R_m = \frac{\Gamma_{out}}{\Gamma^{i+}_{imp} + \Gamma^{at}_{imp}} \tag{1.4}$$

where Γ_{out} is the outgassing/desorption flux density of HI [HI.m^{-2}.s^{-1}] and Γ^{i+}_{imp} and Γ^{at}_{imp} are the implantation flux densities of ions and atoms respectively [HI.m^{-2}.s^{-1}]. Due to the very low slowing down time of implanted particles ($< 10^{-12}$ s), both flux densities can be expressed as a function of the respected incident flux densities and reflection coefficients:

$$\Gamma^j_{imp} = (1 - R^j_n)\Gamma^j_{inc} \tag{1.5}$$

The D desorbs from the wall in the form of molecules. Hence, the flux density of molecules

desorbing from the wall is half the value of Γ_{out}. It is expressed in terms of HI atoms to have the same dimensionnality as the incident and reflected flux densities. The comparison of R_m with 1 indicates the local behaviour of the material w.r.t. HI. When $R_m < 1$, $\Gamma_{out} < \Gamma^{i+}_{imp} + \Gamma^{at}_{imp}$ and the wall retains HI (pumping effect from the plasma point of view). Inversely, when $R_m > 1$, $\Gamma_{out} > \Gamma^{i+}_{imp} + \Gamma^{at}_{imp}$ and the wall releases HI into the plasma (fuelling effect).

4 Plasma-wall interaction during plasma discharges.

The fuel recycling at the wall involves a continuous exchange of particles between the plasma and the wall. The so-called particle balance (also called gas balance) gives a global insight into this exchange. Particle balance is a method performed during and after the plasma discharge which enables to derive the time derivative of the total fuel inventory of the wall $dN_{wall,tot}/dt$ [at.s^{-1}] from measurements of the injected and exhausted particle fluxes and of the plasma content [13]. $dN_{wall,tot}/dt$ is often referred to as *retention flux* or *retention rate*. This balance equation will be introduced in the chapter 3 of this PhD. A review of the particle balance method applied to nuclear fusion reactors can be found in reference [13].

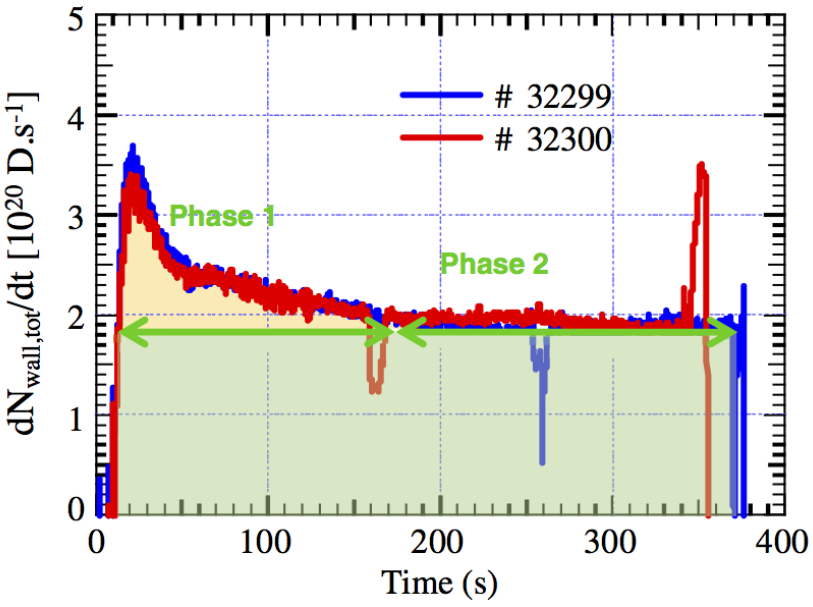

Figure 1.7: Time evolution of the retention flux for two consecutive long discharges in Tore Supra. The time evolution exhibits two phases: first a decay with a e-folding characteristic time of $\sim$ 60 s (phase 1) followed by a stabilisation of the retention flux to a constant value (phase 2). Picture taken from reference [13]. The original figure has been modified.

Figure 1.7 exhibits a typical time evolution of the retention flux during a plasma discharge. The retention flux is positive, which indicates an increase of the wall inventory $N_{wall,tot}$ throughout the discharge: the wall pumps fuel from the plasma. This time evolution

presents two phases. First, a peak in the retention flux always occurs at the start of the discharge. After the peak, the retention flux decays with a characteristic time ranging from 1 to $\sim$ 100 s and tends to saturate. Shorter decays are generally observed in diverted discharges while longer ones occur in limiter plasmas [13]. This first phase is attributed to direct implantation of ions and neutrals in the materials composing the tokamak wall with possible diffusion and trapping into the bulk material. A part of the fuel retained during this first phase, depicted by the beige area in figure 1.7, is retained temporarily during the plasma discharge and is detrapped, outgassed into the vacuum chamber and pumped after the discharge. This part of the retention is referred to as *dynamic retention*. The dynamic retention is material dependent as it was exemplified in the JET tokamak at the end of the 1980s. An order of magnitude higher retention flux during discharge (some 10^{21} D.s^{-1}) has been observed after the replacement of graphite limiter tiles with beryllium tiles [14]. A simultaneous increase of fuel release after discharge has also been noticed.

During the second phase, the retention flux levels off at a constant value. The retention due to fuel implantation and trapping is considered as being saturated at the end of the first phase. Thus, this second retention phase is attributed to co-deposition of HI with eroded wall material forming HI rich layers on top of PFCs. This retention flux is dependent on the plasma conditions. The constant retention flux entails a linear growth of the fuel inventory with the discharge duration (cf. green area in figure 1.7). As a consequence, the fuel co-deposition is considered as the most dominant long-term retention mechanism. In contrast to the dynamic retention, the long-term (or static) fuel retention is defined as the fuel retained in traps during discharge and which remains trapped during several days or months after the discharge.

The wall inventory $N_{wall,tot}$ from the start of the plasma (in reality the variation of the inventory $\Delta N_{wall,tot}$) can be obtained by time integration of the retention flux. This HI wall content can be compared with the HI plasma content. In figure 1.8.a, the time evolution of the plasma content during a Low-confinement mode divertor discharge in the JET-ILW tokamak is shown [15]. The discharge has been performed without pumping by the divertor cryopumps, which ensures a good estimate of the retention flux through the particle balance method. In figure 1.8.a, the time evolution of the retention flux $dN_{wall,tot}/dt$ is also displayed. One can note a high retention flux during the discharge, some 10^{21} D.s^{-1}, very similar to the one observed in JET with beryllium tiles [14]. The time evolution of the resulting wall inventory during the same discharge is displayed in figure 1.8.b. One can note that, at the beginning of the flat-top phase of the discharge (at $t = 50$ s), $N_{wall,tot}$ is already a factor of ~ 4 higher than the plasma content and keeps on increasing. At the end of the flat-top phase (at $t = 62$ s), the wall content is a factor of 6 higher than the plasma content. This factor increases up to 24 during high density High-confinement mode discharge according to Philipps et al. [15]. Almost all these retained HI atoms are released after the discharge and are therefore part of the dynamic retention. In JET-ILW diverted discharges, a ratio of dynamic retention to long-term retention of 10 has been measured [15]. This indicates the prevailing role of dynamic retention during a specific discharge in this machine, mainly due to the time scale of the experimental

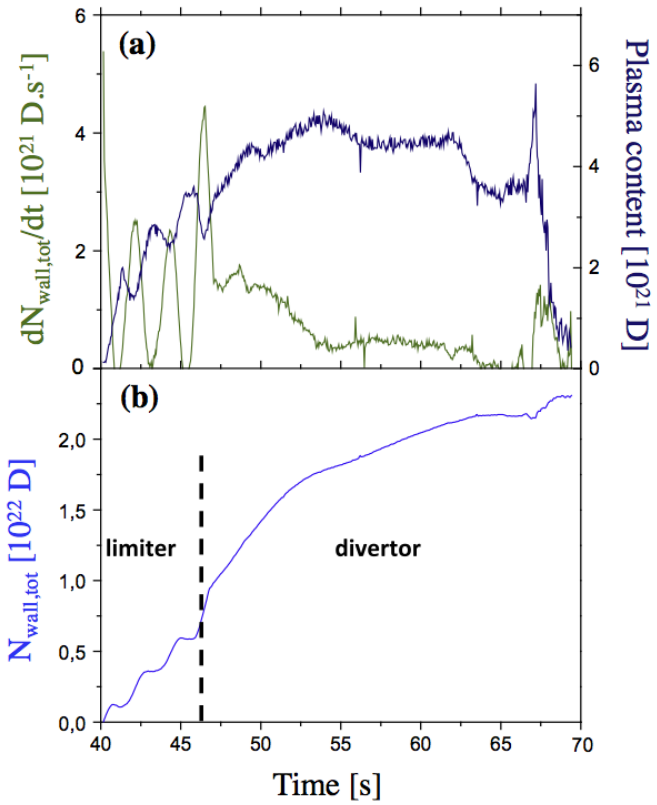

Figure 1.8: Time evolution of the retention flux $dN_{wall,tot}/dt$ (a), of the plasma ion content (a) and of the wall inventory $N_{wall,tot}$ (b) during a L-mode divertor discharge in the JET-ILW (without pumping by the divertor cryopumps). Picture taken from reference [15].

discharges in this reactor (tens of seconds). However the long-term retention dominates the overall retention as it builds up discharge after discharge: in JET-ILW, every 10 discharges, the increase of long-term retention is equal to the dynamic retention during a single discharge.

5 Effect of recycling on the operation and on the performance of nuclear fusion reactors.

As it was seen in the previous section, the wall of nuclear fusion reactors stores fuel and the amount of retained fuel is extremely high and increases discharge after discharge. This characteristic directly affects the operation of current tokamaks and will affect the operation of the future ITER tokamak. First, the tritium inventory in ITER must be limited due to the radioactive nature of tritium and due to its cost of production. The current ITER tritium inventory limit is fixed at 700 g inside the tokamak reactor. This quantity represents a safety limit in case of accident with release of tritium in the neighbourhood of the reactor. The question of the tritium retention has attracted lots of attention from material scientists, especially within the last two decades. The JET-ILW

tokamak has demonstrated a substantial drop of the long-term retention flux of D by more than one order of magnitude (factor of 10 – 20) with the introduction of the Be+W wall [16]. According to Brezinsek et al., the number of $Q = 10$ discharges to reach the tritium inventory limit of 700 g in ITER amounts to 1500 [16]. However, this PhD is focused on the understanding of the consequences of recycling and retention on the operation and the performance of a tokamak discharge with the aim of achieving a $Q = 10$ discharge in ITER.

First, the wall acts as a pump for the plasma. This feature is particularly interesting during the start-up phase of the discharges which is usually performed in limiter configuration with the plasma leant on inboard or outboard limiters. Due to the very low gas pressure at the inlet of the pumping ducts during such limiter phases, the particle flux exhausted by the external pumps is very low. The density control during this critical phase is therefore altered. The pumping effect of the wall, i.e. the dynamic retention, can compensate the lack of external pumping. Be has been selected as material for the ITER first-wall partly for this reason. In JET-ILW, Philipps et al. have measured a flat top retention flux of 10^{21} D.s^{-1} in the beginning of limiter discharges with a moderate temporal decrease. According to them, this dynamic retention is sufficient to provide wall pumping in the start-up phase of ITER discharges [15].

The wall can pump HI from the plasma but can also release them into the plasma. This effect has been exemplified during long-pulse operation in the Tore Supra tokamak with Multilimiter Configuration (from 1988 to 1999). During such operations, a slow rise of the density has been detected which entailed a disruption of the discharges [17]. This loss of density control was attributed to the outgassing of inertially cooled components located in remote areas of the vacuum vessel which were heated by the radiated power from the plasma. The higher the input power, the faster the density raised and the quicker the disruption occurred (cf. figure 1.9). An update of the internal component of the reactor (the CIEL configuration) was necessary to control the wall temperature and to allow such long-pulse operations. Steady-state discharges as long as 6 min were performed with this new configuration [18]. Such phenomenon has not been observed in JET-ILW due to the short duration of the discharges. However, as it was seen in section 4, the dynamic retention reservoir is significant, representing 6 times the usual plasma content. This reservoir is susceptible to empty for moderate temperature increase. In ITER, the first-wall panels have been designed considering steady-state heat flux densities ranging from 1 up to 4.7 MW.m^{-2} and a maximum Be temperature of $\sim$ 670 °C under those steady-state heat loads [6]. This indicates that, during full power operation, the Be first-wall will experience temperature excursions from its base temperature of 70 °C up to its steady-state temperature of 670 °C and will possibly release its fuel content into the plasma. The rate of this release will depend on the rate of the temperature increase and on the rate of all the HI–material interaction processes described in section 3.

Eventually, it has been recently discussed a possible impact of recycling on the tokamak

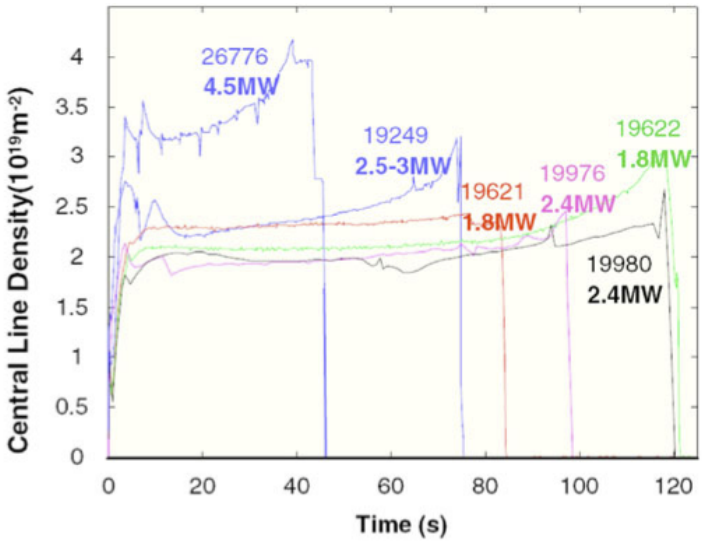

Figure 1.9: Loss of density control observed during long-pulse operation in Tore Supra with the Multilimiter Configuration (from 1988 to 1999). The six plasma pulses differ by the input power coupled to the plasma: the higher the power, the faster the density rises and the quicker the disruption occurs. Picture taken from reference [18].

performances during High confinement mode. When a magnetically confined plasma is heated strongly and a threshold heating power level is exceeded, it may spontaneously transit from a Low confinement (or L-mode) state to a High confinement (or H-mode) state [19]. In H-mode, τ_E is significantly enhanced, typically by a factor of 2. This enhancement is attributed to a local suppression of turbulence in the vicinity of the separatrix which leads to a reduction of transport and a steepening of the edge profiles of density and temperature [20]. This zone of high gradient is often referred to as *pedestal*. The H-mode is the confinement mode foreseen for the $Q = 10$ ITER baseline scenario [21]. During H-mode, quasi-periodic violent relaxations of the pedestal, known as Edge Localised Modes (ELMs), occur with a frequency ranging between 5 and 100 Hz. ELMs lead to a significant expulsion of heat and particles in the SOL with deleterious consequences for the wall. In JET-ILW, a degraded confinement, with a decrease of the energy confinement time by about 30 %, has been observed in high density H-mode baseline scenario w.r.t. the one observed in JET-C [22]. This degraded confinement has been attributed to a delay in the recovery of the pedestal density after an ELM-crash [23]. Such delayed recovery was not observed in JET-C. In figure 1.10, coherently averaged outer midplane profiles of electron density n_e and temperature T_e measured by the high-resolution Thomson scattering system during a H-mode discharge are plotted for three times: before an ELM (0 ms), at the time of maximum drop in the pedestal pressure (1.2 ms) and at the start of the recovery phase of the density profile (5.8 ms). One can note that between 0 ms and 1.2 ms the density decreases in the core (for $R < 3.8$ m) and increases in the SOL (for $R > 3.8$ m). This increase is due to the ELM that has expelled particles from the core. In constrat, the temperature has already reached its maximal drop in both the core and the SOL. Between 1.2 and 5.8 ms, the density further

collapses in the SOL while the temperature has already started to increase due to the heating power entering the pedestal from the plasma core. At $t = 5.8$ ms, the density profile starts to recover [23].

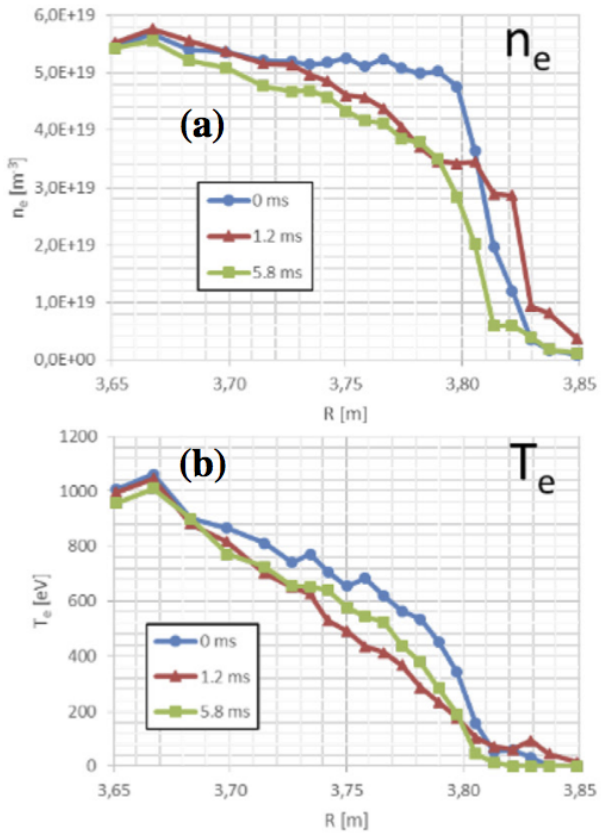

Figure 1.10: Coherently averaged high resolution Thomson scattering profiles of the electron density n_e (a) and temperature T_e (b) during a H-mode discharge in JET-ILW. The profiles are plotted before an ELM (0 ms), at the time of maximum drop in the pedestal pressure (1.2 ms) and at the start of the recovery phase of the density (5.8 ms). Picture taken from reference [23].

The reason for such delayed recovery is still unclear. Due to the short time scale of this phenomenon, the particles lost by the core during the ELM events cannot leave the tokamak system through pumping. The missing particles can only be found in two locations: the divertor or the wall.
Moreover, some interesting phenomena, that were not observed in JET-C, have appeared in the JET-ILW. In figure 1.11, the time evolution of coherently averaged heat flux at the outer divertor plate derived from infrared measurements and of the ion flux obtained from Langmuir probe measurements are shown. The peak of the heat flux at $t = 0$ s and the first peak of ion flux are due to the ELM event. A clear second peak in the outer ion flux is seen 8 ms after the ELM crash. This second peak has no correspondence with a W sputtering peak which indicates that the ions responsible for this second peak have a low energy and originate from the SOL.
Moreover, a high recycling activity has been observed after the ELM crash in the inner

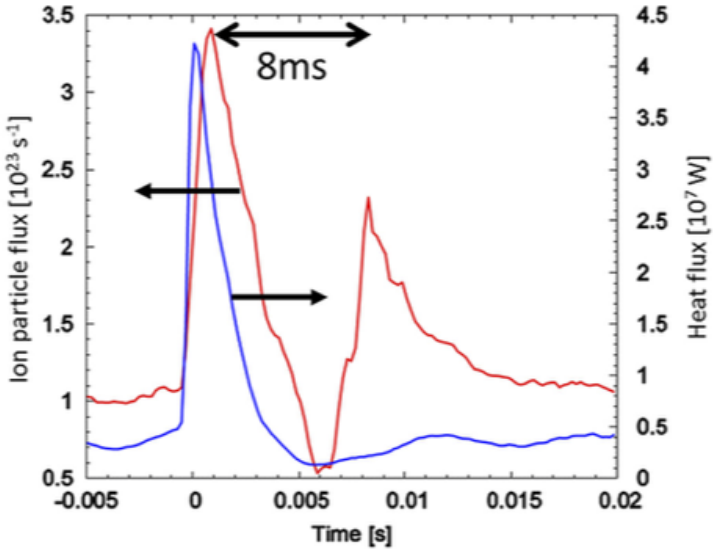

Figure 1.11: Time evolution of coherently averaged heat flux at the outer divertor plate derived from infrared measurements and of the ion flux obtained from Langmuir probe measurements. The peak of heat flux at $t = 0$ s and the first peak of ion flux are due to the ELM event. A clear second peak in the outer ion flux is seen 8 ms after the ELM crash. Picture taken from reference [23].

divertor (cf. figure 1.12). A strong D_α emission is seen on the top of tile 1 which indicates D outgassing apparently due to surface heating during the ELM-crash [23]. Then the D_α decreases within $\sim 5 - 6$ ms. On the contrary, the D_α collapses after the ELM at the inner strike-point and then increases within ~ 4 ms. This drop of the D_α, often referred to as *inverted ELM signature* is produced when a dense and cold plasma, with a D_α emission dominated by recombination, is ionised by the heat flux during the ELM [24]. This indicates a possible detachment at the inner strike-point prior to the ELM. Then, a second drop of the emission occurs at the inner strike-point (cf. figure 1.12 at $t = 11$ ms) which coincides with the secondary peak ion flux observed in the outer divertor. The reason for such coincidence is still not explained.
All these observations indicate a higher recycling activity during ELMs in the JET-ILW which is linked to the change of the wall materials. Still the impact of recycling on the confinement remains unclear and requires further investigations.

6 Experimental study of the hydrogen isotope–material interaction.

The HI–material interaction under tokamak conditions is rather unique in terms of particle fluxes and energies. However, its study remains challenging due to practical difficulties like measurements of local plasma conditions and diagnostics durability. Therefore, material scientists rely on alternative methods to study the interaction between HI and materials. The ion implantation experiments, like ion accelerators (e.g. the Aix Marseille

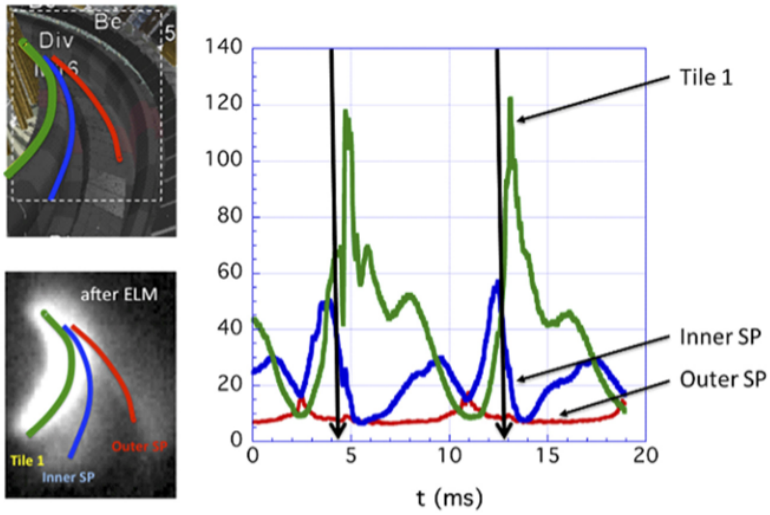

Figure 1.12: Fast camera signals [arb. units] showing the D_α emission in the divertor during a JET-ILW H-mode discharge. The emission from the outer strike-point (red), from the inner strike-point (blue) and on top of the inner divertor tile 1 (green) are shown. The vertical black arrows indicate the occurrence of an ELM event. After the ELM, the D_α emission on top of tile 1 increases strongly and later decays within $\sim 5 - 6$ ms while the emission at the inner strike-point decreases abruptly and later increases. A second drop of the emission occurs at the inner strike-point at $t = 11$ ms which coincides with a D_α peak in the outer divertor. Picture taken from reference [23].

University ion source [25] or the ARTOSS facility [26]) and linear plasma generators (e.g. PSI-2 or Magnum-PSI [27]), enable to study this interaction under well-controlled conditions. Ion accelerators have well defined ion flux densities (up to 10^{20} $m^{-2}.s^{-1}$) and energies (from 100 eV up to 1 MeV). Linear plasma generators provide reactor-like conditions with higher flux densities (up to 10^{25} $m^{-2}.s^{-1}$ for Magnum-PSI) but less well defined impact energies due to the presence of a sheath (from 1 eV to 100 eV).
The resulting HI–material interaction is studied through different analysis techniques. In the following, one provides with a non-exhaustive list of techniques used in the characterisation of this interaction. The HI depth profiles in material can be obtained by Secondary Ion Mass Spectrometry (SIMS) and Nuclear Reaction Analysis (NRA). SIMS consists in launching a focused beam of heavy ions (in general noble gas like Argon) to sputter the material. The secondary ions sputtered from the material are analysed using a mass spectrometer. SIMS can give access to the density profile of HI in both atomic and molecular forms but also of impurities present in the material on depths of up to 100 nm. The measurement is only qualitative due to the variation of ionisation probabilities of the target atoms. Another measurement is therefore required to calibrate the measured density profile. An example of D and D_2 depth profiles obtained with SIMS after D implantation in Be are shown in figures 1.13.a and 1.13.b. The implantation was performed with an energy of 9 keV per D and a D incident flux density of $8 - 10 \times 10^{18}$ $D.m^{-2}.s^{-1}$ [28]. The sample was maintained at 300 K during the implantation phase. The D depth profiles were measured for different fluences (time integral of the incident flux density)

from 6×10^{19} up to 9×10^{22} D.m^{-2}.

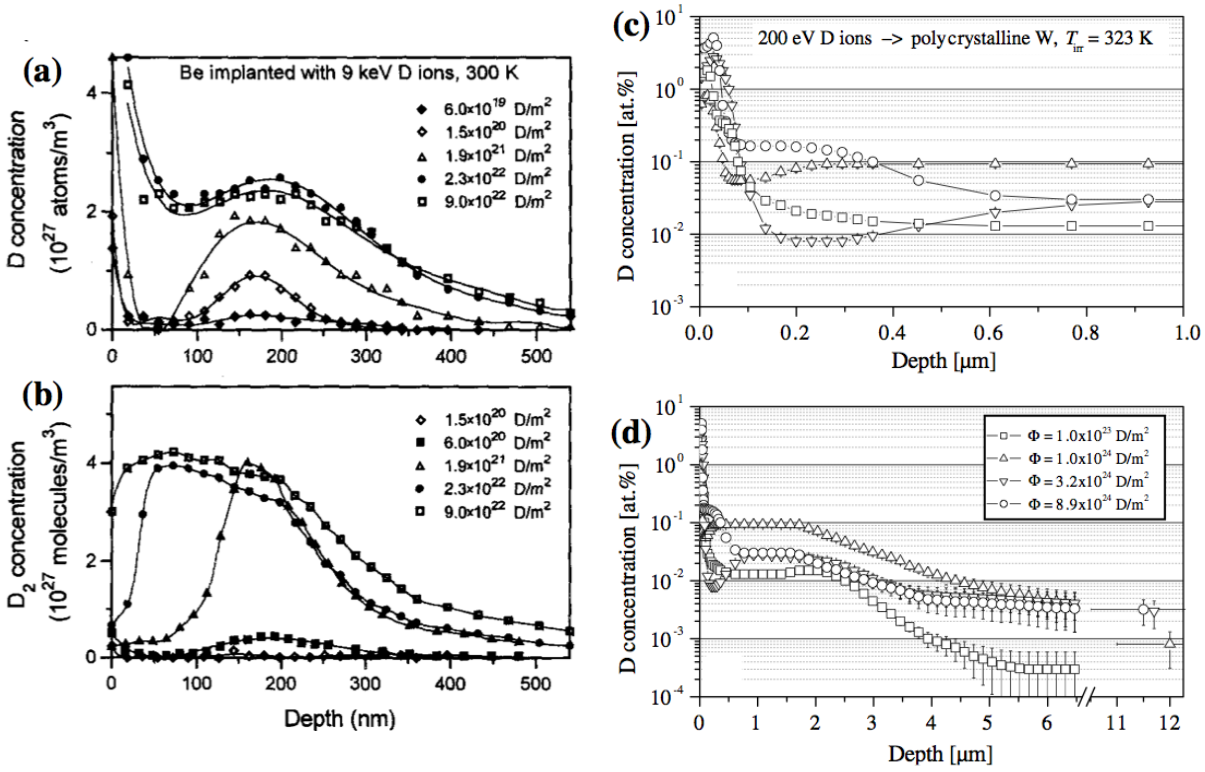

Figure 1.13: Depth profiles of D density (a) and D_2 density (b) measured with SIMS after D implantation in Be at 300 K for different D fluences (picture taken from reference [28]). Depth profiles of D density measured by NRA after D implantation in polycrystalline W at 323 K for different D fluences (c-d) (Picture taken from reference [29]). The figure (c) displays the density in the first micrometer.

NRA is another method used to probe the density profile of HI. In NRA, a projectile ion is launched on the material and reacts with the atom that one wants to probe. The nuclear reaction products are then analysed to extract its density. For example, to probe D in materials, the following nuclear reaction with helium (He) is often used:

$$\mathrm{D} + {}^3\mathrm{He} \rightarrow \mathrm{p} + \alpha \tag{1.6}$$

where p is a proton and α is an alpha particle. The energy of incident ^{3}He ions can be varied (from 500 keV to several MeV) to reach higher depth in the material (up to 7 μm in W). The D density profile can be obtained from the proton yields measured at a given ion energy with the use of a deconvolution method (using the code SIMNRA [30]). An example of NRA depth profiles of D in polycrystalline W is shown in figure 1.13c-d. The implantation was performed with an energy of 200 eV per D and an incident flux density of $3.6 \pm 1.1 \times 10^{19}$ D.m^{-2}.s^{-1} [29]. The sample was maintained at 323 K during the implantation phase. The D depth profiles were measured for different fluences from 1×10^{23} up to 8.9×10^{24} D.m^{-2}.
The density obtained with SIMS and NRA are expressed in [m^{-3}] (cf. figure 1.13.a-b)

but can also be expressed in terms of concentration. The concentration is often expressed in *atomic fraction* [at.fr] which corresponds to the ratio of the density with the material density. The *atomic percent* [at.%] is the atomic fraction expressed in percent (cf. figure 1.13.c-d). The latter unit will often be used in this PhD. The integral of the HI density, obtained with SIMS or NRA, w.r.t. the depth of the material gives the so-called areal inventory of HI [HI.m^{-2}].
To investigate the interaction of HI with traps in materials, the Thermal Desorption Spectroscopy (TDS) is often used. This method is also called Temperature Programmed Desorption (TPD). In TDS, the irradiated material is heated up in a controlled manner (often linearly with time) and the desorption of HI molecules from the sample is simultaneously recorded with a quadrupole mass spectrometer. The obtained desorption flux, or the desorption flux density if the implantation at the surface of the sample was uniform, can be plotted versus the sample temperature. The resulting plot exhibits desorption peaks at given temperatures which give informations on the binding states of HI in all the material sample. Due to the presence of these desorption peaks, this type of plots is often called TDS spectrum. Examples of TDS spectra can be seen in figure 1.14 for the case of D implanted in Be and in W with an energy of 1 keV per D, a flux density of $\sim 1 \times 10^{20}$ D.m^{-2}.s^{-1} and an implantation temperature of 300 K. The TDS were performed for different fluences ranging from 10^{21} up to 10^{25} D.m^{-2}. The integral of the desorption flux density with time gives also access to the areal inventory of HI in the sample. The comparison of the areal inventory obtained with SIMS/NRA and the one obtained with TDS can give an idea of the location of the HI retention. If the areal inventories are equal, HI are retained up to the maximum depth of measurement of SIMS/NRA. Otherwise, some of the HIs are retain more deeply in the sample.

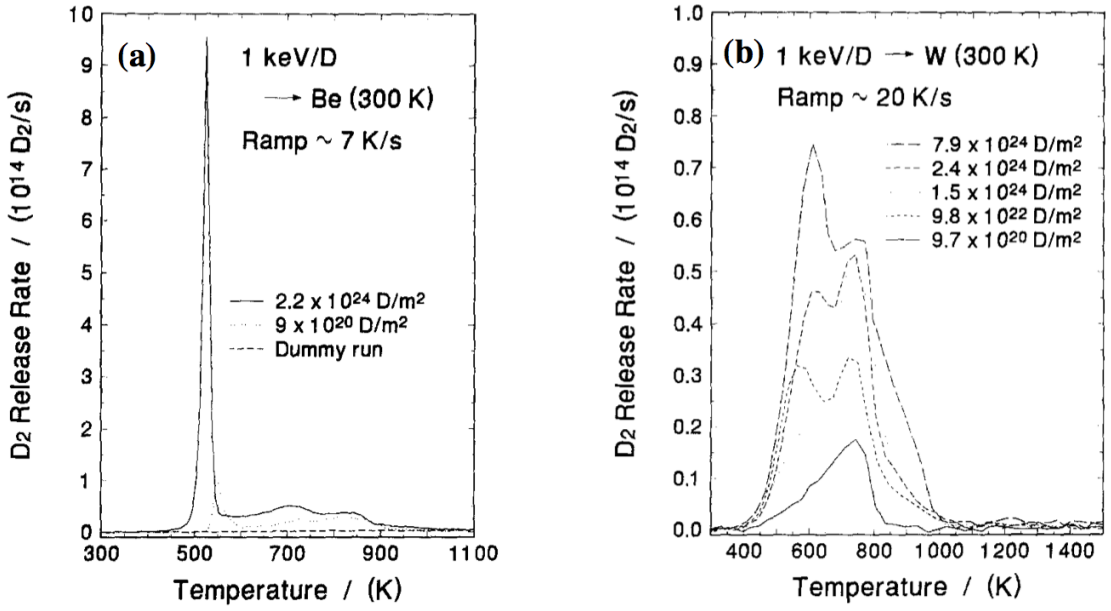

Figure 1.14: TDS spectra of D implanted in Be (a) and in W (b) at 300 K for different fluences. Picture taken from reference [31].

After implantation in accelerators or linear plasma devices, those analysis can be per-

formed ex-situ (in another facility) or in-situ (in the same facility). The latter has the advantage of avoiding the surface contamination of the sample due to air exposure (which is known to alter the results) and to give access to both the dynamic retention and the long-term retention of HI. It must be stated that the presented analysis can be performed on samples removed from fusion reactors. These analysis, called post-mortem analysis, are performed weeks or even months after the tiles removal from the machine and therefore probe only the long-term retention of HI.
The information gained with those experiments and analysis enables to identify the processes and mechanisms governing HI trapping in materials. These experimental results provide the basis for models that enable to predict the HI inventory in material and its dynamics under reactor conditions. Such model will be introduced in chapter 2.

7 Modelling of the plasma-wall interaction with edge plasma transport codes and the lack of description of the desorption dynamics.

Another way to study the plasma-wall interaction is the numerical modelling. Among the numerical tools that scientists have in their hands, the so-called edge-plasma transport codes present the most-advanced description of the plasma-wall interaction. Examples of transport codes are SOLPS [32], EDGE2D-EIRENE [33], EMC3-EIRENE [34] and SolEdge2D-EIRENE [10].
In this PhD, the SolEdge2D-EIRENE code package will be used. This code package is made of two modules: a plasma module, SolEdge2D, and a neutral module, EIRENE. The SolEdge2D version used in the following simulates plasma made of two species: HI ions and electrons. The transport of impurities is not considered. The simulated domain is the core edge and the SOL. For each species, SolEdge2D solves equations for the plasma density n (under the quasi-neutrality assumption, i.e. $n_i = n_e$), the velocity $u_\parallel$ parallel to the magnetic field $\overrightarrow{B}$ (under the ambipolarity assumption, i.e. $u_i = u_e$) and the electrons and ions temperatures T_e and T_i. The perpendicular transport is modelled by an ad-hoc diffusion closure with perpendicular anomalous diffusion coefficients $D_\perp$, $\nu_\perp$, $\chi_{\perp,e}$ and $\chi_{\perp,i}$ for n, u, T_e and T_i respectively. As an example, the perpendicular ion/electron flux density is expressed as $n\vec{v}_\perp = -D_\perp \overrightarrow{\nabla}_\perp n$. The details of the four conservation equations can be found in reference [10]. The EIRENE module models the transport of neutrals originating from recycling at the wall and their interaction with the plasma. It computes the particle, momentum and energy sources for SolEdge2D.
The SolEdge2D code relies on meshes aligned on the magnetic flux surfaces. However, these meshes are not suitable to describe the complex geometry of the wall as it is not necessarily aligned on the flux surfaces. To deal with this issue, SolEdge2D relies on an immerse boundary condition technique inspired from a Computation Fluid Dynamics method, the so-called *penalisation technique*. This approach does not require the mesh grid to be aligned with the wall. More precisely, the grid is kept as orthogonal as possible with the wall and is extended beyond the wall. Mask functions then determine whether

mesh cells belong to the plasma or to the wall and penalisation terms are added to the conservation equations to enforce the boundary conditions at the plasma–wall interface. The penalisation technique enables to handle complex and realistic wall geometries and allows to properly model the plasma-wall interaction in the full vacuum vessel (assuming axisymmetric wall components). The plasma and neutrals quantities are calculated up to the wall, like for example the quantities involved in the fuel recycling (as defined in section 3). In SolEdge2D-EIRENE, these quantities are given along a curvilinear coordinate along the wall: the s coordinate. An example of such coordinate can be found in figure 1.15.a for the case of the WEST tokamak. Moreover, an example of an output along the wall can be seen in figure 1.15.b where the total heat flux density on the WEST tokamak is plotted. More information and examples of outputs will be shown in chapter 3.

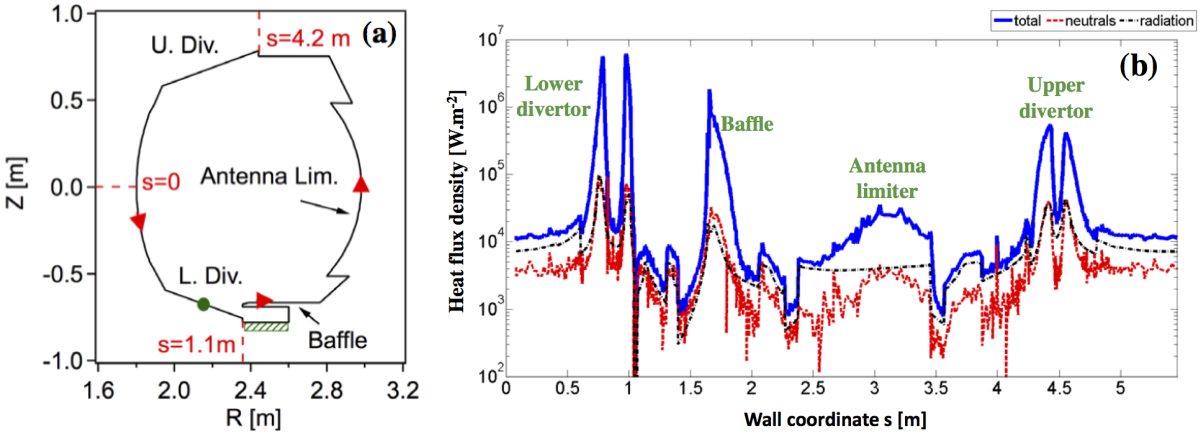

Figure 1.15: (a) Poloidal cross-section of the WEST tokamak with the definition of the curvilinear coordinate along the wall s. (b) Wall distribution of the total heat flux density (blue solid line) in WEST computed with SolEdge2D–EIRENE. The contribution of neutrals (red dashed line) and radiation (black dashed-dotted line) is also displayed. Pictures taken from reference [10].

In edge-plasma transport codes like SolEdge2D-EIRENE, the HI recycling at the wall is handled in general by the neutral solver, i.e. the EIRENE code. The overall local recycling is often defined through the total recycling coefficient that is called $RECYCT$ in EIRENE [35]:

$$RECYCT = \frac{\Gamma^{i+}_{ref} + \Gamma^{at}_{ref} + \Gamma_{out}}{\Gamma^{i+}_{inc} + \Gamma^{at}_{inc}} \tag{1.7}$$

$RECYCT$ can be expressed as a function of the reflection coefficient R^j_n and the molecular recycling coefficient R_m introduced in section 5:

$$RECYCT = \frac{[R^{i+}_n + (1 - R^{i+}_n)R_m]\,\Gamma^{i+}_{inc} + [R^{at}_n + (1 - R^{at}_n)R_m]\,\Gamma^{at}_{inc}}{\Gamma^{i+}_{inc} + \Gamma^{at}_{inc}} \tag{1.8}$$

In EIRENE, the reflection is already handled self-consistently through tabulated reflection coefficients obtained with the TRIM code [35]. The molecular desorption is set ad-hoc by the code user through the specification of $RECYCT$. Indeed, as both R_n^{i+} and R_n^{at} are calculated by EIRENE, setting $RECYCT$ to a fixed value leads to the indirect setting of R_m according to equation 1.8. $RECYCT$ is often set to 1 to force particle conservation in the simulated domain. $RECYCT$ is also set below 1 in inlet pumping ducts to simulate the particle exhaust. In any case, the dynamics of desorption is presently not handled in transport codes.
The purpose of this PhD is to develop an extension for edge plasma transport code, and especially the SolEdge2D-EIRENE code, that allows the modelling of the dynamics of local thermal desorption of hydrogen isotopes from the surface of plasma facing materials. To do so, this module has to model all the physical processes that were presented in section 5. The goal of the introduction of such wall extension is to run auto-consistent plasma-wall simulation with feedback of the wall on the plasma to study the impact of the desorption and retention dynamics on plasma operation (as seen in section 5). The long-term purpose of this endeavour will be to simulate an ELM-like event followed by an inter-ELM phase to study the possible impact of the wall on the delayed recovery of the density profile observed in the JET-ILW. The wall module will therefore be developed bearing this in mind. The next chapter of this PhD is dedicated to the description of this wall module.

Chapter 2

Development of a dynamic thermal desorption module for SolEdge2D-EIRENE.

Contents

In the previous chapter, the recycling process has been presented as well as its potential deleterious effects on plasma operation and performance. However, its experimental study remains challenging. Modelling can help the understanding of such processes. The SolEdge2D-EIRENE code package, with its ability to simulate plasma-wall interaction in realistic wall geometry, is well suited for such modelling effort. However, this code package requires a wall module able to simulate the desorption process to complete the modelling of the recycling dynamics. This chapter focuses on the description of this module, which is named Desorption from Wall ElemEnts (D-WEE).

1 The D-WEE – EIRENE coupling.

The role of the D-WEE module is to ensure communication between the EIRENE code and two other codes required to simulate the dynamics of molecular desorption. As it was seen in chapter 1 section 3, to simulate this dynamics, it is necessary to model the interaction between HI and materials composing the wall of fusion reactors, namely HI implantation, transport, trapping and desorption from the surface. The modelling of all these processes is performed by the code MHIMS (for Migration of Hydrogen Isotopes in Materials). As all this processes are strongly dependent on the wall temperature, a thermal model, called Wall ElemEnts temperature (WEE-temp), has also been developed. To illustrate more concretely the mutual interaction between these two codes, internal to D-WEE, and their external interaction with SolEdge2D-EIRENE, the diagram of the coupling architecture is displayed in figure 2.1.
One can see in this picture that D-WEE only interacts with the EIRENE code. At every EIRENE time step, the following operations are performed:

1. First, SolEdge2D updates the plasma quantities in all the simulated zone, in particular along the wall.

2. Then EIRENE calculates from TRIM tables the reflection coefficient along the wall, $R_n^j(s,t)$ (defined in chapter 1 section 3). Then it updates the particle and energy volume sources in the simulated zone. To do so, EIRENE launches from the wall the right proportion of reflected atoms from the value of $R_n^j(s,t)$ and the right proportion of desorbing molecules from the value of the molecular recycling coefficient along the wall (defined in chapter 1 section 3). EIRENE uses the value of this coefficient calculated by the MHIMS code at the preceding time step, $R_m(s, t - dt)$.

3. EIRENE also calculates the net heat flux density along the wall, $\phi_{net}(s,t)$, and communicates it to WEE-temp. $\phi_{net}(s,t)$ is obtained from a heat flux density balance at the surface of the material. In general, the plasma heat flux density given by SolEdge2D represents the main contribution to this balance. However, the heat flux density from neutral particles and from plasma radiation as well as the energy reflection are also accounted in its calculation. All this physical quantities are calculated by EIRENE.

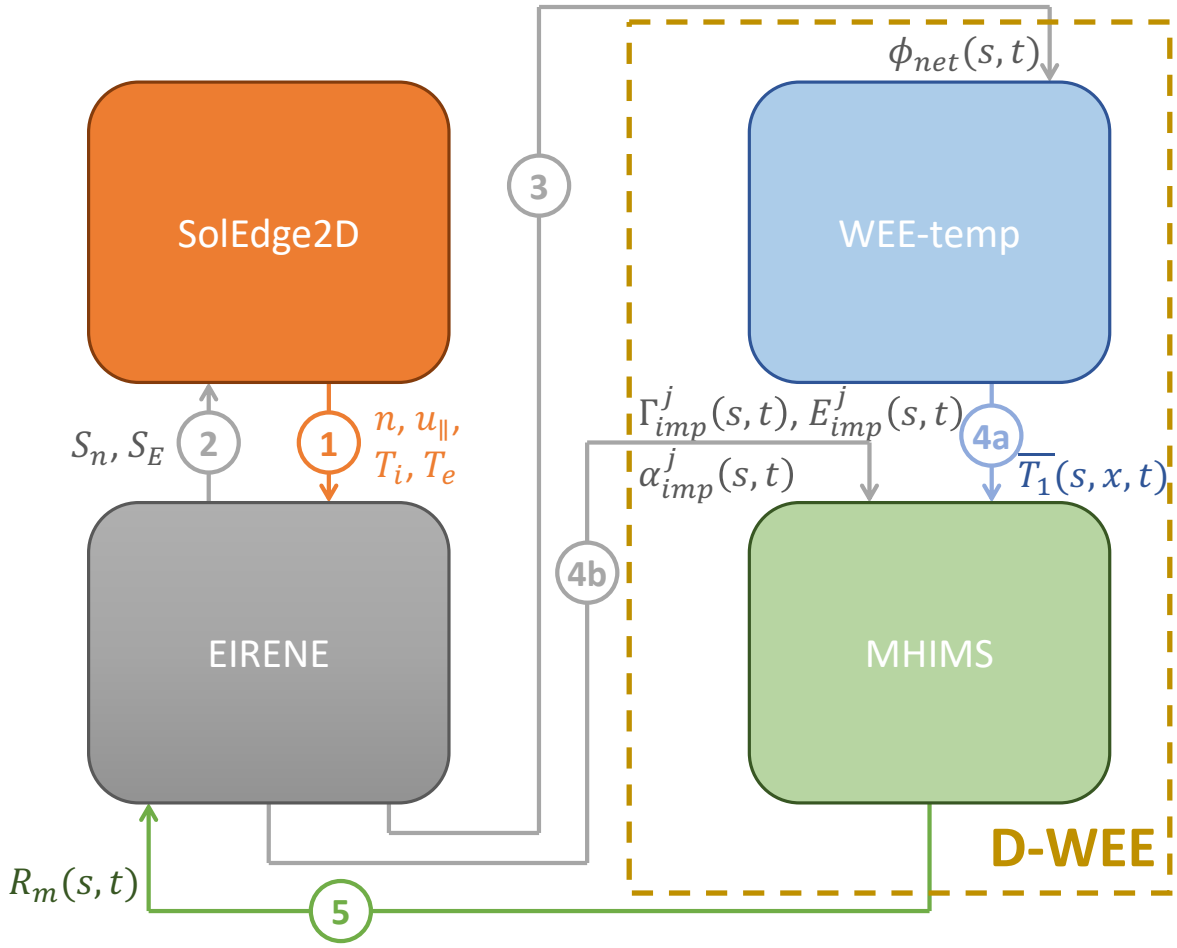

Figure 2.1: Architecture of the coupling between D-WEE and SolEdge2D-EIRENE.

4a. Then WEE-temp can update the temperature profile in the depth of the surface material of the PFCs, $\overline{T_1}(s,x,t)$ (cf. section 3 for a detailed description of the calculation), and communicates it to MHIMS.

4b. EIRENE provides the implantation parameters for both ions and atoms to MHIMS, namely the implantation flux density $\Gamma^j_{imp}(s,t)$, the mean impact energy $E^j_{imp}(s,t)$ and the mean angle of incidence $\alpha^j_{imp}(s,t)$.

5. Consequently MHIMS can calculate the desorption flux density and feeds back it to EIRENE through the molecular recycling coefficient $R_m(s,t)$ (cf. section 2 for a detailed description of the calculation). EIRENE will update the particle and energy sources accordingly at its next time step (cf. step 1).

In addition to the communication between the different codes, D-WEE also manages their parallelisation. Indeed, as it will be seen in the next sections, the equations used in both codes only depend on one spatial dimension in terms of particle and heat transport (the material depth, denoted $\vec{x}$). As a consequence, two neighbouring elements on the wall are independent. This enables both codes to be numerically parallelised in the $\vec{s}$

direction in order to run the code on several CPUs (on supercomputers) to, in fine, decrease the calculation time. This parallelisation is performed through the so-called OpenMP interface. For example, a decrease by a factor of 10 of the computational time has been estimated in the Aix-Marseille University computing center for the execution of MHIMS on 12 CPUs w.r.t. its execution on a single CPU. Due to the recent update of this machine, D-WEE can now be run on up to 32 CPUs.
The architecture of D-WEE and its coupling with EIRENE has been detailed. The next two sections will be dedicated to the description of the two codes of D-WEE, namely the MHIMS code in section 2 and the WEE-temp code in section 3.

2 Modelling of hydrogen isotope–material interaction: the MHIMS code.

As it was seen in the preceding section, the MHIMS code is able simulate HI implantation, transport, trapping and desorption from the surface of materials. MHIMS exists in different versions [36, 37] which have different levels of description of the HI–material interaction and hence different levels of complexity. In this work, the simpler version of MHIMS has been adapted to model the HI dynamics in the complete wall of fusion reactors as required in D-WEE. This section is dedicated to the description of this model.

2.1 Simplified description of the interaction between hydrogen isotope and material.

Before presenting the model used in MHIMS, the physical processes involved in the interaction between HI and material at the microscopic level will be presented. This description will enable to introduce some physical quantities that are used in the model. A HI atom/molecule interacts with a material through forces of electrostatic nature that can be attractive (e.g. Van der Waals forces, electron-proton attraction) or repulsive (e.g. electrostatic repulsion, Pauli repulsion). These forces are all conservative, resulting in a net conservative force $\overrightarrow{F}(\vec{r})$ applied to the atom/molecule, where $\vec{r}$ is the particle position. One can therefore associate to this net force a potential energy $E(\vec{r})$ linked to the force through the following expression: $\overrightarrow{F} = -\overrightarrow{\nabla} E$. Thus, the interaction between HI atom/molecule and material can be defined through this potential energy of interaction. The idealised diagram of the potential energy of interaction between a hydrogen isotope and a given material is displayed as a function of the reaction coordinate in figure 2.2 [7, 38, 36, 39, 40]. The potential energy of interaction between an isolated HI atom (from now on referred to as *HI atom*) and this material is displayed in red solid line while the potential energy between a HI atom in molecular form (from now on referred to as *HI molecule*) and this material is displayed in dashed blue line. The potential energies are defined for one HI atom, either in atomic form or molecular form. The diagram presents local minima of the potential energy which are stable sites for HI and local maxima which are unstable sites. The variation between local minimum and maximum of the potential

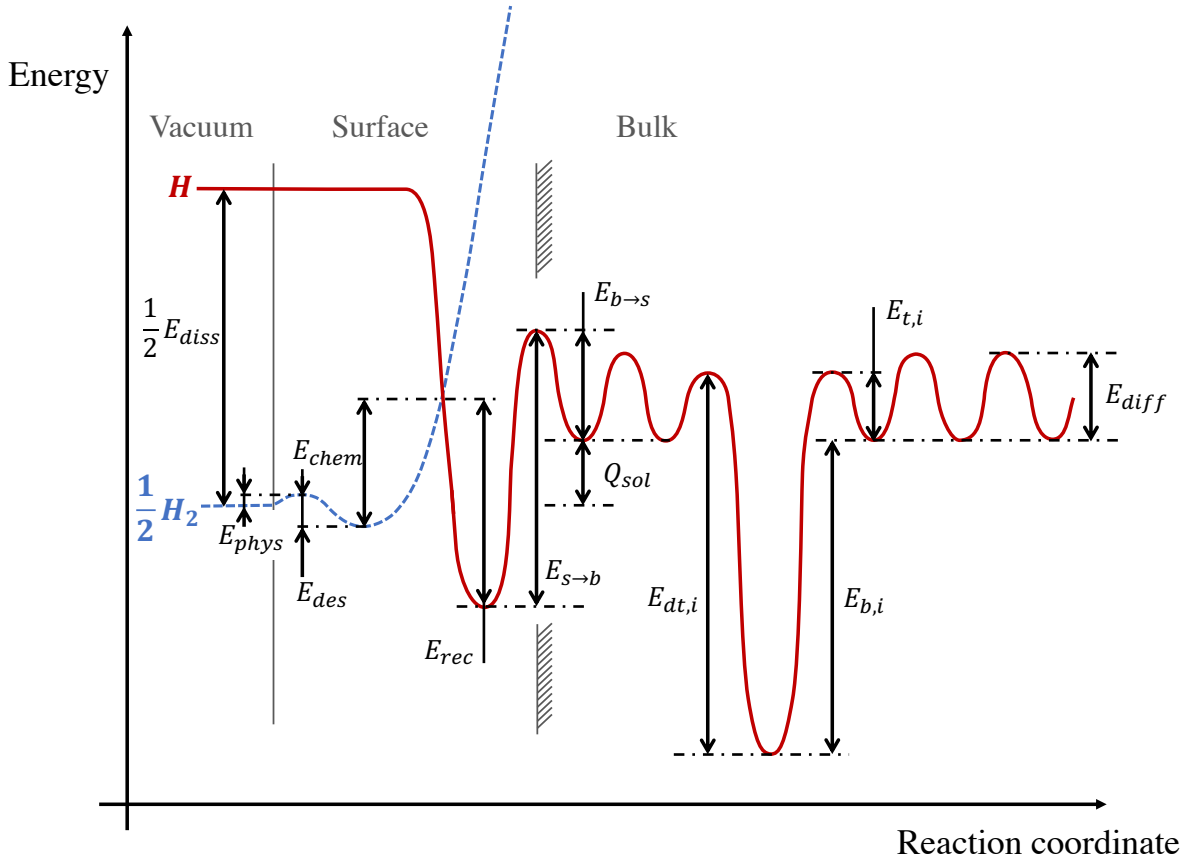

Figure 2.2: Idealised diagram of the potential energy of interaction between hydrogen isotope and material. The potential energy of interaction between an isolated HI atom and the material is displayed in red solid line while the potential energy between a HI atom in molecular form and the material is displayed in dashed blue line. The zero energy level is defined as the potential energy of the latter atom in vacuum. E_{diss} is the energy barrier of dissociation of hydrogen molecule, E_{phys} and E_{chem} are respectively the energy barriers of physisorption and chemisorption, E_{des} is the energy barrier of desorption, E_{rec} is the energy barrier of recombination, $E_{s\to b}$ is the energy barrier for transition from surface material to bulk material, $E_{b\to s}$ is the energy barrier for transition from bulk to surface, E_{diff} is the energy barrier of diffusion, $E_{t,i}$ is the energy barrier of trapping, $E_{b,i}$ is the trap binding energy, and $E_{dt,i} = E_{b,i} + E_{t,i}$ is the energy barrier of detrapping. Q_{sol} is the heat of solution.

energy are often referred to as *energy barrier*. For the sake of simplicity, these energie barriers are denoted E_x in the diagram 2.2 (in reality they should be noted ΔE_x). This potential energy variation represents the work done by the underlying net force that acts on the HI atom. Therefore this energy barrier represents the minimum kinetic energy required for the atom to overcome the energy barrier and thus to jump from its actual stable site to the adjacent stable site. Based on the potential energy diagram 2.2, a brief description of the elementary processes involved in the HI–material interaction will be done. First, the potential energy of a HI molecule is fixed to be zero at an infinite distance

from the surface of the material. Therefore, w.r.t. that origin, the potential energy of an HI atom in vacuum is half the value of the bond-dissociation energy of a H_2 molecule E_{diss} ($E_{diss} = 4.5$ eV).
Now, one will focus on HI–surface material interaction. A HI atom or a HI molecule in vacuum can stick to the surface of the material. This process is called adsorption. The adsorption of a HI atom, often referred to as *chemisorption*, occurs at a minimum of the potential energy curve which corresponds to the chemisorption site, while the adsorption of a HI molecule, often referred to as *physisorption*, occurs at another minimum which corresponds to the physisorption site [40]. The chemisorption sites are closer to the surface due to creation of chemical bonding between the HI and the surface. The physisorption is due to weaker interactions like Van der Waals forces. In order to be physisorbed, a HI molecule in vacuum needs to overcome the energy barrier $2E_{phys}$ where E_{phys} is the energy barrier of physisorption per HI atom. This physisorbed molecule can undertake the reverse process, i.e. desorb from the surface of the material. The desorption of molecule has an energy barrier $2E_{des}$ where E_{des} is the energy barrier of desorption per HI atom. The potential energy of a HI molecule goes to infinity when it approaches the surface. It means that the molecule feels a strong repulsion from the surface of the material (infinite gradient of the potential energy) and indicates that it first needs to dissociate for both hydrogen atoms to be absorbed into the material. The energy barrier per atom associated to this process is E_{chem} [39]. This energy corresponds to the intersection of the potential energy curves of atomic and molecular HIs. Most of the time, this energy is lower than the dissociation energy of HI molecule in vacuum $1/2E_{diss}$. Once dissociated, the two HI atoms will occupy two chemisorption sites. The interaction between HI atoms in vacuum and the surface is attractive (negative gradient of the potential energy). Atoms with thermal energies approaching the surface will either be reflected back to the vacuum or will be chemisorbed at the surface. Two chemisorbed atoms can recombine to form a molecule that will occupy a physisorbed site and which can subsequently desorb. From this diagram, one can easily see that, as the energy for transition of a HI atom from a chemisorbed site to vacuum is higher than $1/2E_{diss} = 2.25$ eV, the release of HI into vacuum only occurs in the form of molecule. This feature was experimentally corroborated in the case of deuterium release from tungsten as, below 1200 K, this release only occurs in molecular form [41] while above 1200 K a little amount of deuterium is directly released in atomic form.
Now the processes involved in the interaction between HI and bulk material will be presented. The chemisorbed HI atoms can penetrate into the bulk material (absorption process) by overcoming the energy barrier $E_{s\to b}$. $E_{s\to b}$ is the energy barrier for the transition from surface to bulk. Once absorbed, HI atoms reside in interstitial sites. This HI atoms are often referred to as solute atoms. From the diagram 2.2, one can see that HI atoms or ions with kinetic energy above $E_{s\to b}$ can overcome this barrier and can directly come into solution (implantation). These atoms/ions will then loose their kinetic energy through elastic collision with the material atoms or friction with the material electrons. Solute HI which are directly below the surface can overcome the energy barrier $E_{b\to s}$ to go to a chemisorption site. Alternatively, it can diffuse from interstitial site to interstitial

site by overcoming the diffusion energy barrier E_{diff}. During its transport by diffusion, the atom can be trapped in material defects. The energy barrier for the trapping process is $E_{t,i}$. Traps are regions in the material lattice with reduced electron density. As a consequence, the potential energy of a HI atom in a trap is lower than the potential energy of a HI atom in an interstitial site. The difference of both potential energies is called the trap binding energy $E_{b,i}$ (i being the kind of trap). The value of the binding energy depends on the nature of the trap. To escape from this trap, the HI atom will have to overcome the energy barrier $E_{dt,i} = E_{b,i} + E_{t,i}$ which is called the detrapping energy.

From experimental considerations, the processes described above are known to be thermally-activated and the rate constants of the reactions, $k(T)$, are often thought as being proportional to an empirical Arrhenius-type law:

$$k(T) \propto A \exp\left(\frac{-E_a}{k_B T}\right) \tag{2.1}$$

where E_a is the activation energy of the reaction [eV], A is a pre-exponential factor [s^{-1}], T is the material temperature [K] and k_B is the Boltzmann constant [$eV.K^{-1}$]. E_a is the minimum energy needed for the reaction to occur and, according to collision theory, the proportion of collisions with energy greater than E_a is proportional to $\exp(-E_a/(k_B T))$. For processes involving one HI atom (like diffusion or trapping), E_a is equal to the energy barrier associated to the process and given in the potential energy diagram 2.2 [39]. For processes involving one HI molecule (like desorption or physisorption), E_a is equal to twice the associated energy barrier [39]. Lastly, two HI atoms are involved in the recombination process and the corresponding activation energy E_a is twice the value of E_{rec} [39]. Concerning the pre-exponential factor A, it includes factors like the frequency of collisions and their orientation. In principle this factor can vary with temperature, although not very much. It is often considered constant.

One last quantity in the potential energy diagram has not been introduced: Q_{sol}. This quantity is called the heat of solution and is of particular interest for HI–metals interaction. Indeed, at moderate pressures and at the thermodynamic equilibrium, the density of hydrogen dissolved in solid metals is described to a good approximation by the empirical relation known as *Sieverts' law*:

$$n_{eq} = S(T)\sqrt{p} \tag{2.2}$$

where n_{eq} [m^{-3}] is the density of dissolved hydrogen in equilibrium with hydrogen at partial pressure p [Pa], and $S(T)$ is the solubility [$m^{-3}.Pa^{-1/2}$]. The solubility is also known as following an Arrhenius law:

$$S(T) = S_0 \exp\left(\frac{-Q_{sol}}{k_B T}\right) \tag{2.3}$$

where Q_{sol} is the activation energy [eV]. Q_{sol} can be either positive or negative, and the metals are accordingly classified as endothermic and exothermic absorbers of hydrogen. This classification has no fundamental significance. The important phenomenological distinction between the groups is that metals for which $Q_{sol} > 0$ display a HI density increasing with increasing temperature, and those for which $Q_{sol} < 0$ have the opposite behaviour. Both W and Be are endothermic hydrogen absorbers [7]. According to Pick and Sonnenberg [39], Q_{sol} can be expressed through the following expression involving the surface energy barriers (cf. diagram 2.2):

$$Q_{sol} = E_{chem} - E_{rec} + E_{s\to b} - E_{b\to s} \tag{2.4}$$

where the physisorption stage has been omitted [39] (meaning $E_{phys} \to 0$ and $E_{des} \to 0$). Note that the equilibrium density n_{eq} is a bulk material property. According to the Sieverts' law, Q_{sol} is also a bulk material property and should be independent on any surface energy barriers. As a consequence, the surface barriers involved in expression 2.4 can only influence the rate at which the equilibrium density is reached.

A simplified description of the elementary processes involved in HI–material interaction has been presented. This description and its associated physical quantities will be used in the following in the derivation of the model considered in MHIMS.

2.2 Reaction-Diffusion equations to model the interaction between hydrogen isotopes and bulk material.

The code MHIMS relies on the so-called Reaction-Diffusion system of equations (R-D equations) to describe the transport and trapping of HI in the bulk of materials. This model, originally introduced by McNabb and Foster in 1963 [42], has been used to describe the interaction of HI with bulk materials such as steel [43, 44], aluminium [45], tungsten [46, 47, 48, 49, 36, 50] and beryllium [51, 52]. In this model, two HI populations are considered: the mobile HI, which can diffuse in the material lattice, and the HI which are trapped in the lattice defects (vacancies, grain boundaries, etc.). These defects are considered as saturable and can only accommodate a single HI. The R-D equations express the time evolution of the density of mobile HI n_m [m^{-3}] and of the density of trapped HI $n_{t,i}$ in the trap of kind i [m^{-3}]. This subsection introduces this system of equations following the derivation done by Krom and Bakker [44]. The hypothesis used in this model will be validated for the materials of interest in this work, namely tungsten (W) and beryllium (Be).

According to Oriani [43], the time-dependent diffusion of mobile HI with trapping may be written as:

$$\frac{\partial n_m(\vec{r},t)}{\partial t} = \overrightarrow{\nabla} \cdot \left(D \overrightarrow{\nabla} n_m \right) - \sum_{i=1}^{N_{trap}} \frac{\partial n_{t,i}(\vec{r},t)}{\partial t} \tag{2.5}$$

where $\vec{r}$ denotes the position in the material [m], D is the diffusion coefficient of the

mobile HI [$m^2.s^{-1}$] and N_{trap} is the number of traps in the material. In both W and Be, the diffusion of mobile HI is a thermally-activated process and the diffusion coefficient can be expressed with an Arrhenius law [7]:

$$D(T) = D_0 \exp\left(\frac{-E_{diff}}{k_B T}\right) \tag{2.6}$$

where E_{diff} is the activation energy of diffusion [eV] (cf. figure 2.2) and D_0 is the diffusion pre-exponential factor [$m^2.s^{-1}$]. In this expression, $T(\vec{r}, t)$ is the material temperature [K]. The sum on the Right-Hand Side (RHS) of equation 2.5 represents the net source term due to the interaction of mobile HI with traps. To derive its expression, one can express the relation between mobile and trapped HIs through the following reaction:

$$[\mathrm{HI}]_\mathrm{m} \leftrightarrows [\mathrm{HI}]_\mathrm{t} \tag{2.7}$$

where $[\mathrm{HI}]_\mathrm{m}$ is a HI atom in an interstitial site (mobile atom) and $[\mathrm{HI}]_\mathrm{t}$ is a HI atom in a trap site.
First, one is interested in the forward direction reaction (trapping of a mobile HI). The time derivative of the density of HI moving from interstitial sites to trap sites of kind i can be expressed as follows:

$$\left.\frac{\partial n_{t,i}}{\partial t}\right|_{m\to t} = -\left.\frac{\partial n_m}{\partial t}\right|_{m\to t} = \nu_{t,i} n_m \tag{2.8}$$

where $\nu_{t,i}$ is the trapping rate coefficient [s^{-1}]. $\nu_{t,i}$ is proportional to:
(1) the frequency of collision in the right orientation of the mobile HI atoms $\nu^0_{t,i}$ [s^{-1}].
(2) the proportion of successful collisions, which can be expressed as $\exp\left(-E_{t,i}/(k_B T)\right)$ where $E_{t,i}$ is the trapping activation energy [eV] (cf. figure 2.2).
(3) the probability that a neighboring site is an empty trap site, which is equal to the ratio between the number of unoccupied trap sites and the total number of unoccupied sites.
Thus, $\nu_{t,i}$ is equal to:

$$\nu_{t,i} = \nu^0_{t,i} e^{-E_{t,i}/(k_B T)} \frac{n_i - n_{t,i}}{(n_{IS} - n_m) + \sum_{i=1}^{N_{trap}} (n_i - n_{t,i})} \tag{2.9}$$

where n_i is the density of the trap of kind i [m^{-3}] while n_{IS} is the interstitial site density [m^{-3}], i.e. the maximum number of mobile particles that can be inserted in the undisturbed lattice (without traps) of the material per unit volume. n_{IS} is an intrinsic property of the undisturbed material lattice and is constant in time and space. Equation 2.9 can further be simplified by assuming that:

(a) $n_m \ll n_{IS}$ (as the solubility of HI in metals is usually low).
(b) $n_i \ll n_{IS}$ (i.e. the traps are isolated).

Both assumptions can be validated for the two materials considered in this PhD. For the interaction of HI with W, it has been shown that W crystallises with a Body-Centered Cubic (BCC) structure [53] and that the stable positions of HI in undisturbed W lattice are Tetrahedral Interstitial Sites (TIS) [54, 55]. As there are 6 TIS per atom in a BCC lattice, the density of solute site in W is $n_{IS,W} = 6\rho_W$ where ρ_W is the W density [m^{-3}]. In figure 1.13.c-d, the NRA profile of D in polycrystalline W shows that the concentration of HI in W at low temperature (at 323 K) does not exceed 10 at.% of W (i.e. $0.1\rho_W$). Assuming that the traps are fully saturated at this temperature (i.e. $n_{t,i} = n_i$ for each trap), the total HI density verifies the following inequalities:

$$n_m + \sum_{i=1}^{N_{trap}} n_i \leq \frac{0.1}{6} n_{IS,W} \tag{2.10}$$

$$n_m + \sum_{i=1}^{N_{trap}} n_i \ll n_{IS,W} \tag{2.11}$$

The inequality 2.11 means that both assumptions (a) and (b) are verified for the case of HI–W interaction. For the case of HI interaction with Be, Be crystallises with a Hexagonal Close-Packed (HCP) structure. According to ab-initio Density Functional Theory (DFT) calculations, the stable positions of HI in pristine Be lattice are Basal-Tetrahedral Interstitial Sites (BTIS) and Octahedral Interstitial Sites (OIS) [56, 57]. As there are 1 BTIS and 1 OIS per atom in a HCP lattice, the density of solute site in Be is $n_{IS,Be} = 2\rho_{Be}$ where ρ_{Be} is the Be density [m^{-3}]. A saturation concentration of ~ 0.35 D/Be in the implantation zone after D implantation at room temperature have been reported in [58, 59]. Assuming again a full saturation of traps at this temperature, the total HI density verifies the following inequality:

$$n_m + \sum_{i=1}^{N_{trap}} n_i \leq \frac{0.3}{2} n_{IS,Be} \tag{2.12}$$

At first sight, the validity of assumptions (a) and (b) cannot be guaranteed. However, as it can be seen in figure 1.13.a, most of the HI inventory (~ 75 %) in saturated Be is in the form of molecules, possibly due to recombination of HI atoms adsorbed at the surface of interconnected porosities [28]. Thus, the remaining 25 % of the inventory represents both the mobile HI and the trapped HI in bulk defects. This means that both assumptions (a) and (b) are also valid for HI–Be interaction. Under these assumptions, the trapping rate coefficient defined in equation 2.9 can be written as:

$$\nu_{t,i} = \nu_{t,i}^0 e^{-E_{t,i}/(k_B T)} \frac{n_i - n_{t,i}}{n_{IS}} \tag{2.13}$$

If one defines the trapping attempt frequency $\nu_{t,i}^*$ as:

$$\nu^*_{t,i}(T) = \nu^0_{t,i} \exp\left(\frac{-E_{t,i}}{k_B T}\right) \tag{2.14}$$

the rate equation of the forward reaction can be written as:

$$\left.\frac{\partial n_{t,i}}{\partial t}\right|_{m\to t} = -\left.\frac{\partial n_m}{\partial t}\right|_{m\to t} = \nu^*_{t,i}(T)\frac{n_i - n_{t,i}}{n_{IS}} n_m \tag{2.15}$$

Now, regarding the backward direction reaction of 2.7, i.e. the detrapping of trapped particle, it can be noted that, due to the validity of assumption (b), traps are isolated and detrapping can only be from a trap to a mobile site. The time derivative of the density of HI moving from trap sites of kind i to interstitial sites can be expressed as follows:

$$\left.\frac{\partial n_{t,i}}{\partial t}\right|_{t\to m} = -\left.\frac{\partial n_m}{\partial t}\right|_{t\to m} = -\nu_{dt,i} n_{t,i} \tag{2.16}$$

where $\nu_{dt,i}$ is the detrapping rate coefficient [s^{-1}]. $\nu_{dt,i}$ is proportional to:
(1) the frequency of collision in the right orientation of the trapped HI atoms $\nu^0_{dt,i}$ [s^{-1}].
(2) the proportion of successful collisions, which can be expressed as $\exp\left(-E_{dt,i}/(k_B T)\right)$ where $E_{dt,i}$ is the detrapping activation energy [eV] (cf. figure 2.2).
(3) the probability that a neighboring site is an empty mobile site, which is equal to the ratio between the number of unoccupied mobile sites and the total number of unoccupied sites.
Thus, $\nu_{dt,i}$ is equal to:

$$\nu_{dt,i} = \nu^0_{dt,i} e^{-E_{dt,i}/(k_B T)} \frac{n_{IS} - n_m}{(n_{IS} - n_m) + \sum_{i=1}^{N_{trap}} (n_i - n_{t,i})} \tag{2.17}$$

Considering the two preceding hypothesis (a) and (b), the probability (3) (i.e. the fraction in equation 2.17) is equal to one and the detrapping rate coefficient becomes:

$$\nu_{dt,i}(T) = \nu^0_{dt,i} \exp\left(\frac{-E_{dt,i}}{k_B T}\right) \tag{2.18}$$

and the rate equation of the backward reaction becomes:

$$\left.\frac{\partial n_{t,i}}{\partial t}\right|_{t\to m} = -\nu_{dt,i}(T) n_{t,i} \tag{2.19}$$

The rate equation of the reaction 2.7, i.e. the total time derivative of HI in the trap site of kind i, can be obtained by adding equations 2.15 and 2.18:

$$\frac{\partial n_{t,i}(\vec{r},t)}{\partial t} = \nu^*_{t,i}(T)\frac{n_i(\vec{r},t) - n_{t,i}(\vec{r},t)}{n_{IS}} n_m(\vec{r},t) - \nu_{dt,i}(T) n_{t,i}(\vec{r},t) \tag{2.20}$$

It can be noticed that the traps density n_i is function of the position $\vec{r}$ but also of the

time t. Indeed, n_i can evolve with time due to the creation of traps linked to material irradiation, to the transport of traps by diffusion and to their annihilation (e.g. by re-crystallisation or by annihilation reaction, like vacancy – self interstitial atom reaction, or by transport up to the surface of the material). The modelling of all these processes requires solving a partial differential equation for each trap of kind i [60, 61]. Such equations won't be detailed here since they have not been considered in the version of MHIMS coupled to SolEdge2D-EIRENE.
Now, the diffusion equation for the mobile HI and the trapping reaction rate, equations 2.5 and 2.20 respectively, can be assembled into a system of equations, hence explaining the name *"Reaction-Diffusion equations"* given to this model:

$$\begin{cases} \dfrac{\partial n_m(\vec{r},t)}{\partial t} = \overrightarrow{\nabla} \cdot \left(D \overrightarrow{\nabla} n_m \right) - \displaystyle\sum_{i=1}^{N_{trap}} \frac{\partial n_{t,i}(\vec{r},t)}{\partial t} & \text{(2.21a)} \\ \dfrac{\partial n_{t,i}(\vec{r},t)}{\partial t} = \nu^*_{t,i}(T) \dfrac{n_i(\vec{r},t) - n_{t,i}}{n_{IS}} n_m - \nu_{dt,i}(T) n_{t,i} & \text{(2.21b)} \end{cases}$$

The code MHIMS relies on these R-D equations 2.21 to describe the interaction between HI and bulk material. A last simplification of these equations is made in MHIMS: it is considered that the transport of HI in materials is mainly one-dimensional, occurring in the direction of the depth of the material (transverse to its surface, denoted $\vec{x}$ in the following). MHIMS has been originally developed to interpret implantation experiments. In such experiments, the implantation flux density at the surface of the sample is in principle uniform, leading to a uniform implantation distribution in the directions transverse to the depth of the material, and therefore to a one-dimensional HI transport by diffusion. The validity of this approximation in the case of a wall model for fusion reactor will be treated later on. Under this hypothesis, the system 2.21 becomes:

$$\begin{cases} \dfrac{\partial n_m(x,t)}{\partial t} = \dfrac{\partial}{\partial x} \left(D(T) \dfrac{\partial n_m}{\partial x} \right) - \displaystyle\sum_{i=1}^{N_{trap}} \frac{\partial n_{t,i}}{\partial t} + S^{i+}_{ext}(x,t) + S^{at}_{ext}(x,t) & \text{(2.22a)} \\ \dfrac{\partial n_{t,i}(x,t)}{\partial t} = \nu^*_{t,i}(T) \dfrac{n_i(x,t) - n_{t,i}}{n_{IS}} n_m - \nu_{dt,i}(T) n_{t,i} & \text{(2.22b)} \end{cases}$$

The volume sources S^{i+}_{ext} and S^{at}_{ext} in equation 2.22a, which have been added to the diffusion equation, represent the volume sources due to implantation of ions and atoms respectively [$\mathrm{m}^{-3}.\mathrm{s}^{-1}$]. They only appear in this equation due to hypothesis (b) which entails that the probability to implant in a trap is null. Both sources can be expressed as follows:

$$S^j_{ext}(x,t) = \Gamma^j_{imp}(t) f_{imp}\left(x, E^j_{imp}(t), \alpha^j_{imp}(t)\right) \quad \text{(2.23)}$$

where $\Gamma^j_{imp}(t)$ [$\mathrm{m}^{-2}.\mathrm{s}^{-1}$] is the particle implantation flux density and f_{imp} is the probability density function of implantation given by the Stopping and Range of Ions in Matter code (SRIM) [62]. This function is a gaussian with mean implantation depth X^j_{imp} and

standard deviation σ^j_{imp}. Both parameters depend on the mean particle impact energy E^j_{imp} [eV] and the mean angle of incidence α^j_{imp} [°].

$$f_{imp}\left(x, E^j_{imp}(t), \alpha^j_{imp}(t)\right) = \frac{1}{\sqrt{2\pi\sigma^j_{imp}(E^j_{imp}(t), \alpha^j_{imp}(t))^2}} \exp\left(-\frac{\left[x - X^j_{imp}(E^j_{imp}(t), \alpha^j_{imp}(t))\right]^2}{2\sigma^j_{imp}(E^j_{imp}(t), \alpha^j_{imp}(t))^2}\right) \tag{2.24}$$

The model of HI–bulk material interaction considered in MHIMS has been presented. However, boundary conditions are needed to solve these R-D equations. To define these boundary conditions, the interaction between HI and the surface of the material needs to be accounted.

2.3 Boundary conditions for the Reaction-Diffusion equations.

The R-D equations considered in MHIMS need Boundary Conditions (B.C.) for n_m to be solved. The simulated zone presents two boundaries: one at the front surface of the material, in direct contact with the plasma, and one at the rear surface of the material. These two boundaries will be treated separately.

First, the front surface (at $x = 0$) is studied. This surface is in direct contact with the plasma. Therefore, its treatment will directly impact the coupling between D-WEE and SolEdge2D-EIRENE. To derive this B.C., one should consider the physical processes that occur at the surface of the material defined in subsection 2.1. However, on the assumption that all these processes do not limit the HI desorption, a simple homogeneous Dirichlet B.C. can be considered in the model:

$$\text{B.C. at } x = 0\text{: } n_m(0, t) = 0 \tag{2.25}$$

According to the potential energy diagram 2.2, this B.C. means that the activation energies $E_{b\to s}$, E_{rec} and E_{des} are low: the transition bulk–surface, the recombination and the desorption steps are assumed to be immediate. The reason for such assumption will be treated later on for the case of HI–W and HI–Be interactions. Under these conditions, the outgassing/desorption flux density of D, Γ_{out} [$\mathrm{m^{-2}.s^{-1}}$], is the diffusive flux density at the material surface:

$$\Gamma_{out}(t) = D(T)\frac{\partial n_m}{\partial x}(0, t) \tag{2.26}$$

The D desorbs from the wall in the form of molecules. Hence, the flux density of molecules desorbing from the wall is half the value of Γ_{out}.

Concerning the rear surface (at $x = L$), the choice of the B.C. will depend on the material

at the surface of the PFC and its thickness. Two types of surface material exist: massive materials, which extend on a depth of several millimeters (e.g. W in ITER monoblock), and coated or deposited materials, which extend on a depth of several micrometers (e.g. W coating on CFC substrate in the vertical tiles of the JET-ILW divertor). For massive materials, their depth is high enough so that no strong effect of this B.C. is expected on the outgassing flux density at the front surface and on the overall HI inventory. Therefore, for that type of materials, the same homogeneous Dirichlet B.C. as for the front surface is considered. For coatings or deposits, the choice of the B.C. can impact the resulting outgassing flux density and the inventory due to their smaller depth. However, it has been shown by post-mortem analysis of ion implanted samples [63] and of JET-ILW samples [64] that very little HI retention has been probed in the substrate material (CFC). This may indicate that the interface between the coated or deposited material and the substrate acts as a diffusion barrier for HI. In that case, a Neumann B.C. with a zero flux density seems to be more appropriate. Therefore the two types of B.C. are available and can be chosen by the user depending on the considered material:

$$\text{B.C. at } x = L: \left| \begin{array}{c} n_m(L,t) = 0 \\ \text{or} \\ D(T)\dfrac{\partial n_m}{\partial x}(L,t) = 0 \end{array} \right. \tag{2.27}$$

2.4 Adaptation of MHIMS to the desorption module for SolEdge2D-EIRENE.

This subsection is dedicated to the adaptation of MHIMS to model the HI dynamics in the complete wall of nuclear fusion reactors as required in the desorption module for SolEdge2D-EIRENE.

First, the equations of MHIMS presented in subsections 2.2 and 2.3 remain valid. Indeed, the one-dimensional approximation used in MHIMS is still appropriate as, in fusion reactors, the gradient width of the plasma flux density at the surface of materials (of the order of millimeters to centimeters) is larger than the characteristic depth of diffusion of HI in the depth of the materials on the time scales of usual plasma discharges in present machines (typically of order of micrometers to millimeters). Therefore, the transport of HI in materials remains one-dimensional, in the direction of the depth of the materials (transverse to its surface). The MHIMS equations can easily be adapted to model HI dynamics in the complete wall of fusion reactors by accounting the variation of plasma conditions along the wall:

$$
\begin{cases}
\dfrac{\partial n_m(s,x,t)}{\partial t} = \dfrac{\partial}{\partial x}\left(D(s,T)\dfrac{\partial n_m}{\partial x}\right) - \displaystyle\sum_{i=1}^{N_{trap}(s)} \dfrac{\partial n_{t,i}}{\partial t} \\
\qquad\qquad + S^{i+}_{ext}(s,x,t) + S^{at}_{ext}(s,x,t) & \text{(2.28a)} \\
\dfrac{\partial n_{t,i}(s,x,t)}{\partial t} = \nu^*_{t,i}(s,T)\dfrac{n_i(s,x) - n_{t,i}}{n_{IS}(s)} n_m - \nu_{dt,i}(s,T) n_{t,i} & \text{(2.28b)} \\
\text{B.C. at } x = 0\text{: } n_m(s,0,t) = 0 & \text{(2.28c)} \\
\text{B.C. at } x = L\text{: } \begin{vmatrix} n_m(s,L,t) = 0 \\ \text{or} \\ D(s,T)\dfrac{\partial n_m}{\partial x}(s,L,t) = 0 \end{vmatrix} & \text{(2.28d)}
\end{cases}
$$

where the s symbol denotes the SolEdge2D-EIRENE curvilinear coordinate along the wall introduced in figure 1.15.a. The variation of implantation conditions are accounted in the two implantation sources S^{i+}_{ext} and S^{at}_{ext}, which are now both function of s. One can note that the diffusion coefficient D, the number of traps N_{trap}, the trapping attempt frequency $\nu^*_{t,i}$, the detrapping frequency $\nu_{dt,i}$, the traps density n_i, and the interstitial site density n_{IS} are also function of s. Indeed, these quantities are all material dependent and the s dependence of these quantities is here to indicate the different materials considered along the wall.

Unlike in the general R-D equations of MHIMS (equation 2.22), the traps density n_i is not function of time anymore. As it was previously said, n_i can evolve with time due to the creation of traps, their diffusion and their annihilation. The modelling of all this processes would require the solving of other partial differential equations with new free parameters (diffusion coefficients, reaction rates, etc.) that would add complexity to the model. Therefore one assumes that the traps creation has saturated, or that the characteristic time of the creation is high w.r.t. the time of simulation. One also assumes that traps are immobile and cannot annihilate. The validity of these assumptions for the modelling of HI–W and HI–Be interactions will be verified later on in this section. Thus, under this assumption, n_i only depends of x and is prescribed at the beginning of the simulation. Three types of trap profile are available and are named traps of type a, b or c. They are defined by the following equations:

$$\underline{\text{Trap type a:}}\ n_i(x) = n_i^a \tag{2.29}$$

$$\underline{\text{Trap type b:}}\ n_i(x) = n_i^b\left(1 - \text{erf}\left(\frac{x}{X_i^b}\right)\right) \tag{2.30}$$

$$\underline{\text{Trap type c:}}\ n_i(x) = \frac{n_i^c}{1 + \exp\left(\dfrac{x - X_i^c}{0.1X_i^c}\right)} \tag{2.31}$$

These arbitrary profiles were chosen to reproduce HI profiles that have been experimentally measured by ion beam analysis (e.g. NRA or SIMS). A composition of these profiles is also possible to define the density profile of a given trap. Example of the three types of profile is shown in figure 2.3. The trap of type "a" has a constant density in the depth of the material, n_i^a. Such profile is suitable for intrinsic traps. The trap of type "b" presents a density maximal at the surface, n_i^b, which decays in the depth of the material following a form function $1-\mathrm{erf}(x/X_i^b)$ with characteristic length X_i^b. This profile is similar to the analytical solution of the linear diffusion equation in a semi-infinite wall with Dirichlet boundary condition at the surface $n_i(0) = n_i^b$. X_i^b can be seen as a diffusion length of the traps, defined as $2\sqrt{D_i^b t}$ where D_i^b is the effective diffusion coefficient of the traps. The trap of type c presents a constant density at the surface, n_i^c, which collapses by half of her value at $x = X_i^c$ with a characteristic decay length $0.1X_i^c$ ($n_i^c \geq n_i(x) \geq 0.95n_i^c$ for $0 \leq x \leq 0.7X_i^c$). Such profile is suitable for traps that are created in the implantation zone.

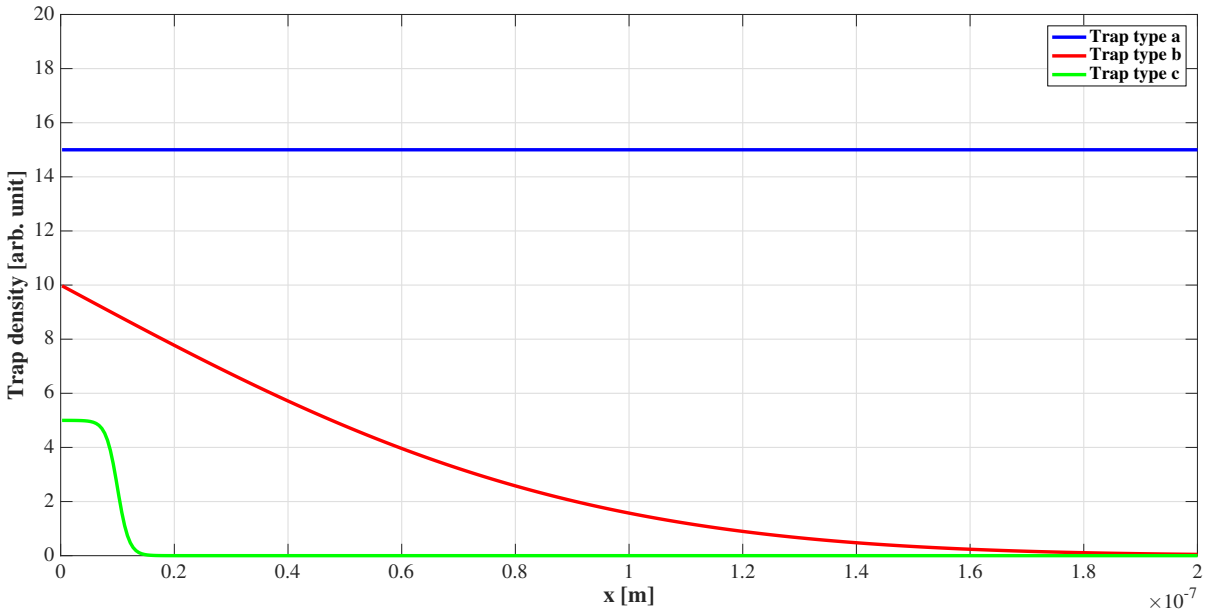

Figure 2.3: Examples of the three different profiles of traps that are available in the version of MHIMS used in D-WEE. They are defined by equations 2.29, 2.30 and 2.31.

The version of MHIMS that has been selected for the D-WEE module is now complete. The question of its interaction with SolEdge2D-EIRENE can be raised. According to the diffusion equation 2.28a of MHIMS, the HI supply is made through the implantation sources of ions and atoms, respectively S_{ext}^{i+} and S_{ext}^{at} , which are each function of the terms Γ_{imp}^j, E_{imp}^j and α_{imp}^j according to equations 2.23 and 2.24. Therefore, the coupling of MHIMS with SolEdge2D-EIRENE is made through these six parameters (three for ions and three for atoms), which are all calculated by the EIRENE code. The feedback of MHIMS to SolEdge2D-EIRENE is performed through the molecular recycling coefficient

R_m, introduced in chapter 1 section 3, which is defined as follows:

$$R_m(s,t) = \frac{\Gamma_{out}(s,t)}{\Gamma^{i+}_{imp}(s,t) + \Gamma^{at}_{imp}(s,t)} \tag{2.32}$$

where Γ_{out} is the desorption flux density defined in equation 2.26. This coefficient should not be confused with the total recycling coefficient as fuel reflection of both ions and atoms should also be considered in its calculation. Again, the flux density of molecules desorbing from the wall is half the value of Γ_{out}. The R_m coefficient is provided to EIRENE which uses it to set the flux density of molecules desorbing from the wall.

Even though the version of MHIMS used in D-WEE is relatively simple in terms of description of HI–material interaction, the addition of a second dimension to the model ($\vec{s}$) leads to a tremendous increase of the computational time required to solve the system of equations 2.28. Indeed, this system is numerically integrated using the finite volume method for the space operator and the so-called Backward Differentiation Formula (BDF) method [65] for the time operator. The reason of this increase is briefly explained in appendix A. The numerical improvements that have been implemented in MHIMS to decrease its computational time are also explained in this appendix. These improvements made a coupling of D-WEE with SolEdge2D-EIRENE achievable.

2.5 Setting of the free-parameters of the R-D equations.

The R-D equations have numerous free parameters which are summed up in table 2.1. These parameters are dependent on the considered couple HI–material and must be set before launching a simulation. The next subsections will be dedicated to the setting of the R-D equations for the case of massive polycrystalline tungsten (PCW) and beryllium (PCBe) which are the material foreseen in the ITER wall. These materials are also presently used in the JET-ILW. The selected data introduced in both subsections represent, in our opinion, the most commonly accepted data in the literature. For a more exhaustive analysis of the available data on hydrogen isotope retention and transport in material, the reader must refer to the article from R.A. Causey for a complete review of HI–material interaction for different materials used in fusion (W, Be, C, etc.) [7], the articles from Roth and Schmid [38], T. Tanabe [66] and Schmid et al. [67] for a review of HI–W interaction and the article from Anderl et al. for a review of HI retention in Be [68].
The free-parameters reported in table 2.1 can be estimated from experimental measurements or from first principle simulations of HI–material interaction. The following, non-exhaustive, technics are often considered as the most reliable:

– For HI diffusion, one can cite two experimental methods to estimate the parameters D_0 and E_{diff}: from the measurement of the outgassing rate of HI from very large dimension samples (e.g. [69]), or from the measurement of the permeation flux of HI through a material sample that separates a chamber with fixed HI pressure and a vacuum chamber (gas permeation technic, e.g. [70]). In both cases, the diffusion

DIFFUSION		
Diffusion pre-exponential factor [$m^2.s^{-1}$]		D_0
Diffusion activation energy [eV]		E_{diff}
TRAPPING		
For each trap	Trapping pre-exponential factor [s^{-1}]	$\nu^0_{t,i}$
	Trapping activation energy [eV]	$E_{t,i}$
	Trap density profile [m^{-3}]	$n_i(x)$
Interstitial site density [m^{-3}]		n_{IS}
DETRAPPING		
For each trap	Detrapping pre-exponential factor [s^{-1}]	$\nu^0_{dt,i}$
	Detrapping activation energy [eV]	$E_{dt,i}$

Table 2.1: Free parameters of the Reaction-Diffusion equations considered in MHIMS.

coefficient is obtained from analytical solution of the Fick's laws. The measurements are done at different temperatures and D_0 and E_{diff} are obtained from the fitting of the so-called Arrhenius-plot of the obtained diffusion values. The values at low temperature are often omitted due to trapping effect that is known to reduce the HI diffusivity. From the numerical point of view, first principle DFT calculations enable to calculate the activation energy of diffusion E_{diff} [54]. The pre-exponential factor can also be obtained from DFT calculation using the transition state theory within the concept of activated complex [55, 54]. In reality the HI diffusion path can involve different solute sites with related energy barriers (like e.g. HI diffusion in Be [71]). DFT based energy barriers of diffusion can be used as inputs for Kinetic Monte-Carlo (KMC) codes. The value of the diffusion coefficient can be calculated from simulations of HI diffusion with KMC codes using the Einstein law of diffusion [56]. This procedure is performed at different temperatures and D_0 and E_{diff} are obtained from the fitting of the Arrhenius-plot of the obtained diffusion values [56].

– For the trapping process, the values of $E_{t,i}$ can be obtained from DFT calculations. However, these values for typical defects are not always available in the literature. Therefore, for limiting the number of free parameters in the R-D equations, the trapping is often considered to be limited by HI diffusion. In that case, the trapping attempt frequency (equation 2.14) can be expressed as a function of the diffusion coefficient, $\nu_{t,i}(T) = D(T)/\lambda^2$, where λ is the distance between two HI interstitial sites [m]. Eventually, λ and n_{IS} are parameters related to the material lattice and can be obtained from DFT calculations.

– For the detrapping process, DFT calculations can give access to both activation energy $E_{dt,i}$ and pre-exponential factor $\nu^0_{dt,i}$. However, both parameters as well as the trap density profile $n_i(x)$ are often used as free-parameters for the fitting of TDS analysis with R-D codes like MHIMS [47, 50, 36, 60]. The number of traps and their corresponding parameters are set to reproduce TDS spectra. The trap density

profiles $n_i(x)$ and their corresponding density profiles of trapped particle $n_{t,i}(x)$ are often initialised before the TDS by considering NRA and SIMS analysis. These analysis give access to the depth profiles of the total HI density and therefore of the sum of the trap densities $n_i(x)$ (assuming that the traps are fully saturated, which is often the case at low temperature). To reduce the number of free-parameters for the TDS fitting, $\nu^0_{dt,i}$ is often assumed to be equal to the Debye frequency, i.e. $\sim 10^{13}$ s^{-1}. This value represents a good approximation in terms of order of magnitude. A more ambitious undertaking lies in the simulation of the implantation phase prior to the TDS analysis. In that case, the R-D model must be completed by a trap creation process that gives the time evolution of the trap density profiles ($n_i(x,t)$, cf. general R-D equation 2.22). This more complicated approach has the benefit of providing some information about the mechanism and the dynamics of the trap creation process [47, 60]. To characterise ion-induced traps, scientists fit TDS analysis of monocrystalline material which were annealed prior to implantation to remove all their traps. HI ions are then implanted in the sample, creating only ion-induced traps. This fitting can be completed by fitting of TDS analysis of implanted polycrystalline materials, experiments that give access to both intrinsic and ion-induced traps of the material. The obtained detrapping energies $E_{dt,i}$ can be compared to values of $E_{dt,i}$ calculated with first principle DFT codes for different kind of traps. This comparison enables to identify the type of trap (grain boundary, mono-vacancy, etc.) [60]. Eventually, to verify the accuracy of the obtained parameterisation, one must try to reproduce several implantation experiments under varying implantation conditions (i.e. flux density, energy and temperature). The more experiments the obtained parameters are able to reproduce, the more robust these parameters can be considered.

2.6 Parameterisation of the R-D equations for polycrystalline tungsten.

The free-parameters that will be considered for HI–W interaction in this PhD will now be presented. First, one will focus on the W lattice parameters used in the R-D equations and which were quickly introduced during the derivation of these equations (cf. subsection 2.2). One remembers that W crystallises with a BCC structure [53]. DFT based calculations have shown that the stable positions of HI in undisturbed W lattice are TIS [54, 55]. As there are 6 TIS per atom in a BCC lattice, the density of solute site in W is $n_{IS,W} = 6\rho_W$. Moreover, distance between two TIS can be estimated from the BCC lattice parameters of W. Concerning HI diffusion, the commonly accepted value for the diffusion coefficient is based on the experiments by Frauenfelder [69] which were performed at high temperatures (1100 – 2400 K) with an expected negligible effect of trapping. These experiments give an activation energy $E_{diff} = 0.39$ eV and a pre-exponential factor $D_0 = 4.1 \times 10^{-7}$ m^2.s^{-1}. DFT calculations from Heinola and Ahlgren have given a lower activation energy $E_{diff} = 0.21$ eV and $D_0 = 5.2 \times 10^{-8}$ m^2.s^{-1} [55]. They also proposed a new fit of the Frauenfelder's experimental data by only considering

the points above 1500 K and obtained a new experimental diffusion coefficient with a lower activation energy $E_{diff} = 0.25 \pm 0.08$ eV and $D_0 = 1.58^{+1.9}_{-0.77} \times 10^{-7}$ m^2.s^{-1} [55]. A better agreement of their diffusion coefficient obtained from DFT with the new fitted diffusion coefficient can be noticed. This indicates that the first fit done by Frauenfelder was probably affected by trapping at temperature lower than 1500 K. More recent DFT calculations from Fernandez et al. have confirmed this lower activation energy of diffusion $E_{diff} = 0.20$ eV, and give a pre-exponential factor $D_0 = 1.9 \times 10^{-7}$ m^2.s^{-1} [54]. Both parameters are in very good agreement with the high temperature fitting of the Frauenfelder's data and even lie within the respective error bars. The parameters from Fernandez et al. [54] will be considered in the following. A summary of the selected value of parameters can be found in table 2.2.

DIFFUSION		
Parameter	Value	From
D_0	1.9×10^{-7} m^2.s^{-1} (for H)	DFT [54]
E_{diff}	0.2 eV	DFT [54]
TRAPPING		
Parameter	Value	From
$\nu^0_{t,i}$	$D_0/{\lambda_W}^2$	—
λ_W	111.7 pm	Experiment [72] and DFT [54]
$E_{t,i}$	0.2 eV	—
n_{IS}	$6\rho_W$	DFT [54]
ρ_W	6.3382×10^{28} m^{-3}	[53]
DETRAPPING		
Parameter	Value	From
$\nu^0_{dt,i}$	10^{13} s^{-1}	—

Table 2.2: Free parameters of the Reaction-Diffusion equations considered in MHIMS for HI–W interaction [60].

Regarding the setting of traps parameters, one will consider the parameterisation proposed by Hodille et al. for PCW. In reference [60], MHIMS was used to reproduce the TDS analysis performed by Ogorodnikova et al. [47] on such type of W. Prior to the analysis, the PCW sample, maintained at a temperature of 300 K, was submitted to a D ion flux density around 2.5×10^{19} D.m^{-2}.s^{-1} up to a fluence of 1.0×10^{23} D.m^{-2}. The implantation energy was 200 eV per D. These implantation conditions can be considered as being representative of conditions found in nuclear fusion reactors. The experimental TDS spectrum is displayed in blue solid line in figure 2.4 and exhibits two peaks positioned approximately at 440 K for the highest intensity peak and at $\sim$ 600 K for the lowest intensity peak. The simulated TDS spectrum, obtained after simulation of the implantation phase and of the subsequent TDS, is displayed in green solid line in the same figure and presents a very good agreement with the experimental TDS spectrum. The simulation was performed considering the parameters given in table 2.2. Hodille et

al. identified three traps: two intrinsic traps and one ion-induced trap. The parameters for each trap obtained from the simulation are reported in table 2.3.

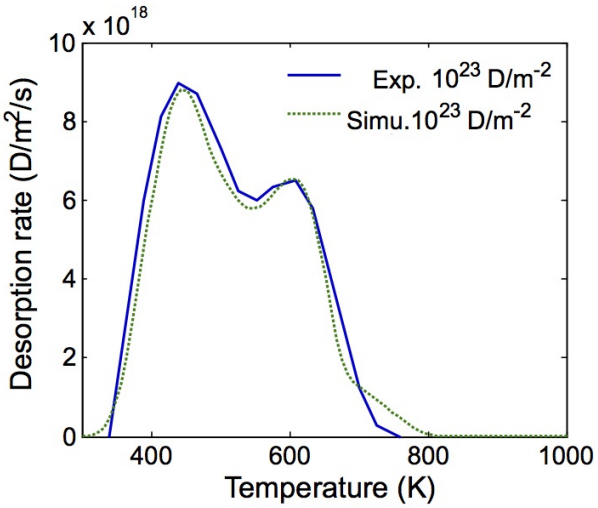

Figure 2.4: TDS spectrum of a polycrystalline tungsten sample performed by Ogorodnikova et al. [47] (blue solid line). The implantation experiment and the subsequent TDS was reproduced by Hodille et al. (green solid line) with MHIMS to parameterise the model. The picture is taken from reference [60].

	Trap parameters	Type of defects
Trap 1	$E_{dt,1} = 0.85$ eV $n_1 = 0.13$ at.%	Intrinsic: dislocations and/or Fe impurities
Trap 2	$E_{dt,2} = 1.00$ eV $n_2 = 0.035$ at.%	Intrinsic: grain boundaries
Trap 3	$E_{dt,3} = 1.50$ eV $n_3^{surf} = 15$ at.% $n_3^{bulk}(x = 0) = 1$ at.%, $x_{diff} = 1.0$ μm	Ion-induced: VOH or VCH vacancy complex

Table 2.3: Trap parameters obtained by Hodille et al. for the fitting with MHIMS of the TDS analysis made by Ogorodnikova et al. [47] (cf. TDS spectra in figure 2.4). The trap densities are given in at.% of W. For intrinsic traps, the trap densities are constant in all the depth of the material and equal to the values presented in this table (n_1 and n_2 respectively). The ion-induced trap presents two damaged zones: a highly damaged zone at the surface, which saturates at the value n_3^{surf}, and a damaged zone extending in the depth of the material up to a depth x_{diff} with a maximum density n_3^{bulk} at the surface.

From the obtained trap parameters, Hodille et al. has drawn the following conclusions about the nature of traps:

– The trap 1 has a detrapping energy of 0.85 eV. It is an intrinsic trap with constant density in the depth of the material (cf. table 2.3). By comparing the detrap-

ping energy with values obtained from DFT, this trap can be identified as being dislocations and/or Fe impurities present in the PCW sample.

- The trap 2 has a detrapping energy of 1.00 eV. It is also an intrinsic trap with constant density in the depth of the material (cf. table 2.3). By comparing the detrapping energy with values obtained from DFT, this trap can be identified as being the grain boundaries of the PCW sample.

- The trap 3 has a detrapping energy of 1.50 eV. This trap is induced by the D ions implantation and, from DFT based detrapping energies, can be attributed to vacancies filled with light impurities (e.g. VOH or VCH). Hodille et al. considered two areas of creation of this trap: a damaged zone in the implantation zone, with a creation footprint given by the ion implantation source defined in equation 2.23, and a damaged zone in the bulk of the material related to a trap diffusion process, probably of light impurities like O or C as suggested by experiments [73, 74]. The depth profile of this bulk damaged zone has the same functional form as the trap of kind (b) (equation 2.30), with was set ad-hoc by Hodille et al. The choice of this functional form was based on experimental NRA and SIMS HI depth profiles reported in the literature in both SCW [75, 76] and PCW [29]. To estimate the range of diffusion of the impurities x_{diff}, Hodille et al. has reproduced experimental NRA D depth profiles obtained by Alimov et al. [75] after implantation of SCW with 200 eV D ions with an incident flux density of 1×10^{21} D.m^{-2}.s^{-1} up to a fluence of 2×10^{24} D.m^{-2} at different temperatures. From that fitting procedures, he was able to estimate a diffusion length x_{diff} for each implantation temperature, and therefore a value of the diffusion coefficient of light impurities for each temperature from the expression $x_{diff} = 2\sqrt{D_{LI}(T)t}$. Assuming that this diffusion coefficient follows an Arrhenius law, he obtained the following expression for the diffusivity of impurity in W [60]: $D_{LI}(T) = 4 \times 10^{-13} \exp\left(-0.22/(k_B T)\right)$. This expression can be used to estimate a penetration depth of trap 3 in the bulk for given implantation temperature and time.

The strength of the parameters obtained by Hodille et al. was confirmed by further simulations and confrontations to experimental results. With these parameters, MHIMS was able to reproduce with a relatively good agreement the evolution of retention with fluence measured by Ogorodnikova et al. [47] for two implantation temperatures (300 K and 473 K) on three orders of magnitude of D fluence (cf. figure 2.5.a). Moreover, these parameters were successfully used to reproduce the evolution of D retention with the implantation temperature obtained by Tian et al. [77] for similar implantation conditions as in the case of Ogorodnikova et al. [47] (cf. figure 2.5.b). To reproduce it, Hodille et al. only modified the diffusion depth of the bulk damaged zone x_{diff} which is function of time and temperature.
Now, one will discuss the two assumptions taken in the version of MHIMS used in D-WEE in the case of W. First, one will focus on the hypothesis of fixed trap density profiles $n_i(x)$ taken in subsection 2.4. One will discuss the validity of this hypothesis for the traps obtained by Hodille et al. for PCW (reported in table 2.3) and within the

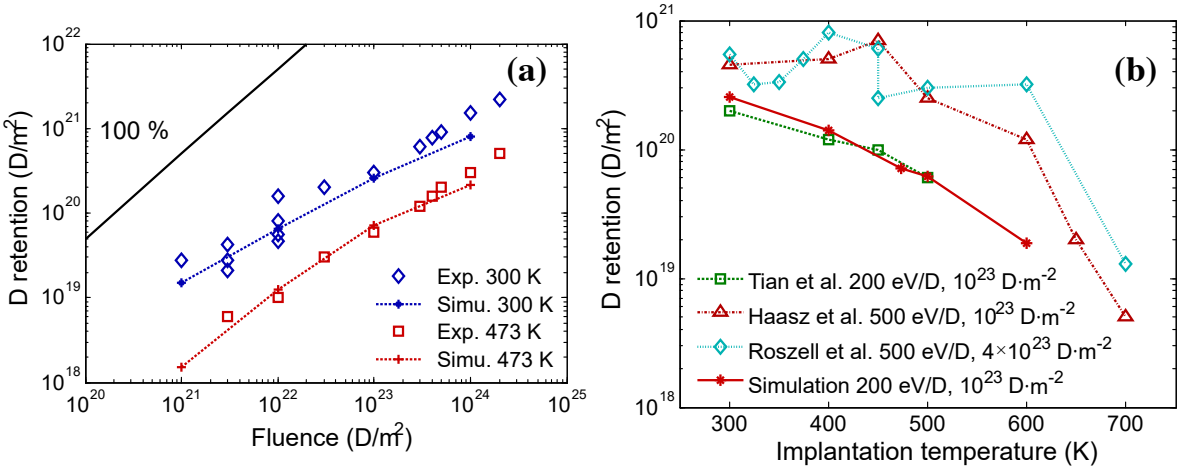

Figure 2.5: (a) Evolution of the D retention in PCW as a function of fluence experimentally obtained by Ogorodnikova et al. [47] for two implantation temperatures (300 K and 473 K). This evolution has been reproduced by Hodille et al. with the MHIMS code considering the parameters of HI–W interaction presented in this subsection (dashed lines). (b) Evolution of the D retention in PCW as a function of the sample temperature experimentally obtained by Tian et al. [77] (green squares). This evolution has also been reproduced by Hodille et al. with the MHIMS code using the same parameters (red solid line). Both pictures are taken from reference [60].

context of tokamak environment. One remembers that $n_i(x)$ can evolve with time due to trap creation, transport and annihilation. Concerning the trap creation process, which only concerns trap 3 in the case of PCW, the two damaged zones (implantation zone and bulk zone) have two distinct creation dynamics. For the implantation zone, Hodille et al. used a growth of the trap density in $(1 - \exp(-t/\tau))$ with a time constant τ function of the implantation sources (equation 2.23). Such creation process was introduced by Ogorodnikova et al. [47] in their study of D implantation in PCW. A maximum time constant of the exponential growth can be extracted from the model, which is given for the maximum HI implantation range. Under realistic implantation conditions in tokamaks, one has estimated a maximum time constant of trap creation of $\sim$ 30 min, which means that the trap creation process in the implantation zone saturates after $\sim$ 2 h of operations. This duration must be compared with the effective operation time of a tokamak during an experimental campaign. As an example, according to reference [78], the JET-ILW 1 and JET-ILW 2 campaigns have reached similar total plasma times: $\sim$ 5/6 h in limiter phase and $\sim$ 13/14 h in divertor phase. From that comparison, one can reasonably consider that the trap density in the implantation zone has reached the saturation value. Concerning the damaged zone in the bulk, NRA depth profiles obtained by Alimov et al. [75] show that this damaged zone has already been created after 2000 s of D ion irradiation under tokamak relevant conditions (200 eV D ions with an incident flux density of 1×10^{21} D.m^{-2}.s^{-1}). One can reasonably think that this bulk damaged zone quickly develops in PCW found in fusion reactors. Concerning trap transport and

annihilation, it has been experimentally shown that dislocations (and therefore trap 1) begin to annihilate at 800 K which is a temperature that is only found in the vicinity of the strike-points in tokamaks. Moreover, W recrystallises at a temperature above 1800 K. This means that grain boundaries (i.e. trap 2) in PCW cannot annihilate at the wall temperature found in tokamaks. Eventually, first principle DFT calculation reported that the activation energy of diffusion for vacancies in W is higher than 1.7 eV [54]. This activation energy increases up to 2.52 eV when the vacancy is filled with a HI atom. Such high activation energies indicate that the vacancies are unlikely to diffuse and annihilate. One can conclude that the assumption of fixed trap density profiles taken in subsection 2.4 is reasonable for W under tokamak conditions.
Moreover, in subsection 2.3, one assumes that the surface processes are not rate limiting, which leads to the consideration of a homogeneous Dirichlet B.C. at the surface in MHIMS (equation 2.28c). Experimental measurements from Bisson et al. [25] suggest that the recombination of HIs is not the rate limiting step during their TDS analysis of a PCW sample submitted to an ion exposure at low flux density and low fluence. This observation suggests that the considered B.C. is valid. It must be stipulated that, in his fitting of the TDS of Ogorodnikova, Hodille et al. has considered this Dirichlet B.C. Other authors have used such B.C. in their study of HI retention in W [49, 79]. In his study of very low energy (0.3 eV) D ion implantation experiments, Hodille et al. had to integrate a surface model in MHIMS [60, 80]. To describe all the surface processes presented in subsection 2.1, Hodille et al. used the surface model proposed by Pick and Sonnenberg [39]. In this model, it is considered that a solute HI must go to a chemisorption site prior to recombine and to desorbe (the physisorption of molecules is neglected). The direct recombination of HI atoms coming from the bulk material is not considered. The strength of this surface model lies in the fact that, as demonstrated by Pisarev and Ogorodnikova [81], this model is the only surface model in the literature able to recover the Sieverts' law (equation 2.2) under steady-state conditions. In this model, the outgassing flux density, Γ_{out}, is expressed as a function of the surface density of chemisorbed HI atoms n_{surf} [at.m^{-2}] [39, 80]:

$$\Gamma_{out}(t) = \nu_{rec}(T) {n_{surf}}^2 = \frac{2\nu_{rec}^0}{\lambda_{chem}} \exp\left(\frac{-2E_{rec}}{k_B T}\right) {n_{surf}}^2 \tag{2.33}$$

where $\nu_{rec}(T)$ is the recombination rate coefficient, ν_{rec}^0 is the frequency factor of recombination [s^{-1}], λ_{chem} is the distance between two chemisorption sites [m] and E_{rec} is the energy barrier of recombination per atoms (defined in subsection 2.1 and in figure 2.2) [eV]. In this model, the material surface has a limited number of chemisorption sites, defined as n_{CS} [m^{-2}]. It is convenient to introduce the coverage of the surface, $\theta = n_{surf}/n_{CS}$, which indicates the filling level of the chemisorption sites. When the surface is fully saturated, θ is equal to 100 %. In the Pick and Sonnenberg model, the outgassing flux density has an inherent upper limit, that cannot be exceeded, which is obtained for a fully saturated surface. On figure 2.6.a, the outgassing flux density calculated for W from equation 2.33 is plotted for different surface coverage θ (and therefore for different surface density n_{surf}). This calculation was performed considering the ac-

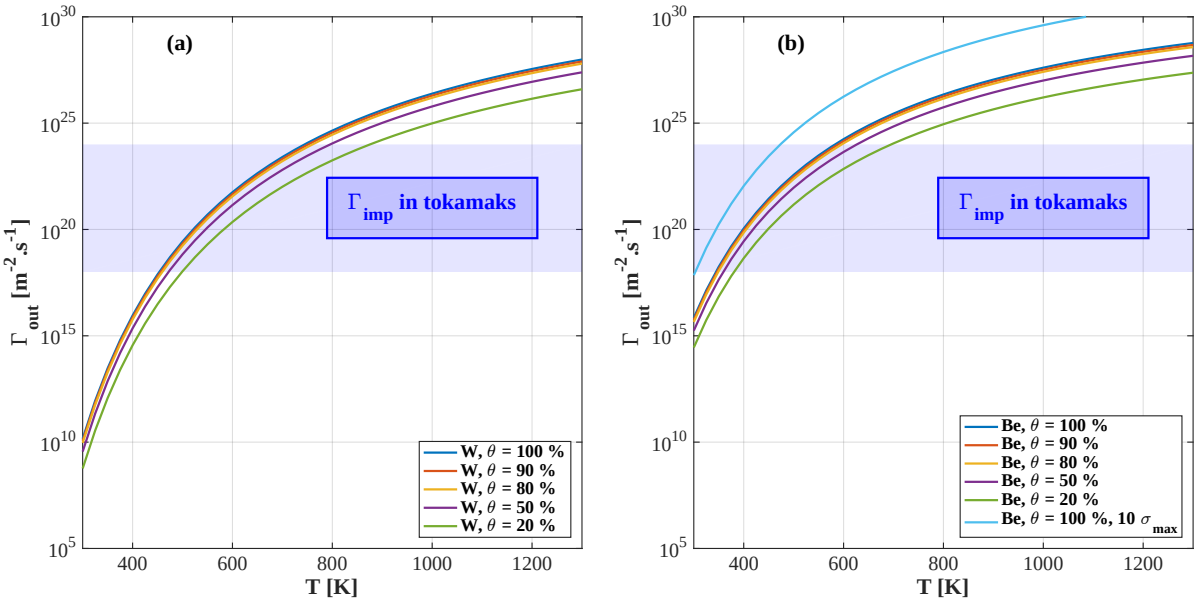

Figure 2.6: Evolution of the outgassing flux density Γ_{out} given in the Pick and Sonnenberg model (cf. equation 2.33) as a function of the temperature. Γ_{out} is plotted in the case of W (a) and Be (b) for different values of the coverage of the chemisorption sites θ. According to the Pick and Sonnenberg, the maximum outgassing flux density is defined for a saturated surface, i.e. for $\theta = 100$ % (blue curves in (a) and (b)). The blue shaded area represents the interval of implantation flux density Γ_{imp} that can be found in tokamaks. For the zones where the shaded area is above the curve for $\theta = 100$ %, the molecular recycling coefficient R_m remains below 1.

tivation energy of recombination reported by Hodille et al. [80], $E_{rec} = 0.69$ eV, which is in agreement with both experimental and DFT values reported in the literature. The number of chemisorption sites at the surface of W was given by Markelj et al. [82]: $n_{CS} = 6.9{\rho_W}^{2/3}$. For the specific case where $\theta = 100$ %, the surface is saturated and the plot represents the maximum HI outgassing flux density that can be obtained from the model of Pick and Sonnenberg for W. The blue shaded area represents the interval of implantation flux density Γ_{imp} that can be found in tokamak environment. The shaded zone above the plot of maximum Γ_{out} (given for $\theta = 100$ %) represents the zone where the molecular recycling coefficient R_m can be way below 1. For the case of W, this condition is obtained for an implantation temperature between 300 and 700 K depending on the implantation flux density. This condition means that the material acts as an infinite pump, which is obviously unphysical. This model does not verify the saturation of the wall materials under implantation conditions found in nuclear fusion reactors as seen in chapter 1 section 4. This indicates that the Pick and Sonnenberg model is invalid, or more probably incomplete, to describe the surface processes under such conditions. On the contrary, it will be shown in subsection 2.8 that the Dirichlet B.C. considered in MHIMS enables such saturation of the wall materials.

2.7 Parameterisation of the R-D equations for polycrystalline beryllium.

Now, one will focus on the available parameters of the R-D equations for the interaction between HI and Be. As introduced in subsection 2.2, Be crystallises with a HCP structure. According to ab-initio DFT calculations, the stable positions of HI in pristine Be lattice are BTIS and OIS [56, 57]. As there are 1 BTIS and 1 OIS per atom in a HCP lattice, the density of solute site in Be is $n_{IS,Be} = 2\rho_{Be}$. Concerning HI diffusivity in Be, Abramov et al. [70] have experimentally determined the diffusion coefficient of D in Be using the gas-driven permeation technique. Two different high purity PCBe materials were used in the experiments (respectively 99 % and 99.8 % purity). Abramov et al. obtained the two following diffusion coefficients for the two respective PCBe: $D(T) = 8.0 \times 10^{-9} \exp(-0.36/(k_B T))$ and $D(T) = 6.7 \times 10^{-9} \exp(-0.29/(k_B T))$. These values are considered as the most reliable ones in the literature due to the fact that Abramov et al. have taken into account the effect of the oxide layer in the calculation of both diffusion coefficients. More recently, Wensing et al. [71] have estimated the diffusion coefficient of H in Be from KMC simulation using DFT based energy barriers along the diffusion path [56]. They obtained, from the method described in subsection 2.5, the following diffusion coefficient for HI in Be: $D(T) \approx (1 \times 10^{-6}/\sqrt{A}) \exp(-0.40/(k_B T))$ $\mathrm{m^2.s^{-1}}$ where A is the mass number of the considered HI. One can note a rather good agreement between the activation energy of diffusion obtained by Wensing et al. and the one obtained by Abramov et al. for the 99 % purity PCBe, while a discrepancy is noticed with the 99.8 % purity sample. Moreover, three orders of magnitude discrepancy can be seen between the experimental pre-exponential factors and the one obtained by Wensing et al. These discrepancy can be explained by the tendency of Be to absorb O. The presence of such impurities (and therefore traps for HI) is known to reduce the effective diffusion of HI. In agreement with the definition of the diffusion process in the R-D equations, which is considered as the one in a perfect lattice, the value obtained by Wensing et. al will be considered. A summary of the selected parameters for HI–Be interaction can be found in table 2.4.

Regarding the trapping process, HI implanted in Be is retained in the implantation zone (cf. SIMS profiles in figure 1.13.a-b) up to a saturation ratio of ~ 0.35 D/Be (i.e. a density of 35 at.%) [68, 58, 59]. As a consequence, single crystalline Be and polycrystalline Be do not exhibit a strong difference in terms of HI trapping. The areal inventory of saturation is function of the maximum depth reached by the implanted HIs and therefore of their impact energy [68]. For an implantation of D in Be with an impact energy of 1 keV per D, a flux density of $\sim 1 \times 10^{20}$ $\mathrm{D.m^{-2}.s^{-1}}$ and an implantation temperature of 300 K, Haasz et al. have reported a D areal inventory of saturation of 2.7×10^{21} $\mathrm{D.m^{-2}}$ [31]. This saturation is reached at a fluence of $\sim 10^{24}$ $\mathrm{D.m^{-2}}$. If one assumes that the impact energy of 1 keV is representative of the maximum impact energy that will experience the ITER first-wall, the areal inventory of saturation reported by Haasz et al. will be the upper limit of the T areal inventory in the ITER first-wall due to implantation process. The maximum T inventory in the ITER first-wall can therefore be estimated assuming a surface of the first-wall of 600 $\mathrm{m^2}$ [6] which amounts to ~ 8 g of T. This represents

DIFFUSION		
Parameter	Value	From
D_0	$\sim \frac{1 \times 10^{-6}}{\sqrt{A}}$ m^2.s^{-1}	KMC [71]
E_{diff}	0.4 eV	KMC [71]
TRAPPING		
Parameter	Value	From
$\nu^0_{t,i}$	$D_0/{\lambda_{Be}}^2$	—
λ_{Be}	157.7 pm	DFT [83]
$E_{t,i}$	0.4 eV	—
n_{IS}	$2\rho_{Be}$	DFT [83]
ρ_{Be}	12.2×10^{28} m^{-3}	[84]
DETRAPPING		
Parameter	Value	From
$\nu^0_{dt,i}$	10^{13} s^{-1}	—

Table 2.4: Free parameters of the Reaction-Diffusion equations considered in MHIMS for HI–Be interaction.

only 1.3 % of the T safety limit in ITER (cf. chapter 1 section 5). TDS spectrum of D implanted in Be up to saturation exhibit three desorption peaks (cf. figure 1.14.a) [31]: a sharp low temperature peak at $\sim$ 500 K (reported at $\sim$ 450 K in more recent TDS experiment [85]) which contains the majority of the D inventory and two broader peaks at high temperature (700 and 800 K) with a much lower amplitude. TDS spectra with increasing incident fluences exhibit a sequential occupation of the high-temperature peaks at low fluences followed by the emergence of the low-temperature peak at a given threshold fluence (which depends on the HI impact energy, e.g. $\sim 10^{21}$ D.m^{-2} for 1 keV D ions) when the high-temperature peaks saturate [86, 85]. The SIMS analysis performed by Alimov et al. present the same behaviour (cf. figure 1.13a-b): at low fluence, the density of D atoms increases with a footprint similar to the implantation source, up to a fluence from which the D_2 molecules form. Alimov et al. have attributed the D retained in atomic form to irradiation vacancies. Transmission electron microscopy of post-implantation Be samples was performed and revealed small bubbles of 1 nm radius which increasingly interconnect with rising fluence up to the sample surface [87]. These results suggest that the high-temperature peaks are related to vacancies created during implantation while the low-temperature peak may be related to D adsorbed at the surface of the interconnected cavities.

Concerning the modelling of HI trapping in Be, one will focus on the work presently done by Matveev et al. [61] which represents, to our knowledge, the most advanced attempt of modelling HI–Be interaction. Matveev et al. have developed a code called Coupled Reaction Diffusion Systems (CRDS) which, as its name suggests, is based on the R-D equations. The simulated TDS spectra of D in Be at different D fluences obtained by

Matveev et al. [61] with the CRDS code are displayed in figure 2.7. The simulations qualitatively reproduce the experimental TDS spectra obtained by Reinelt et al. [85] after implantation of 1 keV D ions in Be at different fluences, with an initial formation of high-temperature peaks followed by the appearance of the low-temperature peak at a given fluence. It must be stated that the implantation phase was not simulated. To

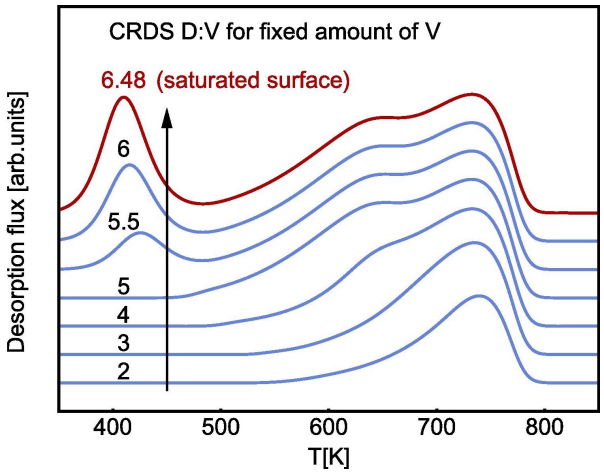

Figure 2.7: Simulated thermal desorption spectra obtained by Matveev et al. [61] with the CRDS code for different Deuterium:Vacancy ratios corresponding to different D fluences. The density of vacancies is fixed to 2.5 at.% and is uniform up to a 50 nm depth (maximum implantation range of 1 keV D ions). The CRDS accounts for trapping of multiple D in a single vacancy as suggested by DFT simulations (5 D per vacancy in the case of Be). As soon as vacancies are filled up to 5 D atoms per vacancy, D starts to accumulate in the chemisorption sites at the surface, which yields a low-temperature desorption peak in TDS. Picture taken from reference [61].

reproduce the TDS, Matveev et al. have considered a uniform trap extending up to a 50 nm depth (maximum implantation range of 1 keV D ions) to model the vacancies. This trap can accommodate multiple D in a single vacancy as suggested by DFT simulations (5 D per vacancy in the case of Be). The CRDS accounts for trapping of multiple D in a single trap through a more complex reaction-diffusion model [61]. The trap density was fixed to 2.5 at.% to recover the experimental inventory found in the saturated high-temperature peaks. For the low-temperature peak, Matveev et al. have used the Pick and Sonnenberg model introduced in subsection 2.6. The desorption flux density is function of the surface density of chemisorbed D (cf. equation 2.33). To account for an increasing D fluence before the TDS, they have filled the vacancies with a Deuterium:Vacancy ratios corresponding to the desired D fluence. As soon as vacancies are filled up to 5 D atoms per vacancy, they are saturated and D starts to accumulate in the chemisorption sites at the surface, which yields to the appearance of the low-temperature desorption peak in TDS.

One will see whether the work done by Matveev et al. can be adapted to the MHIMS model. Concerning the high-temperature peaks attributed to multiple trapping in vacancies, MHIMS can model them with one trap which can accommodate a single HI atom

and which extends up to the maximum range of implantation. As it can be seen in figure 2.8, the high-temperature peak from the experimental TDS spectrum of D implanted in Be performed by Reinelt et al. [85] can be reproduced with MHIMS. The diffusion and lattice parameters used during the simulation are reported in table 2.4. The trap parameters are reported in table 2.5. The implantation phase has not been simulated. At the beginning of the TDS, the trap 3 is assumed to be saturated with D as suggested by the experimental saturation of the high-temperature peaks.

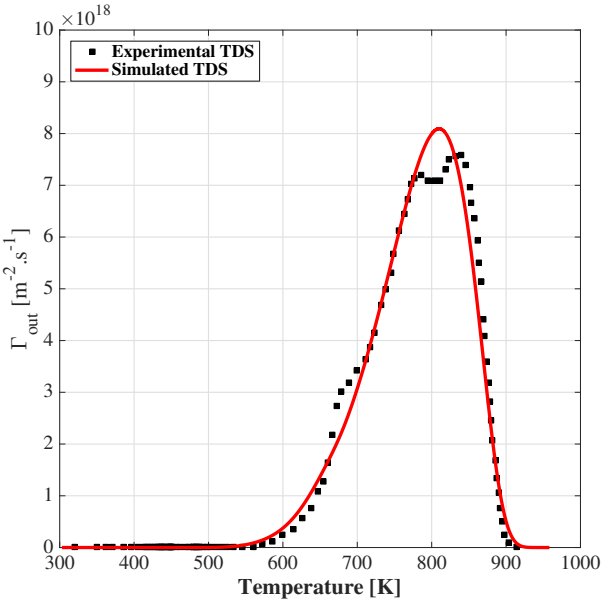

Figure 2.8: High-temperature peak of the TDS spectrum of D implanted in Be at 320 K reported by Reinelt et al.[85] (black points). The TDS peak was reproduced with MHIMS to parameterise the model (red solid line).

	Trap type	Traps parameters
Ion-induced trap (vacancy)	c	$E_{dt,3} = 1.82$ eV $n_3^c(x = 0) = 10.3$ at.%, $X_3^c = 60$ nm

Table 2.5: Trap parameters obtained through the fitting with MHIMS of the high temperature desorption peak of the TDS analysis made by Reinelt et al. [85] after the implantation of 1 keV D ions in Be at 320 K. The damaged zone of the identified trap extends in the implantation zone (with profile of type "c") with a characteristic length X_3^c. The reader is referred to subsection 2.4 and figure 2.3 for more information about the profile of this trap. The trap density is given in at.% of Be.

Concerning the low-temperature peak, MHIMS cannot simulate it as the surface processes are not simulated so far. However, some ambiguities can be noticed in the surface model used by Matveev et al. to reproduce this peak:

– The simulated peak is much broader than the experimental peak. Such broad peak,

due to the recombination and subsequent desorption of chemisorbed HI atoms, is characteristic of a second order kinetic process [71].

- To obtain an areal inventory in this peak similar to the experimental one, Matveev et al. had to increase the surface density of chemisorption sites n_{CS} by a factor of 10 w.r.t. the nominal surface density [61]. They justify this increase by the increase of the effective surface area linked to the formation of interconnected cavities and porosities in Be during the implantation. However, this treatment does not allow to reproduce the evolution of the saturation of retention with the impact energy [68]. Indeed, for a similar implantation flux density but two different impact energies, this model will give exactly the same inventory in the low-temperature peak. For the higher impact energy case, D will implant deeper but will eventually diffuse up to the surface, filling the chemisorbed sites up to the same level as for the lower energy case.

- Eventually, as it was seen in subsection 2.6, the outgassing flux density in the Pick and Sonnenberg model has an inherent upper limit, that cannot be exceeded, which is obtained for a fully saturated surface. In figure 2.6.b, this outgassing flux density, calculated for the case of Be using equation 2.33, is plotted for different surface coverage θ. This calculation was performed considering the activation energy of recombination $E_{rec} = 0.5$ eV and the number of chemisorption sites at the surface of Be $n_{CS} = 2.21 \times 10^{19}$ m^{-2} reported by Matveev et al. [61]. For the specific case where $\theta = 100$ %, the surface is saturated and the plot represents the maximum HI outgassing flux density that can be obtained from the model of Pick and Sonnenberg for Be. The blue shaded area represents the interval of implantation flux density Γ_{imp} that can be found in tokamak environment. The shaded zone above the plot of maximum Γ_{out} (given for $\theta = 100$ %) represents the zone where the molecular recycling coefficient R_m can be way below 1. For Be, this condition is obtained for an implantation temperature between 300 and 600 K depending on the implantation flux density. As for W, the model does not verify the saturation of the wall materials under implantation conditions found in nuclear fusion reactors. To overcome this issue, Matveev et al. have proposed an activation energy of recombination E_{rec} function of the surface coverage with a transition to a barrier free recombination for a saturated surface (i.e. $E_{rec} = 0$ for $\theta = 100$ %). Still this approach requires further analysis and simulations to confirm its validity.

To conclude, the modelling of the low-temperature desorption peak still requires improvement. As the majority of the HI areal inventory of saturation (75 %) is found in this peak, one conclude that the modelling of a Be wall is not possible with the present knowledge.
Last but not least, according to Anderl et al., the HI areal inventory of saturation seems to be constant up to 600 K [68]. At such temperature, the trap responsible for the low-temperature peak should not be filled and the areal inventory should in principle be lower than the one for implantation at room temperature. This was confirmed by a TDS analysis done by Reinelt et al. after a D implantation in Be at a temperature of 530 K [85]

(to our knowledge, the only TDS of D implanted into Be at such temperature published in the literature). The TDS spectra obtained for an implantation at 320 K and at 530 K are displayed in figure 2.9. The low-temperature peak is not occupied in the 530 K implantation experiment. Instead, two peaks have appeared at $\sim$ 575 K and at $\sim$ 725 K indicating a change of the interaction between D and Be. Overall, the retention is similar for both experiments. Reinelt et al. have attributed the latter peak to a possible higher amount of oxygen in the Be sample after implantation at 530 K. The reason for the peak at 575 K is still unclear. Reinelt et al. have suggested the formation of BeD_2 (hydride) during the implantation. Unfortunately, no modelling effort has been undertaken in the fusion community to understand and to simulate this change of interaction. It must be pointed out that the base temperature of the JET-ILW is 473 K (200 °C) while the ITER first-wall will have a base temperature of 343 K (70 °C). The understanding of this change of interaction is therefore critically important as these results suggest that the ITER first-wall will not behave like the JET-ILW first-wall in particular during the start-up phase of the discharge.

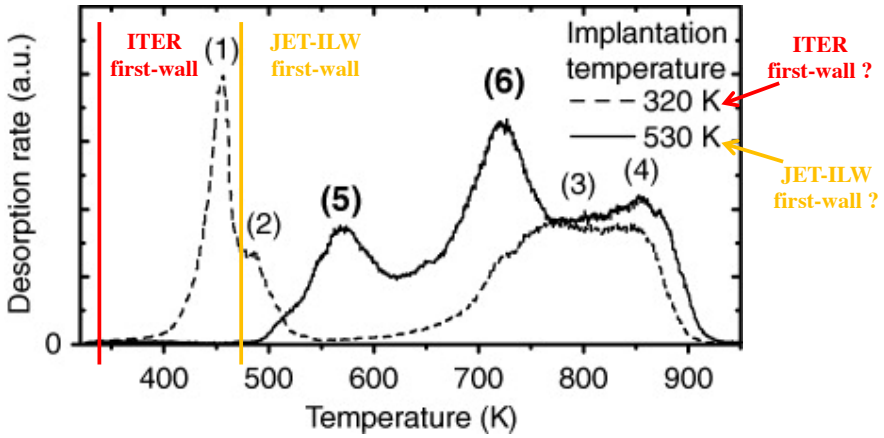

Figure 2.9: TDS spectra of D implanted into Be at temperatures of 320 and 530 K. Retention in the high-temperature peak is not affected. The low-temperature peak is not occupied in the 530 K implantation experiment. Instead, two peaks have appeared at $\sim$ 575 K and at $\sim$ 725 K indicating a change of the interaction between D and Be at high temperature of exposure. Picture taken and adapted from reference [85].

2.8 Analytical model of saturation of wall inventory and confrontation to MHIMS simulation results.

As it was shown in chapter 1 section 4, it is experimentally observed during tokamak operation a saturation of the dynamic retention with a characteristic time ranging from 1 to 100 s. A wall model aiming to simulate this dynamic retention, like MHIMS in our context, must reproduce this behaviour. To verify this, a D implantation in W is simulated with MHIMS considering three different implantation temperatures: 300 K, 500 K

and 800 K. A W sample of 1 mm depth is loaded with both D^+ and D with implantation conditions (flux density and energy, similar for the three simulations) consistent with divertor conditions. A normal incidence of the particles w.r.t. the material surface is considered for both ions and atoms. The parameters of implantation are gathered in table 2.6.

Implantation parameters	D^+	D
Γ^j_{imp} [$m^{-2}.s^{-1}$]	1.0×10^{21}	0.5×10^{21}
E^j_{imp} [eV]	100	50
α^j_{imp} [°]	90	90
X^j_{imp} [nm]	2.7	1.8

Table 2.6: Implantation parameters for both D^+ and D considered in the simulation of D implantation in W. The values of the corresponding mean implantation ranges X^{i+}_{imp} and X^{at}_{imp} calculated by the SRIM code are also given.

Concerning MHIMS parameterisation, the parameters obtained by Hodille et al. for the interaction of D with polycrystalline tungsten are used (cf. subsection 2.6). The parameters set by Hodille et al. are summed up in table 2.2. The diffusion coefficient from DFT is taken in [54]: $D(T) = 1.9 \times 10^{-7} \exp(-0.2/(k_B T))$ $m^2.s^{-1}$. This diffusion coefficient was calculated for hydrogen. To take into account the isotope effect, the diffusion pre-exponential factor is divided by $\sim \sqrt{2}$, the square root of the mass ratio between D and H. For the traps, the free-parameters (detrapping energies and trap density profiles) obtained by Hodille et al. through fitting of TDS experiments (cf. subsection 2.6) are used. Three traps are considered: two intrinsic traps and one trap induced by plasma irradiation. The free-parameters of these traps are reported in table 2.7. The intrinsic traps have a flat depth profile (type "a" profile, cf. figure 2.3). Their density is equal to the value reported in the table. The plasma-induced trap presents two damaged zones like the ones reported in subsection 2.6: a highly damaged zone in the implantation zone (with profile of type "c") and a damaged zone extending in the depth of the material (with profile of type "b"). The densities reported in table 2.7 for trap 3 (n^i_3) are the maximum trap densities of each profile (at the surface of the material). The characteristic depths of each profile (X^i_3) are also reported in the table. These parameters are considered to be appropriate for a W material submitted to divertor-like irradiation conditions. More information will be given on the density profile of trap 3 in the introduction of the simulation of the dynamics of the JET wall during plasma operation (cf. chapter 4 subsection 1.1). Moreover, the reader is referred to subsection 2.4 and figure 2.3 for more information about the different profiles of trap and their parameterisation.
In figure 2.10.a, the time evolution of the molecular recycling coefficient is displayed for the three different implantation temperatures. One can see in this figure that R_m tends to 1 for the three temperatures. The D areal inventory seems to saturate simultaneously (cf. figure 2.10.b) as its time derivative tends to zero. In reality, this time derivative, which can also be named retention flux density, becomes negligible w.r.t. the total implantation flux density / the outgassing flux density (both flux density are similar as

	Trap type	Trap parameters
Intrinsic trap 1	a	$E_{dt,1} = 0.85$ eV $n_1^a = 0.13$ at.%
Intrinsic trap 2	a	$E_{dt,2} = 1.00$ eV $n_2^a = 0.035$ at.%
Plasma-induced trap 3	b and c	$E_{dt,3} = 1.5$ eV $n_3^b(x=0) = 1$ at.%, $X_3^b = 10.8$ μm $n_3^c(x=0) = 15$ at.%, $X_3^c = 30$ nm

Table 2.7: Trap parameters used in the simulation of D implantation in W. The trap densities are given in at.% of W. For intrinsic traps (type "a"), the trap densities are constant in all the depth of the material and equal to the values presented in this table (n_1^a and n_2^a respectively). The plasma-induced trap presents two damaged zones: a highly damaged zone at the surface (with profile of type "c") and a damaged zone extending in the depth of the material (with profile of type "b"). The densities reported for trap 3 (n_3^i) are the densities of trap at the surface of the material. The characteristic depths of each profile (X_3^i) are also reported. The reader is referred to subsection 2.4 and figure 2.3 for more information about the profiles of trap.

$R_m = 1$) and the areal inventory still increases slowly. The time to reach this seeming saturation ranges between 1 and 10 s depending on the temperature of the material. This simultaneous behaviour can be understood by analysing the diffusion equation 2.22a in the R-D equations. This equation can be reformulated as follows:

$$\frac{\partial}{\partial t}\left(n_m(x,t) + \sum_{i=1}^{N_{trap}} n_{t,i}(x,t)\right) = \frac{\partial}{\partial x}\left(D(T)\frac{\partial n_m}{\partial x}\right) + S_{ext}^{i+}(x,t) + S_{ext}^{at}(x,t) \tag{2.34}$$

The sum in parenthesis in the Left-Hand Side (LHS) is the total D density. The total D areal inventory, Inv, is obtained through spatial integration of this equation:

$$\begin{aligned}
\int_0^L \frac{\partial}{\partial t}\left(n_m(x,t) + \sum_{i=1}^{N_{trap}} n_{t,i}(x,t)\right) dx &= \int_0^L \frac{\partial}{\partial x}\left(D(T)\frac{\partial n_m}{\partial x}\right) dx \\
&\quad + \int_0^L S_{ext}^{i+}(x,t)dx + \int_0^L S_{ext}^{at}(x,t)dx \\
\frac{d}{dt}\left\{\int_0^L \left(n_m(x,t) + \sum_{i=1}^{N_{trap}} n_{t,i}(x,t)\right) dx\right\} &= D(T)\frac{\partial n_m}{\partial x}(L,t) - D(T)\frac{\partial n_m}{\partial x}(0,t) \\
&\quad + \Gamma_{imp}^{i+}(t) + \Gamma_{imp}^{at}(t) \\
\frac{dInv(t)}{dt} &= D(T)\frac{\partial n_m}{\partial x}(L,t) - D(T)\frac{\partial n_m}{\partial x}(0,t) \\
&\quad + \Gamma_{imp}^{i+}(t) + \Gamma_{imp}^{at}(t)
\end{aligned} \tag{2.35}$$

From the simulation results, one can see that the desorption flux density at the rear

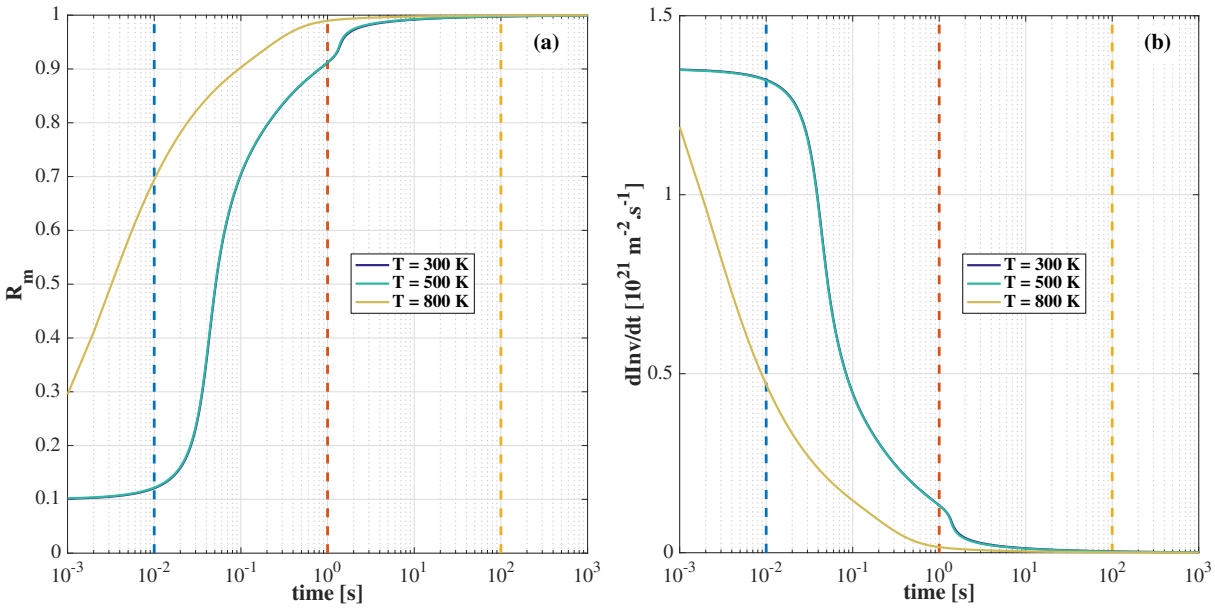

Figure 2.10: Time evolution of the molecular recycling coefficient R_m (a) and of the time derivative of the total D areal inventory (b) for a simulation of implantation of D in a W sample. The implantation parameters are listed in table 2.6 while the parameters for HI–W interaction considered in MHIMS are summed up in table 2.2 and in table 2.7. The implantation is performed at three different sample temperatures: 300 K, 500 K and 800 K. The plots for $T = 300$ K and $T = 500$ K overlap. For all the simulations, R_m tends to 1 indicating a saturation of the wall inventory. The vertical dashed lines indicate the three times at which are plotted the density profiles of mobile and trapped particles in figures 2.12, 2.13 and 2.14.

surface at $x = L$ (the first term in the RHS of the last equation of 2.35) is negligible even after 1000 s for the simulation at $T = 800$ K (the mobile D did not reach the rear boundary of the material). In addition, one can recognise the outgassing flux density Γ_{out} in the second term of the RHS of the last equation. Therefore equation 2.35 can be reformulated to express the relation between R_m and Inv:

$$\begin{aligned} R_m(t) &= \frac{\Gamma_{out}(t)}{\Gamma^{i+}_{imp}(t) + \Gamma^{at}_{imp}(t)} \\ R_m(t) &= 1 - \frac{dInv(t)}{dt} \times \frac{1}{\Gamma^{i+}_{imp}(t) + \Gamma^{at}_{imp}(t)} \end{aligned} \tag{2.36}$$

From equation 2.36, one can easily see that R_m tends to 1 when the following condition is verified:

$$R_m(t) \to 1 \Leftrightarrow \frac{dInv(t)}{dt} \ll \Gamma^{i+}_{imp}(t) + \Gamma^{at}_{imp}(t) \tag{2.37}$$

This condition indicates that the evolution of the inventory must be low w.r.t. the total implantation flux density.

To understand qualitatively how the HI inventory saturates in response to HI implantation, a simplified description of material implantation is introduced. This description was first used by B. L. Doyle in 1982 [88] and more recently by K. Schmid [79] and by Hodille et al. [60]. In this description, the external source of implantation is considered as a homogeneous point source at a depth equal to the mean implantation depth. In our case, one will consider two point sources of implantation with respective mean implantation depth $x = X_{imp,1}$ and $x = X_{imp,2}$ (as there are two implantation sources S_{ext}^{i+} and S_{ext}^{at}). No information on the nature of the implanted particles is given (ions or atoms). It is only assumed that the second implanted specie implants deeper than the first one (i.e. $X_{imp,1} < X_{imp,2}$). Additionally, the temperature in the material will be assumed constant in space and time. Moreover, one is interested in the stationary state. Under all these assumptions, the diffusion equation in the R-D equations becomes:

$$\frac{\partial}{\partial x}\left(D(T)\frac{\partial n_m}{\partial x}\right) + \Gamma_{imp,1}\delta(x - X_{imp,1}) + \Gamma_{imp,2}\delta(x - X_{imp,2}) = 0 \tag{2.38}$$

Equation 2.38 can be solved assuming the Dirichlet B.C. 2.25 at the front surface and either the Dirichlet B.C. or the Neumann B.C 2.27 at the rear surface. For the case of a Neumann B.C. at the rear surface, the solution of equation 2.38 is:

$$\begin{cases} \text{for } x \in [0, X_{imp,1}],\ n_m(x) = \left[\dfrac{\Gamma_{imp,1}}{D(T)} + \dfrac{\Gamma_{imp,2}}{D(T)}\right] x & \text{(2.39a)} \\ \text{for } x \in [X_{imp,1}, X_{imp,2}],\ n_m(x) = \dfrac{\Gamma_{imp,2}}{D(T)} x + \dfrac{\Gamma_{imp,1}}{D(T)} X_{imp,1} & \text{(2.39b)} \\ \text{for } x \in [X_{imp,2}, L],\ n_m(x) = \dfrac{\Gamma_{imp,2}}{D(T)} X_{imp,2} + \dfrac{\Gamma_{imp,1}}{D(T)} X_{imp,1} = n_m^{MAX} & \text{(2.39c)} \end{cases}$$

where the maximum value of the density n_m^{MAX} has been defined. This profile is illustrated in figure 2.11.
For the case of a Dirichlet B.C. at the rear surface, the solution of equation 2.38 is:

$$\begin{cases} \text{for } x \in [0, X_{imp,1}],\ n_m(x) = \left[\dfrac{\Gamma_{imp,1}}{D(T)}\left(1 - \dfrac{X_{imp,1}}{L}\right) + \dfrac{\Gamma_{imp,2}}{D(T)}\left(1 - \dfrac{X_{imp,2}}{L}\right)\right] x \\ \text{for } x \in [X_{imp,1}, X_{imp,2}],\ n_m(x) = \left[-\dfrac{\Gamma_{imp,1}}{D(T)}\dfrac{X_{imp,1}}{L} + \dfrac{\Gamma_{imp,2}}{D(T)}\left(1 - \dfrac{X_{imp,2}}{L}\right)\right] x \\ \qquad\qquad + \dfrac{\Gamma_{imp,1}}{D(T)} X_{imp,1} \\ \text{for } x \in [X_{imp,2}, L],\ n_m(x) = \left[-\dfrac{\Gamma_{imp,1}}{D(T)}\dfrac{X_{imp,1}}{L} - \dfrac{\Gamma_{imp,2}}{D(T)}\dfrac{X_{imp,2}}{L}\right] x \\ \qquad\qquad + \left[\dfrac{\Gamma_{imp,2}}{D(T)} X_{imp,2} + \dfrac{\Gamma_{imp,1}}{D(T)} X_{imp,1}\right] \end{cases} \tag{2.40}$$

This profile is also illustrated in figure 2.11. Actually, under realistic implantation conditions in fusion reactor, the D mean ranges $X_{imp,1}$ and $X_{imp,2}$ do not exceed 50 nm in

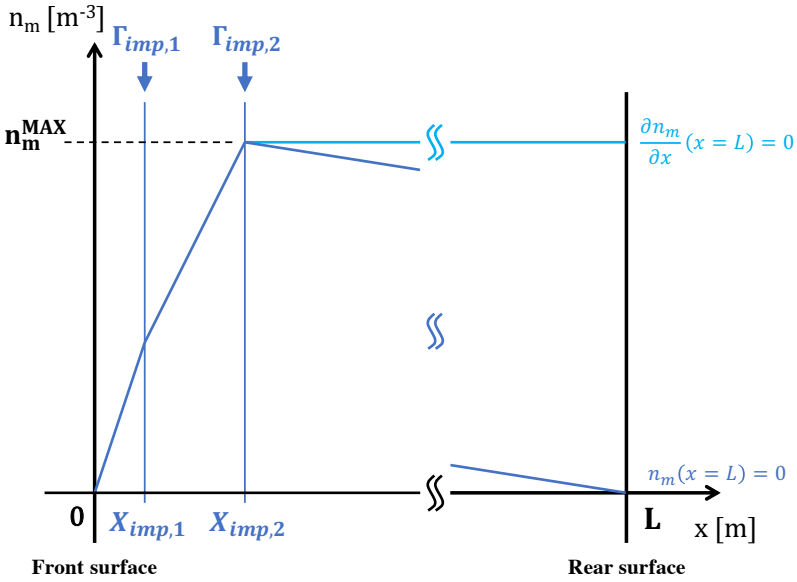

Figure 2.11: Schematic of the steady-state density profile of mobile HI in the simplified description of HI implantation in material. The two externals sources of implantation are considered as point sources at their respective mean implantation ranges $x = X_{imp,1}$ and $x = X_{imp,2}$. The two different bulk profiles (for $X_{imp,2} \leq x \leq L$), corresponding to the use of a Dirichlet boundary condition at the rear surface (dark blue line) and of a Neumann boundary condition (light blue line) (equations 2.27), are also depicted.

both W and Be. As it was previously said in subsection 2.3, the Dirichlet B.C. should be used for massive surface material with a depth L of about several millimeters. Therefore, the following relation holds, $X_{imp,i} \ll L$, and the gradient of n_m in the zone $[X_{imp,2}, L]$ in equation 2.40 is very weak. It can even be considered null in a length of several $X_{imp,2}$ (referred as $kX_{imp,2}$) so that the profile of mobile can be approximated as follows:

$$\begin{cases} \text{for } x \in [0, X_{imp,1}],\ n_m(x) \approx \left[\dfrac{\Gamma_{imp,1}}{D(T)} + \dfrac{\Gamma_{imp,2}}{D(T)}\right] x & \text{(2.41a)} \\ \text{for } x \in [X_{imp,1}, X_{imp,2}],\ n_m(x) \approx \dfrac{\Gamma_{imp,2}}{D(T)} x + \dfrac{\Gamma_{imp,1}}{D(T)} X_{imp,1} & \text{(2.41b)} \\ \text{for } x \in [X_{imp,2}, kX_{imp,2}],\ n_m(x) \approx \dfrac{\Gamma_{imp,2}}{D(T)} X_{imp,2} + \dfrac{\Gamma_{imp,1}}{D(T)} X_{imp,1} = n_m^{MAX} & \text{(2.41c)} \end{cases}$$

One can recognise the density profile for the Neumann B.C. case 2.39. The outgassing flux density can be obtained using the similar equations 2.39a and 2.41a:

$$\Gamma_{out} = D(T) \frac{\partial n_m}{\partial x}(0) = \Gamma_{imp,1} + \Gamma_{imp,2} \tag{2.42}$$

And the resulting molecular recycling coefficient is:

$$R_m = \frac{\Gamma_{out}}{\Gamma_{imp,1} + \Gamma_{imp,2}} = 1 \tag{2.43}$$

The condition of full recycling is verified by both analytical profiles of mobile D 2.39 and 2.41. This analytical profile can be confronted to the results of the simulations presented earlier in this subsection. The profiles are extracted at three times during the simulations: at 0.01 s, 1 s and 100 s. On figure 2.10.a, one can see that at $t = 0.01$ s, R_m is way below 1 for the three temperatures of implantation. For $t = 1$ s, R_m is around 0.9 for the simulation at 300 K and 500 K, while it has already saturated at 1 for the simulation at 800 K. At $t = 100$ s, R_m has reached a value of 1 for the three simulations. The profiles of n_m at the three selected times are plotted for an implantation temperature of 300 K, 500 K and 800 K in figures 2.12.a, 2.12.b and 2.12.c respectively. The analytical density profiles obtained from equation 2.39/2.41 are also displayed as well as the mean implantation ranges for ions X_{imp}^{i+} and for atoms X_{imp}^{at} (whose values are reported in table 2.6). A very good agreement between the analytical profiles and the simulated profiles can be observed in the implantation zone ($0 \leq x \leq 30$ nm) for the cases where R_m has reached 1, i.e. at $t = 100$ s for the three implantation temperatures and at $t = 1$ s for the implantation temperature of 800 K. At $t = 0.01$ s, the density profile of mobile is still building up for the three temperatures. At $t = 1$ s for the simulation at 300 K and 500 K, the diffusion front in the depth of the material is not distant enough from the implantation zone to have an almost flat density profile of mobile in the zone $x > X_{imp,2}$. One can clearly see that the density profiles for each implantation temperature tend to the analytical profiles when the implantation time increases. Thus, this analytical profile 2.39/2.41 can be seen as a upper limit of the density profile of mobile particles.
Now, one is interested in the profile of trapped particles. To estimate an analytical stationary profile, the steady-state of the trapping equation 2.22b is studied:

$$\frac{\partial n_{t,i}(x,t)}{\partial t} = 0 \Leftrightarrow n_{t,i}(x) = \frac{n_i(x)}{1 + \dfrac{\nu_{dt,i}(T)}{\nu_{t,i}^*(T)} \dfrac{n_{IS}}{n_m(x)}} \tag{2.44}$$

Therefore, considering the analytical stationary profile of n_m (equations 2.39/2.41), the density profile of $n_{t,i}$ can be expressed using equation 2.44. As an example, this expression is used to calculate the profiles of $n_{t,i}$ for the traps 1 and 3 defined for the simulations presented earlier in this subsection. These traps are arbitrarily selected due to their highly different detrapping energies. The conclusions presented in the following also apply to the trap 2. The profiles of $n_{t,i}$ at the three selected times are respectively plotted for an implantation temperature of 300 K, 500 K and 800 K in figures 2.13.a, 2.13.b and 2.13.c for the trap number 1 and in figures 2.14.a, 2.14.b and 2.14.c for the trap number 3. The analytical density profiles obtained from equation 2.44 are also displayed. The same conclusions as for the profile of n_m can be drawn for $n_{t,i}$ in the two considered traps: a very good agreement between the analytical profiles and the simulated profiles in the

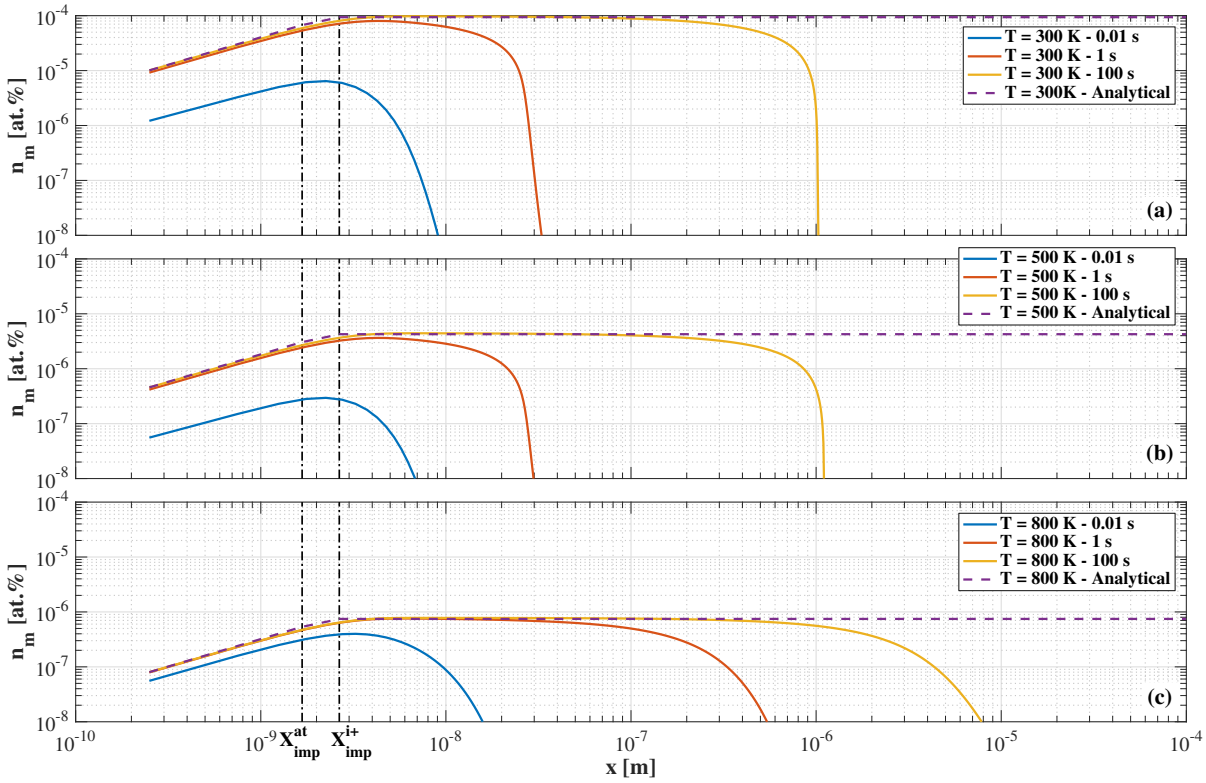

Figure 2.12: Density profile of mobile D obtained in the simulation of D implantation in a W sample with MHIMS. The profiles are plotted for three different times in the simulation: 0.01 s, 1 s and 100 s. The implantation is performed at three different sample temperatures: 300 K, 500 K and 800 K. The respective profiles are plotted in figures (a), (b) and (c). The analytical density profiles obtained from equation 2.39/2.41 are also plotted. The density is expressed in at.% of W. The implantation mean ranges for ions X^{i+}_{imp} and for atoms X^{at}_{imp} in the simulations are also indicated.

implantation zone ($0 \leq x \leq 30$ nm) for the aforementioned cases where R_m has reached 1 and the profiles for each implantation temperature tend to the analytical profiles when the implantation time increases. Thus, this analytical profile 2.44 can also be seen as a upper limit of the profile of $n_{t,i}$ to which the MHIMS model converges.
The equilibrium filling ratio of each trap can be defined from equation 2.44:

$$R_{eq,i}(x) = \frac{n_{t,i}(x)}{n_i(x)} = \frac{1}{1 + \dfrac{\nu_{dt,i}(T)}{\nu^*_{t,i}(T)} \dfrac{n_{IS}}{n_m(x)}} \tag{2.45}$$

When $R_{eq,i} = 100$ %, the traps are locally fully saturated, while when $R_{eq,i} = 0$ % they are locally empty. In addition, if it is considered that only diffusion limits trapping, meaning $\nu^*_{t,i}(T) = D(T)/\lambda^2$, and if one considers the maximum density of mobile n_m^{MAX}

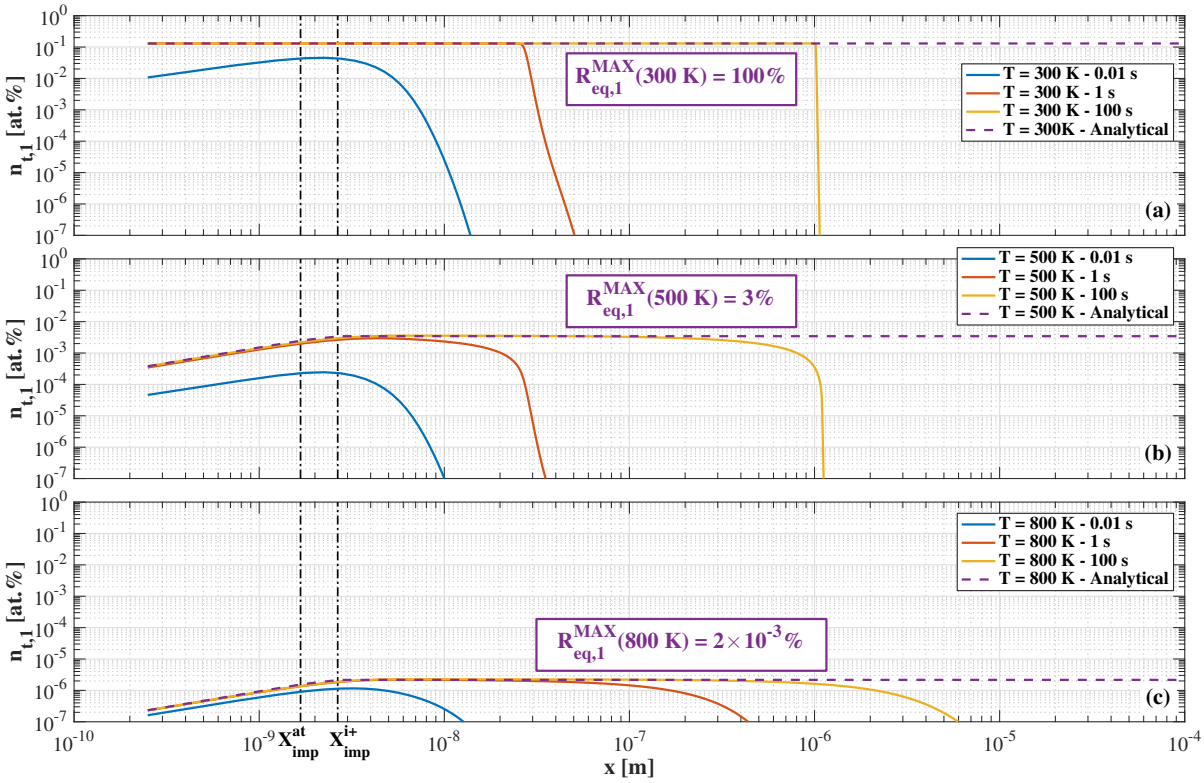

Figure 2.13: Density profile of D trapped in trap 1 obtained in the simulation of D implantation in a W sample with MHIMS. The profiles are plotted for three different times in the simulation: 0.01 s, 1 s and 100 s. The implantation is performed at three different sample temperatures: 300 K, 500 K and 800 K. The respective profiles are plotted in figures (a), (b) and (c). The analytical density profiles of trapped D, obtained from equation 2.44, are also plotted. The mean implantation ranges for ions X^{i+}_{imp} and for atoms X^{at}_{imp} in the simulations are also indicated. The maximum filling ratio of the trap $R^{MAX}_{eq,1}$, as defined by equation 2.46, is also given for the three implantation temperatures.

defined in equation 2.39.c/2.41.c, a maximum filling ratio can be defined:

$$R^{MAX}_{eq,i} = \frac{1}{1 + \frac{\nu_{dt,i}(T)\lambda^2}{D(T)} \frac{n_{IS}}{n^{MAX}_m}}$$

$$R^{MAX}_{eq,i} = \frac{1}{1 + \frac{\nu_{dt,i}(T)\lambda^2}{D(T)} \frac{n_{IS} D(T)}{\Gamma_{imp,2} X_{imp,2} + \Gamma_{imp,1} X_{imp,1}}}$$

$$R^{MAX}_{eq,i} = \frac{1}{1 + \frac{\nu_{dt,i}(T)\lambda^2 n_{IS}}{\Gamma_{imp,2} X_{imp,2} + \Gamma_{imp,1} X_{imp,1}}} \tag{2.46}$$

Equation 2.46 shows that the maximum equilibrium filling ratio of a given trap only

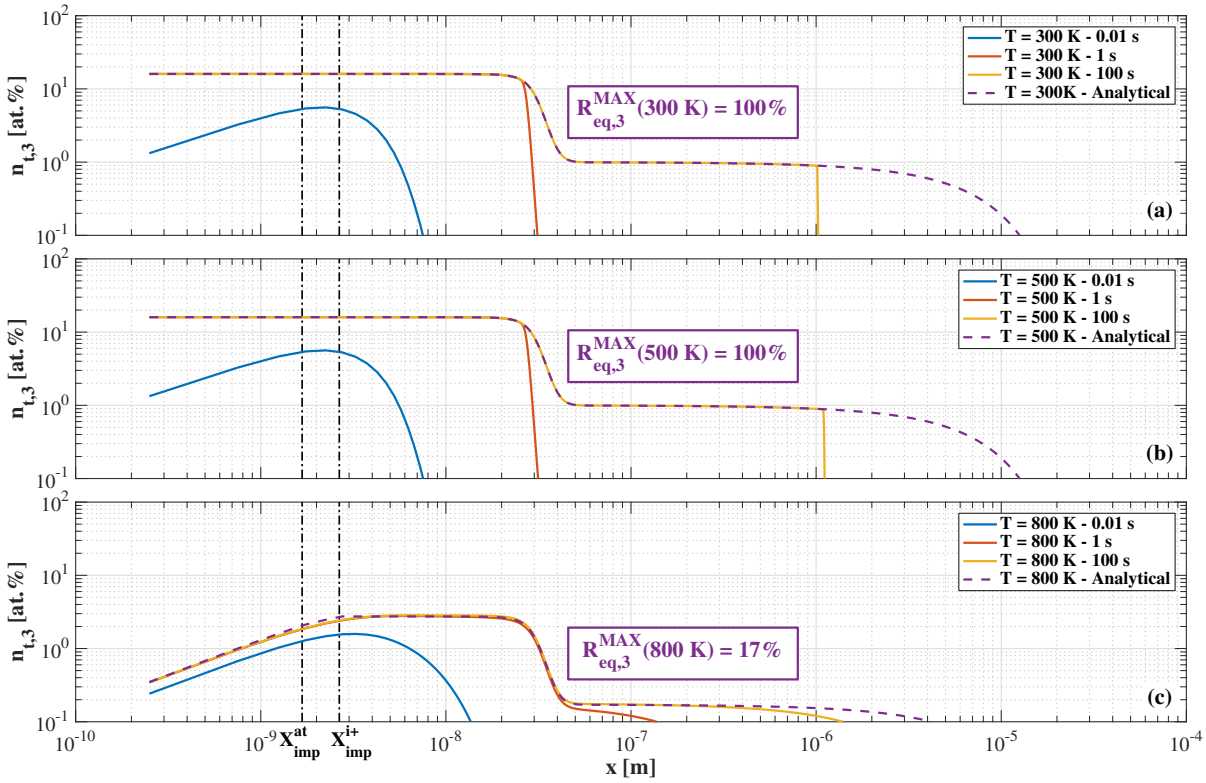

Figure 2.14: Density profile of D trapped in trap 3 obtained in the simulation of D implantation in a W sample with MHIMS. The profiles are plotted for three different times in the simulation: 0.01 s, 1 s and 100 s. The implantation is performed at three different sample temperatures: 300 K, 500 K and 800 K. The respective profiles are plotted in figures (a), (b) and (c). The analytical density profiles of trapped D, obtained from equation 2.44, are also plotted. The mean implantation ranges for ions X_{imp}^{i+} and for atoms X_{imp}^{at} in the simulations are also indicated. The maximum filling ratio of the trap $R_{eq,3}^{MAX}$, as defined by equation 2.46, is also given for the three implantation temperatures.

depends on the detrapping frequency of the trap $\nu_{dt,i}$ (and therefore on its detrapping energy and on the implantation temperature) but also on the implantation conditions (given by the product of the implantation flux density with the respective mean implantation range). The value of $R_{eq,i}^{MAX}$ is given for the three simulations done in this subsection in figure 2.13 for trap 1 and in figure 2.14 for trap 3. At 300 K both traps are fully saturated. At 500 K, trap 3 is still saturated while trap 1 remains empty during implantation with a maximum filling ratio of 3 %. At 800 K, trap 1 is completely empty while trap 3 is partially filled with a $R_{eq,i}^{MAX}$ of 17 %. Overall, trap 3 retains more efficiently D due to its higher detrapping energy. Moreover, one can note by comparing figures 2.12, 2.13 and 2.14 that the D density in each trap $n_{t,i}$ is much higher than the density of mobile D n_m for the three temperatures of implantation. This indicates that the D inventory is predominantly found in the traps in these three simulations. One can wonder whether that is always true. The necessary condition to have a HI inventory predominantly in the traps can be expressed using the expression of n_m^{MAX} 2.39.c/2.41.c and the expression of

the maximum trapping ratio $R_{eq,i}^{MAX}$ 2.46 as follows:

$$\begin{aligned} &\frac{n_{t,i}^{MAX}}{n_m^{MAX}} \gg 1 \Leftrightarrow \frac{R_{eq,i}^{MAX} n_i(x)}{n_m^{MAX}} \gg 1 \\ &\frac{n_{t,i}^{MAX}}{n_m^{MAX}} \gg 1 \Leftrightarrow n_i(x) \gg \underbrace{\frac{\Gamma_{imp,2} X_{imp,2} + \Gamma_{imp,1} X_{imp,1}}{D(T)} + \frac{\nu_{dt,i}(T)\lambda^2}{D(T)} n_{IS}}_{n_i^{MIN}} \end{aligned} \tag{2.47}$$

Equation 2.47 gives a necessary condition on the trap density to have an inventory predominantly in the traps: the trap density must exceed a value identified as n_i^{MIN}. n_i^{MIN} is expressed as a sum of two terms. The first term can be identified as n_m^{MAX} and only depends on the implantation conditions and on the diffusion coefficient. The second term depends on the trap itself through the detrapping frequency (in reality the ratio between the detrapping frequency and the diffusion coefficient gives an Arrhenius expression involving the binding energy of the trap). Hence, n_i^{MIN} depends strongly on the material temperature. Its value can be calculated for W and for Be to see whether the condition 2.47 is verified for both materials in a temperature interval representative of fusion reactor conditions. An extreme implantation condition is considered for the calculation (only one implanted specie, $\Gamma_{imp} = 1 \times 10^{24}$ m^{-2}.s^{-1}, $E_{imp} = 1$ keV) as it maximises the value of n_m^{MAX} and therefore n_i^{MIN}. n_i^{MIN} is calculated for 4 random detrapping energies (0.8, 1.2, 1.6 and 2.0 eV) and considering the parameters for W and Be given in table 2.2 and table 2.4 respectively. The results are plotted in figure 2.15.a for W and figure 2.15.b for Be. The plots present a similar trend. First a decreasing part is seen at low temperature. This part is common for all the detrapping energies (the plots overlap) and is due to the preponderance of n_m^{MAX} in the value of n_i^{MIN}. This part is therefore strongly dependent on the implantation conditions and can be seen as a upper limit. Then the curves change of variation and n_i^{MIN} increases with the temperature. The lower the detrapping energy, the sooner this change of variation occurs: the second term in n_i^{MIN} becomes preponderant. From figure 2.15.a, one can see that any trap in W with detrapping energy above 1.2 eV and with density above 1 at.% satisfies the condition 2.47 in all the temperature range. The trap 3 of the W considered in the simulations presented in this subsection (cf. table 2.7) fulfills both criteria: this trap will host the majority of the D inventory under any implantation conditions. This fact is corroborated by the simulation results (cf. the density profiles 2.12 and 2.14). Concerning the traps number 1 and 2, the condition 2.47 is fulfilled in a limited temperature region. At first sight, this condition is not fulfilled for both traps between 300 and 400 K. One must be aware that a factor of 10 decrease of the implantation flux density ($10^{24} \rightarrow 10^{23}$ D.m^{-2}.s^{-1}, which is still a strong flux density) would lead to a similar decrease of n_m^{MAX} and therefore a similar decrease of n_i^{MIN} in the low temperature region. Thus, the condition 2.47 can be considered as satisfied for traps 1 and 2 in the low temperature region. The temperature intervals of validity for trap 1 and trap 2 can respectively be estimated as being $300 - 800$ K and $300 - 1000$ K. This is again confirmed by the simulation results for trap 1 as, from the density profiles displayed in figures 2.12 and 2.13, one can noticed that the density of trapped D is always

higher than the density of mobile D for the three implantation temperatures. For Be (cf. 2.15.b), if one omits the low temperature part of the curves which is strongly dependent on the implantation conditions, one can see that any trap with a detrapping energy above 0.8 eV and with a density above 1 at.% satisfies the condition 2.47 in all the temperature range. This condition is satisfied by the trap identified in subsection 2.7 (cf. table 2.5) which has enabled the fit of the high temperature peak of the Be TDS.

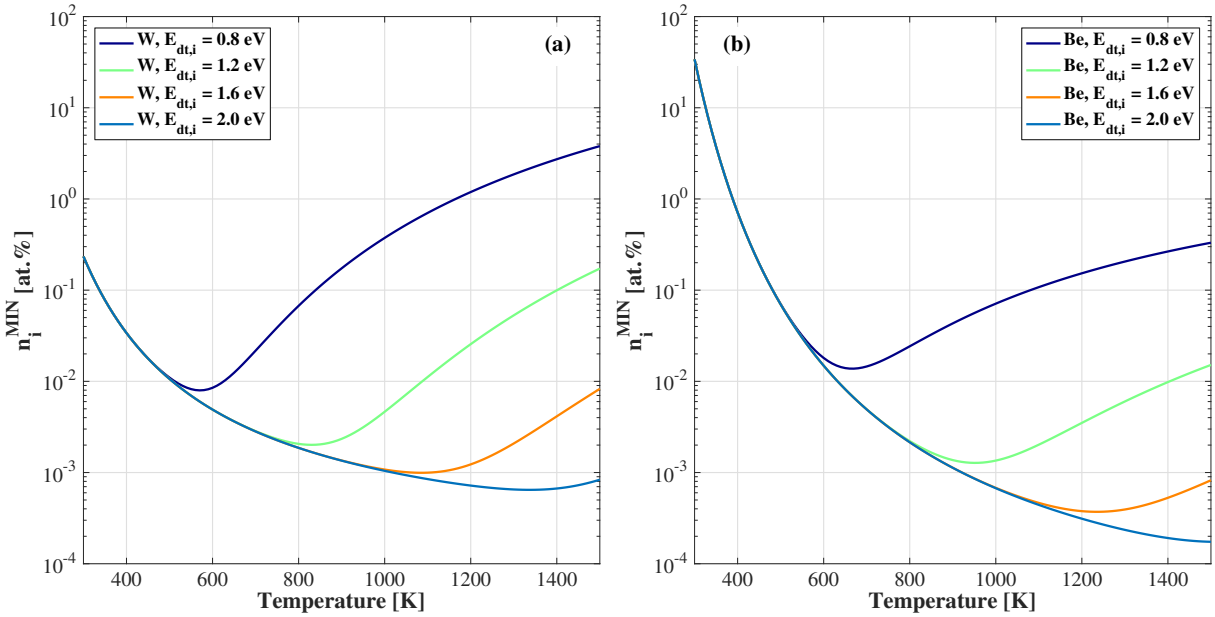

Figure 2.15: Minimum trap density n_i^{MIN} that must be exceeded by the traps to have a HI inventory mostly found in traps (condition 2.47) rather than in solute sites. n_i^{MIN} is calculated considering extreme implantation conditions ($\Gamma_{imp} = 1 \times 10^{24}$ m^{-2}.s^{-1}, $E_{imp} = 1$ keV) so that the plots represent a upper limit of the condition 2.47. The calculation is made for both tungsten (a) and beryllium (b) considering different values of the detrapping energy.

One can conclude that for both W and Be, D will be predominantly retained in bulk material traps during plasma operation. As a consequence, the maximum equilibrium filling ratio $R_{eq,i}^{MAX}$ represents also a simple parameter that indicates how the total HI inventory builds up in a material during plasma operation. This analytical parameter will be used in the analysis of the different simulations of the wall dynamics of the JET tokamak presented in chapter 4.

3 Modelling of the thermal response of plasma facing components: the WEE-temp code.

In the previous section, a model of HI–material interaction based on R-D equations has been introduced. The HI diffusion coefficient and the trapping and detrapping frequencies

involved in this model follow Arrhenius type laws which strongly depend on the material temperature. Therefore the calculation of the temperature profile in the depth of the material is required in all the vacuum chamber.
A thermal model must be selected with the aim of the modelling of an ELM-like event with SolEdge2D-EIRENE. Such model needs to meet specific requirements. To illustrate this, figure 2.16 shows the time evolution of the surface temperature measured by infrared thermography at two locations in the outer divertor of the JET tokamak during a H-mode discharge. The black solid line represents the surface temperature at the outer strike-point while the red solid line represents the surface temperature at a remote location in the outer SOL. Both temperatures exhibit the same time evolution during the H-mode phase (for 8 s $\leq t \leq$ 14 s):

- A gradual increase on the time scale of about several seconds (indicated by the yellow arrow in figure 2.16) due to the steady-state heat load. This evolution depends on the design of the considered PFC, i.e. its geometry, its material layers (thickness and thermal properties) and its cooling technique (inertially cooled or actively-cooled).

- Sharp temperature peaks ($\sim$ 120 °C) which overlap the gradual temperature increase. These peaks are due to ELM heat bursts striking the divertor on a millisecond time scale.

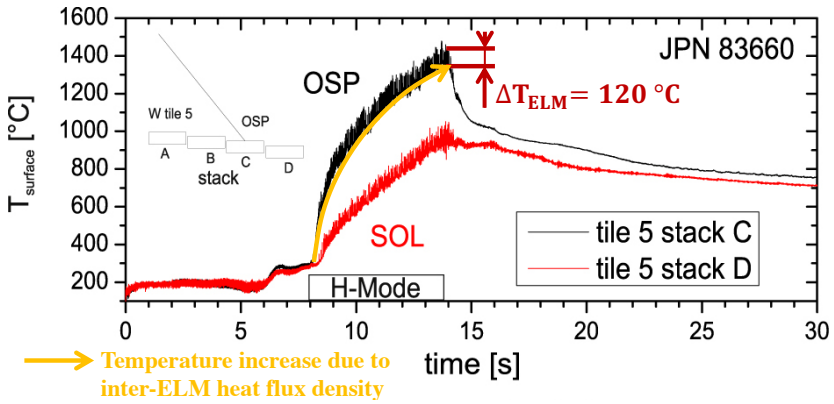

Figure 2.16: Time evolution of the surface temperature measured by infrared thermography for discharge #83660 in the JET tokamak. The temperature is displayed at two locations: at the outer strike-point (tile 5 stack C, black solid line) and at a remote location in the outer SOL (tile 5 stack D, red solid line). Picture taken and adapted from reference [89].

The modelling of both time scales of the temperature evolution is required if one wants to accurately model the desorption dynamics during ELMs. To catch the gradual temperature increase, the heat equation needs to be solved considering the complex geometry of the PFCs, its different materials and the appropriate boundary condition which models the cooling technique. This boundary condition is usually applied at few tenths of millimeter depth from the PFC surface (at the rear surface for an inertial PFC, at the inner

side of the cooling tube for an actively-cooled PFC). Moreover, the temperature peaks related the transient ELM heat loads are localised in a very thin layer at the surface of the PFC. To evaluate the thickness of this layer, a spatial scale representing the thermal penetration depth is introduced:

$$\Delta x = \sqrt{a\Delta t} = \sqrt{\frac{\lambda}{\rho c_p}\Delta t} \tag{2.48}$$

where a is the thermal diffusivity of the surface material [$m^2.s^{-1}$], λ is its thermal conductivity [$W.m^{-1}.°C^{-1}$], ρ its volumetric mass density [$kg.m^{-3}$] and c_p its specific heat [$J.kg^{-1}.°C^{-1}$]. As an example, this quantity can be evaluated considering the properties of tungsten at 100 °C [84] (minimum thermal diffusivity) and a temperature calculation every microsecond during the ELM transient:

$$\Delta x_{ELM} = \sqrt{\frac{165}{19279 \times 132} \times 10^{-6}} \sim 10\ \mu\text{m} \tag{2.49}$$

Thus, the use of a discretisation method to solve the heat equation would require a simulated domain extending up to tenths of millimeters with a highly refined grid at the material surface (with a size of $\sim \Delta x_{ELM}$). Such resolution would be expensive in terms of computational time and resources. Last but not least, as it was seen in the previous section, the HI–material interaction is limited to a thin layer of the surface materials found in the JET-ILW and ITER tokamaks. Indeed, the interface between coated or deposited material and its substrate (CFC or W) seems to act as a diffusion barrier for HI (cf. subsection 2.3) which indicates that the HI inventory is found in the coated or deposited materials (which do not exceed a depth of 50 μm). For massive Be tiles, the HI–Be interaction is limited to the implantation zone with a maximum depth of 50 nm (cf. subsection 2.7). Only massive W can present diffusion and trapping of HI in a depth higher than 100 μm (in intrinsic traps 1 and 2, cf. subsection 2.6). However, the diffusion time to reach for example a depth of 1 mm at 500 K (temperature at which trap 1 is still partly filled with HI, cf. figure 2.13) is 140 s which is way above the time of usual plasma discharges in JET. As a consequence, the domain simulated with MHIMS (and therefore the domain where the temperature must be calculated) should not exceed 1 mm depth. This questions the real need to solve the heat equation in the entire PFC domain.
Therefore, the decision was made to develop a new thermal model, WEE-temp, which fulfill the aforementioned requirements. Under simplifying assumptions, this model solves the heat equation in the domain simulated by MHIMS while taking into account the PFC design. Moreover, its relative simplicity and its flexibility make this model suitable to simulate the different PFCs composing the wall of fusion reactors. This section is dedicated to the description of this model.

3.1 Assumptions and general equation of the thermal model.

Before introducing the general equations of the WEE-temp code, many assumptions are considered to simplify the model:
(1) The complex geometry and the design of the PFC are approximated by a slab geometry made of a superposition of material layers.
(2) The material thermal properties are assumed to be constant (no variation with temperature).
(3) The material thermal properties are assumed to be isotropic.
(4) Thermal radiation from the PFC surfaces is neglected and the lateral surfaces are considered insulated.
(5) The net heat flux density (taking into account the plasma and the radiation contributions) on the PFC top surface, ϕ_{net}, is considered uniform.
A sketch of the considered slab geometry is shown in figure 2.17. The slab is defined in its associated cartesian coordinate system with basis $(\vec{e}_x,\vec{e}_y,\vec{e}_z)$ by three lengths L_x, L_y and L_z respectively. Due to the moderate lengths L_y and L_z, the PFC basis $(\vec{e}_x,\vec{e}_y,\vec{e}_z)$ is aligned with the local SolEdge2D-EIRENE wall curvilinear basis $(\vec{e}_x,\vec{e}_s,\vec{e}_\varphi)$. The two types of cooling technology, i.e. inertially-cooling and actively-cooling, are modelled by imposing the appropriate boundary condition at the PFC rear surface (at $x = L_x$), respectively a zero heat flux density (insulated surface) and a convective boundary condition with a coolant at a temperature T_{cool}.

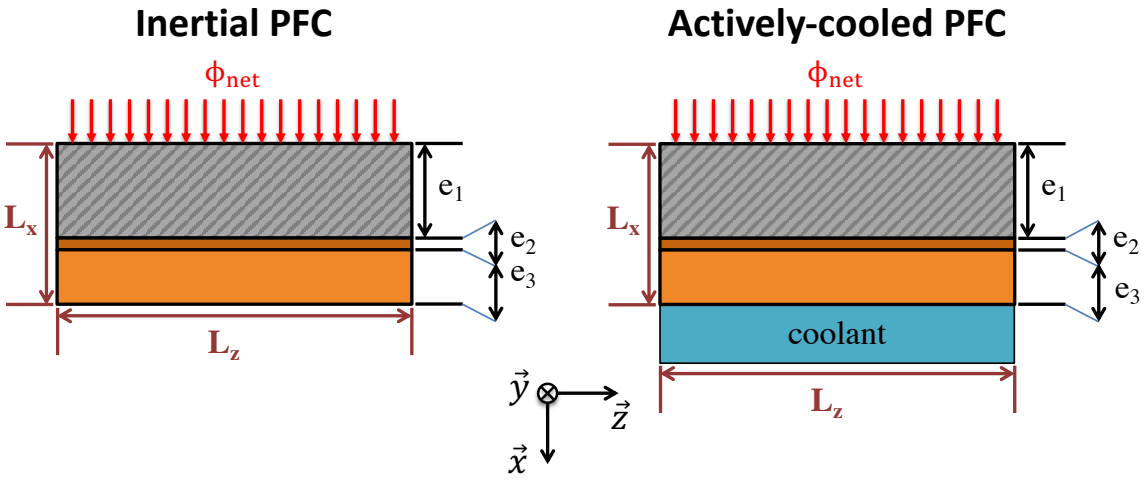

Figure 2.17: Schematics of the PFC simplified slab geometry considered in WEE-temp. The PFC is made of a superposition of material layers (three different layers in this example). Inertially-cooled PFCs and actively-cooled PFCs differ from the boundary condition imposed at the rear surface (at $x = L_x$), i.e. a zero heat flux density (insulated surface) and a convective boundary condition with a coolant at a temperature T_{cool} respectively.

Now the heat equation used in WEE-temp can be introduced. Under the assumptions (1-5), this equation for a PFC with N material layers, with the considered boundary conditions (B.C.) and the initial condition (I.C.), in the cartesian coordinate system

defined in figure 2.17 is written as follows [90, 91]:

$$
\begin{cases}
\rho_i c_{p_i} \dfrac{\partial T_i(x,y,z,t)}{\partial t} = \lambda_i \dfrac{\partial^2 T_i}{\partial x^2} + \lambda_i \dfrac{\partial^2 T_i}{\partial y^2} + \lambda_i \dfrac{\partial^2 T_i}{\partial z^2} & \text{(2.50a)} \\
\text{B.C. at } x = x_0 = 0\text{: } -\lambda_1 \dfrac{\partial T_1}{\partial x}(0,y,z,t) = \phi_{net}(t) & \text{(2.50b)} \\
\text{B.C. at } x = x_i = \displaystyle\sum_{j=1}^{i<N} e_j\text{: } \begin{aligned} -\lambda_i \frac{\partial T_i}{\partial x}(x_i,y,z,t) &= \frac{1}{R_{c_i}} \times [T_i(x_i,y,z,t) - T_{i+1}(x_i,y,z,t)] \\ &= -\lambda_{i+1} \frac{\partial T_{i+1}}{\partial x}(x_i,y,z,t) \end{aligned} & \text{(2.50c)} \\
\text{B.C. at } x = x_N = L_x\text{: } \begin{cases} -\lambda_N \dfrac{\partial T_N}{\partial x}(L_x,y,z,t) = 0 \text{ for inertial PFCs} \\ \text{or} \\ -\lambda_N \dfrac{\partial T_N}{\partial x}(L_x,y,z,t) = h\,[T_N(L_x,y,z,t) - T_{cool}] \text{ for actively-cooled PFCs} \end{cases} & \text{(2.50d)} \\
\text{B.C. at } y = 0 \text{ and } y = L_y\text{: } -\lambda_i \dfrac{\partial T_i}{\partial y}(x,0,z,t) = -\lambda_i \dfrac{\partial T_i}{\partial y}(x,L_y,z,t) = 0 & \text{(2.50e)} \\
\text{B.C. at } z = 0 \text{ and } z = L_z\text{: } -\lambda_i \dfrac{\partial T_i}{\partial z}(x,y,0,t) = -\lambda_i \dfrac{\partial T_i}{\partial z}(x,y,L_z,t) = 0 & \text{(2.50f)} \\
\text{I.C.: } \begin{cases} T_i(x,y,z,0) = T_0 \text{ for inertial PFCs} \\ \text{or} \\ T_i(x,y,z,0) = T_{cool} \text{ for actively-cooled PFCs} \end{cases} & \text{(2.50g)}
\end{cases}
$$

where T_i is the temperature of the i^{th} layer [°C], ϕ_{net} is the net heat flux density normal to the PFC surface [W.m^{-2}], T_0 the initial uniform temperature of the inertial PFC (e.g. at the start of a day of operation) [°C] and T_{cool} is the coolant temperature [°C] for actively-cooled PFCs. Equation 2.50c expresses the heat transfer at the interface between two adjacent layers which are in imperfect contact (at the coordinate $x = x_i$). R_{c_i} [°C.(W.m^{-2})$^{-1}$] is called the contact resistance of this interface ($R_{c_i} = 0$ for two layers in perfect contact). Eventually, for actively-cooled PFCs, equation 2.50d states the heat exchange by convection with the coolant with a heat convection coefficient h [W.m^{-2}.°C^{-1}].

The system 2.50 can be averaged over the intervals $[0, L_y]$ and $[0, L_z]$. Taking into account the lateral boundary conditions 2.50d and 2.50e, the temperature partial derivatives with

respect to y and z in equation 2.50a vanish and the system 2.50 becomes:

$$\begin{cases} \rho_i c_{p_i} \dfrac{\partial \overline{T_i}(x,t)}{\partial t} = \lambda_i \dfrac{\partial^2 \overline{T_i}}{\partial x^2} & \text{(2.51a)} \\ \text{B.C. at } x = x_0 = 0\text{: } -\lambda_1 \dfrac{\partial \overline{T_1}}{\partial x}(0,t) = \phi_{net}(t) & \text{(2.51b)} \\ \text{B.C. at } x = x_i = \sum_{j=1}^{i<N} e_j\text{: } \begin{aligned} -\lambda_i \dfrac{\partial \overline{T_i}}{\partial x}(x_i,t) &= \dfrac{1}{R_{c_i}} \times \left[\overline{T_i}(x_i,t) - \overline{T_{i+1}}(x_i,t)\right] \\ &= -\lambda_{i+1} \dfrac{\partial \overline{T_{i+1}}}{\partial x}(x_i,t) \end{aligned} & \text{(2.51c)} \\ \text{B.C. at } x = x_N = L_x\text{: } \begin{cases} -\lambda_N \dfrac{\partial \overline{T_N}}{\partial x}(L_x,t) = 0 \text{ for inertial PFCs} \\ \text{or} \\ -\lambda_N \dfrac{\partial \overline{T_N}}{\partial x}(L_x,t) = h\left[\overline{T_N}(L_x,t) - T_{cool}\right] \text{ for actively-cooled PFCs} \end{cases} & \text{(2.51d)} \\ \text{I.C.: } \begin{cases} \overline{T_i}(x,0) = T_0 \text{ for inertial PFCs} \\ \text{or} \\ \overline{T_i}(x,0) = T_{cool} \text{ for actively-cooled PFCs} \end{cases} & \text{(2.51e)} \end{cases}$$

where $\overline{T_i}$ is the averaged temperature of the i^{th} layer defined as follows:

$$\overline{T_i}(x,t) = \frac{1}{L_y L_z} \int_0^{L_y} \int_0^{L_z} T_i(x,y,z,t) dy dz \tag{2.52}$$

In order to simplify the resolution of the system, the following change of variable is considered:

$$\begin{cases} \Delta T_i(x,t) = \overline{T_i}(x,t) - T_0 \text{ for inertial PFCs} \\ \text{or} \\ \Delta T_i(x,t) = \overline{T_i}(x,t) - T_{cool} \text{ for actively-cooled PFCs} \end{cases} \tag{2.53}$$

which implies:

$$\frac{\partial(\Delta T_i)}{\partial t} = \frac{\partial \overline{T_i}}{\partial t}, \quad \frac{\partial(\Delta T_i)}{\partial x} = \frac{\partial \overline{T_i}}{\partial x}, \quad \frac{\partial^2(\Delta T_i)}{\partial x^2} = \frac{\partial^2 \overline{T_i}}{\partial x^2} \tag{2.54}$$

Thus, the system 2.51 becomes:

$$\begin{cases} \rho_i c_{p_i} \dfrac{\partial\left(\Delta T_i\right)(x,t)}{\partial t} = \lambda_i \dfrac{\partial^2\left(\Delta T_i\right)}{\partial x^2} & \text{(2.55a)} \\ \text{B.C. at } x = x_0 = 0\text{: } -\lambda_1 \dfrac{\partial(\Delta T_1)}{\partial x}(0,t) = \phi_{net}(t) & \text{(2.55b)} \\ \text{B.C. at } x = x_i = \sum_{j=1}^{i<N} e_j\text{: } \begin{aligned} -\lambda_i \dfrac{\partial(\Delta T_i)}{\partial x}(x_i,t) &= \dfrac{1}{R_{c_i}} \times \left[\Delta T_i(x_i,t) - \Delta T_{i+1}(x_i,t)\right] \\ &= -\lambda_{i+1} \dfrac{\partial(\Delta T_{i+1})}{\partial x}(x_i,t) \end{aligned} & \text{(2.55c)} \\ \text{B.C. at } x = x_N = L_x\text{: } \left| \begin{array}{l} -\lambda_N \dfrac{\partial(\Delta T_N)}{\partial x}(L_x,t) = 0 \text{ for inertial PFCs} \\ \text{or} \\ -\lambda_N \dfrac{\partial(\Delta T_N)}{\partial x}(L_x,t) = h \Delta T_N(L_x,t) \text{ for actively-cooled PFCs} \end{array} \right. & \text{(2.55d)} \\ \text{I.C.: } \Delta T_i(x,0) = 0 & \text{(2.55e)} \end{cases}$$

Invoking the Duhamel theorem of superposition [91], the solution of system 2.55 can be expressed as follows:

$$\Delta T_i(x,t) = \int_0^t \phi_{net}(\tau) \frac{\partial T_i^{step}(x, t-\tau)}{\partial t}\, d\tau \tag{2.56}$$

where T_i^{step} is the solution of the following auxiliary problem:

$$\begin{cases} \rho_i c_{p_i} \dfrac{\partial T_i^{step}(x,t)}{\partial t} = \lambda_i \dfrac{\partial^2 T_i^{step}}{\partial x^2} & \text{(2.57a)} \\ \text{B.C. at } x = x_0 = 0\text{: } -\lambda_1 \dfrac{\partial T_1^{step}}{\partial x}(0,t) = 1 & \text{(2.57b)} \\ \text{B.C. at } x = x_i = \sum_{j=1}^{i<N} e_j\text{: } \begin{aligned} -\lambda_i \dfrac{\partial T_i^{step}}{\partial x}(x_i,t) &= \dfrac{1}{R_{c_i}} \times \left[T_i^{step}(x_i,t) - T_{i+1}^{step}(x_i,t)\right] \\ &= -\lambda_{i+1} \dfrac{\partial T_{i+1}^{step}}{\partial x}(x_i,t) \end{aligned} & \text{(2.57c)} \\ \text{B.C. at } x = x_N = L_x\text{: } \left| \begin{array}{l} -\lambda_N \dfrac{\partial T_N^{step}}{\partial x}(L_x,t) = 0 \text{ for inertial PFCs} \\ \text{or} \\ -\lambda_N \dfrac{\partial T_N^{step}}{\partial x}(L_x,t) = h T_N^{step}(L_x,t) \text{ for actively-cooled PFCs} \end{array} \right. & \text{(2.57d)} \\ \text{I.C.: } T_i^{step}(x,0) = 0 & \text{(2.57e)} \end{cases}$$

T_i^{step} is the PFC temperature response to a unit heat flux density step [°C.$(\text{W.m}^{-2})^{-1}$]. In the following, it will be called the PFC step response.

To obtain the general equation of WEE-temp, one will focus on the resolution of the

Duhamel integral 2.56 (the PFC step response calculation will be addressed in the next subsection). To solve this convolution integral, one will use the property of Laplace transform w.r.t. that type of integral. First the Laplace transform $F(p)$ of a function $f(t)$ has to be introduced:

$$\mathscr{L}\left[f(t)\right] \equiv F(p) = \int_0^{+\infty} e^{-pt} f(t) dt \tag{2.58}$$

where p is the Laplace transform variable (complex number). The inversion formula is:

$$\mathscr{L}^{-1}[F(p)] \equiv f(t) = \frac{1}{2\pi i} \int_{\gamma - i\cdot\infty}^{\gamma + i\cdot\infty} e^{pt} F(p) dp \tag{2.59}$$

where γ is a real number so that the contour path of integration is in the region of convergence of $F(p)$. Using the properties of the Laplace transform w.r.t. convolution and derivative of function [91], one can calculate the Laplace transform of ΔT_i:

$$\begin{aligned} \mathscr{L}\left[\Delta T_i(x,t)\right] &= \mathscr{L}\left[\phi_{net}(t)\right] \cdot \mathscr{L}\left[\frac{\partial T_i^{step}(x,t)}{\partial t}\right] \\ &= \mathscr{L}\left[\phi_{net}(t)\right] \cdot \left(p\mathscr{L}\left[T_i^{step}(x,t)\right] + \cancel{T_i^{step}(x,0)}\right) \\ &= \mathscr{L}\left[\phi_{net}(t)\right] \cdot p\mathscr{L}\left[T_i^{step}(x,t)\right] \end{aligned} \tag{2.60}$$

where the initial condition 2.57e has been accounted. Now it is arbitrarily considered that ϕ_{net} consists of a series of $N_\phi(t)$ step changes $\Delta\phi_k$ [W.m^{-2}] at time t_k:

$$\phi_{net}(t) = \sum_{k=1}^{N_\phi(t)} \Delta\phi_k \mathcal{H}(t - t_k) \tag{2.61}$$

where $\mathcal{H}$ is the Heaviside step function. The Laplace transform of ϕ_{net} can easily be obtained from Laplace transform table [91]:

$$\begin{aligned} \mathscr{L}\left[\phi_{net}(t)\right] &= \sum_{k=1}^{N_\phi(t)} \Delta\phi_k \mathscr{L}\left[\mathcal{H}(t - t_k)\right] \\ &= \sum_{k=1}^{N_\phi(t)} \Delta\phi_k \frac{e^{-t_k p}}{p} \end{aligned} \tag{2.62}$$

Equation 2.62 can be introduced in equation 2.60:

$$\begin{aligned} \mathscr{L}\left[\Delta T_i(x,t)\right] &= \left(\sum_{k=1}^{N_\phi(t)} \Delta\phi_k \frac{e^{-t_k p}}{p}\right) \cdot p\mathscr{L}\left[T_i^{step}(x,t)\right] \\ &= \sum_{k=1}^{N_\phi(t)} \left(\Delta\phi_k e^{-t_k p} \mathscr{L}\left[T_i^{step}(x,t)\right]\right) \end{aligned} \tag{2.63}$$

ΔT_i can be obtained by inverting equation 2.63 using table of inversion [91]:

$$\begin{aligned}\Delta T_i(x,t) &= \mathscr{L}^{-1}\left\{\sum_{k=1}^{N_\phi(t)}\left(\Delta\phi_k e^{-t_k p}\mathscr{L}\left[T_i^{step}(x,t)\right]\right)\right\}\\ &= \sum_{k=1}^{N_\phi(t)}\left(\Delta\phi_k \mathscr{L}^{-1}\left\{e^{-t_k p}\mathscr{L}\left[T_i^{step}(x,t)\right]\right\}\right)\\ &= \sum_{k=1}^{N_\phi(t)}\Delta\phi_k T_i^{step}(x,t-t_k)\end{aligned} \tag{2.64}$$

Equation 2.64 can be inserted in equation 2.53 to recover the temperature field:

$$\left|\begin{array}{l}\overline{T_i}(x,t) = T_0 + \displaystyle\sum_{k=1}^{N_\phi(t)}\Delta\phi_k T_i^{step}(x,t-t_k) \text{ for inertial PFCs}\\ \qquad\qquad\qquad\qquad \text{or}\\ \overline{T_i}(x,t) = T_{cool} + \displaystyle\sum_{k=1}^{N_\phi(t)}\Delta\phi_k T_i^{step}(x,t-t_k) \text{ for actively-cooled PFCs}\end{array}\right. \tag{2.65}$$

Eventually, the general equation of WEE-temp is obtained by considering the poloidal variation of the heat flux density ϕ_{net} along the wall ($\vec{s}$ direction) in the last equation:

$$\left|\begin{array}{l}\overline{T_i}(s,x,t) = T_0(s) + \displaystyle\sum_{k=1}^{N_\phi(s,t)}\Delta\phi_k(s) T_i^{step}(s,x,t-t_k(s)) \text{ for inertial PFCs}\\ \qquad\qquad\qquad\qquad \text{or}\\ \overline{T_i}(s,x,t) = T_{cool}(s) + \displaystyle\sum_{k=1}^{N_\phi(s,t)}\Delta\phi_k(s) T_i^{step}(s,x,t-t_k(s)) \text{ for actively-cooled PFCs}\end{array}\right. \tag{2.66}$$

where T_0, T_{cool} and T_i^{step} are function of the variable s as they depend on the PFC which is in the position s on the wall. Therefore, provided that an analytical or semi-analytical calculation of the PFC step response is possible, the WEE-temp general equation 2.66 can give the temperature profile in the zone simulated in MHIMS (limited to the material layer at the surface T_1) without calculating the temperature profile in the whole PFC. Indeed, this profile, as well as the PFC design (material layers and cooling technique), are accounted in the calculation of the step response. This calculation is made using the so-called quadrupole method [92] and is detailed in appendix B. This method gives the temperature in the Laplace space, equation B.30, which is then inverted using the inversion formula 2.59 to go back to the time space. This integral cannot be calculated analytically but can be estimated numerically using an appropriate algorithm. In WEE-temp, such inversion is done using the De Hoog's algorithm [93].

To illustrate the calculation of the temperature using equation 2.66, a PFC made of three material layers is considered (cf. figure 2.17). The PFC technical specifications are shown in table 2.8. The different layers are assumed to be in perfect contact ($R_{c_i} = 0$).

Layer number	Material	Thickness e_i (mm)	λ_i (W.m^{-1}.°C^{-1})	c_{p_i} (J.kg^{-1}.°C^{-1})	ρ_i (kg.m^{-3})
1	W	11	165	132	19279
2	Cu OFHC	1	377	387	8720
3	CuCrZr	1.5	320	376	376

Table 2.8: Technical specifications of the PFC considered in the example of surface temperature calculation. The material thermal properties are taken at 100 °C.

This PFC is submitted to a net heat flux density ϕ_{net} displayed in figure 2.18.a in black solid line. ϕ_{net} can be decomposed in three step changes (cf. figure 2.18.a): $\Delta\phi_1 = +2$ MW.m^{-2} at $t_1 = 1$ s (red area), $\Delta\phi_2 = +1$ MW.m^{-2} at $t_2 = 3$ s (green area) and $\Delta\phi_3 = -0.5$ MW.m^{-2} at $t_3 = 4$ s (blue area). According to equation 2.64, the surface temperature variation, $\Delta T_1(0,t)$, is equal to the sum of the surface temperature variations $\Delta T_1^1(0,t)$, $\Delta T_1^2(0,t)$ and $\Delta T_1^3(0,t)$ respectively due to the three step changes $\Delta\phi_1$, $\Delta\phi_2$ and $\Delta\phi_3$:

$$\begin{aligned} \Delta T_1(0,t) &= \Delta T_1^1(0,t) + \Delta T_1^2(0,t) + \Delta T_1^3(0,t) \\ \Delta T_1(0,t) &= \Delta\phi_1 T_1^{step}(0,t-t_1) + \Delta\phi_2 T_1^{step}(0,t-t_2) + \Delta\phi_3 T_1^{step}(0,t-t_3) \end{aligned} \tag{2.67}$$

where the step response values $T_1^{step}(0,t-t_k)$ are calculated through inversion of equation B.23. This calculation is illustrated in figure 2.18.b in the case of an inertial PFC and in figure 2.18.c in the case of an actively-cooled PFC (with $h = 36352$ W.m^{-2}.°C^{-1}).

As it was previously said, the calculation of the PFC step response requires a numerical calculation of the inverse Laplace transform of equation B.30. According to the general equation of WEE-temp 2.66, such inversion has to be done multiple times per time step. The number of inversions per time step is:

$$N_{inv}(t) = \sum_{i=1}^{N_s} N_\phi(i,t) N_x(i) \tag{2.68}$$

where N_s is the number of points along the wall (given by SolEdge2D-EIRENE), $N_\phi(s,t)$ the number of step changes considered for $\phi_{net}(s,t)$ (lower or equal to the number of time steps), and $N_x(s)$ the number of points in the depth of the material (given by MHIMS). This number can increase drastically so that the N_{inv} numerical inversions become extremely time-consuming. In appendix C, the properties of the Laplace transform are used to calculate analytical asymptotic expressions of the step response for short time ($t \to 0$) and for long time ($t \to +\infty$). These analytical expressions are valid for a limited interval of the time domain. They are used in their interval of validity to calculate the value of the step response in the general equation of WEE-temp 2.66 instead of the time-consuming numerical inversion of equation B.30.

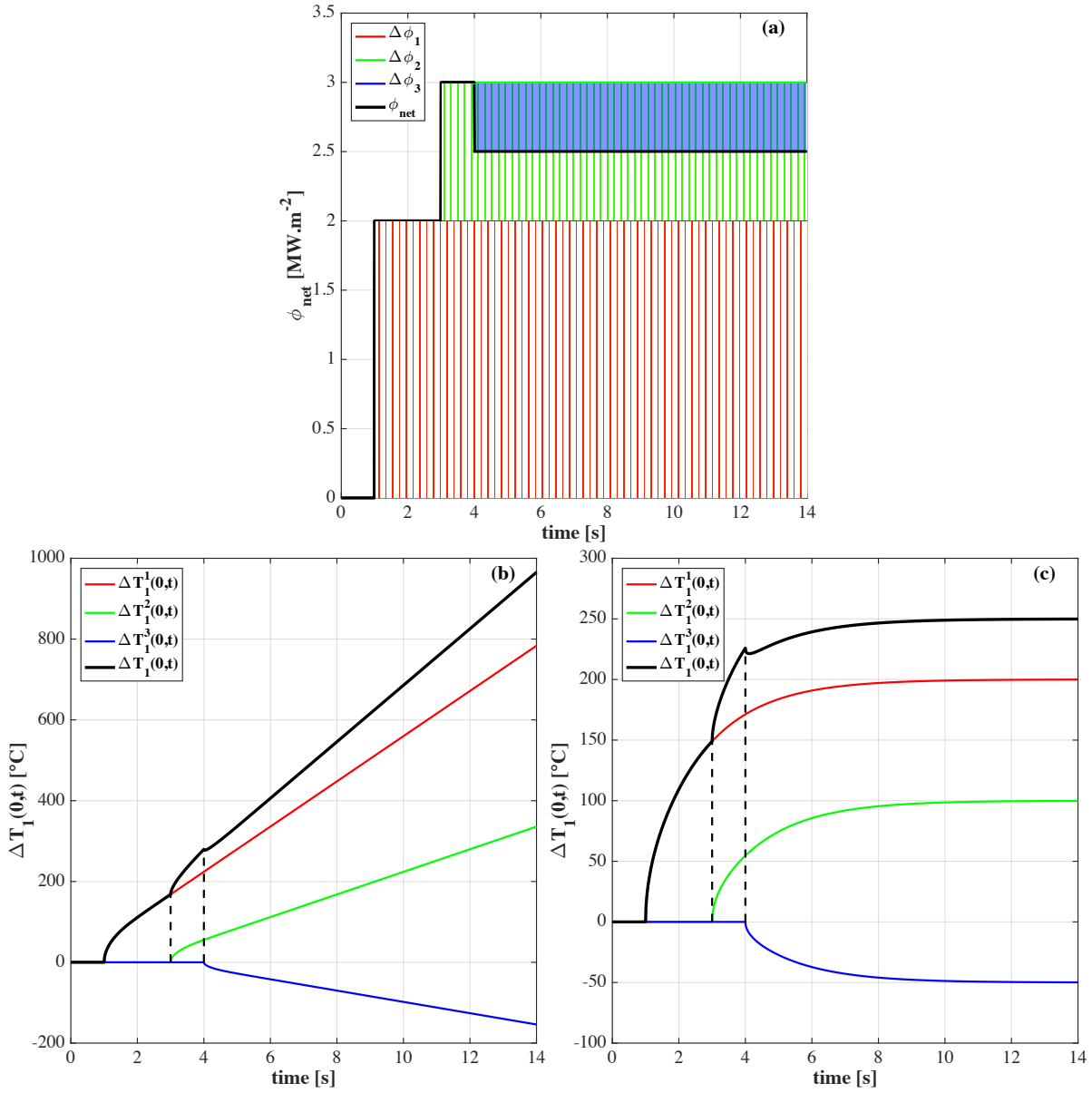

Figure 2.18: (a) Time evolution of the net heat flux density ϕ_{net} (black solid line) imposed to a PFC made of three material layers (cf. table 2.8 for the layer specifications). ϕ_{net} is decomposed in three step changes $\Delta\phi_k$ depicted in colored areas in (a). The corresponding temperature variations $\Delta T_1^k(0,t)$ are displayed with the same colors for an inertially-cooled PFC (b) and an actively-cooled PFC (c). The overall temperature variation at the PFC surface $\Delta T_1(0,t)$ is the sum of these three temperature variations (black solid lines).

Before going further, the validity of the assumptions considered in WEE-temp needs to be discussed. Assumptions (1) and (2) are purely arbitrary but are necessary to simplify the resolution of the heat equation. Assumption (3) about the isotropic thermal properties is valid for most of materials used in fusion except for Carbon Fiber Composite (CFC) which has a thermal conductivity λ higher by a factor of three in the direction of the fibers than in the directions transverse to the fibers [84]. In any case, CFC fibers are always oriented in the direction perpendicular to the PFC surface ($\vec{x}$ in figure 2.17) to maximise the heat removal efficiency. Therefore, the hypothesis of a purely 1D heat transport in the $\vec{x}$ direction can be assumed in that case. One can note that the equation 2.66 and the system 2.57 are still valid under the 1D hypothesis except that $\overline{T_i}$ is not the mean temperature anymore but the local temperature. Concerning assumption (4), one can note that Be and W have a low emissivity of ~ 0.2. Therefore, for a surface temperature of 1000 °C, a Be/W surface emits a radiative heat flux density of 3.0×10^{-2} MW.m^{-2} (according to the Stefan-Boltzmann law), which is negligible w.r.t. the plasma and radiation heat flux densities. For CFC, this heat flux density is higher (1.2×10^{-1} MW.m^{-2}), due to a higher emissivity of 0.8, but is still negligible. This also justifies the fact that the lateral surfaces — which are only cooled by radiation — are assumed to be insulated. Eventually, the validity of assumption (5) about the uniformity of ϕ_{net} on the PFC top surface will depend on the dimensions of the PFC tile. In the toroidal direction, the typical length L_y of divertor PFCs does not exceed few tenth of centimeters and one does not expect a strong variation of ϕ_{net} on such characteristic length. Therefore assumption (5) should in principle be valid in the divertor region. However it is not valid anymore for the first-wall as, in present tokamak, first-wall PFCs are not axisymmetric. In any case, the toroidal symmetry of plasma-wall interaction is one of the simplifying assumption of SolEdge2D-EIRENE. In the poloidal direction, the assumption should be valid in remote areas (away from the strike-points, i.e. remote divertor and first-wall during diverted plasma phase) as ϕ_{net} is in principle dominated by plasma radiation in those regions. However, close to the plasma strike-points, ϕ_{net} is more peaked and the assumption is not valid anymore as the length of the tile in that direction, L_y, is superior or equal to the so-called e-folding length of the heat flux density (λ_ϕ, often referred to as λ_q in the literature [94]) measured experimentally. Again, the strong hypothesis of a purely 1D heat transport in the $\vec{x}$ direction can also be assumed in that case.

3.2 Model adjustments for actively-cooled PFCs.

Operating a tokamak in steady-state requires actively-cooled PFCs. With the perspective of the WEST and ITER projects, which are meant to operate in such condition, a special attention has been paid to the modelling of this type of PFCs. Two technologies of actively-cooled PFCs have been developed for the next generation of fusion devices: the flat tile design (cf. figure 2.19.a) and the monoblock design (cf. figure 2.19.c). Calculating the temperature distribution in components with such a complex geometry requires Finite Element Methods (FEM). As it was previously said, these time-consuming methods cannot be directly coupled with a transport code for computational reasons.
The thermal behaviour of actively-cooled PFCs are defined by two engineering parame-

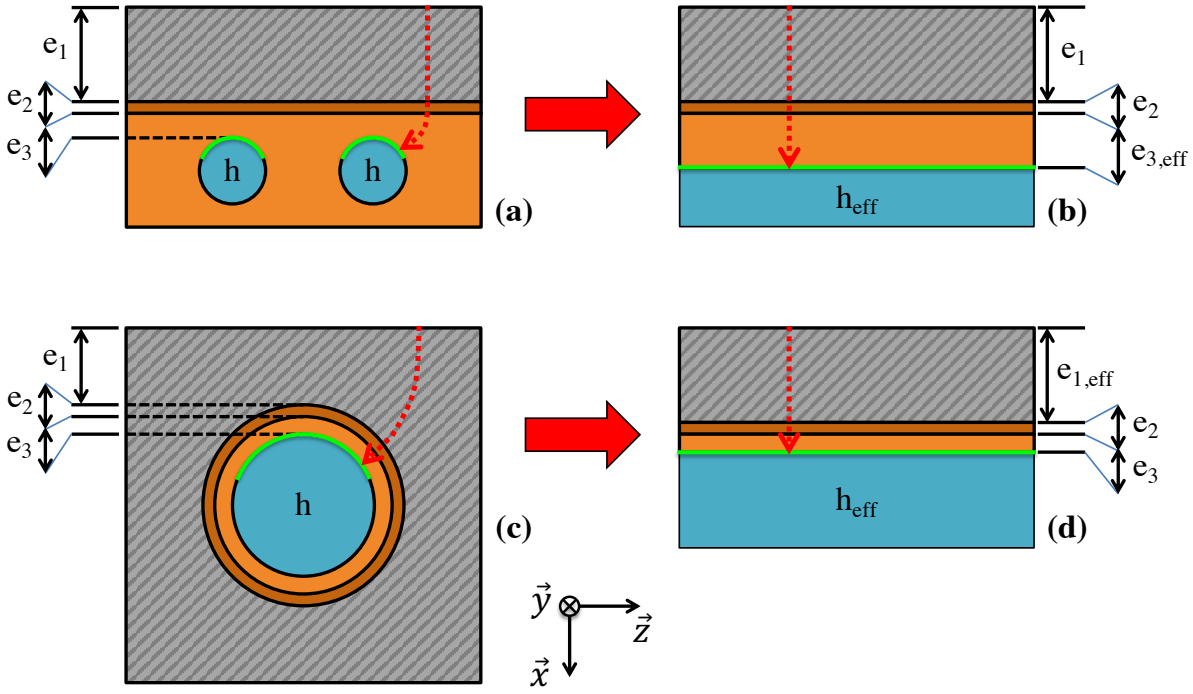

Figure 2.19: Flat tile (a) and monoblock (c) PFC designs with three material layers. Their corresponding representations in WEE-temp are displayed in (b) and (d). Typical heat flux density lines are represented in red. The green lines highlight the wetted area at the material-coolant interface for both real and model geometries. The i^{th} material layer thickness and the heat transfer coefficient between the heat sink and the coolant are defined as e_i and h respectively. $(e_{j,eff},\ h_{eff})$ refers to the pair of parameters adjusted in WEE-temp to reproduce the real thermal behaviour of actively-cooled PFCs.

ters: the stationary surface temperature increase per W.m^{-2}, $\Delta T_{stat}/\phi_{in}$ [°C.(W.m^{-2})$^{-1}$], and the heating/cooling time constant τ_{PFC} [s] which defines the time to reach the stationnary state. Both parameters are specified during the design phase of the PFCs. For example, the monoblocks of the ITER divertor are designed to reach a steady-state surface temperature increase of $\Delta T_{stat} = 1000$ °C (for which the steady-state surface temperature, $T_{stat} = \Delta T_{stat} + T_{cool} = 1070$–$1120$ °C, is below the W recrystallisation temperature of 1300–1400 °C) for a steady-state heat flux density of $\phi_{in} = 10$ MW.m^{-2} [95] (maximum heat flux density that can be evacuated by actively-cooling). They are meant to reach steady-state within 5–6 s leading to a time constant τ_{PFC} of ~ 2 s. To reproduce the thermal behaviour of the real PFC, WEE-temp has to take into account geometrical effects: in the complex PFC geometry, the lines of heat flux density between the surface and the coolant are curved and of variable lengths as illustrated in figures 2.19.a and 2.19.c, which is not the case in the 1D model (cf. figure 2.19.b and 2.19.d). Moreover, in the real PFC, the surface exposed to the plasma heat flux is not necessarily equal to the area of heat exchange at the cooling pipe level (cf. green lines in figures 2.19.a and 2.19.c), whereas in the 1D model the two surfaces are equal by construction (cf. figure

2.19.b and 2.19.d). To determine the PFC 1D equivalent geometry, the thickness of the layer where the coolant pipe is inserted, e_j (j being this layer number), and the heat transfer coefficient, h, are adapted according to:

$$\begin{cases} \dfrac{\Delta T_{stat}}{\phi_{in}} = \displaystyle\sum_{i=1}^{N} \frac{e_i}{\lambda_i} + \sum_{i=1}^{N-1} R_{c_i} + \frac{1}{h} & \text{(2.69a)} \\ \Delta T_1(0, t = 3\tau_{PFC}) = 95\ \%\Delta T_{stat} & \text{(2.69b)} \end{cases}$$

where one recognises that equation 2.69a is the long time asymptote for the surface temperature of actively-cooled PFCs (equation C.29 with $x = 0$). The code is able to select, among all the pairs of parameters strictly verifying relation 2.69a, the one that better approximates relation 2.69b [96]. In the following, ($e_{j,eff}$, h_{eff}) refers to this pair of adjusted parameters.

To illustrate this procedure, a benchmark between a FEM code (taking into account the 2D PFC complex geometry) and the adjusted 1D model is achieved. The results from FEM are taken as references to be reproduced by the adjusted model. Two simulations are performed. In the first simulation, the mean surface temperature is calculated using the linear 2D heat equation (the materials properties are assumed to be constant and taken at $T = 100$ °C in [84]). In the second simulation, the non-linear 2D heat equation (the temperature dependence of material properties is taken into account) is used instead. Both simulations are performed with the FEM code CAST3M [97]. An ITER-like monoblock of 30 mm in length (L_z) and 29 mm in depth (L_y) is considered. The layers 1, 2 and 3 (cf. figure 2.19.c) are made of tungsten, copper and CuCrZr alloy, respectively. They are considered in perfect thermal contact ($R_{c_i} = 0$). The material thicknesses are $e_1 = 6$ mm (minimum thickness between the surface and the coolant pipe), $e_2 = 1$ mm and $e_3 = 1.5$ mm. The coolant temperature is $T_{cool} = 70$ °C and the heat transfer coefficient is $h = 77940$ W.m^{-2}.°C^{-1} [98]. For both cases, the response to a 10 MW.m^{-2} heat flux density step has been calculated using CAST3M to obtain the two engineering parameters required for the adjusting procedure: $\Delta T_{stat}/\phi_{in} = 77.3$ °C.(MW.m^{-2})$^{-1}$ and $\tau_{PFC} = 1.00$ s for the linear case, $\Delta T_{stat}/\phi_{in} = 94.0$ °C.(MW.m^{-2})$^{-1}$ and $\tau_{PFC} = 1.44$ s for the non-linear one. The procedure of adjustment acts on the pair (e_1, h) and is displayed in figure 2.20.a for the linear case and 2.20.b for the non-linear one: among all the pair strictly verifying equation 2.69a (red curves), the one that better approximates equation 2.69b (blue curves) is selected. A pair ($e_{1,eff}$, h_{eff}) = (6.8 mm, 34700 W.m^{-2}.°C^{-1}) is found for the linear case (cf. figure 2.20.a) and ($e_{1,eff}$, h_{eff}) = (9.5 mm, 33900 W.m^{-2}.°C^{-1}) for the non-linear case (cf. figure 2.20.b).
To test the efficiency of the adjusting procedure, a benchmark is performed between the adjusted 1D model and CAST3M. The monoblock is submitted to a 10 MW.m^{-2} heat flux density during 20 s to reach its steady-state. Then a substantial increase of the heat flux density to 260 MW.m^{-2} during 400 μs is applied, followed by a return to a 10 MW.m^{-2} heat flux density until $t = 20.02$ ms. These heat load conditions are consistent with an ELM – inter-ELM cycle for a type I ELM, with an ELM frequency $\nu_{ELM} = 50$ Hz, an

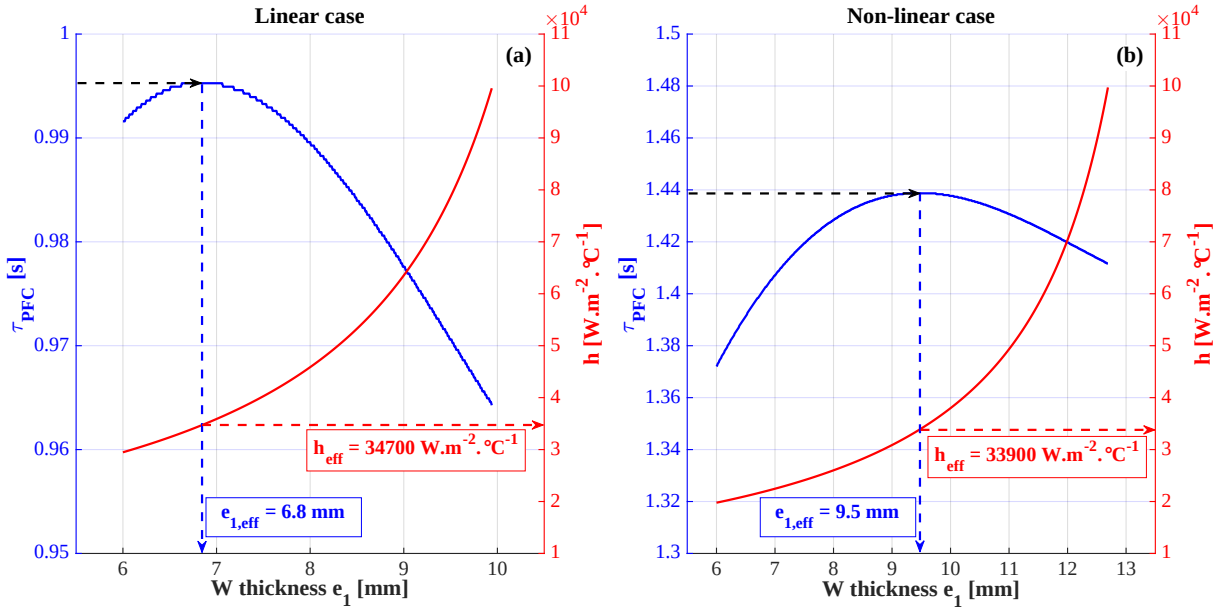

Figure 2.20: Procedure of adjustment of the pair (e_1, h) for an ITER-like monoblock to reproduce its engineering parameters $\Delta T_{stat}/\phi_{in}$ and τ_{PFC}. Both parameters were obtained from the resolution of the 2D linear and non-linear heat equations with the finite element code CAST3M: $\Delta T_{stat}/\phi_{in} = 77.3$ °C.(MW.m^{-2})$^{-1}$ and $\tau_{PFC} = 1.00$ s for the linear case with the material properties taken at $T = 100$ °C, $\Delta T_{stat}/\phi_{in} = 94.0$ °C.(MW.m^{-2})$^{-1}$ and $\tau_{PFC} = 1.44$ s for the non-linear case. Among all the pair (e_1, h) strictly verifying equation 2.69a (red curves), the one that better approximates equation 2.69b (blue curves) is selected. A pair ($e_{1,eff}$, h_{eff}) = (6.8 mm, 34700 W.m^{-2}.°C^{-1}) is found for the linear case (a) and ($e_{1,eff}$, h_{eff}) = (9.5 mm, 33900 W.m^{-2}.°C^{-1}) for the non-linear case (b).

ELM duration $\tau_{ELM} = 400$ μs and an ELM energy $W_{ELM} = 100$ kJ.m^{-2}. The resulting mean surface temperatures are displayed in figures 2.21.a and 2.21.b for the linear case and in figures 2.21.c and 2.21.d for the non-linear case. Figures 2.21.a and 2.21.c show the temperature response to the 10 MW.m^{-2} heat flux density step. Figures 2.21.b and 2.21.d focus on the first three milliseconds of the ELM – inter-ELM cycle. The adjusting procedure enables the 1D model to be in good agreement with CAST3M for the linear simulation (cf. figure 2.21.a), leading to a largest relative error of +1.7 % and a largest absolute error of +13 °C for the response to the steady-state heat load. Concerning the ELM – inter-ELM cycle (cf. figure 2.21.b), the largest relative error is +1.0 % and the largest absolute error is +11 °C. Therefore one can consider that the adjusted 1D model is able to rectify the geometrical effects that take place in the real monoblock. Concerning the non-linear simulation, the adjusting procedure is also able to compensate both the geometrical effects and the temperature dependence of materials properties (cf. figure 2.21.c; the largest relative error is −3.5 % and the largest absolute error is −20 °C). However, during the ELM (cf. figure 2.21.d), the 1D model underestimates the value of the surface temperature (−51 °C at the end of the ELM, which represents a relative error of −3.9 % on the temperature and of −17 % on the temperature increase w.r.t.

the steady-state temperature). Indeed, at the time scale of the ELM, the temperature response at the surface is only driven by the thermal effusivity of the surface material $E_1 = \sqrt{\lambda_1 c_{p_1} \rho_1}$ (cf. PFC step response when $t \to 0$ in appendix C). Therefore, this error can be partially corrected by considering the first material (i.e. W) properties at the stationary temperature ($\sim$ 1000 °C). For this temperature, the new set of adjusted parameters is $(e_{1,eff},\ h_{eff}) = (6.0\text{ mm},\ 31000\text{ W.m}^{-2}.^{\circ}\text{C}^{-1})$. This new configuration leads to a lower relative error (-1.4 % on the temperature and -5.9 % on the temperature increase during the ELM) and a lower absolute error (-18 °C) for the ELM period (cf. figure 2.21.d).

To summarise, handled in the right way, the 1D adjusted model is able to accurately reproduce the thermal behaviour of actively-cooled PFCs. For example, by considering the first material properties at the inter-ELM mean surface temperature, errors due to strong transient events can be lowered.

3.3 Model adjustments for inertial PFCs.

Up to now, our attention was focused on the modelling of actively-cooled PFCs. Indeed, the initial goal of this PhD was to study the wall dynamics in the case of the W environment of the WEST tokamak (whose wall is made of such type of PFCs). Unfortunately, it was not possible to carry on this study in the time scale of this PhD due to the lack of experimental data required for the confrontation to experiment (cf. chapter 4). Therefore, it was decided to concentrate our effort on the JET-ILW tokamak which has the mix of materials that will be used in ITER (W in the divertor and Be in the first-wall). The JET-ILW vacuum vessel is composed of inertially-cooled PFCs with complex geometries, especially in the divertor. An example of such complex geometry is shown in figure 2.22.a where a Computer Assisted Drawing (CAD) of the tile n°1 of this divertor is depicted. Of course, the simple slab geometry considered in WEE-temp is not suitable to model such type of PFC. However, one can try to recover some thermal characteristics of this type of PFCs by adjusting the only geometrical parameter used in WEE-temp, i.e. the thickness of the materials.
First, one can have a look at what will be the temperature profile given by WEE-temp after a plasma discharge (when $t \gg t_{end}$ where t_{end} is the time at which the discharge ended). The tile temperature is given by the general equation of WEE-temp 2.66 while the step response is calculated using the asymptote for long time C.36 (as it is considered

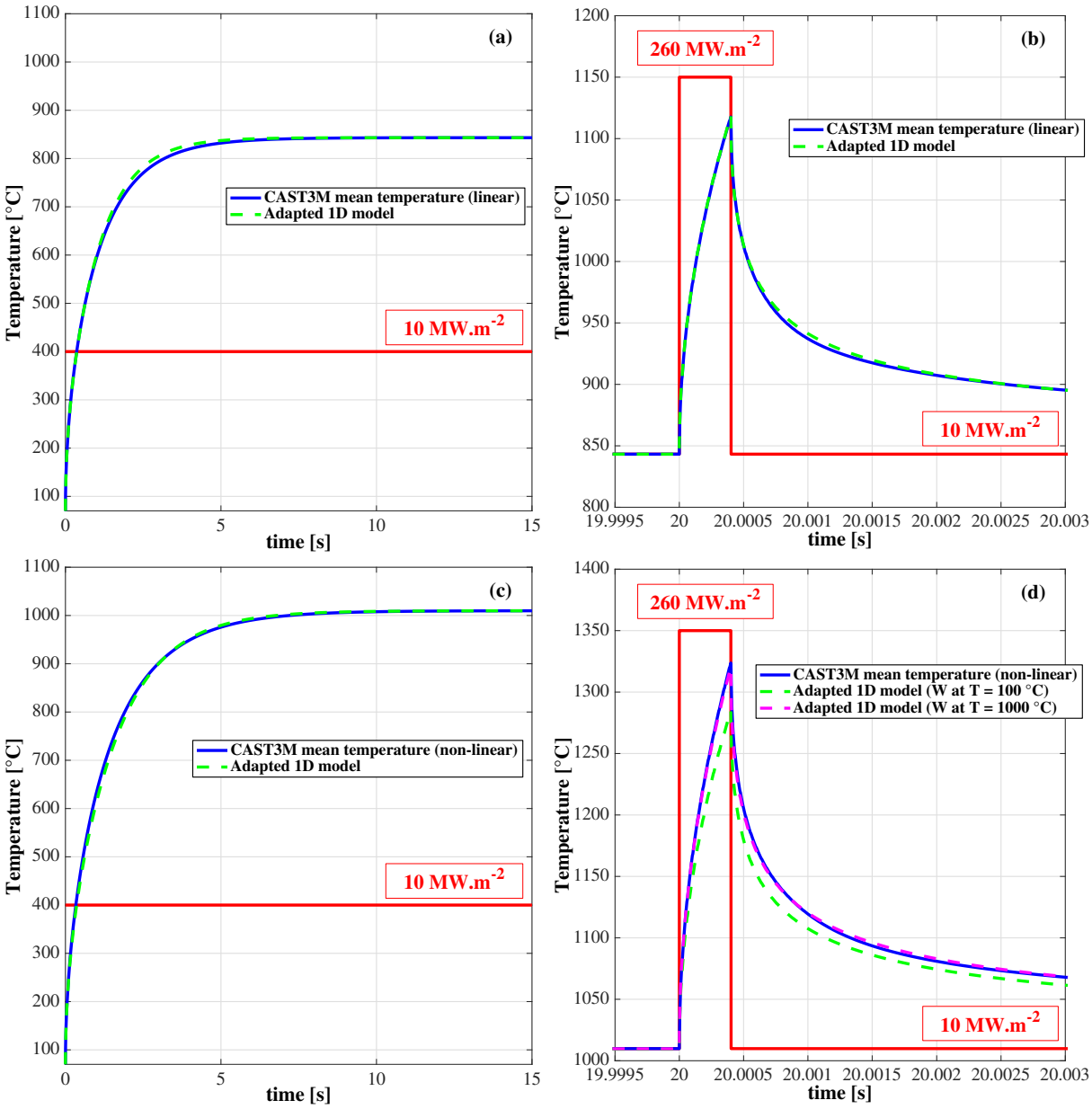

Figure 2.21: Comparison between the mean surface temperature of an ITER-like monoblock calculated with the finite element modelling code CAST3M and the one calculated with the adjusted 1D model. First, a 10 MW.m^{-2} heat flux density is applied (cf. figures (a) and (c)) until $t = 20$ s to ensure the steady-state to be reached in the monoblock. Then an ELM is triggered during 400 μs, leading to an increase of the heat flux density up to 260 MW.m^{-2}. It is followed by an inter-ELM period (cf. figures (b) and (d)). Comparisons are performed both with a linear CAST3M simulation ((a) and (b)) and with a non-linear one ((c) and (d)). The 1D thermal model is adjusted considering the material properties at $T = 100$ °C. In figure (d), the 1D thermal model is also used considering the tungsten properties at $T = 1000$ °C, showing the importance of the first material layer in the surface temperature calculation during transients.

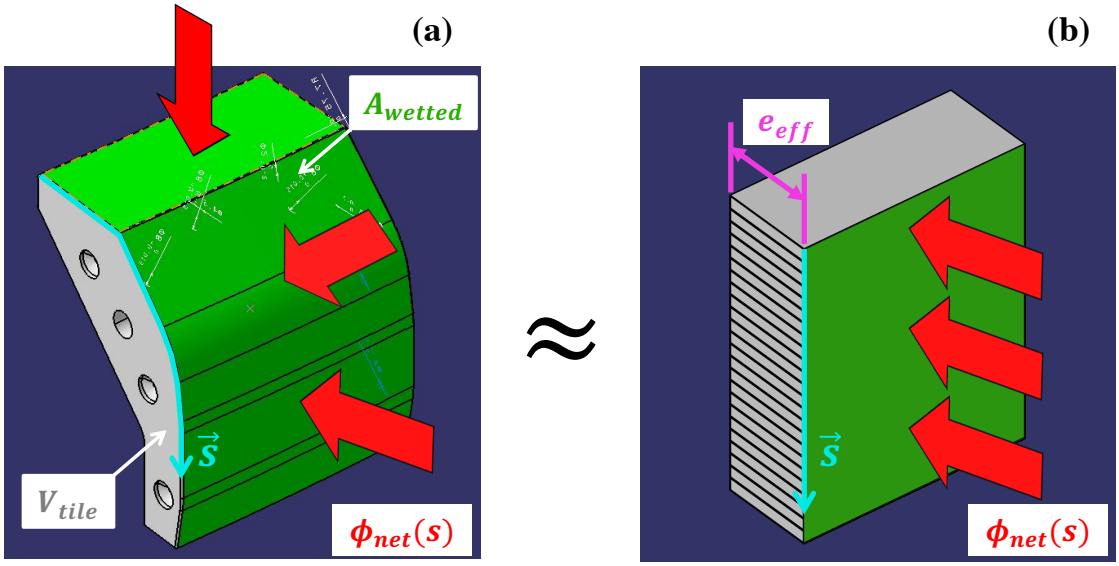

Figure 2.22: CAD drawing of the tile n°1 of the JET-ILW divertor (a) and equivalent "unfolded" slab geometry considered in the WEE-temp code (b). The s curvilinear coordinate along the poloidal cross-section of the wall is plotted in cyan. The net heat flux density perpendicular to the surface of the tile is depicted by the red arrows. V_{tile} is the volume of the tile while A_{wetted} is its area exposed to the plasma heat flux (green area). e_{eff} is the effective thickness of the slab geometry used in WEE-temp. It is defined as $e_{eff} = V_{tile}/A_{wetted}$.

that $t - t_{end} > t_{\infty}^{min}$):

$$
\begin{aligned}
&\underline{\text{for } 0 \leqslant x \leqslant e_1\text{:}} \\
&\overline{T_1}(s,x,t) = T_0(s) + \sum_{k=1}^{N_\phi(s,t)} \Delta\phi_k(s) T_i^{step}(s,x,t-t_k(s)) \\
&\overline{T_1}(s,x,t) = T_0(s) + \sum_{k=1}^{N_\phi(s,t)} \Delta\phi_k(s) \left(\frac{1}{C_1(0)}(t-t_k(s)) \right. \\
&\qquad\qquad \left. + \frac{1}{C_1(0)} \left[A_1(x) - \frac{C_2(0)}{C_1(0)} \right] \right) \qquad (2.70) \\
&\overline{T_1}(s,x,t) = T_0(s) + \frac{1}{C_1(0)} \sum_{k=1}^{N_\phi(s,t)} \Delta\phi_k(s)(t-t_k(s)) \\
&\qquad + \frac{1}{C_1(0)} \left[A_1(x) - \frac{C_2(0)}{C_1(0)} \right] \cancel{\sum_{k=1}^{N_\phi(s,t)} \Delta\phi_k(s)}
\end{aligned}
$$

where the last sum is $\phi_{net}(s,t)$ and is null after the end of the discharge. The remaining sum represents the integral of ϕ_{net} w.r.t. time (it is the area under the black curve in figure 2.18). Thus, it is the energy fluence that had been deposited at the position s

during the discharge. It will be noted $\mathscr{F}_E$ in the following. Taking into account the expression of $C_1(0)$ (cf. equations C.24 and C.31), equation 2.70 becomes:

$$\begin{aligned}
&\underline{\text{for } 0 \leqslant x \leqslant e_1\text{:}} \\
&\overline{T_1}(s,x,t) = T_0(s) + \frac{1}{\sum_{i=1}^{N} \frac{\lambda_i(s)e_i(s)}{a_i(s)}} \sum_{k=1}^{N_\phi(s,t)} \Delta\phi_k(s)(t - t_k(s)) \\
&\overline{T_1}(s,x,t) = T_0(s) + \frac{1}{\sum_{i=1}^{N} \rho_i(s)c_{p_i}(s)e_i(s)} \int_0^{t_{end}} \phi_{net}(s)dt \\
&\overline{T_1}(s,x,t) = T_0(s) + \frac{\mathscr{F}_E(s)}{\sum_{i=1}^{N} \rho_i(s)c_{p_i}(s)e_i(s)}
\end{aligned} \tag{2.71}$$

If one assumes that ϕ_{net} was uniform on the top wetted surface of the tile (noted A_{wetted}) during all the discharge, one obtains the temperature of the tile in function of the energy that has been accumulated by the tile during the discharge:

$$\begin{aligned}
&\underline{\text{for } 0 \leqslant x \leqslant e_1\text{:}} \\
&\overline{T_1}(s,x,t) = T_0(s) + \frac{E_{tile}}{A_{wetted} \sum_{i=1}^{N} \rho_i(s)c_{p_i}(s)e_i(s)} \\
&\overline{T_1}(s,x,t) = T_0(s) + \frac{E_{tile}}{\sum_{i=1}^{N} \rho_i(s)c_{p_i}(s)V_i(s)}
\end{aligned} \tag{2.72}$$

where V_i is the volume of the i^{th} material layer. In general, inertial PFC are made of one main material with in some case a coating or a deposit at the surface. These surface layers do not exceed several tenth of micrometers. For example, the tile 1 of JET-ILW displayed in figure 2.22.a is mainly made of CFC with a W-coating at the top surface with a thickness of 15 μm and a Be deposit layer of up to 40 μm. Thus the volume of these surface layers are negligible and equation 2.72 can be further simplified by only considering the main material layer:

$$\begin{aligned}
&\underline{\text{for } 0 \leqslant x \leqslant e_1\text{:}} \\
&\overline{T_1}(s,x,t) \approx T_0(s) + \frac{E_{tile}(s)}{\rho(s)c_p(s)V_{tile}(s)}
\end{aligned} \tag{2.73}$$

where ρ and c_p are associated to the main material layer and V_{tile} is the tile volume (approximately equal to the volume of the main material layer). Again the s variable is here to identify the PFC which is in the position s on the wall. Actually, equation 2.73 also holds for the real PFC with complex geometry. Moreover, the PFC wetted area in SolEdge2D-EIRENE is equal to the one of the real PFC by construction. Thus, one can define an equivalent slab geometry of the PFC by defining an effective thickness, $e_{eff} = V_{tile}/A_{wetted}$, which ensures that WEE-temp will give the accurate temperature between discharges (provided that the energy accumulated by the tile, given by the SolEdge2D-EIRENE simulation, is correct). This technic seems to be appropriate for PFC with a

roughly slab geometry. For more complex PFC, WEE-temp considers consecutive slabs which, once unfolded, have a global volume equivalent to the one of the real tile. An example of this equivalent "unfolded" slab geometry for the JET-ILW tile 1 is displayed in figure 2.22.b. For this tile, the main material is CFC and this CFC layer has an effective thickness e_{eff} of 38.5 mm.
Nevertheless, it is seen from temperature measurement, through embedded thermocouples for example, that the temperature of inertial tile experiences a slow decay between discharges. Indeed, the heat accumulated by the tile during a plasma discharge is dissipated by surface radiation and by heat conduction into the tokamak structure. To mimic this cooling, heat extraction is allowed at the rear side of the PFC by imposing a convection type boundary condition with a very low heat convection coefficient. Hence, inertial PFCs are modelled as actively-cooled PFCs. For the tile 1 of the JET-ILW, a heat convection coefficient of 100 $W.m^{-2}.°C^{-1}$ is considered. The corresponding step response of the surface temperature of this tile, calculated by WEE-temp, is shown in figure 2.23. The step response tends to the asymptote for actively-cooled PFC (green dashed line) in $\sim$ 4000 s which indicates a cooling time of $\sim$ 1 h. The insert exhibits the step response during the first twenty seconds (standard time period of a discharge in JET). One can see that the inertial PFC asymptote for long time (magenta dashed line) is still an asymptote of the step response during the time period of the discharge: the inertial behaviour of the tile during plasma is conserved. More critical analysis of this simplified approach will be done in chapter 4 where the simulation of the dynamics of desorption during a JET discharge will be studied.

4 Application of the WEE-temp code: simulation of the temperature of the WEST vacuum vessel during steady-state and ELM-like heat loads.

In this section, the WEE-temp code presented in the previous section will be used to simulate the thermal response of the WEST wall during steady-state and ELM-like heat loads. The WEST project consists in transforming Tore Supra in an X-point divertor configuration while extending its long pulse capability to test the ITER divertor components under combined heat and particle loads in a tokamak environment [99, 100]. This transformation requires a number of changes in the PFCs. Their new configuration is shown in figure 2.24.
The new set of PFCs consists in:

- The lower divertor, which follows the design and manufacturing processes foreseen for the ITER divertor elements: assembly of W monoblocks, high conductivity copper and copper alloy CuCrZr.

- The inner bumpers and outer limiter: flat W-coated carbon composite tiles attached to a copper alloy CuCrZr heat sink by means of a spring system.

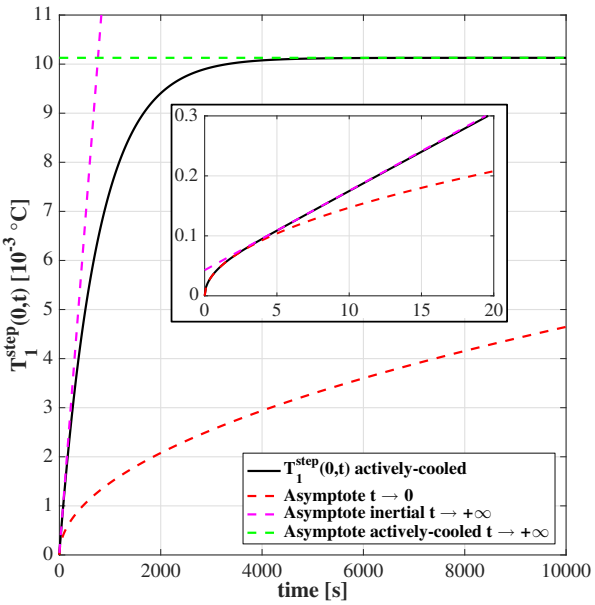

Figure 2.23: Step response of the surface temperature of the JET-ILW tile 1 calculated by WEE-temp (black solid line). This tile is modelled as an actively-cooled PFC with a very low heat convection coefficient to mimic the cooling by heat conduction in the tokamak structure. The step response tends to the asymptote for actively-cooled PFC (green dashed line) in $\sim$ 4000 s which indicates a cooling time of $\sim$ 1 h. The insert exhibits the step response during the first twenty seconds (standard time period of a discharge in JET). The inertial PFC asymptote for long time (magenta dashed line) is still an asymptote of the step response during the time period of the discharge, showing that the inertial behaviour of the tile during plasma is conserved.

- The upper divertor, based on a heat sink technology similar to the ITER first-wall: assembly of copper alloy CuCrZr, high conductivity copper and stainless steel, with a tungsten coating instead of beryllium for ITER.
- The antenna protections: assembly of flat W-coated carbon composite tiles, high conductivity copper and copper alloy CuCrZr.
- The lower divertor baffle and vacuum vessel protections against Vertical Displacement Events (VDE) and ripple losses: set of W-coated copper alloy CuCrZr plates with cooling channels drilled inside.
- The actively cooled stainless steel wall, featuring a "waver" structure [101].

The WEST PFCs 3D geometry has been simplified and adapted to the 1D thermal model following the method described in subsection 3.2. The engineering parameters to reproduce, i.e. $\Delta T_{stat}/\phi_{in}$ and τ_{PFC}, are listed in table 2.9. The thermal time constants range between 2 and 20 s, showing that discharge durations of $40 - 60$ s are required to reach a full steady-state over the whole vacuum vessel. The thicknesses e_i and $e_{j,eff}$ as well as the effective heat transfer coefficients h_{eff}, resulting from the adjusting procedure described in subsection 3.2, are also given. For each PFC, the effective thickness $e_{j,eff}$ is

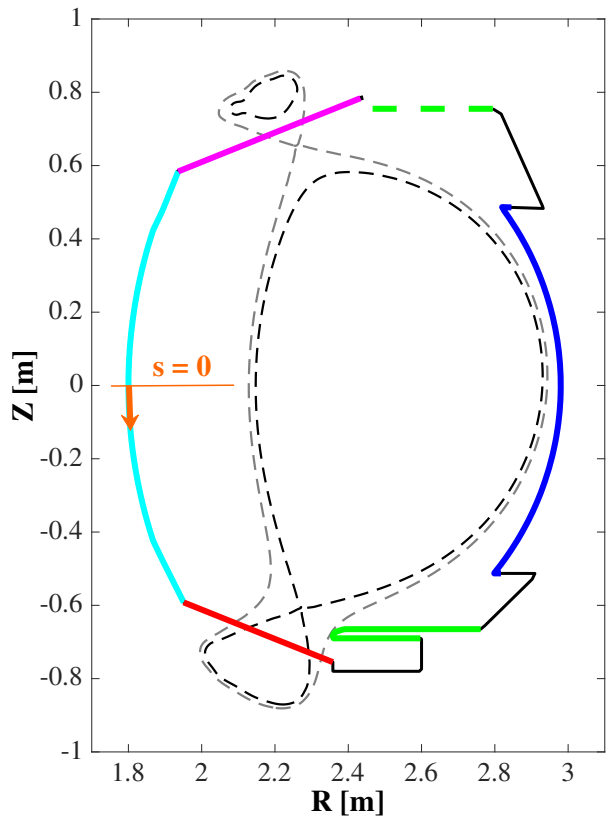

Figure 2.24: WEST main PFCs and wall geometry used in the SolEdge2D-EIRENE simulation: lower divertor (red solid line), inner bumper (light blue solid line), upper divertor (magenta solid line), ripple and VDE protections (green dashed line), stainless steel wall (black solid line), antenna protection or outer limiter (dark blue solid line) and baffle (green solid line). The origin and direction of the s coordinate along the wall are also displayed.

written with a bold font (other values e_i are taken from the real PFC geometry). The considered cooling temperature is $T_{cool} = 70$ °C. The step responses to a heat flux density

		Lower divertor	Inner bumper / Outer limiter	Upper divertor	Antenna protection	Baffle / VDE protections	SS wall
$\Delta T_{stat}/\phi_{in}$ [°C.(W.m^{-2})$^{-1}$]		1.0×10^{-4}	5.0×10^{-4}	4.8×10^{-5}	1.0×10^{-4}	1.3×10^{-4}	6.6×10^{-4}
τ_{PFC} [s]		2	20	1	2	5	10
e_i [mm]	W	8 ⇒ **11**	15×10^{-3}	15×10^{-3}	15×10^{-3}	15×10^{-3}	—
	CFC – N11	—	20	—	6	—	—
	Cu OFHC	1	2	—	1	—	—
	CuCrZr	1.5	3 ⇒ **4**	3 ⇒ **7**	3 ⇒ **7**	4 ⇒ **17**	—
	SS 316 L	—	—	—	—	—	2 ⇒ **8**
h_{eff} [W.m^{-2}.°C^{-1}]		3.6×10^4	2.5×10^3	4.0×10^4	2.0×10^4	1.4×10^4	7.2×10^3
h [W.m^{-2}.°C^{-1}]		1.0×10^5	4.0×10^4	4.0×10^4	4.0×10^4	4.0×10^4	4.0×10^4

Table 2.9: Steady-state mean surface temperature increase per W.m^{-2} $\Delta T_{stat}/\phi_{in}$, thermal time constant τ_{PFC}, material thicknesses e_i and $e_{j,eff}$ and effective heat transfer coefficients h_{eff} of the WEST PFCs. The $e_{j,eff}$ values are written in bold. The heat transfer coefficient h, resulting from FEM simulations, is given for comparison.

$\phi_{net} = 1$ MW.m^{-2} of the WEST PFCs are displayed in figure 2.25. The colour code is the same as in figure 2.24. One can see the importance of adapting the PFC geometry (see subsection 3.2) by comparing the two red curves, which correspond to the lower divertor monoblock: using the pair $(e_1,\ h)$, instead of $(e_{1,eff},\ h_{eff})$, leads to a relative error of -65 % on τ_{PFC} and of -42 % on $\Delta T_{stat}/\phi_{in}$.

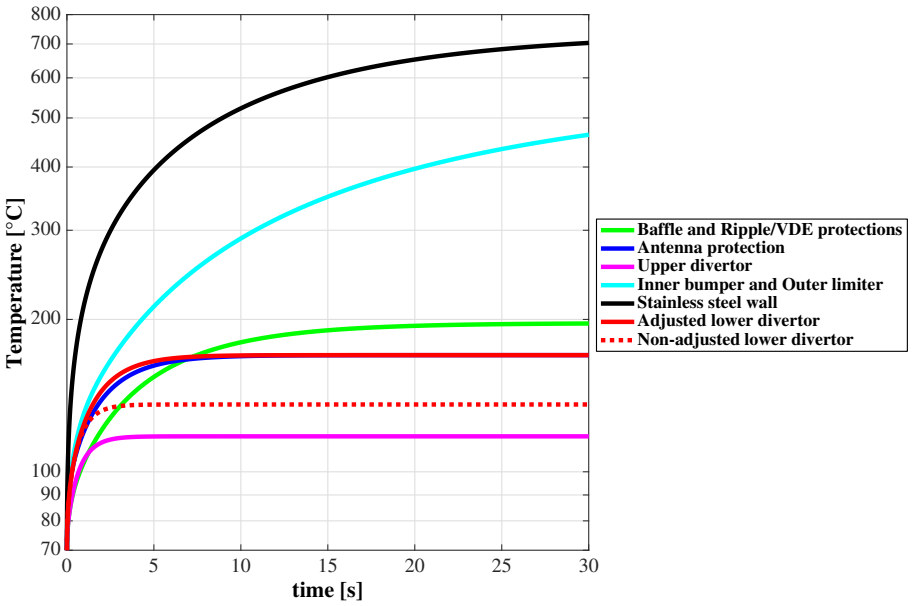

Figure 2.25: WEST PFCs surface temperature response to a heat flux density step $\phi_{net} = 1$ MW.m^{-2}. The colour code is the same as in figure 2.24. The red solid and red dashed lines are the lower divertor calculated responses using the pairs $(e_{1,eff},\ h_{eff})$ and $(e_1,\ h)$, respectively.

Now WEE-temp is applied to two different cases involving the WEST tokamak to show its abilities during both steady-state and transient heat loads. First, the temperature calculation is applied to a SolEdge2D-EIRENE simulation of a pure deuterium WEST discharge with a density at the separatrix $n_{sep} = 2 \times 10^{19}$ m^{-3}, a power crossing the separatrix $P_{SOL} = 7.4$ MW and a midplane heat flux density e-folding length $\lambda_\phi^{sep,up} = 7$ mm. The integrated incident power on the different PFCs, P_{inc}, is listed in table 2.10. The distributions along the wall of the steady-state net heat flux density ϕ_{net} (including

	Lower divertor	Baffle	Antenna protection / Outer limiter	VDE protections	Upper divertor	Inner bumper	SS wall
P_{inc} [MW]	5.32	0.65	0.07	0.04	0.79	0.28	0.23

Table 2.10: Incident power, P_{inc}, on the different WEST PFCs calculated by SolEdge2D-EIRENE for a discharge with $P_{SOL} = 7.4$ MW.

radiation and neutral contributions) and of the resulting steady-state surface temperature are displayed in figure 2.26 (the definition of the wall coordinate s and colour code are explicated in figure 2.24).

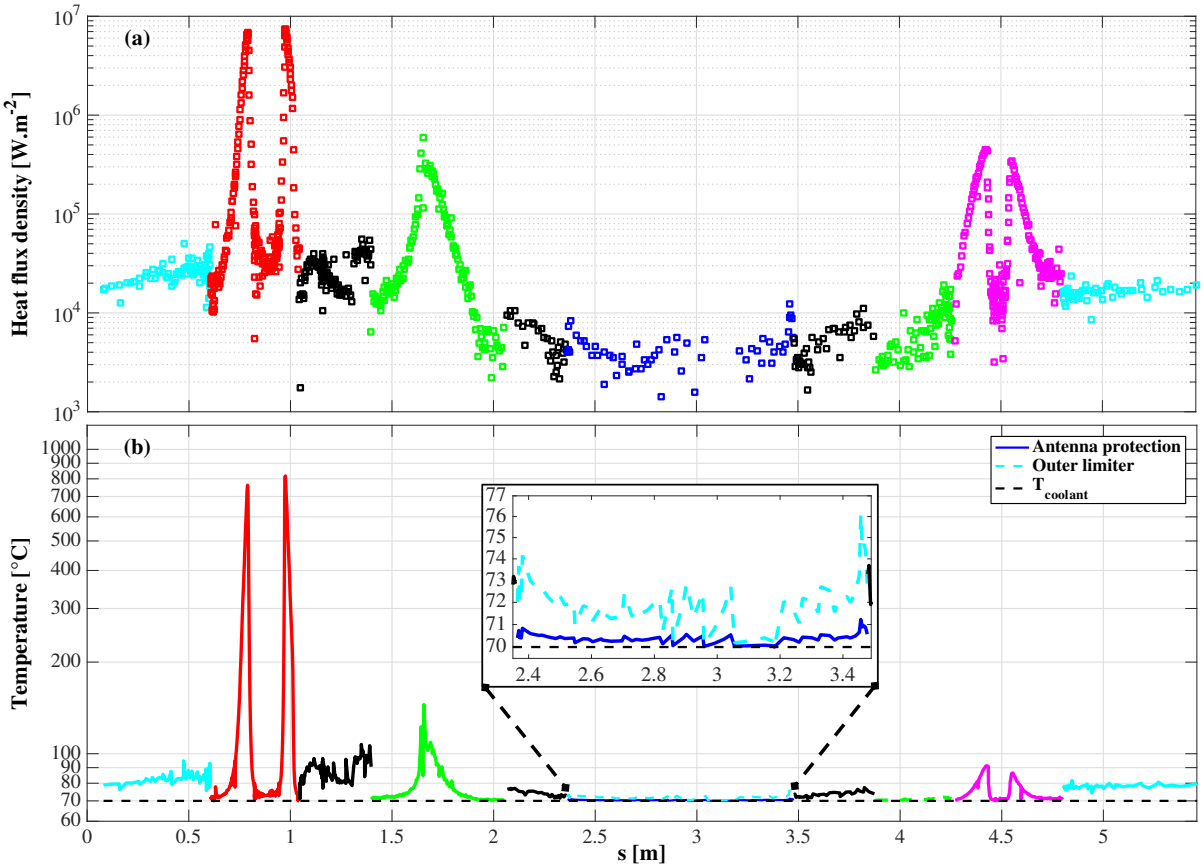

Figure 2.26: (a) Net heat flux density ϕ_{net} and (b) steady state surface temperature distributions along the WEST wall. The definition of the wall coordinate s and the colour code are explicated in figure 2.24. The insert concentrates on the outer part of the vessel where the plasma is intercepted by the antenna protections or the outer limiter, depending on the toroidal location.

The heat flux density reaches $\sim$ 8 MW.m^{-2} on the lower divertor and $\sim$ 1 MW.m^{-2} on the baffle and on the upper divertor. The surface temperature — assuming a flat surface, without shaping — remains lower than 200 °C everywhere, except on the lower divertor where it reaches $\sim$ 820 °C. The discontinuities in the temperature distribution or differences for an almost identical heat load (e.g. the baffle and the upper divertor) are due to the differences in the design of the PFCs, more specifically to the specified value of $\Delta T_{stat}/\phi_{in}$.

Now the thermal response of the WEST divertor to an ELM-like heat load will be simulated. The power deposition during an ELM is roughly extrapolated from the steady-state profile calculated previously. The energy expelled per ELM, ΔW_{ELM} [J], is given by $\Delta W_{ELM} \approx \alpha_{ELM} P_{SOL}/\nu_{ELM}$ where ν_{ELM} the ELM frequency [Hz]. An empirical value for α_{ELM} is typically 0.4 for Type I ELMs [102]. Considering an ELM duration τ_{ELM}, the power load during an ELM is:

$$P_{ELM} = \frac{\Delta W_{ELM}}{\tau_{ELM}} = \frac{\alpha_{ELM} P_{SOL}}{\tau_{ELM} \nu_{ELM}} \tag{2.74}$$

Only a fraction of this power ($\sim$ 60 %) impacts the divertor [103]. The wetted area is increased by a factor $\sigma_{ELM} \sim 1.3 - 1.4$ w.r.t. the inter-ELM phase [104] and the asymmetry between the inner and outer divertor legs is set to $r_{i:o} \sim 2:1$ [105]. In the case of WEST, representative values are $\nu_{ELM} \sim 50$ Hz and $\tau_{ELM} \sim 400$ μs. P_{SOL} and the inter-ELM divertor profile of the heat flux density is taken from the SolEdge2D-EIRENE steady-state simulation described above. First, the divertor is submitted to this steady-state heat density. The ELM triggers at $t = t_{ELM} = 20$ s which is a sufficient time for the divertor to reach its steady-state temperature. The result is shown in figure 2.27. In this figure, the s axis is oriented to highlight the inboard heat flux density which is stronger during the ELM. Figure 2.27.a displays the heat load during the ELM cycle. The ELM triggers at $t - t_{ELM} = 0$ s in this figure. In figure 2.27.b, the surface temperature profile along the wall is shown during the ELM – inter-ELM cycle. The increase in surface temperature remains limited with a maximum of $\Delta T_{ELM}^{max} \sim +130$°C at the inner strike-point where the heat flux density is the highest during the ELM. The surface temperature at the end of the ELM period is quasi-identical to the steady-state value in all the divertor, with a maximum difference of $\sim +9$°C w.r.t. the temperature prior to the ELM at the inner strike-point.

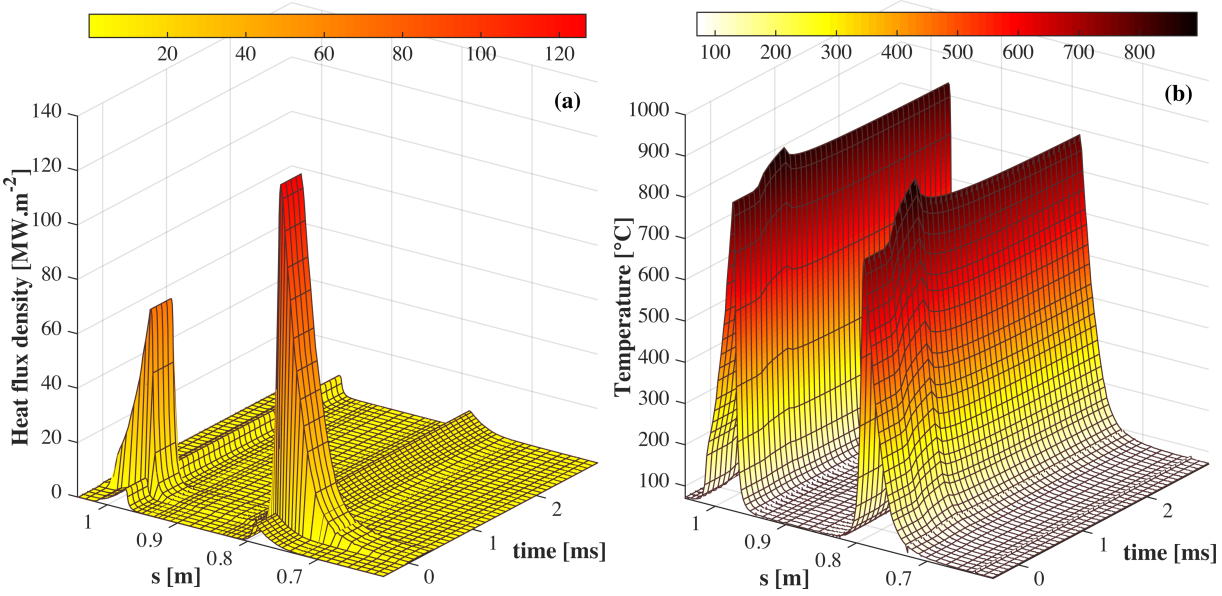

Figure 2.27: (a) Heat flux density and (b) surface temperature distributions on the lower divertor during an ELM-like event and the subsequent inter-ELM phase. The ELM triggers at $t - t_{ELM} = 0$ s and lasts 400 μs. At the end of the inter-ELM phase ($t - t_{ELM} = 1/\nu_{ELM}$) the steady-state surface temperature is almost recovered.

To illustrate this, one will focus on the calculation of the temperature profile at the inner strike-point with wall coordinate s_{ISP}. During this simulation, the net heat flux density on the inner strike-point is decomposed into three step changes:

$$\begin{aligned}\phi_{net}(s_{ISP}, t) = \Delta\phi_{net}^{steady}(s_{ISP})\mathcal{H}(t-0) \\ +\Delta\phi_{net}^{ELM}\mathcal{H}(t-t_{ELM}) - \Delta\phi_{net}^{ELM}\mathcal{H}(t-(t_{ELM}+\tau_{ELM}))\end{aligned} \tag{2.75}$$

According to the general equation of WEE-temp 2.66, the temperature profile in the first material layer during the ELM (for $t \geq 20$ s) is:

$$\begin{aligned} T_1(s_{ISP},x,t) = \quad & \Delta\phi_{net}^{steady}(s_{ISP})T_1^{step}(s_{ISP},x,t-0) \\ & +\Delta\phi_{net}^{ELM}(s_{ISP})\left[T_1^{step}(s_{ISP},x,t-t_{ELM})\right. \\ & \left. -T_1^{step}(s_{ISP},x,t-(t_{ELM}+\tau_{ELM}))\right] \end{aligned} \tag{2.76}$$

One can identify two temperature variations, one due to the steady-state heat flux density ΔT_1^{steady} and one due to the ELM heat flux density ΔT_1^{ELM}:

$$\begin{aligned} \Delta T_1^{steady}(s_{ISP},x,t) &= \Delta\phi_{net}^{steady}(s_{ISP})T_1^{step}(s_{ISP},x,t-0) \\ \Delta T_1^{steady}(s_{ISP},x,t) &= 6.9\times10^6 \times T_1^{step}(s_{ISP},x,t-0) \end{aligned} \tag{2.77}$$

$$\begin{aligned} \Delta T_1^{ELM}(s_{ISP},x,t) &= \Delta\phi_{net}^{ELM}(s_{ISP})\left[T_1^{step}(s_{ISP},x,t-t_{ELM})\right. \\ &\qquad \left. -T_1^{step}(s_{ISP},x,t-(t_{ELM}+\tau_{ELM}))\right] \\ \Delta T_1^{ELM}(s_{ISP},x,t) &= 126.8\times10^6\times\left[T_1^{step}(s_{ISP},x,t-20.0)\right. \\ &\qquad \left. -T_1^{step}(s_{ISP},x,t-(20.0+400.0\times10^{-6}))\right] \end{aligned} \tag{2.78}$$

The divertor monoblock specifications defined in table 2.9 are the same as the ones of the PFC used in the example of subsection 3.1. Therefore, its surface temperature step response is plotted in figure C.1.b. One can see in this figure that, in the time interval of the ELM – inter-ELM phase ($20.0 \leq t \leq 20.0 + 1/\nu_{ELM}$), the value of the step response T_1^{step} in ΔT_1^{steady} (equation 2.77) can be calculated analytically using the long time asymptote for actively-cooled PFC (equation C.29) as the value of the time is greater than t_∞^{min}. On the contrary, both values of the step response in ΔT_1^{ELM} can be calculated using the short time asymptote (equation C.17) as the value of the time variable in both step responses is lower than t_0^{max}. In figure 2.28.a are plotted the temperature profiles in the first material layer of the monoblock (W) at the inner strike-point before the ELM (at $t - t_{ELM} = 0$ s, i.e. due to the steady-state heat load), at the end of the ELM (at $t - t_{ELM} = \tau_{ELM}$) and at the end of the inter-ELM phase (at $t - t_{ELM} = 1/\nu_{ELM}$). The temperature variation due to the ELM ΔT_1^{ELM} is plotted in figure 2.28.b at the end of the ELM and at the end of the inter-ELM phase. It is calculated using equation 2.78 and the short time asymptote expression (equation C.17). One can see in this figure that the pulse heating due to the ELM is essentially concentrated in a thin layer at the monoblock surface ($\Delta T_1^{ELM} > 0$ for $0 \leq x \leq 0.5$ mm). After the ELM, the heat accumulated at the surface is efficiently transported into the depth of the material due to the high conductivity of W to such a point that, at the end of the inter-ELM phase, the temperature profile is almost similar to the one prior to the ELM (cf. figure 2.28.a).

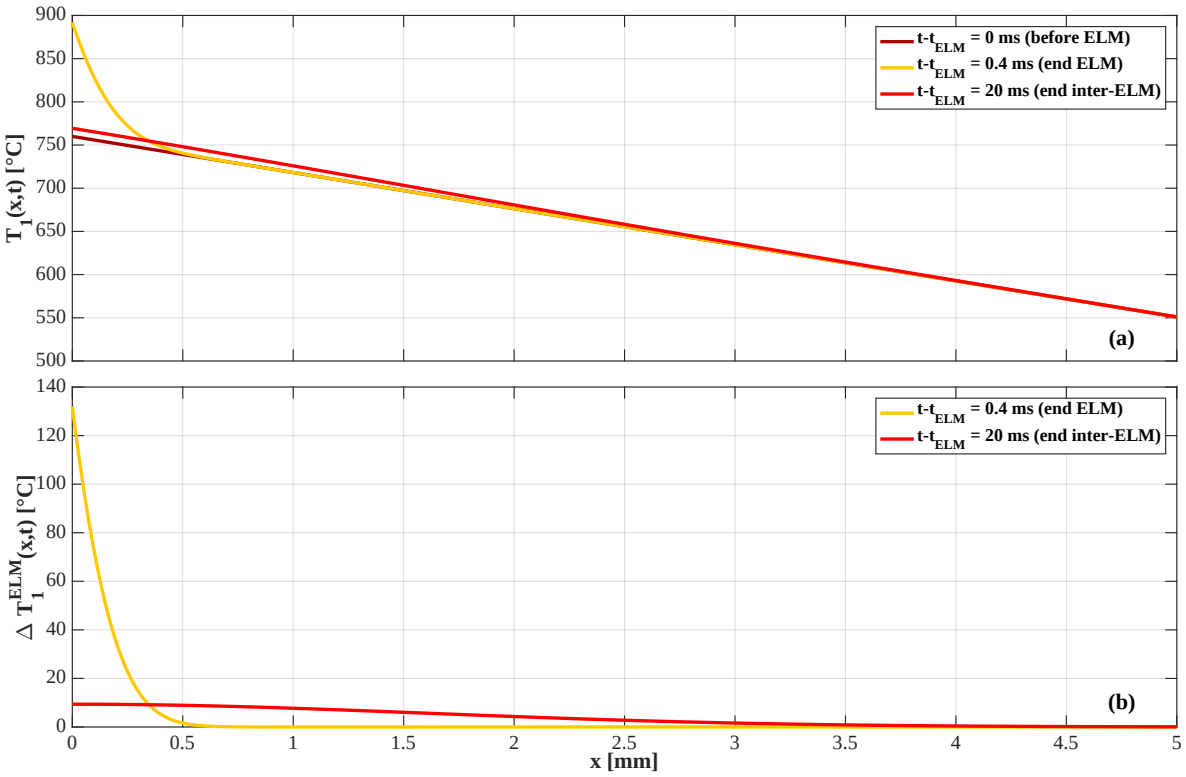

Figure 2.28: Depth profiles of the temperature (a) and of the temperature variation (b) at the end of the ELM-like heat load ($t - t_{ELM} = \tau_{ELM} = 400$ μs) and at the end of the inter-ELM phase ($t - t_{ELM} = 1/\nu_{ELM} = 20$ ms) at the inner strike-point. The temperature depth profile prior to the ELM is also displayed in (a).

5 Methodology of simulation of an ELM – inter-ELM phase with SolEdge2D-EIRENE coupled to D-WEE.

Now that the D-WEE module has been introduced, one question remains: how will one perform a simulation of an ELM – inter-ELM phase? What methodology should be followed to reach this purpose? The conception of this methodology will be guided by some requirements and by being aware of the capabilities of SolEdge2D-EIRENE to fulfill these requirements:

→ First, the wall needs to be initialise in terms of local fuel inventory, desorption flux density and temperature. It is fundamental to determine this local wall state as it sets its behaviour w.r.t. the fuel (pumping or fuelling areas) and the available fuel reservoir/inventory before transient events like ELMs. Ideally, the local wall state should be representative of the experimental one during a plasma discharge.

→ For the particle inventory, the initialisation can be partly done by taking into account the post-mortem analysis: TDS and NRA analysis of samples removed from the reactor can be used to parameterise MHIMS (to obtain their detrapping energy and the depth profiles of traps and of the corresponding trapped HI). However, it

is remembered that those analysis are done weeks or even months after the sample removal and give only access to the traps responsible for the long-term retention. Consequently, traps responsible for the dynamic retention cannot be probed.

→ The trap settings obtained from post-mortem analysis can be completed by parameterisation obtained through in-situ analysis of sample implanted in ion accelerators or linear plasma generators (cf. chapter 1 section 6). The in-situ analysis can be performed directly after the implantation and give access to both the dynamic and long-term retention reservoirs. Still the implantation conditions in those devices are not representative of the one found in fusion reactors. The parameterisation of traps obtained from these implantation experiments must be cross-checked with the parameterisation obtained from post-mortem analysis to identify the missing traps that can be responsible for the dynamic retention.

→ Once their parameterisation selected, the traps responsible for the dynamic retention must be initialised in terms of local inventory. No experimental technics are available to initialise this inventory. Modelling is the only way to achieve this goal. The easiest solution would be to simulate a complete plasma discharge with SolEdge2D-EIRENE coupled to D-WEE. However, one must be aware that regular SolEdge-EIRENE simulations of steady-state plasmas require several months of computation on supercomputers to simulate approximately one second of plasma. Moreover, simulations with SolEdge2D-EIRENE can only be done with a fix magnetic configuration. As a consequence, the simulation of a complete discharge, which in general lasts more than 10 s, cannot be envisaged with this code.

A methodology that overcomes the modelling limitations of SolEdge2D-EIRENE while allowing the initialisation of the wall is proposed. This methodology is represented in the flowchart 2.29. It is divided in four simulation steps:

1. A synthetic plasma discharge is built from successive SolEdge2D-EIRENE simulations of steady-state plasmas. This synthetic discharge can be used as a plasma background for D-WEE.

2. Then D-WEE is run in standalone mode (independently of SolEdge2D-EIRENE) to simulate a sequence of plasma discharges. This simulation enables to initialise the wall and in particular the traps responsible for the dynamic retention.

3. The wall state at a desired time during a discharge can be calculated and then be used as an initial condition for a coupled SolEdge2D-EIRENE – D-WEE simulation. The simulation is run until a new steady-state has been reached if the feedback of D-WEE as an impact on the steady-state plasma obtained in the simulation of step 1.

4. Eventually, a synthetic ELM-like event can be triggered to investigate the wall response to this event and its potential effect on the plasma.

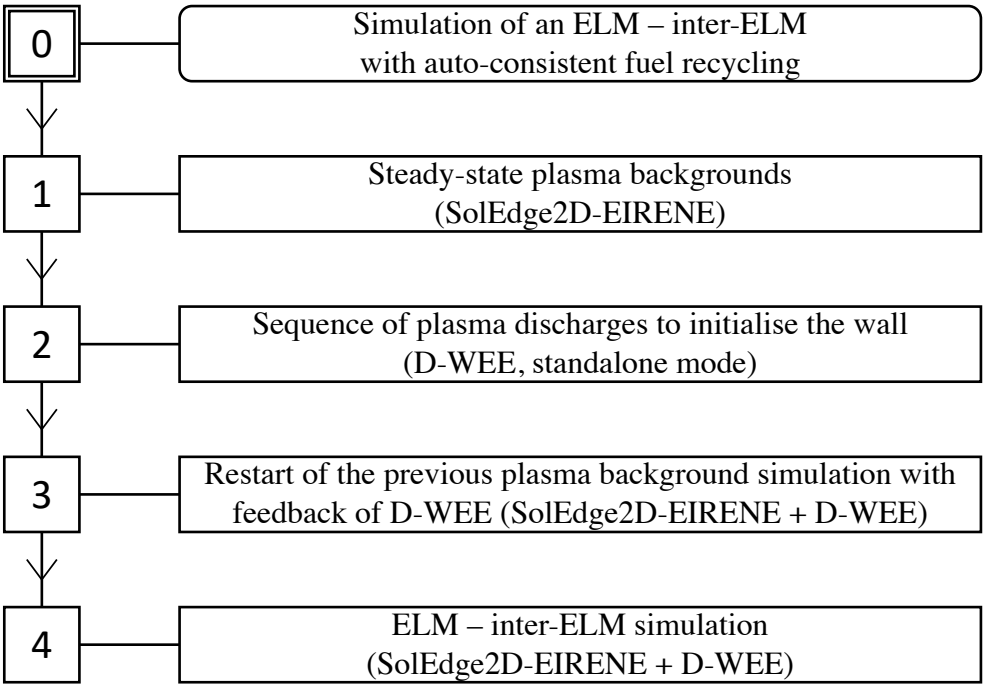

Figure 2.29: Flowchart of an ELM – inter-ELM simulation performed with the SolEdge2D-EIRENE code with feedback of D-WEE.

Unfortunately, due to numerical issues related to the thermal code WEE-temp, steps 3 and 4 could not be performed in the time scale of this PhD. As it was seen in subsection 3.1, the net heat flux density $\phi_{net}(s,t)$ is decomposed in step changes. As $\phi_{net}(s,t)$ evolves with time, the number of corresponding step changes, $N_\phi(s,t)$, also evolves with time. Even though the heat flux density does not vary significantly after the restart of the simulation (step 3) w.r.t. its steady-state value (obtained in step 1), numerical fluctuations result in a little variation of ϕ_{net} at each time step of D-WEE during coupled simulations. $N_\phi(s,t)$ is therefore incremented at every time steps. The longer the simulation, the higher the number of step changes is. At some point this number becomes so high that the simulation crashes due to memory overflow or freezes due to the high number of required numerical Laplace inversions of the step response. A method must be developed to limit the number of these step changes and to account for these step changes only when they are significant. Work is ongoing to solve this issue. However, this numerical problem does not arise in the simulation of step 2 as the number of step changes in those simulations remains limited due to the fixed plasma backgrounds calculated with SolEdge2D-EIRENE. The next two chapters are dedicated to the steps 1 and 2 of this methodology. The simulation of step 2 will also be used to investigate the wall dynamics during a sequence of plasma discharges.

Conclusion of chapter 2:

– A module, named D-WEE, has been developed to complete the description of the recycling of hydrogen isotopes (HI) in SolEdge2D-EIRENE. To do so, D-WEE adds the dynamics of thermal desorption of molecules of HI from the wall. D-WEE is made of two internal codes: MHIMS and WEE-temp.

– MHIMS describes the interaction between HI and the surface material of the wall through the so-called reaction-diffusion system of equations. It simulates implantation, diffusion, trapping and desorption of HI. MHIMS has been strongly improved from a numerical point of view to decrease its computational time while preserving its computational accuracy. For the moment, MHIMS does not take into account surface effects. The models available in the literature to treat those effects as well as the parameters required in those models have shown some inconsistencies under tokamak relevant implantation conditions which would lead to a large overestimation of the pumping effect by the wall. The modelling of HI–Be interaction requires the treatment of those surface processes as almost 75 % of the total HI inventory found in Be is possibly adsorbed at the surface of interconnected cavities within the implantation zone. Moreover, a clear change of the HI–Be interaction with the implantation temperature is observed and has been highlighted by Reinelt et al. [85]: the TDS spectra obtained after D implantation in Be at 320 K (base temperature of the ITER Be first-wall) and at 530 K (temperature of the JET-ILW Be first-wall) exhibit highly different patterns. No modelling effort has been undertaken in the fusion community to simulate and to understand this change of interaction. As a consequence, the present knowledge does not permit the modelling of HI–Be interaction. For HI–W interaction, the parameterisation proposed by Hodille et al. through fitting of the implantation experiment and subsequent TDS analysis performed by Ogorodnikova et al. [47] has been selected. The strength of this parameterisation was confirmed by further simulations and confrontations to experimental results with different implantation conditions.

– WEE-temp calculates the temperature depth profile in the surface material of PFCs (the zone simulated by MHIMS). It has the capability to model actively-cooled PFCs and inertial PFCs, in both steady-state and transient conditions like ELMs, assuming that PFCs have a slab geometry made of a superposition of material layers. A special attention has been paid to the modelling of actively-cooled PFCs in the perspective of the WEST and ITER projects. Adjustments of the model have been proposed in order to reproduce the thermal behaviour of the real actively-cooled PFCs. For inertial PFCs, an adjustment of the model has been suggested to mimic the cooling of the PFCs between discharges (due to heat dissipation into the tokamak structure) while preserving their inertial behaviour during the discharges.

– A methodology in four steps has been proposed to simulate an ELM – inter-ELM phase with SolEdge2D-EIRENE coupled to D-WEE. The first two steps enable to initialise the wall (in terms of local fuel inventory, desorption flux density and temperature) prior to the simulation of an ELM – inter-ELM phase. Step 3 is a restart of the SolEdge2D-EIRENE simulation of step 1 and aims to calculate a new steady-state plasma with SolEdge2D-EIRENE due to the modification of the recycling introduced by the feedback of D-WEE. The step 4 is the ELM – inter-ELM simulation. Due to numerical issues, related to the step decomposition of the heat flux density performed in WEE-temp, steps 3 and 4 could not be achieved in the time scale of this PhD. The two next chapters are dedicated to the steps 1 and 2 of this methodology.

Chapter 3

Simulation of a JET plasma discharge with SolEdge2D-EIRENE and confrontation to experiment.

Contents

In chapter 2, the D-WEE dynamic thermal desorption module has been presented. Moreover, a methodology has been proposed to model an ELM – inter-ELM phase with SolEdge2D-EIRENE coupled to D-WEE. This chapter focuses on the first step of this methodology: the definition of a synthetic plasma discharge. This discharge will be used as background input for D-WEE simulations to initialise the wall in terms of deuterium inventory, desorption flux and wall temperature. This synthetic discharge is composed of independent steady-state plasmas computed with SolEdge2D-EIRENE.

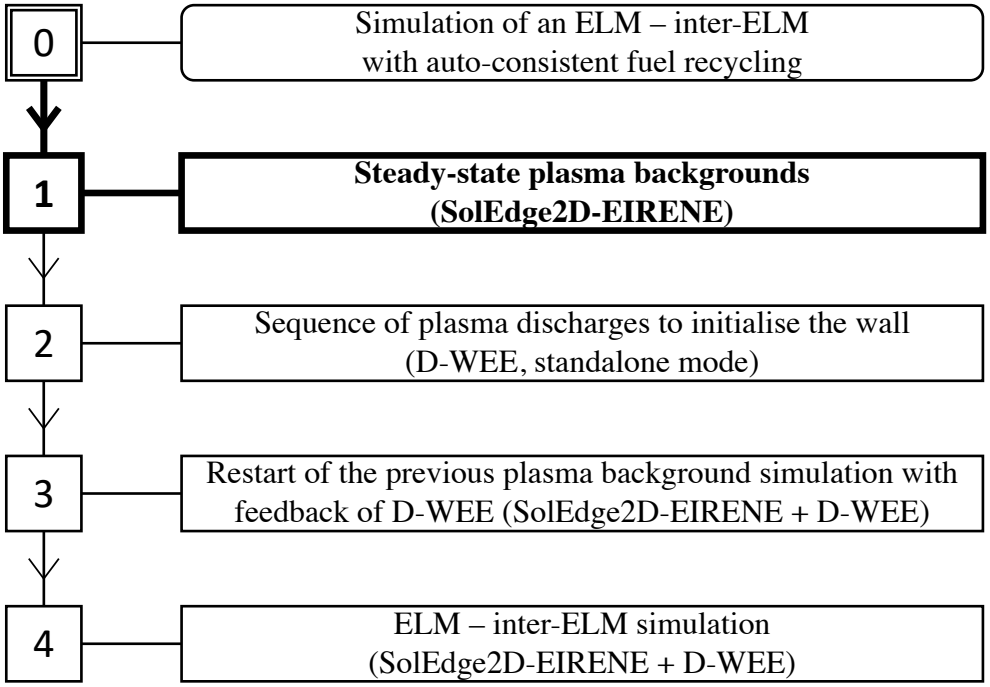

In the following, such methodology is applied to the JET tokamak. A discharge has been selected and each of its steady-state phases has been simulated with SolEdge2D-EIRENE. As it was seen in chapter 2 subsection 2.8, the local filling level of traps, and therefore the local HI inventory, is strongly dependent on the implantation conditions. Thus, the simulation results have been confronted to the available experimental measurements to assess the relevancy of the plasma-wall interaction obtained in the different simulations.

1 Experiment: JET Pulse Number 89044.

The present study focuses on the JET pulse number 89044 (#JPN89044, pure D plasma, $B_t = 2.4$ T, $I_p = 2$ MA), which was done during the JET-ILW 3 campaign (2015-2016). This discharge has been chosen because it was the first one of a monday morning session. Therefore one expects a strong dynamic retention during this discharge as the continuous outgassing that occurred during the weekend must have emptied the traps responsible for this dynamic retention.

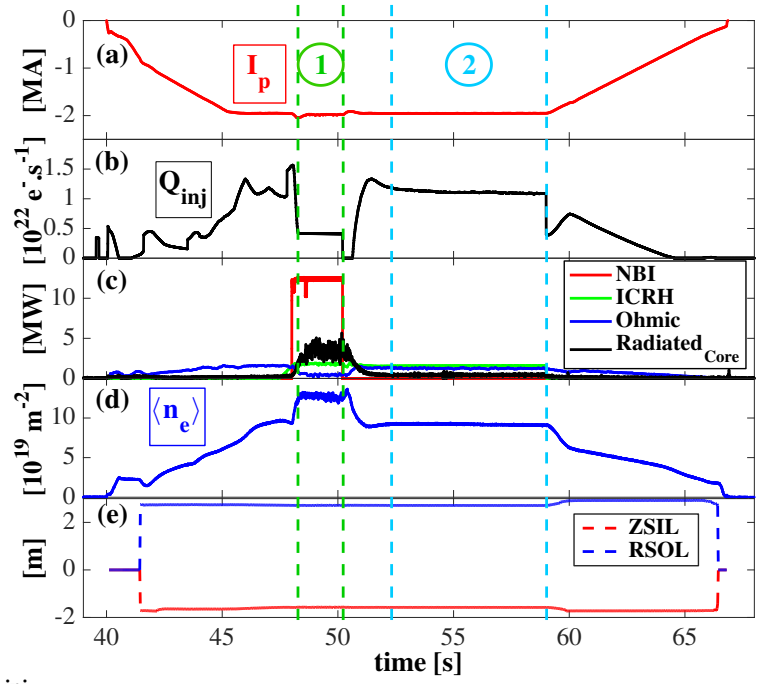

Figure 3.1: Time evolution of pulse parameters for #JPN89044: (a) plasma current I_p, (b) gas puff injection rate Q_{inj}, (c) input and radiated powers, (d) line-integrated electron density $\langle n_e \rangle$, (e) inner strike-point vertical position $ZSIL$ and outer strike-point horizontal position $RSOL$ (cf. figure 3.8 for the JET coordinates). Two steady-state phases, labelled 1 and 2, are identified. They are characterised by constant pulse parameters.

The time evolution of the pulse parameters are plotted in figure 3.1. The plasma is run in diverted configuration with inner and outer strike-points located on the top of vertical tile 3 and on the horizontal tile 5 Stack C respectively (cf. figure 3.3.b). This configuration is maintained during 24.9 s while the total pulse duration is 26.9 s. This indicates that the two inner limiter phases (at the beginning and at the end of the pulse) have a negligible time duration.

From figure 3.1, two steady-state phases are clearly identified. They are defined by constant magnetic equilibrium (X-point configuration and strike-points location), particle injection rate, heating power and plasma density:

(1) H-mode phase: from 48.3 s to 50.3 s. 15 MW of total heating power is injected in the plasma. The Neutral Beam Injection (NBI) contribution, P_{NBI}, is 12.5 MW, the Ion Cyclotron Resonance Heating (ICRH) contribution, P_{ICRH}, is 2 MW and the Ohmic contribution, P_{Ohm} is 0.5 MW. The plasma is fuelled from the Gas Introduction Module (GIM) number 11 (situated in the divertor base inner ring, cf. figure 3.2) with a puff injection rate, Q_{inj}, of 4.1×10^{21} D.s^{-1}. The NBI also fuels the plasma from the core with an injection rate, Q_{NBI}, of 1.5×10^{21} D.s^{-1} (not shown in figure 3.1, constant injection during this phase). The upstream line-integrated electron density $\langle n_e \rangle$ is 1.2×10^{20} m^{-2}.

(2) L-mode phase: from 52 s to 59 s. 2.9 MW of total heating power ($P_{ICRH} = 1.6$ MW and $P_{Ohm} = 1.3$ MW). Deuterium is injected from the tokamak outer midplane (GIM

4) with an injection rate of 4.1×10^{21} D.s^{-1} and from the top of the machine (GIM 7) with an injection rate of 6.9×10^{21} D.s^{-1} (both with density feedback). The upstream line-integrated electron density $\langle n_e \rangle$ is 9.2×10^{19} m^{-2}.

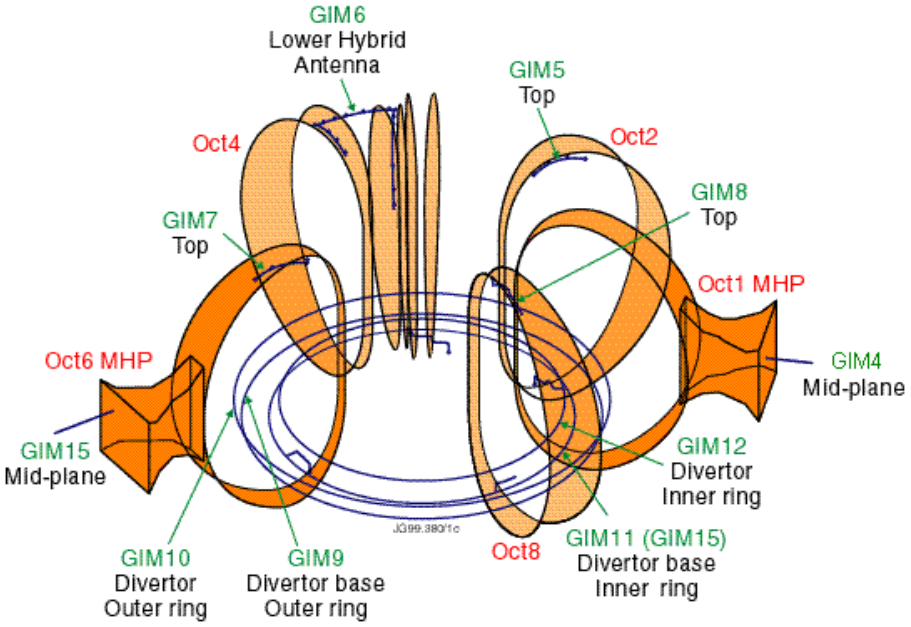

Figure 3.2: JET Gas Introduction Module (GIM) positions in the JET vacuum vessel.

In figure 3.3, two magnetic equilibria are displayed: one during the H-mode phase at $t = 49$ s and the second one during the L-mode phase at $t = 54$ s. For the H-mode phase, the magnetic surfaces seem to be shifted towards the Outer MidPlane (OMP). However, in the divertor region, the magnetic surfaces are superimposed (cf. figure 3.3.b). Therefore, the main plasma-wall interaction zones between phase 1 and 2 are similar. In the following, the same magnetic equilibrium will be considered in the two phases.
In figure 3.4, the OMP profiles of the electron density n_e and of the electronic temperature T_e are displayed. These profiles are measured using the High Resolution Thomson Scattering diagnostic (HRTS). In JET, HRTS consists in a high intensity laser beam which is injected in the plasma at a frequency of 20 Hz in the OMP of the reactor (cf. figure 3.3.a for the laser beam trajectory). The laser interacts with the electrons of the plasma which emit a radiation at the same frequency as the laser one. This radiation is collected by a spectrometer. n_e is obtained from the intensity of the scattered radiation and T_e from the broadening, through Doppler Effect, of the collected spectrum [106]. Figure 3.4 highlights the difference in the confinement regime of the two plasma phases. Indeed, phase 1 presents higher density and temperature at the plasma core than phase 2. These higher quantities are linked to the formation of a pedestal of the density and of the temperature at the edge of the plasma (cf. figure 3.4 from $R = 3.75$ m to $R = 3.82$ m). Therefore, phase 1 is a H-mode phase while phase 2 is a L-mode phase.
Due to the impossibility to simulate the plasma ramp-up and ramp-down phases with SolEdge2D-EIRENE, these two steady-state phases will be assumed to be relevant in estimating the overall plasma-wall interaction of this discharge. Please notice that this

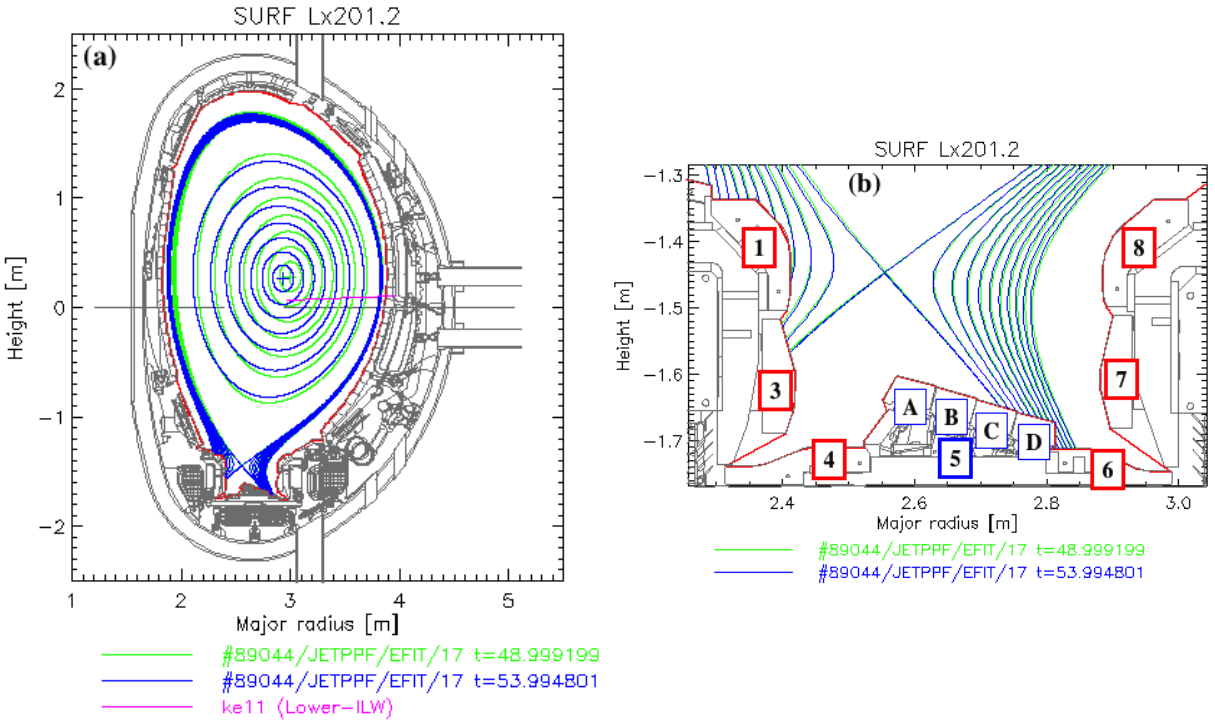

Figure 3.3: EFIT reconstructions of the #JPN89044 magnetic equilibrium during phase 1 (green) and phase 2 (blue): (a) full JET vacuum vessel, (b) zoom in the divertor. The divertor tile numbers and the different stacks of the tile 5 are indicated in figure (b). The HRTS laser beam path is displayed in magenta in figure (a).

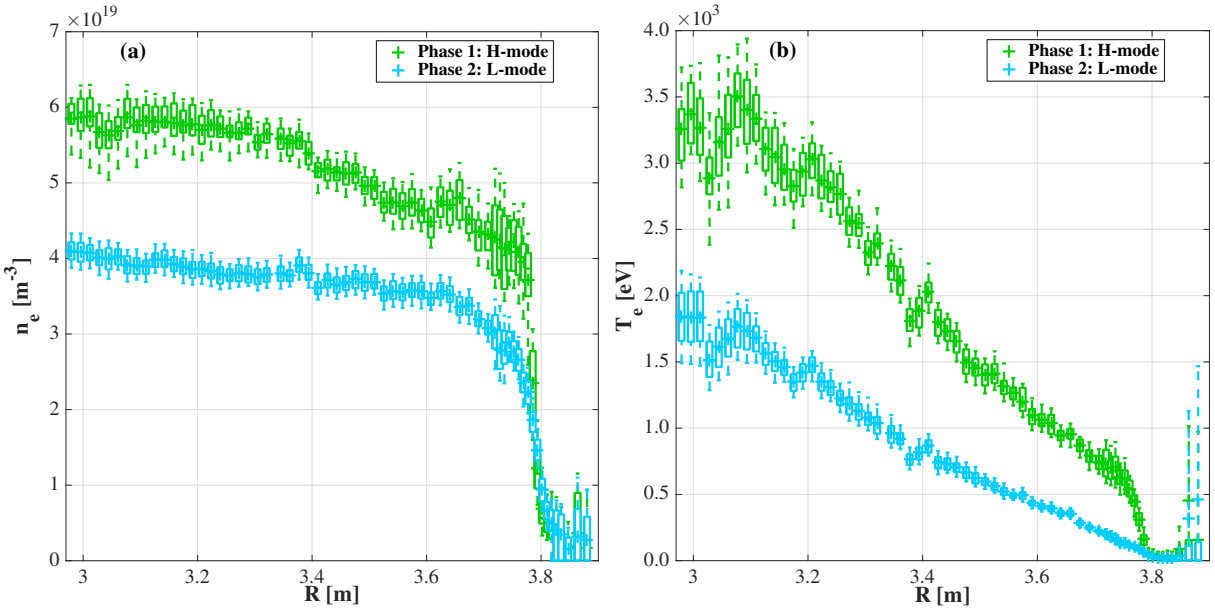

Figure 3.4: HRTS outer midplane profiles of (a) the electron density n_e and (b) the electronic temperature T_e during the H-mode phase (green) and the L-mode phase (blue)

assumption is strong and probably wrong. Indeed, both of them only represent 35 % of

the pulse duration (65 % of the duration of the plasma current flat-top phase). However, almost 60 % of the total integrated ion fluence on the divertor measured by Langmuir probes is deposited during this two phases (cf. figure 3.5: 2.6×10^{24} D^+ during the two phases, 4.3×10^{24} D^+ during the whole discharge). If one only considers the flat-top phase, this percentage increases to 72 %. This indicates that most of the integrated fluence of the discharge is deposited during this two phases. Thus, the considered assumption seems reasonable.

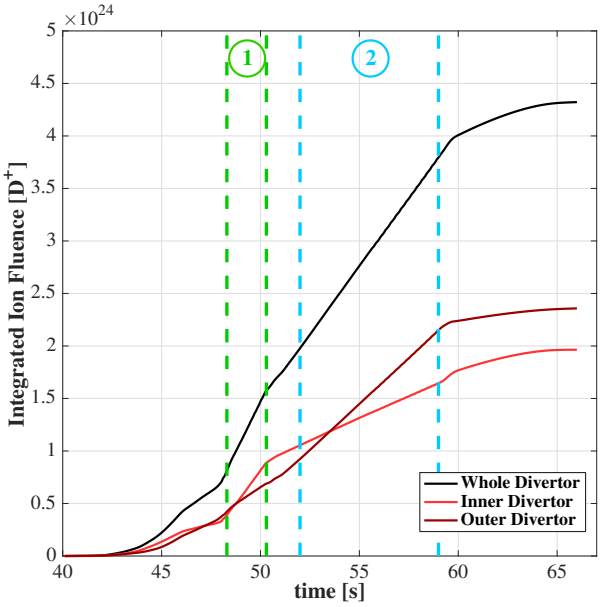

Figure 3.5: Total integrated ion fluence measured in the divertor by Langmuir probes during #JPN89044 (black solid line). The inner divertor integrated fluence (red solid line) and the outer divertor integrated fluence (brown solid line) are also displayed. The two steady-state plasma phases identified in figure 3.1 are delimited by the dashed lines.

The two previously identified phases have to be simulated with the SolEdge2D-EIRENE code to define a steady-state plasma background for each phase. The next section is dedicated to the modelling of the H-mode phase while the section 3 will be dedicated to the modelling of the L-mode phase.

2 Simulation of the H-mode plasma (phase 1) with SolEdge2D-EIRENE.

2.1 Definition of the inputs needed for the SolEdge2D-EIRENE simulation.

In this subsection, the inputs required for the SolEdge2D-EIRENE simulation will be presented. Before that, the author would like to introduce a method of representation of the experimental data: the boxplot. In the following, this method will often be used

to promptly depict the statistics of a measured data sample in a given time period (e.g. during one of the two plasma phases). The convention used for the boxplot representation is defined in figure 3.6. The spacings between the different parts of the box indicate the degree of dispersion and skewness in the data. In the case of this particular boxplot, if the locations of the different marks are equally spaced, the data should be normally distributed.

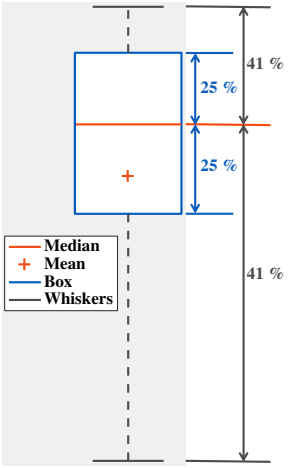

Figure 3.6: Boxplot convention used in the present manuscript. The red line represents the median value of the data sample while the red cross represents its mean value. The blue box depicts the lower and the upper quartiles. The lower whisker depicts the 9^{th} percentile while the upper whisker depicts the 91^{st} percentile.

The SolEdge2D-EIRENE simulation grid used for the simulation of both plasma phases is displayed in figure 3.7. This grid is aligned on the magnetic flux surfaces and is based on the magnetic equilibrium corresponding to the H-mode phase displayed in figure 3.3.a. The simulated domain is decomposed in 6 zones which are solved in parallel to reduce the computation time. In the following, the simulated region in the edge of the core (in yellow in figure 3.7) will be referred to as *edge*. In figure 3.7, the JET-ILW complex wall is displayed in black. The simulation grid extends beyond the wall, hence demonstrating the term immerse boundary condition technique used in the code.
The EIRENE code requires the definition of the wall materials to set the reflection properties of the fuel. The materials have been chosen to be representative of the mix of materials encountered in the JET-ILW. Such material distribution will enable the direct confrontation of the SolEdge2D-EIRENE simulation results to experimental measurements. Such confrontation will be presented at the end of this chapter and in chapter 4. The wall configuration considered for the simulation of both phases is shown in figure 3.8.a. A Be first-wall (yellow solid line) and a W divertor (grey solid line) are considered. A Be surface is also assumed on the top of HFGC tile and of tile 1 (orange solid line), in agreement with post-mortem analysis that revealed the presence of a thick (up to 40 μm) Be co-deposit layers in this zone of JET-ILW [107]. Please notice that the hypothesis that one have made on the co-deposit distribution is questionable. Indeed, post-mortem analysis made after the ILW 2 campaign (therefore representative of the wall mix-material

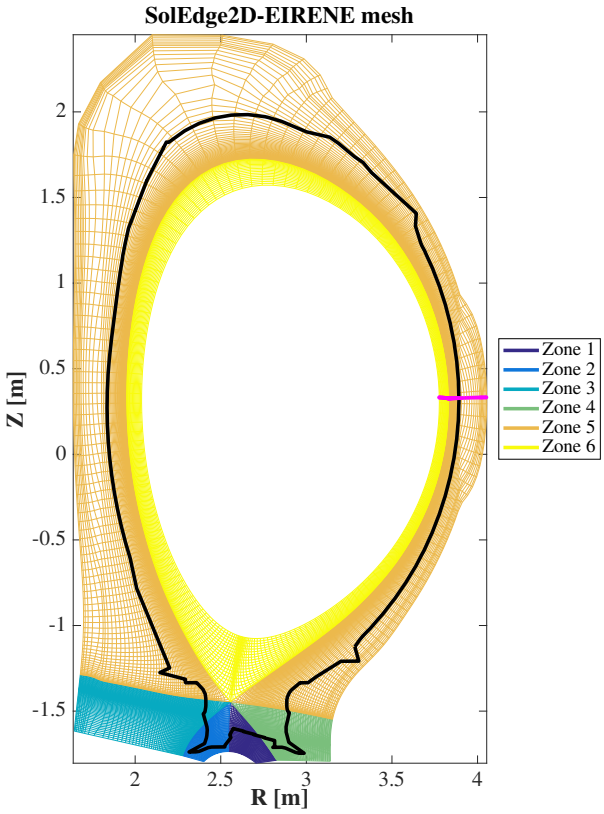

Figure 3.7: SolEdge2D-EIRENE simulation grid for the #JPN89044. The outer midplane grid points used for the autofit procedure are displayed in magenta.

of #JPN89044 run during the ILW 3 campaign) have also revealed a non-negligible Be areal density on top of the vertical part of tile 1 (up to 5×10^{22} D.m^{-2}, i.e. $\sim$ 400 nm thick co-deposit) [108]. The tiles 4, 6, 7 [108, 109] and 5 stack D [110] also exhibit a Be co-deposit layer that one can hardly neglect ($\sim 1 \times 10^{22}$ D.m^{-2}, i.e. $\sim$ 80 nm thick). The mean ion range for D implantation into Be at normal incidence for a D impact energy of 1 keV is 25 nm [68]. This indicates that the interaction zone of incident D ions with Be is way below the thickness of these Be co-deposit layers. Therefore, Be should have been considered at the surface of the divertor tiles, except in the tile 5 stacks A, B and C where W seems to remain at the surface [110]. Some published JET-ILW simulations with the EDGE2D-EIRENE code have been performed considering a full-Be wall even in the divertor region [111].
Concerning particle exhaust, two pumping regions are set in the two divertor throats (where the pumping ducts are located, cf. figure 3.8.a). Indeed, as the plasma is run in diverted configuration, the deuterium pressure in the main chamber is negligible w.r.t. the pressure in the divertor region. Deuterium is therefore mainly exhausted by the cryopump located in the sub-divertor [112]. The total recycling coefficient $RECYCT$ (cf. chapter 1 section 7) is manually specified in both of these regions in order to control the pumping flux amplitude. This specific value of $RECYCT$ at the pump will now be referred to as *pump albedo*. Elsewhere, the $RECYCT$ value is set to unity in order to

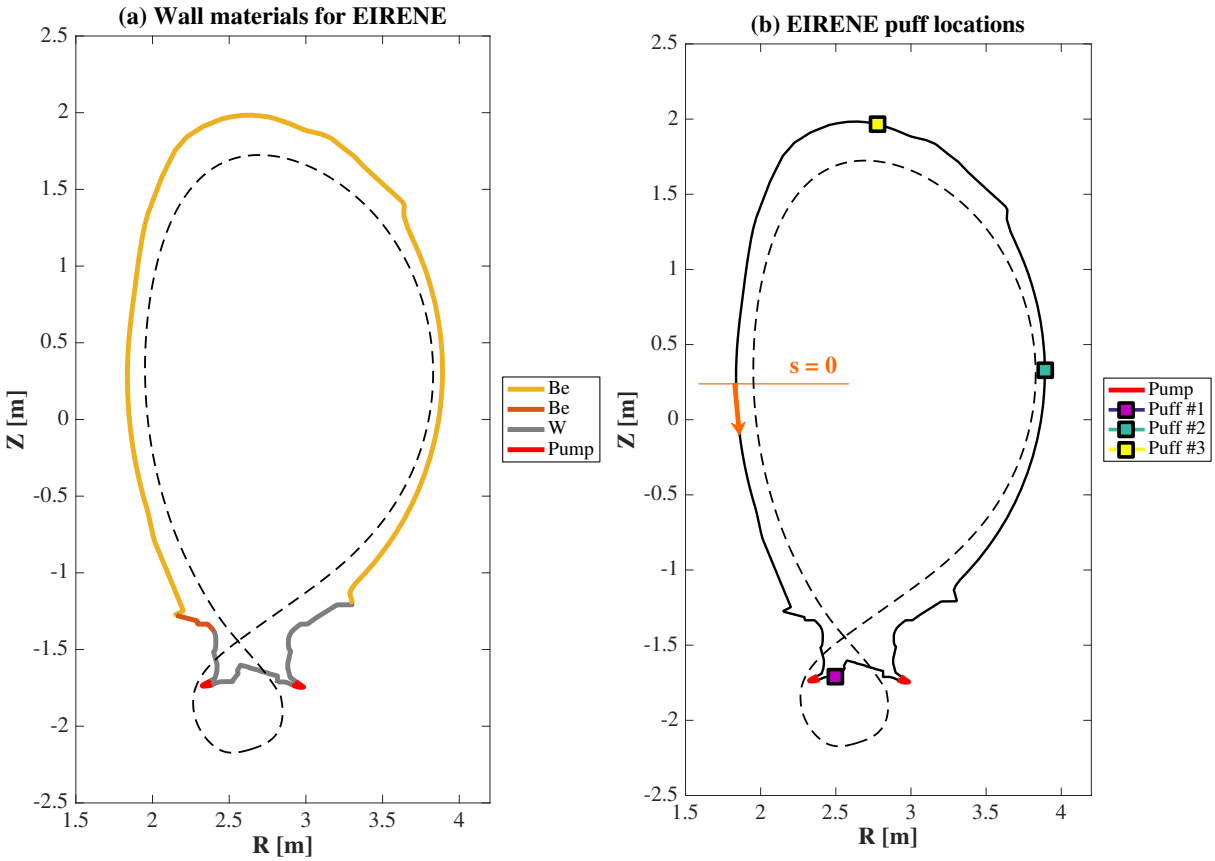

Figure 3.8: Poloidal distribution of the wall materials and pumps used in the EIRENE code (a) and poloidal locations of the different puffs required in the simulation (b). The curvilinear coordinate along the wall, s, is also defined in (b).

ensure particle conservation. Therefore the molecular recycling coefficient R_m defined in chapter 1 section 3 is equal to one and all the incoming ion flux density is recycled as neutrals. The proportion of reflected atoms and of desorbed molecules is directly calculated by the EIRENE code.

The deuterium supply has also to be set in the simulation. The gas puff locations are displayed in figure 3.8.b. These locations respect the experimental puff locations of the considered discharge (cf. section 1). For the H-mode phase, the gas puff injects particles only from the GIM 11 ($Q_{inj} = 4.1 \times 10^{21}$ D.s^{-1} from puff number 1 in figure 3.8.b). It has to be pointed out that the NBI contribution to the fuelling of the reactor during the H-mode phase ($Q_{NBI} = 1.5 \times 10^{21}$ D.s^{-1}) cannot be neglected in the simulation. However, it is not a direct input of the code. In section 2.2, one explains how this contribution is indirectly considered as particles injected from the core-edge interface.

To end up with the EIRENE inputs, the AMJUEL database is considered as atomic and molecular database. The number of particles launched at each iteration is set to 240000 in order to ensure good statistics and to limit the noise inherently present in the Monte-Carlo method used in EIRENE.

The delicate part of the simulation setup is the definition of the perpendicular anomalous

diffusion coefficients $D_\perp$, $\chi_{\perp,e}$ and $\chi_{\perp,i}$ defined in chapter 1 section 7. In the following, both phases will be simulated using a special SolEdge2D-EIRENE operation mode called *autofit*. In this operation mode, the user can prescribe radial profiles of density (n_e) and temperatures (T_e and T_i) at a given poloidal location. SolEdge2D-EIRENE will then try to fit the prescribed profiles by adjusting the diffusion coefficients while solving the rest of the domain. These diffusions coefficients will therefore be radial dependent: $D_\perp(r)$, $\chi_{\perp,e}(r)$ and $\chi_{\perp,i}(r)$. Such way to constrain the diffusion coefficients is particularly interesting when one is willing to confront the simulation results to experimental measurements (which is what will be done later in this report). The OMP is chosen as poloidal location for the reference profiles since it has been shown experimentally that the transport from the core to the SOL is localised there. Moreover, the HRTS line of sight is also situated at the OMP and the experimental profiles measured with this diagnostic, introduced in figure 3.4, can be used as references for the autofit. In figure 3.9, the H-mode phase HRTS measurements of n_e and T_e in the zone of interest are displayed using the aforementioned boxplots. The scattering of the measurements for both quantities is very large and the skewness of the data is negative in the core and positive in the SOL region. Indeed, some HRTS measurements during the H-mode phase can coincide with ELMs which entail a release of particle and energy in the SOL. Therefore the density and temperatures in the core are lower during these events and both increase in the SOL at the same time.

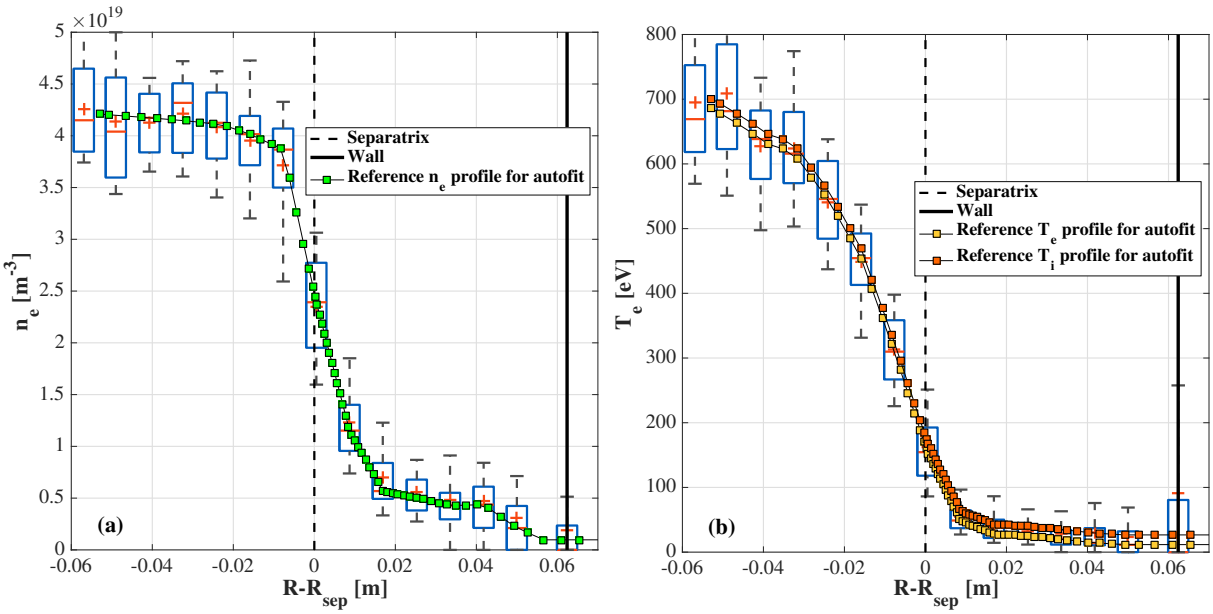

Figure 3.9: Autofit reference profiles of (a) the electron density n_e and (b) the electronic temperature T_e for the SolEdge2D-EIRENE simulation of the H-mode phase. The boxplots represent the data samples measured in the time period of the H-mode phase with HRTS. Due to the lack of measurement of the ionic temperature T_i in the SOL, an offset of 15 eV is assumed in the reference T_i profile w.r.t. the reference T_e profile.

Now one has to define reference profiles for n_e, T_e and T_i at the OMP grid points (cf. the

magenta line in figure 3.7) from the HRTS profiles displayed in figure 3.9. These profiles have to be representative of the inter-ELM mean profiles. To achieve this, one has opted for the following approach:

- In the pedestal and the SOL, the median values of the respective quantity at each probed position have been chosen as references (cf. figure 3.9). They are considered to be representative of the inter-ELM mean value in the time interval of the H-mode phase (as the probability to have an HRTS measurement during an ELM is low). The reference value at each grid point have been calculated using linear interpolation between these median values.
- In the edge, (from $R - R_{sep} \leq 0.03$ m) the value of the plasma quantity at each grid point are arbitrarily chosen such as to respect the gradient of the quantity in the core region.

Due to the lack of reliable measurement of the ionic temperature T_i in the SOL, an offset of 15 eV is assumed for the reference T_i profile w.r.t. the reference T_e profile (cf. figure 3.9.b).
Eventually, specified conditions have to be set at the boundaries of the simulated domain, i.e. at the wall and at the core-edge interface. In the parallel direction, the so-called Bohm boundary conditions, $\left|u_{\parallel}^{se}\right| \geq c_s = \sqrt{\frac{T_e + T_i}{m_i}}$, are imposed at the Magnetic Pre-Sheath Entrance (MPSE) [10]. Concerning the temperature equation, the parallel electron heat flux density, respectively parallel ion heat flux density, at the MPSE is set to $q_{\parallel,e}^{se} = \gamma_e n_e u_{\parallel}^{se} T_e$, $q_{\parallel,i}^{se} = \gamma_i n_i u_{\parallel}^{se} T_i$ respectively [10]. The sheath heat transmission coefficient for electron and ion are set to $\gamma_e = 4.5$ and $\gamma_i = 2.5$. As far as it concerns the core-edge interface, the autofit procedure goes hand in hand with the use of Dirichlet boundary condition for density and temperature. The value of n, T_e and T_i imposed at this boundary is set to the value at this interface of the respective reference profiles (cf. figure 3.9).

2.2 Flux balances and convergence of the simulation to a stationary plasma.

Once the SolEdge2D-EIRENE simulation is launched, the plasma evolves and converges to a steady state. One is interested in having a simulated steady-state plasma which is representative of the experimental steady-state plasma. In appendix D, two convergence criteria, one for particle and one for energy, are described. These criteria are based on multi-system particle flux (herein referred to as *flux*) and power balances. The experimental steady-state plasma satisfies these criteria which entails that the SolEdge2D-EIRENE solution has to satisfy it as well.

Now one will apply the two steady-state criteria (D.11-D.23) to the case of the #JPN89044 SolEdge2D-EIRENE simulation with the autofit procedure. In reality, due to the inherent conservative nature of the SolEdge2D-EIRENE equations, the code will evolve up to

a steady state which satisfy both criteria. Therefore the user has to constrain the code to find an equilibrium state which is similar to the experimental equilibrium state. In the following, the criteria will be rearranged to have the input contributions in the LHS and the output contributions in the RHS. The different terms in both systems are colored to highlight their different situations in the simulation: in red the direct, controllable, inputs of the code, in green the indirect inputs, and in blue the code outputs.
First this color code will be applied to the case of the flux balance system D.11:

$$\begin{cases} Q_{NBI} + Q_{inj} = Q_{pump,tot} - \cancel{\dfrac{dN_{wall,tot}}{dt}} \\ Q_{NBI} + Q^{D}_{EDGE\rightarrow CORE} = Q^{D^+}_{CORE\rightarrow EDGE} \\ Q^{D^+}_{CORE\rightarrow EDGE} + S^{D^+}_{EDGE+SOL} = Q^{D^+}_{SOL\rightarrow wall} \end{cases} \quad [\text{at.s}^{-1}] \tag{3.1}$$

where Q_{NBI} is the NBI injection flux, Q_{inj} is the total gas puff injection flux, $Q_{pump,tot}$ is the total D pumping flux, $N_{wall,tot}$ is the number of D particles in the wall (wall inventory), $Q^{D}_{EDGE\rightarrow CORE}$ is the flux of unconfined D neutrals going from the edge to the core, $Q^{D^+}_{CORE\rightarrow EDGE}$ is the flux of deconfined D ions flowing from the core to the edge, $S^{D^+}_{EDGE+SOL}$ is the net ion source in the EDGE+SOL domain (the domain simulated by SolEdge2D-EIRENE), which is the sum of the positive ionisation source and the negative recombination source in the EDGE+SOL region, and $Q^{D^+}_{SOL\rightarrow wall}$ is the ion flux flowing from the SOL to the wall. Equation 1 is the steady-state condition for the Vacuum Vessel (VV) flux balance, equation 2 is the steady-state condition for the core flux balance while equation 3 is the steady-state condition of the flux balance of EDGE+SOL domain. The wall contribution in equation 1, $dN_{wall,tot}/dt$, has been cancelled out as the particle conservation assumption at the wall ($RECYCT = 1$) entails that the wall particle inventory does not evolve, thus $dN_{wall,tot}/dt = 0$. Moreover in the case of the autofit procedure, the use of a Dirichlet boundary condition for the density at the core-edge interface implies that $Q^{D^+}_{CORE\rightarrow EDGE}$ is an output of the code. Therefore, the SolEdge2D-EIRENE user only has to force the pumping flux $Q_{pump,tot}$ to compensate the external fuelling rates Q_{NBI} and Q_{inj} through the pump albedo term. For the H-mode phase, this yields to:

$$Q_{pump,tot} = Q_{NBI} + Q_{inj} = 1.5 \times 10^{21} + 4.1 \times 10^{21} = 5.6 \times 10^{21} \text{ D.s}^{-1} \tag{3.2}$$

The time evolution of the different terms of equations 1, 2 and 3 of the system 3.1 are respectively displayed in figures 3.10 a, b and c for the case of the H-mode phase simulation. The values of the two fuelling rates Q_{NBI} and Q_{inj} correspond to the experimental H-mode phase values defined in section 1. The difference between the LHS and RHS of the different equations are also displayed. For $t \geq 500$ ms, the three steady-state criteria are fulfilled. The pump albedo had to be set to a value of 0.69 to ensure the value of $Q_{pump,tot}$ defined in equation 3.2, which is the case for $t \geq 430$ ms (cf. figure 3.10.a). $Q^{D^+}_{CORE\rightarrow EDGE}$ then evolved to the proper value which fulfills equation 2 (cf. $t \geq 450$ ms in figure 3.10.b). Then the recycling slightly evolves (cf. figure 3.10.c) and equilibrates after $t \geq 500$ ms.
One can wonder how $Q^{D^+}_{CORE\rightarrow EDGE}$ is coupled to $Q_{pump,tot}$. First one will remind the

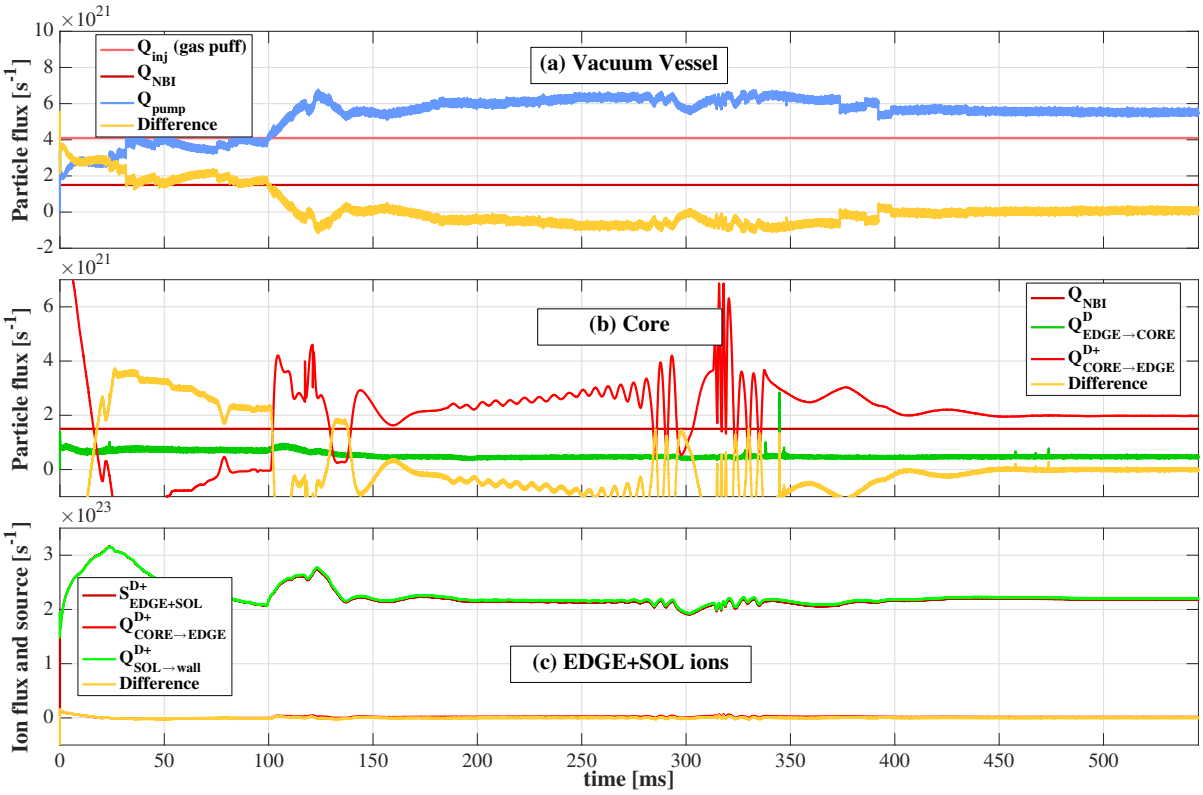

Figure 3.10: Illustration of the multi-system particle balances for the SolEdge2D-EIRENE simulation of the H-mode phase: (a) the overall tokamak vacuum vessel, (b) the core region (not simulated by SolEdge2D-EIRENE) and (c) the ions in the simulated domain (EDGE+SOL region). These flux balances are controlled during all the simulation to ensure that steady state is reached and that it is representative of the experimental steady state.

expression of $Q^{D^+}_{CORE\rightarrow EDGE}$. The core and edge flux surfaces being isodensity surfaces, this ion flux can be written as follows:

$$Q^{D^+}_{CORE\rightarrow EDGE} = \iint_{S_{CORE}} D_\perp(r)\,\nabla_\perp n_i(r)\,dS = S_{CORE} D_\perp(r_{S_{CORE}})\,\nabla_\perp n_i(r_{S_{CORE}}) \quad (3.3)$$

where S_{CORE} is the surface of the core-edge interface, $r_{S_{CORE}}$ is the radial position of this interface at the OMP and $\nabla_\perp n_i$ is the perpendicular gradient of density. The autofit procedure forces this gradient at the core-edge interface by adjusting $D_\perp(r_{S_{CORE}})$. When $Q_{pump,tot}$ is higher than the external fuelling rate, the plasma density decreases in the simulated domain. The autofit detects this decrease and corrects it by increasing $D_\perp$: the simulated domain is artificially fuelled by the core. Such situation can be seen in the considered simulation between $t = 175$ s and $t = 400$ s (cf. figure 3.10.a).

The power balance of the simulation had also to be controlled. As it has been done for the flux balance criterion, the criterion D.23 is rearranged and written using the

aforementioned color code:

$$\begin{cases} P_{NBI} + P_{ICRH} + P_{Ohm} - S^{E,rad}_{CORE} = P^{\{D^+ + e^-\}}_{CORE \to EDGE} \\ P^{\{D^+ + e^-\}}_{CORE \to EDGE} + S^{E,\{D^+ + e^-\}}_{EDGE+SOL} = P^{\{D^+ + e^-\}}_{SOL \to wall} \end{cases} \tag{3.4}$$

where P_{NBI} is the NBI injected power, P_{ICRH} the ICRH injected power, P_{Ohm} the ohmic power, $S^{E,rad}_{CORE}$ is the core radiative energy source while $P^{\{D^+ + e^-\}}_{CORE \to EDGE}$ is the unconfined power carried by ions and electrons going from the edge to the core, $S^{E,\{D^+ + e^-\}}_{EDGE+SOL}$ is the net energy source due to interaction with neutrals in the EDGE+SOL domain and $P^{\{D^+ + e^-\}}_{SOL \to wall}$ is the energy flux going from the SOL to the wall. The latter does not have to be confused with the plasma net heat flux coupled to the wall. Indeed, the reflected energy flux on the wall surface would have to be accounted in the calculation of this heat flux. Equation 1 is the steady-state condition of the core power balance while equation 2 is the steady-state condition of the {D ions+electrons} power balance in the EDGE+SOL domain.
As one can see, in autofit mode, the user cannot directly interfere in the power balance. This is again due to the use of a Dirichlet boundary condition for temperature at the core-edge interface. The magnetic flux surface in the core and in the edge being isothermal, the plasma power flowing at the core-edge interface in SolEdge2D-EIRENE is given by the following expression:

$$\begin{aligned} P^{\{D^+ + e^-\}}_{CORE \to EDGE} &= \iint_{S_{CORE}} \left(n_i(r) \chi_{\perp,i}(r) \nabla_\perp T_i(r) + n_e(r) \chi_{\perp,e}(r) \nabla_\perp T_e(r) \right) dS \\ &= S_{CORE} \left[n_i \chi_{\perp,i} \nabla_\perp T_i + n_e \chi_{\perp,e} \nabla_\perp T_e \right] (r_{S_{CORE}}) \end{aligned} \tag{3.5}$$

where $\nabla_\perp T_i$ and $\nabla_\perp T_e$ are the ionic and electronic temperature gradients respectively. Again, both gradients are forced by the autofit through the modification of the diffusion coefficients $\chi_{\perp,i}(r)$ and $\chi_{\perp,e}(r)$. Therefore, the steady-state value of this power is implicitly given by the reference profiles of n_e, T_e and T_i that the user imposes at the start of the simulation. However, some doubts exist in the location of the separatrix. Indeed, the magnetic equilibrium reconstruction which provides its position is subjected to errors due to the required magnetic data and the assumptions made in the reconstruction. For example, an uncertainty in the separatrix position of ± 5 mm has been estimated in the DIII-D tokamak [113]. Such spacial uncertainty, in a region of huge gradient of the plasma quantities, can lead to a substantial error on the resulting power flowing in the SOL. However, this uncertainty introduces a new degree of freedom for the simulation: in autofit mode, a feedback loop on the separatrix position is available to constrain the power flowing from the core to the simulated domain. In reality, its position is imposed by the magnetic equilibrium which is fixed in the simulation. Thus, the feedback loop acts on the position of the reference profiles with respect to the separatrix to control the value of $P^{\{D^+ + e^-\}}_{CORE \to EDGE}$. The users has to define a reference value for this power, called P_{in} in the following, that SolEdge2D-EIRENE will automatically achieve.

This reference value is given by the equation 1 of the system 3.4. To calculate it for the H-mode phase simulation, the experimental input powers are considered (cf. section 1) and the radiative energy sink in the core, $S^{E,rad}_{CORE}$, has been estimated by bolometry measurements ($S^{E,rad}_{CORE} = 3.5$ MW). An extra radiative power ($S^{imp,rad}_{EDGE+SOL} = 1.5$ MW) has also been added to take into account the experimental impurity radiation in the SOL (as no impurities are considered in the simulation).

$$\begin{aligned} P_{in} &= P_{NBI} + P_{ICRH} + P_{Ohm} - S^{E,rad}_{CORE} - S^{imp,rad}_{EDGE+SOL} \\ P_{in} &= 12.5 + 2 + 0.5 - 3.5 - 1.5 = 10 \text{ MW} \end{aligned} \tag{3.6}$$

Now that the value of P_{in} is defined for the H-mode phase simulation, the power balance of the simulated domain (equation 2 in the system 3.4) has to be monitored. The time evolution of the different terms of this equation are displayed in figure 3.11. The value of P_{in} is also plotted in red dotted line. For $t \geq 200$ ms, $P^{\{D^+ + e^-\}}_{CORE \rightarrow EDGE}$ has converged to the reference P_{in} value. One can also note that the value of the net energy source in the simulated domain, $S^{E,\{D^+ + e^-\}}_{EDGE+SOL}$, is positive and reach a constant value of ~ 1 MW during all the simulation. This additional positive energy source indicates that the energy recycling at the W divertor targets (due to high plasma temperature) supersedes the radiative source in the EDGE+SOL domain. The difference between the LHS and the RHS of equation 3.4 is also displayed in yellow. As for the particle balance, after $t \geq$ 500 ms, this difference tends to zero and the simulation can finally be considered as converged.

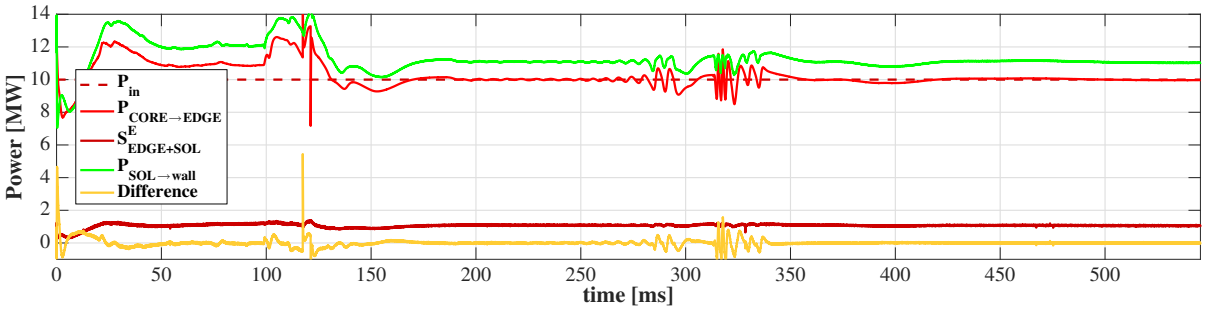

Figure 3.11: Illustration of the power balance of the system {D ions + electrons} in the simulated domain (EDGE+SOL) for the SolEdge2D-EIRENE simulation of the H-mode phase. The superscript $\{D^+ + e^-\}$ is omitted in the different quantities in the legend.

It has to be pointed out that the oscillations that are present in figures 3.10 and 3.11 from 200 ms to 350 ms are numerical oscillations due to the autofit procedure. Indeed, the autofit feedback loop is controlled through different gains that are manually set by the user. These oscillations are due to an attempt to speed up the convergence of the simulation by increasing the different gains of the autofit.
The steady-state OMP density and temperature profiles obtained with SolEdge2D-EIRENE are displayed in figures 3.12 and 3.13 respectively. As one can see in figure 3.12.b, the reference profiles were all shifted by 1.6 mm in the core direction which indicates that

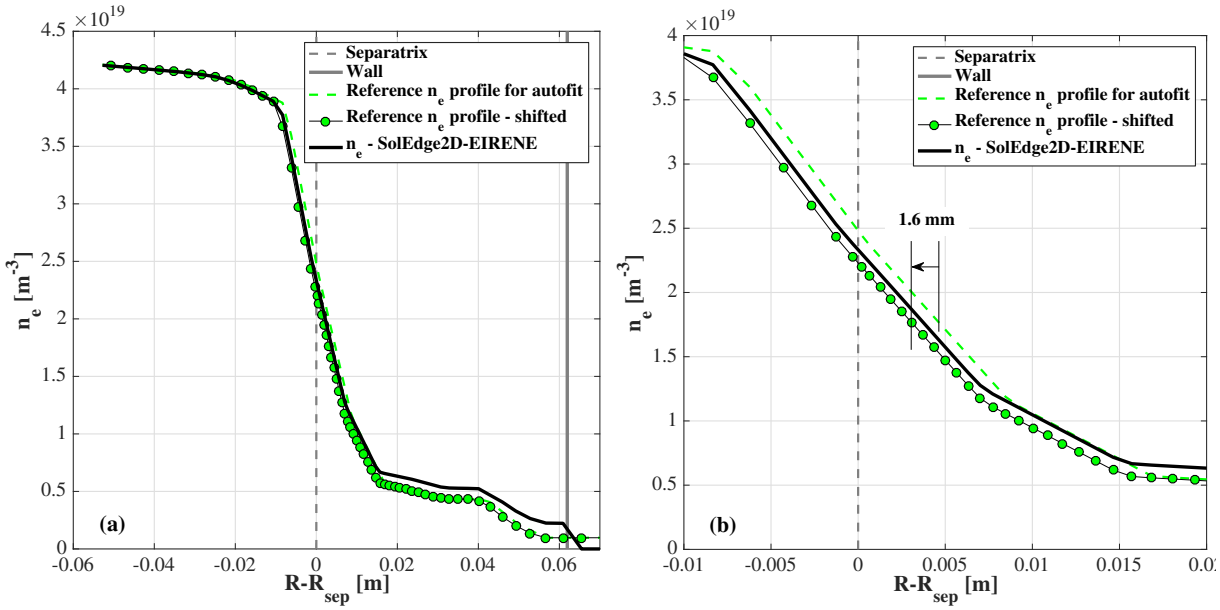

Figure 3.12: SolEdge2D-EIRENE steady-state outer midplane profiles of the electronic density n_e (black solid line) in the full simulated domain (a) and zoomed in the separatrix vicinity (b) for the H-mode phase simulation. The shifted autofit reference profiles (green circle markers) and the initial autofit profiles (green dashed line) are also plotted.

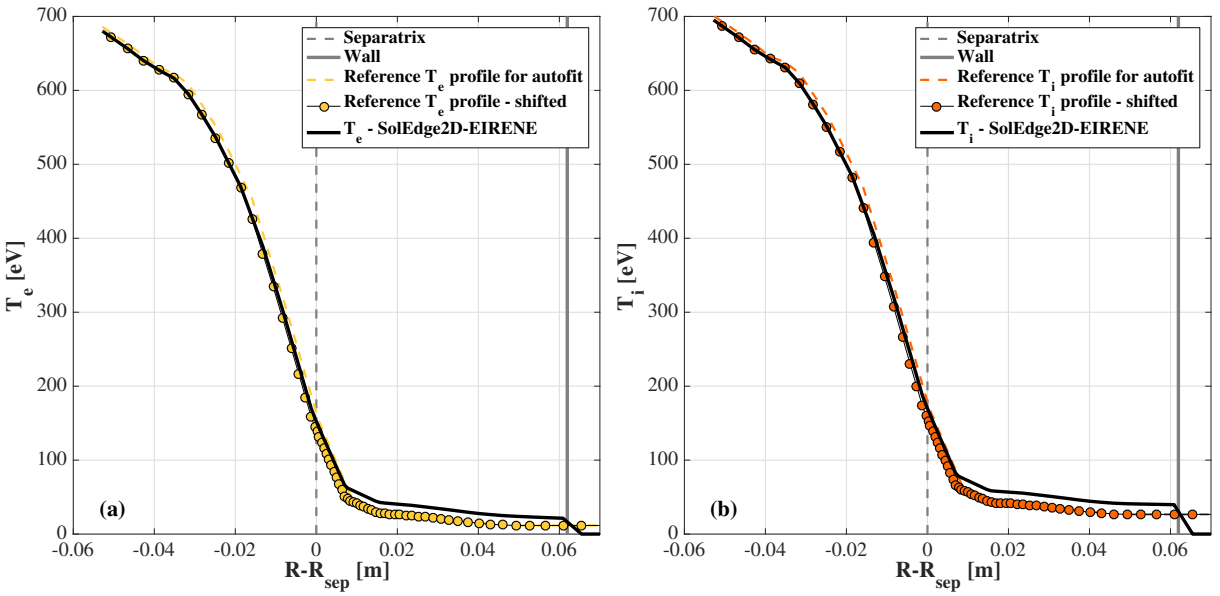

Figure 3.13: SolEdge2D-EIRENE steady-state outer midplane profiles (black solid lines) of (a) the electronic temperature T_e and (b) the ion temperature T_i for the H-mode phase simulation. The respective shifted autofit reference profiles (circle markers) and initial autofit profiles (dashed line) are also plotted.

the initial separatrix position overestimated the power flowing in the SOL. The agreement between the reference profiles and the obtained profiles are correct except in the far-SOL where the simulation overestimates the density and both temperatures. It was

not possible to monitor the simulation to ensure a better agreement with the reference profiles. The reason for such discrepancies is still unclear. Among the possible reasons, one could cite the overestimation of the power P_{in} due to uncertainties in the coupling of the different injected powers with the plasma or due to an underestimation of the core radiative source $S_{EDGE+SOL}^{E,\{D^+ + e^-\}}$. An inaccurate wall material distribution (as pointed out in the subsection 2.1) could also play a role in this phenomenon as it is known that a low-Z material (like beryllium or carbon) in the divertor induces a colder SOL (due to a lower energy recycling source in the SOL [114]). Further simulations would have been necessary to isolate the real cause of these discrepancies.

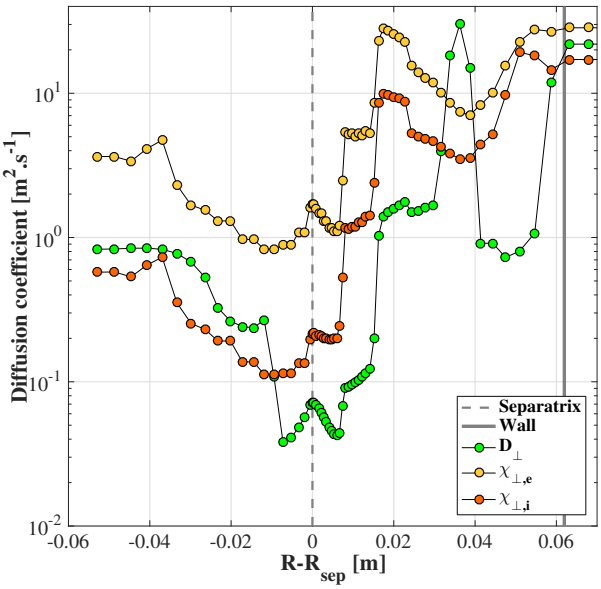

Figure 3.14: Steady-state outer midplane profiles of the perpendicular anomalous diffusion coefficients $D_\perp$, $\chi_{\perp,e}$ and $\chi_{\perp,i}$ given by the autofit procedure for the H-mode phase.

Eventually, the steady-state OMP profiles of the diffusion coefficients $D_\perp$, $\chi_{\perp,e}$ and $\chi_{\perp,i}$ for the H-mode phase are displayed in figure 3.14. A drop of the three diffusion coefficients in the pedestal region can be observed which indicates the presence of a transport barrier in the vicinity of the separatrix. Moreover, a drop in the density diffusion coefficient can be observed in the far-SOL (for $R - R_{sep} \geq 0.4$ m) which is probably linked to the presence of a density shoulder in the far-SOL [115].

2.3 Analysis of the SolEdge2D-EIRENE steady-state plasma.

In this subsection, the steady-state plasma obtained for the SolEdge2D-EIRENE simulation of the H-mode phase will be studied.
In figure 3.15.a, the 2D poloidal map of the ion density n_i (equal to the electron density due to the electro-neutrality assumption used in SolEdge2D) is displayed. A zoom in the divertor is shown in the lower part of the figure. First, one can notice that the edge region is denser than the divertor region. Morevover, the peak densities in the divertor (4.1×10^{19} m^{-3} in the inner divertor, 3.4×10^{19} m^{-3} in the outer divertor) are slightly

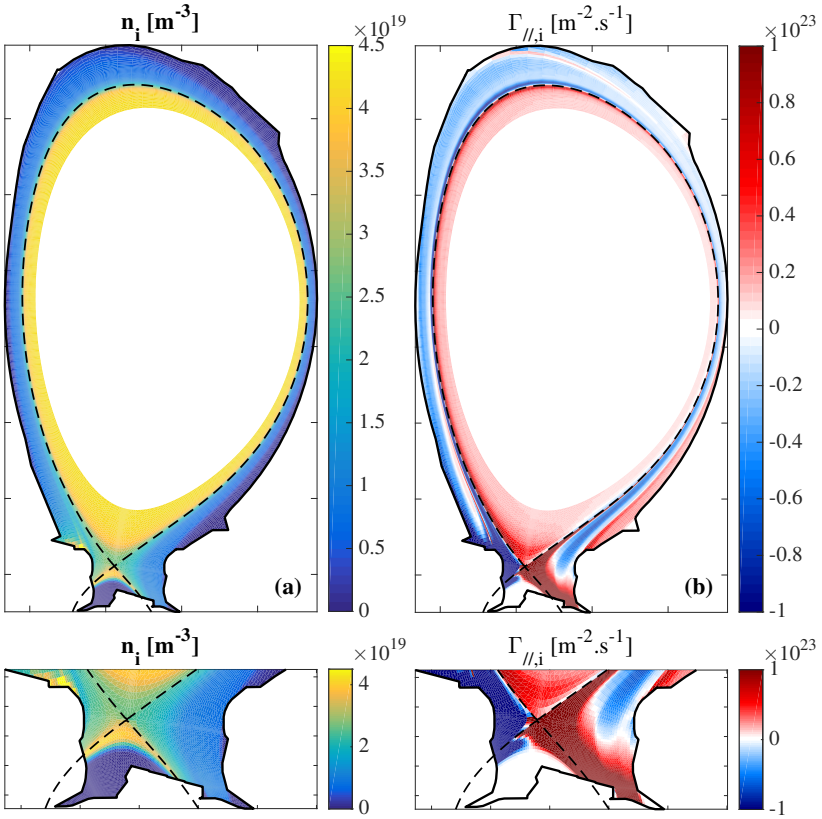

Figure 3.15: SolEdge2D-EIRENE 2D maps of the ion density n_i (a) and of the parallel ion flux density $\Gamma_{\parallel,i}$ (b) for the H-mode phase. The upper figures represent the full JET poloidal cross-section while the lower figures represent a zoom in the divertor region.

higher than at the OMP separatrix position (2.3×10^{19} m^{-3}). This indicates that the divertor is in the transition between the so-called *sheath-limited regime* and *high-recycling regime* of heat transport [116] in the vicinity of the two strike-points (which is confirmed by parallel profile of density and electron temperature). An overdense region can be seen in the inner side of the divertor, more precisely in the top part of tile 1. Such high density indicates a high plasma recycling region. Two reasons might explain such phenomenon. First the magnetic topology, with the magnetic flux surfaces being almost normal to the wall surface in this region (cf. lower part of figure 3.3.b), can generate a flux of recycled neutrals on the front of the plasma flux and therefore an ionisation close to the plasma impact point. The second explanation could be the material at the surface of the wall in this region. Indeed, the high density region extends in front of the Be co-deposit defined as input in EIRENE (cf. figure 3.8.a). Therefore the recycling in this region is dominated by D_2 molecules with very low energy, which are likely to ionise in front of the wall. The 2D poloidal map of the parallel ion flux density $\Gamma_{\parallel,i}$ is plotted in figure 3.15.b. This figure highlights the bipolarity of the particle flux in the SOL due to the Debye sheath at the wall surface. A front of negative flux can be seen close to the tile 8 in the outer divertor (cf. lower part of figure 3.15.b) where the magnetic flux surfaces are almost tangential to the wall surface.

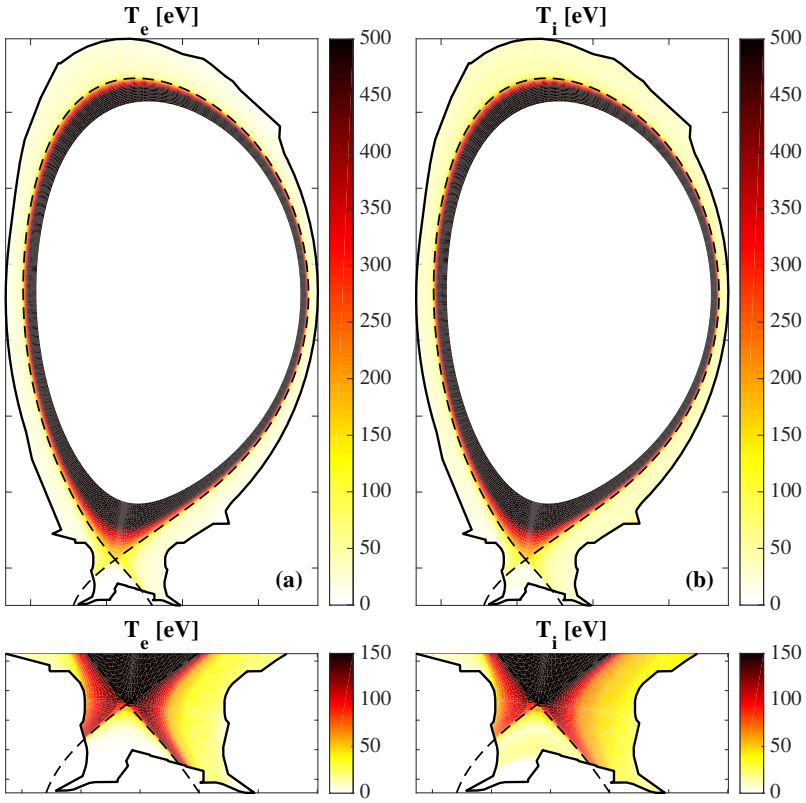

Figure 3.16: SolEdge2D-EIRENE 2D maps of the electronic temperature T_e (a) and of the ionic temperature T_i (b) for the H-mode phase. The upper figures represent the full JET poloidal cross-section while the lower figures represent a zoom in the divertor region.

The 2D maps of the electronic temperature and of the ionic temperatures (T_e and T_i respectively) are shown in figure 3.16. From the upper figures, one can note that both temperatures are lower than 200 eV in all the SOL. Furthermore, in both lower figures which exhibit a zoom in the divertor, T_e and T_i remain high up to both targets. The peak values of T_e and T_i in the inner divertor target are respectively 111 and 74 eV, while in the outer divertor targets the peak values are respectively 121 and 81 eV. From figure 3.13, the OMP separatrix values of T_e and T_i are 150 eV and 170 eV respectively. Therefore, T_e moderately decreases along the field lines while T_i reduces by a factor of ~ 2. Still the target temperatures are very high and the divertor operates in a transitional regime of heat transport. Such high temperatures seem to be inherent to divertor with tungsten targets [114] as such high-Z material induces an extra energy source in the SOL due to energy recycling at the targets. This effect is present in the H-mode phase simulation as a net energy source term for ions and electrons $S^{E,\{D^+ + e^-\}}_{EDGE+SOL}$ is observed (~ 1 MW, cf. figure 3.11). An inaccurate wall material distribution in the divertor, as pointed out in subsection 2.1, is probably responsible for such high temperatures. As a consequence, due to acceleration in the sheath, very high ion impact energies can be expected in the vicinity of the strike-points.
Finally, the 2D maps of the total neutral pressure P_{tot} and of the positive ion source

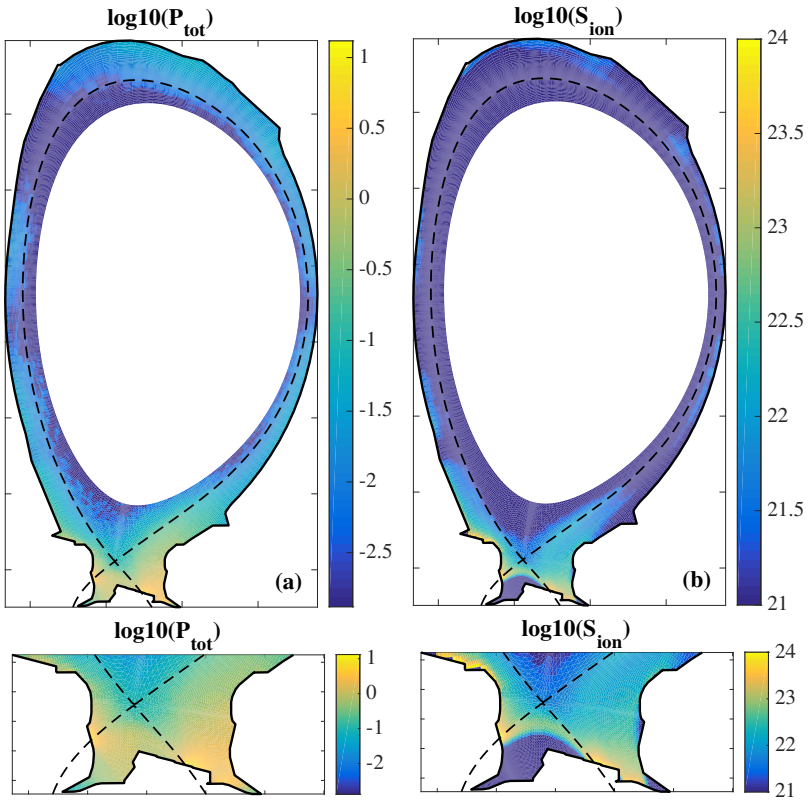

Figure 3.17: SolEdge2D-EIRENE 2D maps of the total pressure P_{tot} [Pa] (a) and of the ionisation source S_{ion} [$m^{-3}.s^{-1}$] (b) for the H-mode phase. Both quantities are plotted in logarithmic scale. The upper figures represent the full JET poloidal cross-section while the lower figures represent a zoom in the divertor region.

(from ionisation) S_{ion} are plotted in figure 3.17. Of course, the D neutrals are mainly located in the divertor due to the diverted magnetic topology. P_{tot} reaches a value of up to 10 Pa at both strike-points. It may be observed that the region of high pressure is more extended in the outer divertor than in the inner divertor. This is due the outer horizontal target which entails a more opened SOL configuration than the inner vertical target. It results a lower plasma temperature in the outer far-SOL (cf. figure 3.16). Finally, the ionisation source is mainly located in the divertor. A strong recycling can be observed in the vicinity of both strike-points but also on top of the tile 1 and of the HFGC tile. The latter one entails the presence of the high density region stated above.

2.4 Plasma conditions at the targets.

The main interest of the SolEdge2D-EIRENE backgrounds for the wall dynamics simulation is the assessment of the plasma conditions at the wall. In order to verify the consistency of these conditions, the simulation results have to be confronted to experimental measurements. The main diagnostics to quantify the plasma conditions at the wall are the Langmuir Probes (LP). Such probes are conducting tips electrically insulated from the wall. A voltage is applied to these probes to attract either the electrons

(positive voltage) or the ions (negative voltage) [117]. The probe voltage (V) is swept and the current flowing in the probe (I) is recorded as a function of V. Both local n_e and T_e can be determine from this $I-V$ characteristic [118]. Moreover, when the bias voltage on the probe is sufficiently negative w.r.t. the plasma potential, the electron are fully repealed and the probe collects the so-called *ion saturation current* I_{sat}. The ion saturation current density, J_{sat}, can be obtained by dividing I_{sat} by the probe collecting area. According to standard sheath theory [116], J_{sat} is proportional to the ion parallel flux density $\Gamma_{\parallel,i}$ at the sheath entrance:

$$J_{sat} = e\Gamma_{\parallel,i} = en_e c_s \tag{3.7}$$

where e is the elementary charge ($e = 1.6022 \times 10^{19}$ C) and c_s is the ion sound speed defined in subsection 2.1. Due to its thickness, no ion sources are present in the sheath and the incident ion flux density on the wall, $\Gamma_{inc,i}$, can be obtained by projection of $\Gamma_{\parallel,i}$:

$$\Gamma_{inc,i} = \sin(\alpha) J_{sat}/e \tag{3.8}$$

where α is the angle between the magnetic field line and the wall surface. Therefore, the J_{sat} measurement is a good indicator of the ion flux density interacting with the wall material.

The JET tokamak is equipped with LPs both in the divertor and in the first-wall limiters. However, the first-wall probes were not operational during #JPN89044 so that only the divertor probe measurements will be presented. The JET divertor is equipped with 3 LP arrays situated at different toroidal locations. In the JET nomenclature, these locations are referred to as *divertor modules* A, B and C. Each array contains 36 LPs. Due to technical issue, some of these LPs are faulty. The active LPs for each module during #JPN89044 are displayed in green in figure 3.18.(a-c). Moreover, during this discharge, the LP voltage sweeping to obtain the $I-V$ characteristic was too fast to accurately estimate n_e and T_e. Still the J_{sat} measurements are provided. J_{sat} obtained with SolEdge2D-EIRENE can be confronted to these experimental measurements.

The results for the three divertor modules are displayed in figure 3.18(d-f). The experimental J_{sat} measurements during this phase are plotted using the boxplot representation defined in subsection 2.1. Both experimental and simulated profiles are plotted versus the s curvilinear wall coordinate defined in figure 3.8.b. At first sight, the agreement between the simulated and the experimental J_{sat} is rather good in the outer divertor. In the inner divertor, J_{sat} is underestimated in the strike-point vicinity while a good estimation can be noticed in the far-SOL. However, a clear shift between the experimental data and the simulation results is observed. The inner and outer experimental peaks are closer than the simulated J_{sat} peaks: the strike-points were probably closer in the experiment.

Indeed, one must be aware that the so-called intrashot EFIT reconstruction was used in the simulation. This magnetic reconstruction is based on magnetic probe measurements only and is known to present inaccuracies in the divertor region. A new equilibrium reconstruction has been performed with experimental data constrains [119]. This reconstruction method exhibits a better estimation of the strike-points location, most of the

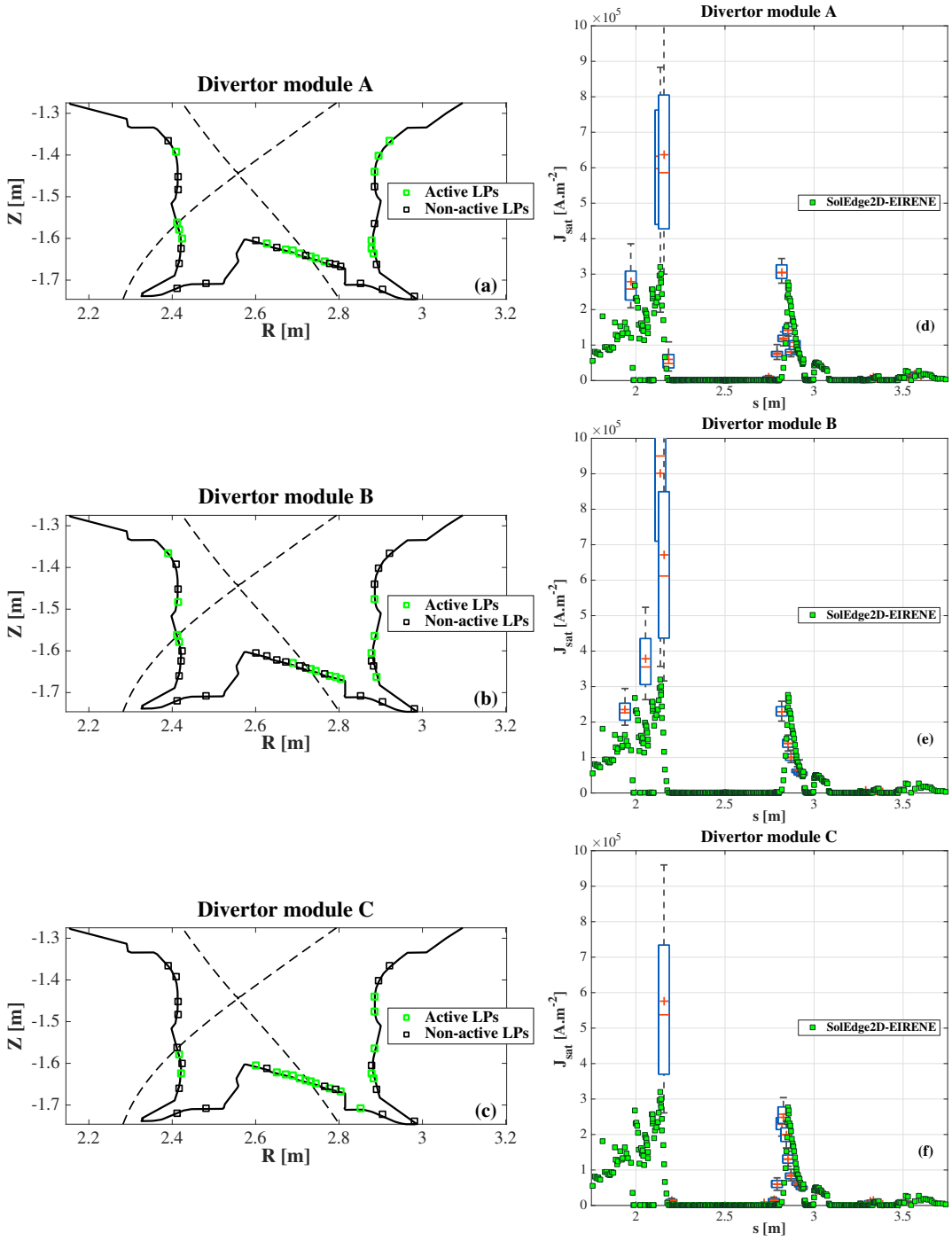

Figure 3.18: Active (green squares) and non-active (black squares) Langmuir probes (LP) in the three divertor modules A (figure a), B (figure b) and C (figure c) during #JPN89044. The corresponding saturation current density (J_{sat}) measurements for the H-mode phase are displayed with respect to the wall LP coordinates using the boxplot representation (d-f). The SolEdge2D-EIRENE steady-state wall profiles of J_{sat} for the H-mode phase is also displayed (green filled square in figures d-e). The reader can refer to figure 3.8.b for the definition of s, the curvilinear coordinate along the wall.

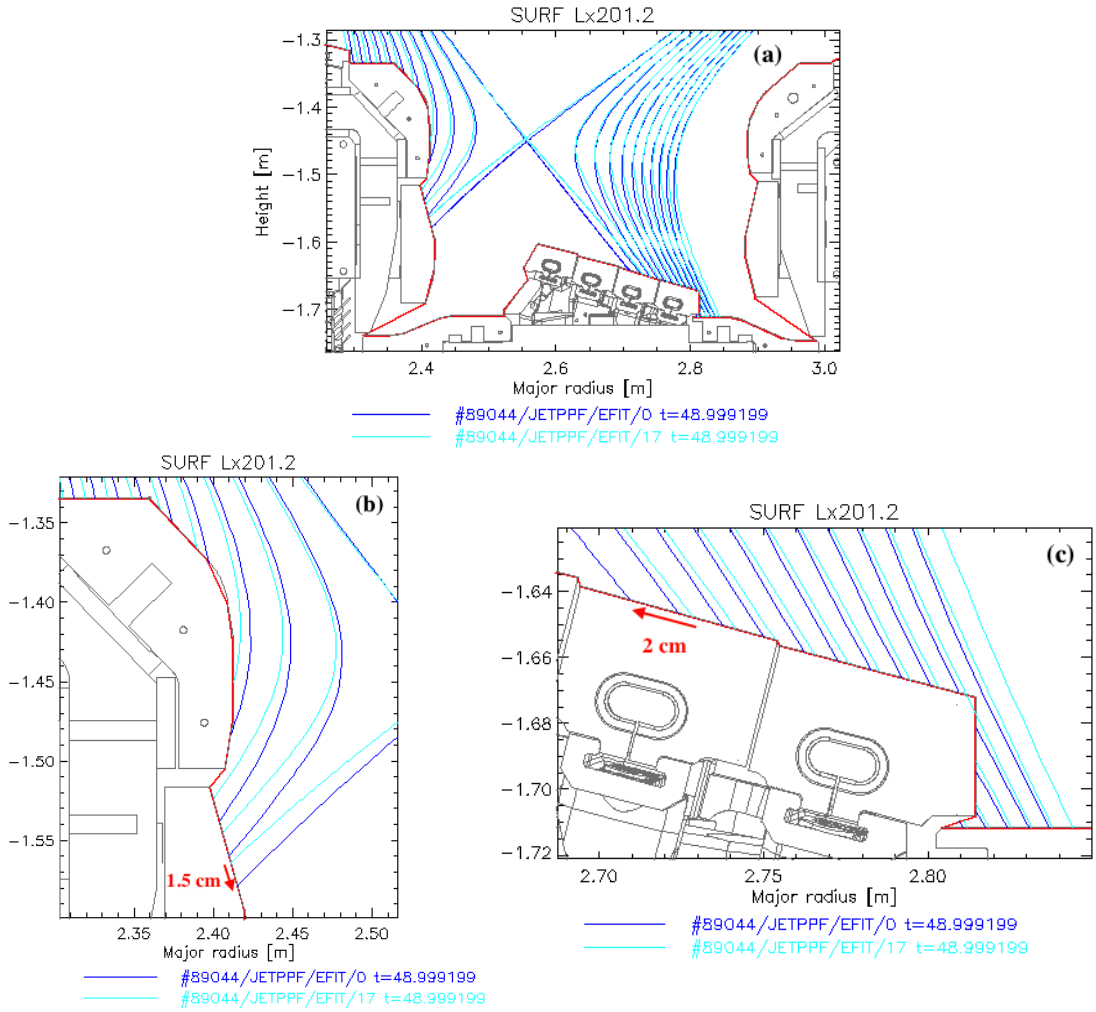

Figure 3.19: EFIT reconstructions of the #JPN89044 magnetic equilibrium during the H-mode phase: in cyan the equilibrium calculated with magnetic probe measurements only (the one considered in the SolEdge2D-EIRENE simulation) and in blue the equilibrium calculated using experimental data constrains. The whole divertor region is plotted in figure (a). A zoom in the inner target and in the outer target are displayed in figures (b) and (c) respectively.

time in agreement with infrared camera measurements. This new equilibrium is plotted in blue in figure 3.19. The magnetic equilibrium used in the simulation is also displayed in cyan. The new equilibrium presents closer strike-points (cf. figure 3.19.a) while no impact can be seen in the core region. This confirms the first impression seen in figures 3.18.(d-f). The inner strike-point is shifted by 1.5 cm (cf. figure 3.19.b) while the outer strike-point is shifted by 2 cm (cf. figure 3.19.c). Unfortunately, SolEdge2D-EIRENE simulations of the JET tokamak are time-demanding and it was not possible to relaunch a simulation with the more accurate magnetic field mapping.
However, as a first approximation, the LPs location can be shifted to allow a direct confrontation between the simulation and the experiment. The result of such shift is presented in figure 3.20 where the inner target J_{sat} profile (left figures) and the outer target

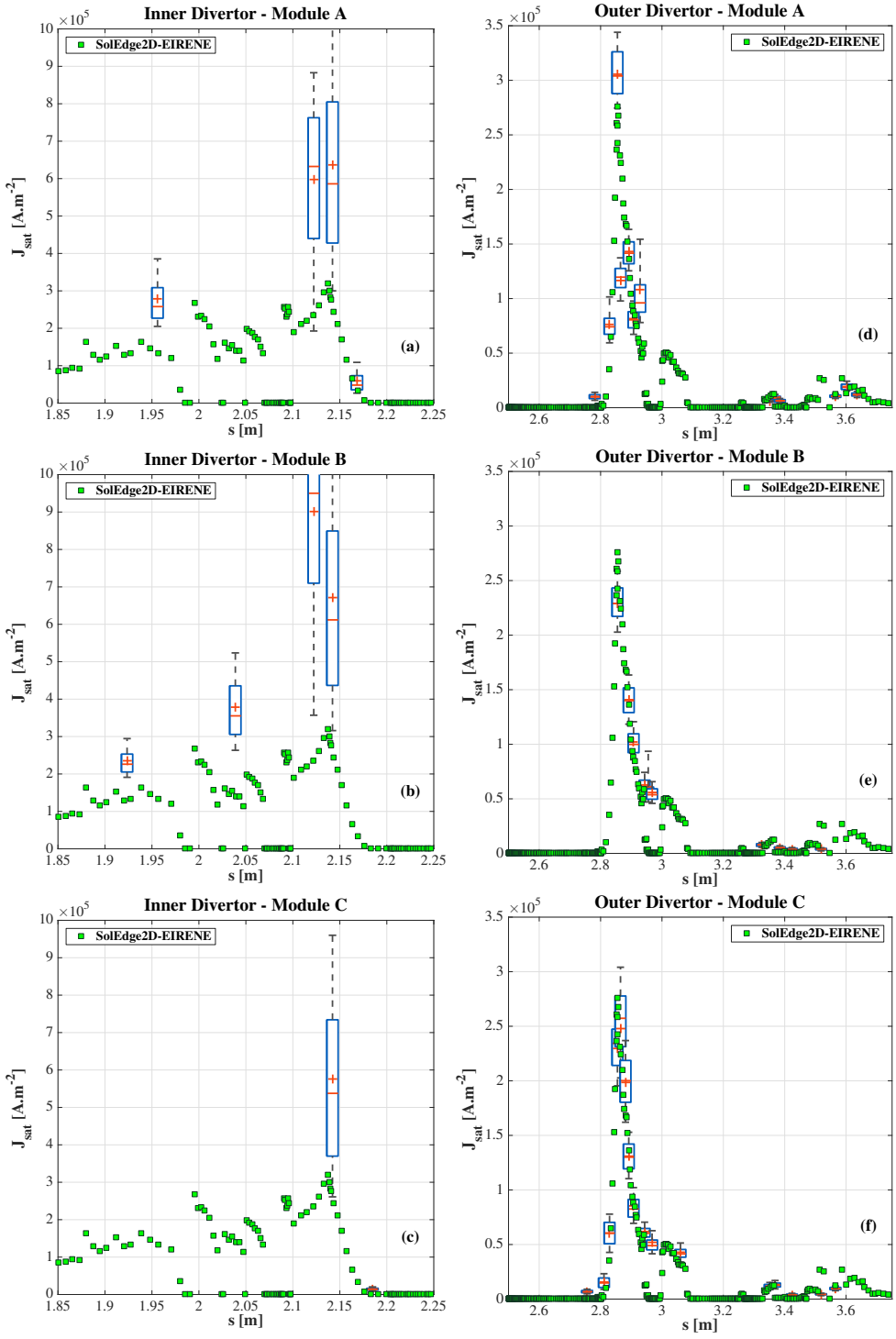

Figure 3.20: Inner target profile (left figures) and outer target profile (right figures) of J_{sat} for the H-mode phase (regular scale). The LP measurements are displayed using the boxplot representation while the simulated J_{sat} profile is displayed with green filled squares. The experimental data are shifted by 1.5 cm for the inner target and by 3.7 cm for the outer target.

J_{sat} profile (right figures) are plotted for the different divertor modules. The locations of the inner LPs are shifted by 1.5 cm (the strike-point shift observed in figure 3.19.b). An extra shift was considered for the outer LPs (overall shift of 3.7 cm) in order to align the experimental and the simulated J_{sat} peaks. Again, in the outer target, an excellent agreement between the simulation and the experiment is observed. If one compares the peaks for the divertor module A (figure 3.20.d), SolEdge2D-EIRENE underestimates the J_{sat} peak by 8 % (2.76×10^5 A.m^{-2} for the simulation, 3.0×10^5 A.m^{-2} for the LP). However, a slight toroidal asymmetry can be seen in the experimental measurements, with lower J_{sat} peaks in the divertor modules B (2.29×10^5 A.m^{-2}) and C (2.48×10^5 A.m^{-2}, shifted by 2 cm w.r.t. the peaks in modules A and B). In the close-SOL (from the J_{sat} peak to $s \approx 3.10$ m), the simulated J_{sat} matches the measured J_{sat} in the three modules: the simulation catches the proper decrease of ion flux density on the target. The same observation can be done in the PFR. However, the results in the inner target are not satisfactory. Overall, the simulation underestimates J_{sat} by ~ 50 % in all the SOL. One can observe a huge scattering of the experimental measurements in the strike-point vicinity. The sweeping of the strike-point on the LPs due to magnetic perturbations can explain such type of scattered measurements. Moreover, the plasma at the inner target is probably very disturbed. The ELMs, which are known to induce an enhanced recycling activity in the inner divertor as seen in chapter 1 section 5, might play a role in this bad agreement. Eventually, the questionable choice of W in this region of the divertor (cf. subsection 2.1) could also be responsible for this disagreement. Indeed, with a Be target, the recycling would have been dominated by D_2 desorption, inducing a stronger ionisation source in front of the target surface.
In figure 3.21, the same plots are displayed in logarithmic scale to highlight the PFR and the far-SOL measurements. In the outer divertor, the simulated J_{sat} is in the same order of magnitude as the experimental one in both region. However, its decrease is stronger in the PFR than in the experiment (cf. figure 3.21 for 2.75 m $< s <$ 2.85 m). In the outer vertical tiles, the two magnetic reconstructions are overlapped and the shift of the experimental data is not justified. Without this shift, the agreement is around 50 % on tiles 7 and 8. The decrease of J_{sat} is also caught in the shadowed region of tiles 7 and 8 (for 3.3 m $< s <$ 3.6 m) but slightly overestimated (~ -60 %). These relative agreements must be put in perspective with the toroidal asymmetry of the LPs measurements, which exhibit a 50 % difference on tile 7 if one considers the J_{sat} probed in the divertor module A or in the module C. In the inner divertor, only two LPs are available in the PFR. One can note that the J_{sat} decrease is well matched close to the strike-point (cf. figure 3.21.a for 2.15 m $< s <$ 2.2 m) but not further away (cf. figure 3.21.c).
In conclusion, the SolEdge2D-EIRENE simulation for the H-mode phase exhibits a very good agreement with experimental measurements J_{sat} in all the outer divertor. The estimation is less accurate in the inner divertor. Therefore, one can globally rely on the estimation of the incident ion flux density on the outer divertor given by SolEdge2D-EIRENE.

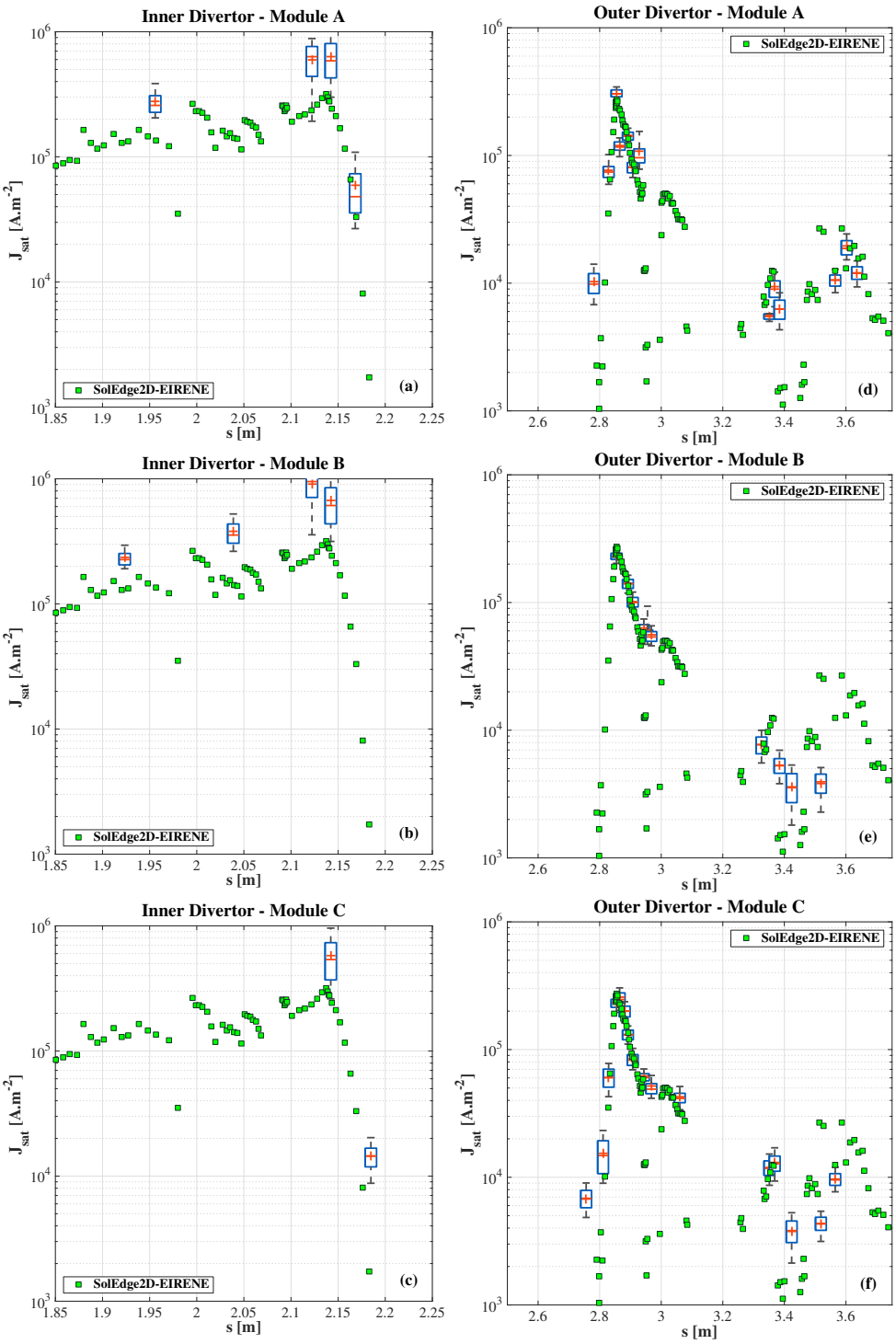

Figure 3.21: Inner target profile (left figures) and outer target profile (right figures) of J_{sat} for the H-mode phase (logarithmic scale). The LP measurements are displayed using the boxplot representation while the simulated J_{sat} profile is displayed with green filled squares. The experimental data are shifted by 1.5 cm for the inner target and by 3.7 cm for the outer target.

2.5 SolEdge2D-EIRENE results used as inputs in D-WEE.

Now one is interested in the SolEdge2D-EIRENE results which are required as inputs for D-WEE. These results will be plotted along the wall of the JET tokamak using the s curvilinear coordinate defined in figure 3.8.b.

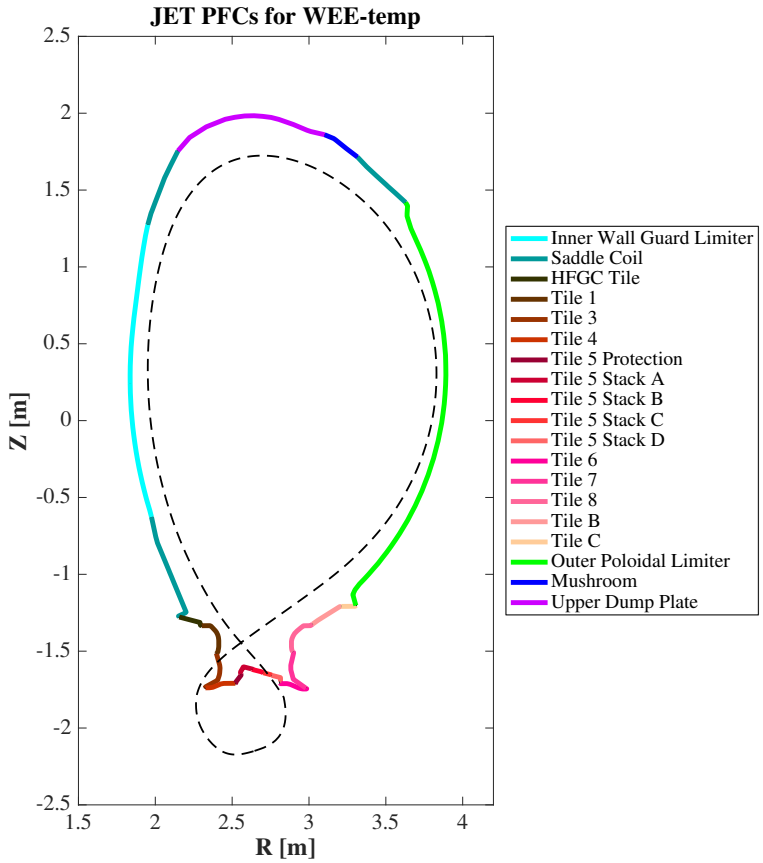

Figure 3.22: JET poloidal cross-section with the different PFCs considered in the thermal model WEE-temp. These PFCs are indicated in all the figures presenting wall distribution along the JET wall of a given quantity. For the sake of clarity, the divertor will be indicated as a single zone in those figures. The divertor starts from the HFGC Tile up to the Tile C. Three zones are made with Saddle Coil PFCs. They will be referred to as *Inner Lower Protection*, *Outer Upper Protection* and *Inner Upper Protection*.

The results for the H-mode phase appear in figure 3.23. The different PFCs composing the JET wall are also indicated. The distribution of these PFCs on the wall is displayed in figure 3.22. Please note that the divertor PFCs are not indicated in figure 3.23 for the sake of clarity. The implanted ion flux density (Γ_{imp}^{i+}) presents two peaks in the strike-point locations ($\sim 2 \times 10^{22}$ m^{-2}.s^{-1}) with high impact energy (~ 600 eV) due to the high plasma temperatures found at both strike-points. An ion flux density plateau with value around 10^{22} m^{-2}.s^{-1} is also present on top of tile 1 and on the HFGC tile where the high plasma density region has been observed. In the outer vertical targets (for 3.2 m $\leq s \leq$ 4 m, from tile 6 to tile C), Γ_{imp}^{i+} ranges between 10^{20} and 10^{21} m^{-2}.s^{-1} with impact energy around 150 eV. For atoms, Γ_{imp}^{at} ranges between 10^{20} and 10^{21} m^{-2}.s^{-1} in

all the divertor, with some excursion above 10^{21} m^{-2}.s^{-1} on top of tile 1, on the HFCG tile and on tile 8. Their impact energy remains below 100 eV with excursions up to 200 eV on tile 1 and tile 8. In the first-wall, Γ_{imp}^{i+} remains globally between 10^{20} and 10^{21} m^{-2}.s^{-1} while the range of Γ_{imp}^{at} is one order of magnitude lower. The impact energy stays between 100 and 200 eV for both type of particles. One can note a higher atom flux density (between 10^{20} and 10^{21} m^{-2}.s^{-1}) in the inner lower protection with a much lower impact energy (between 10 and 30 eV). The mean angle of incidence is also plotted in figure 3.23.c. It remains between 60° and 70° for the ions in all the wall, while its value is around 40° for the atoms. The value of this mean angle for ions is explained by the sheath deviation effect for ions while its value for the atoms is explained by their deconfined nature which entails a random angle of impact on the wall surface. Eventually, the energy flux density remains below 0.1 MW.m^{-2} in all the first-wall, the outer vertical target and the PFR. One can note a stronger heat flux density above 0.2 MW.m^{-2} on tile 1, HFGC tile and tile 6, with excursions in the strike-points vicinity up to 4.2 MW.m^{-2} and 5.9 MW.m^{-2} at the inner and outer strike-points respectively.

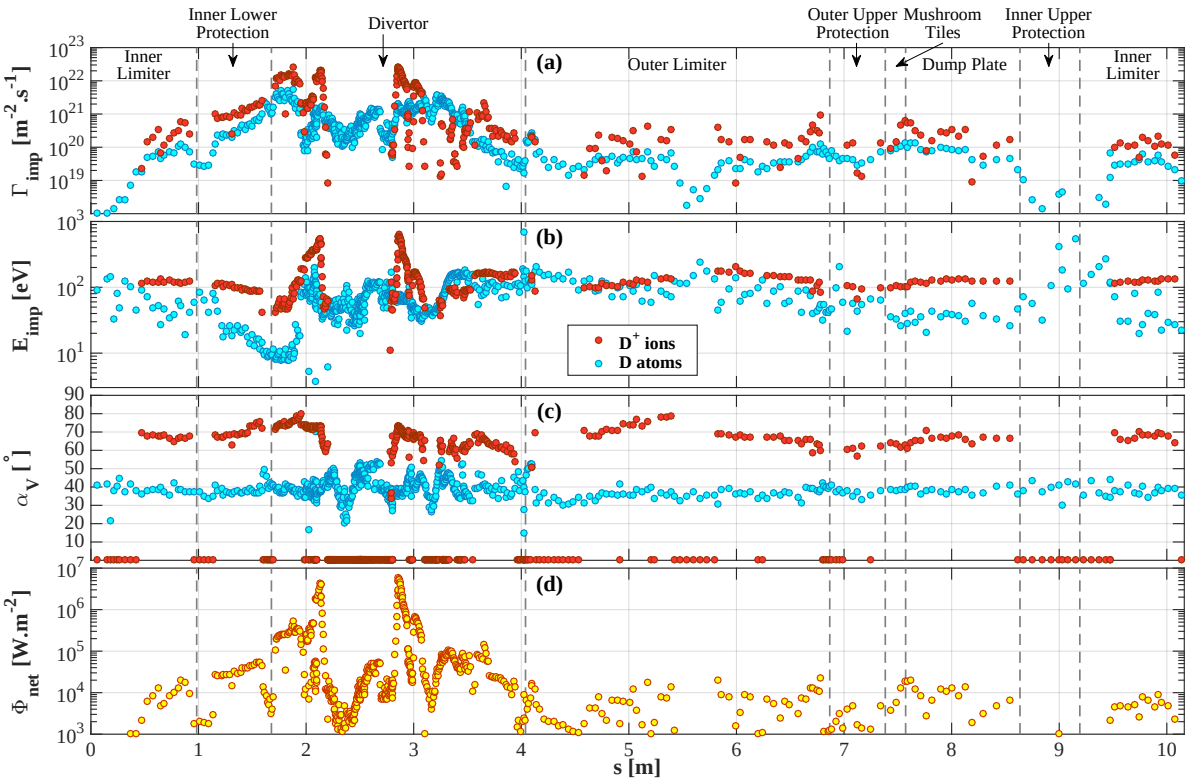

Figure 3.23: SolEdge2D-EIRENE simulation results for plasma phase 1 (H-mode): distribution along the wall of (a) the implanted particle flux density Γ_{imp}, of (b) the impact energy E_{imp}, of (c) the mean angle of incidence α_V and of (d) the net energy flux density Φ_{net}. These quantities are required as inputs for the D-WEE module. The first three quantities are plotted for both ions and atoms. The definition of the s curvilinear coordinate can be found in figure 3.8.b.

3 Simulation of the L-mode plasma (phase 2) with SolEdge2D-EIRENE.

This section will focus on the simulation of the #JPN89044 plasma phase 2 (L-mode) identified in section 1. The simulation description will be more concise than for the H-mode phase simulation as both cases share the same modelling methodology.

3.1 Definition of the inputs needed for the SolEdge2D-EIRENE simulation.

The SolEdge2D-EIRENE inputs in both phases are similar for the magnetic equilibrium (and therefore for the grid), for the wall materials, for the pumping region and for the boundary conditions (cf. subsection 2.1). The L-mode inputs differ for the gas puff locations and injection rates. Again, the locations respect the experimental puff locations of the considered discharge (cf. section 1). The particles are injected from the OMP ($Q_{inj} = 4.1 \times 10^{21}$ D.s^{-1} from puff number 2 in figure 3.8.b) and from the top of the machine ($Q_{inj} = 6.9 \times 10^{21}$ D.s^{-1} from puff number 3). No NBI fuelling is considered as the NBI heating is switch off during the L-mode phase.

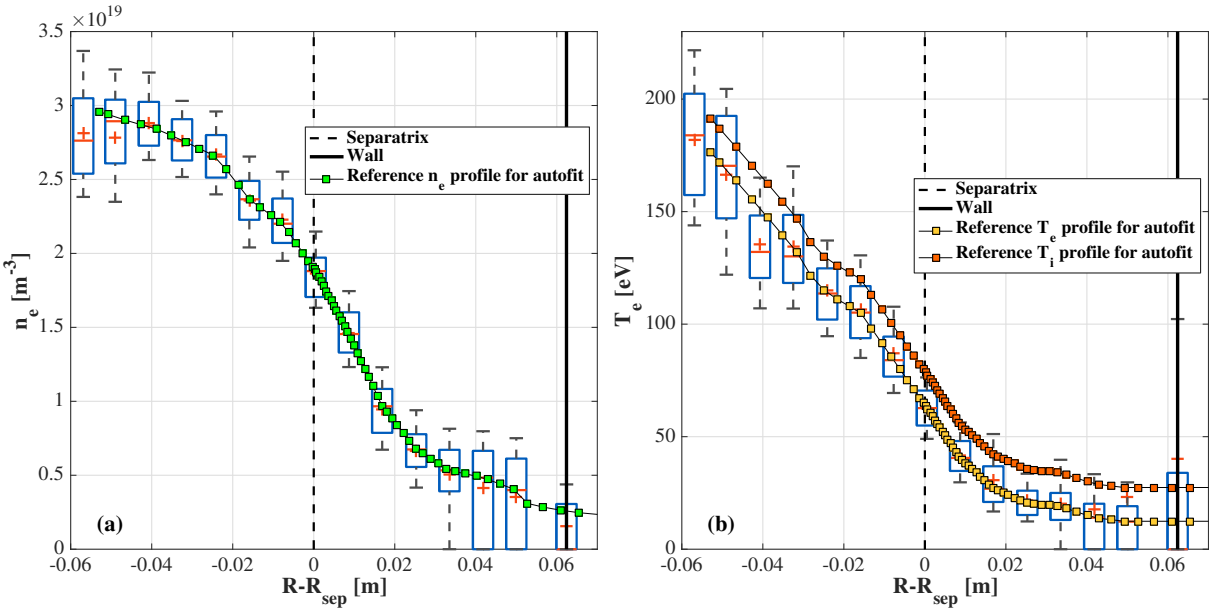

Figure 3.24: Autofit reference profiles of (a) the electron density n_e and (b) the electronic temperature T_e for the SolEdge2D-EIRENE simulation of the L-mode phase. The boxplots represent the data samples measured in the time period of the L-mode phase with HRTS. Due to the lack of measurement of the ionic temperature T_i in the SOL, an offset of 15 eV is assumed in the reference T_i profile w.r.t. the reference T_e profile.

Furthermore, the autofit reference profiles for n_e, T_e and T_i for the L-mode phase simulation are displayed in figure 3.24. The L-mode phase HRTS measurements of n_e and T_e in the zone of interest are also displayed using the boxplots. The pedestal and SOL

data samples seem to be more symmetric than in the H-mode phase: the samples appear to be normally distributed. The far-SOL measurements are more scattered and one can question the reliability of these measurements. The reference profiles for n_e and T_e are defined with the methodology defined in subsection 2.1. As for the H-mode phase, an offset of 15 eV is assumed for the T_i profile w.r.t. the reference T_e profile (cf. figure 3.24.b).

3.2 Flux balances and convergence of the simulation to a stationary plasma.

The L-mode simulation has to be monitored to ensure a correct steady-state plasma representative of the experimental one. The steady-state criterion for the flux balance (system 3.1) also apply to this simulation. Once again, the pumping flux $Q_{pump,tot}$ has to compensate the external fuelling rate through the pump albedo term. This time, only the total gas puff rate Q_{inj} (from all the operating GIMs) is considered as the NBI system is switched off. For the L-mode phase, this yields to:

$$Q_{pump,tot} = Q_{NBI} + Q_{inj} = 0 + (4.1 + 6.9) \times 10^{21} = 11 \times 10^{21} \text{ D.s}^{-1} \tag{3.9}$$

The time evolution of the different terms of equations 1, 2 and 3 of the system 3.1 are respectively displayed in figure 3.25 a, b and c for the case of the L-mode phase simulation. The difference between the LHS and RHS of the different equations are also displayed. As for the H-mode phase simulation, the pump albedo value is monitored to achieve the condition 3.9 on the pumping flux. One can observe in figure 3.25.a that for 300 ms $\leq t \leq$ 450 ms an inappropriate value of this albedo can lead to an overestimation of the pumping flux, which is compensated by a stronger ion flux at the core-edge interface $Q^{D^+}_{CORE\rightarrow EDGE}$. A final albedo value of 0.92 was necessary to achieve the condition 3.9, which is the case for $t \geq 500$ ms. Then $Q^{D^+}_{CORE\rightarrow EDGE}$ tends to balance the neutral flux reaching the core $Q^{D}_{EDGE\rightarrow CORE}$ (cf. figure 3.25.b). However, for $t \geq 500$ ms, the steady state in the core is not entirely achieved and the recycling source in the EDGE+SOL domain is still slightly increasing (cf. figure 3.25.c).
As for the H-mode simulation, the power balance 3.4 is also monitored and the input power in the simulated domain, $P^{\{D^+ + e^-\}}_{CORE\rightarrow EDGE}$, is set through the feedback loop on the position of the reference profiles w.r.t. the separatrix. The reference value for this feedback loop is again calculated thanks to the steady-state power balance of the core region (equation 1 in 3.4):

$$\begin{aligned} P_{in} &= P_{NBI} + P_{ICRH} + P_{Ohm} - S^{E,rad}_{CORE} \\ P_{in} &= 0 + 1.6 + 1.3 - 0.4 = 2.5 \text{ MW} \end{aligned} \tag{3.10}$$

where the experimental input powers defined in section 1 have been considered and the radiative energy sink in the core, $S^{E,rad}_{CORE}$, has been estimated by bolometry measurements. The power balance of the simulated domain (equation 2 in the system 3.4) can now be monitored for the L-mode phase case. The time evolution of the different terms of this equation are displayed in figure 3.26. The value of P_{in} is also plotted in red dotted line.

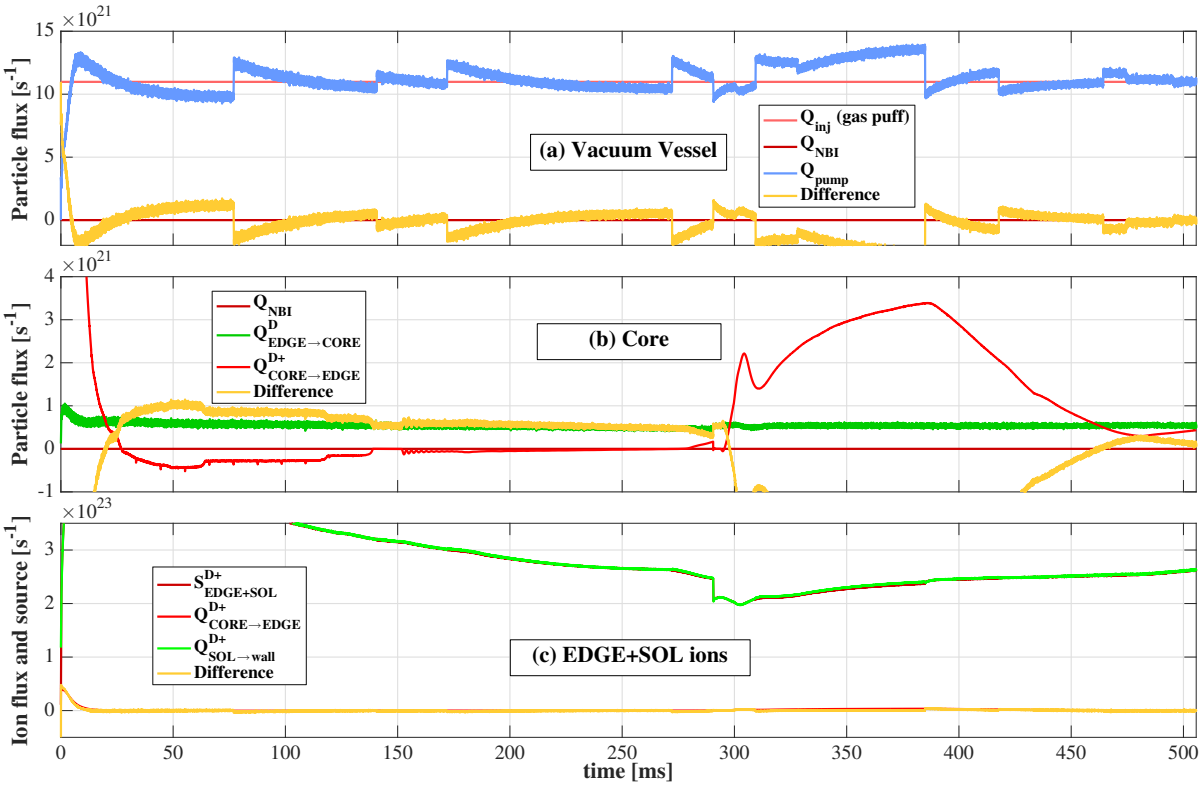

Figure 3.25: Illustration of the multi-system particle balances for the SolEdge2D-EIRENE simulation of the L-mode phase: (a) the overall tokamak vacuum vessel, (b) the core region (not simulated by SolEdge2D-EIRENE) and (c) the ions in the simulated domain (EDGE+SOL region). These flux balances are controlled during all the simulation to ensure that steady state is reached and that it is representative of the experimental steady state.

Unlike the H-mode phase, the value of the net energy source in the simulated domain, $S^{E,\{D^+ + e^-\}}_{EDGE+SOL}$, is negative and reaches a constant value of ~ -1.5 MW for $t \geq 450$ ms: the radiative source in the EDGE+SOL domain supersedes the energy recycling source. The difference between the LHS and the RHS of equation 2 in 3.4 is also displayed in yellow. For $t \geq 500$ ms, the difference between the RHS and the LHS tends to zero and the simulation can be considered as converged. However, one can observe that the $P^{\{D^+ + e^-\}}_{CORE \rightarrow EDGE}$ has still not converged to its reference value: the power flowing in the simulated domain is underestimated ($P^{\{D^+ + e^-\}}_{CORE \rightarrow EDGE} = 2.38$ MW). The feedback loop on the profiles position is still acting to increase this power. Such behaviour can also explain the rise of the particle recycling source seen in figure 3.25.a. In conclusion, the simulation cannot be considered fully converged. Due to the time duration of this simulation and the necessity to have a plasma background to perform the wall dynamics simulations, it was not possible to obtain a fully converged simulation for this phase.
The steady-state OMP density and temperature profiles obtained with SolEdge2D-EIRENE are displayed in figures 3.27 and 3.28 respectively. As one can see in figure 3.27.b, the

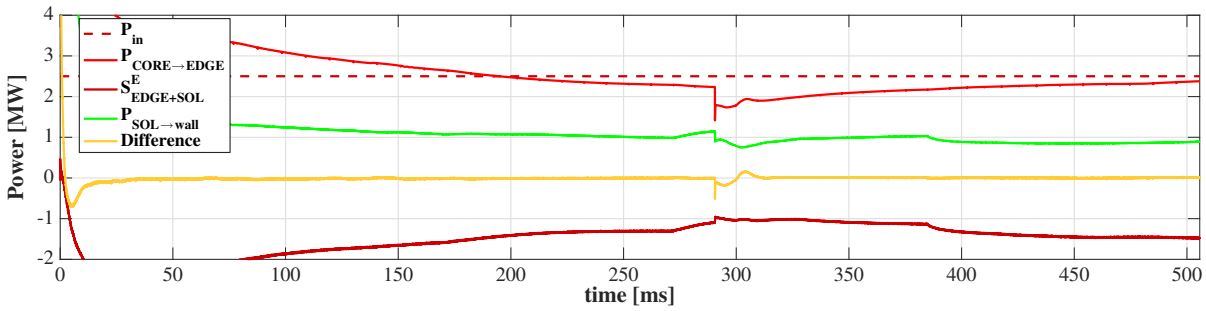

Figure 3.26: Illustration of the power balance of the system {D ions + electrons} in the simulated domain (EDGE+SOL) for the SolEdge2D-EIRENE simulation of the L-mode phase. The superscript $\{D^+ + e^-\}$ is omitted in the different quantities in the legend.

reference profiles were all shifted by 3.6 mm in the core direction which indicates that initially the separatrix position overestimated the power flowing in the SOL. As it was indicated previously, $P^{\{D^+ + e^-\}}_{CORE \rightarrow EDGE}$ is underestimated at the considered simulation time and this shift is likely to diminish. The obtained profiles fit very well the reference profiles in all the simulated domain. The lower input power of the simulation certainly allows the autofit to find a correct solution.

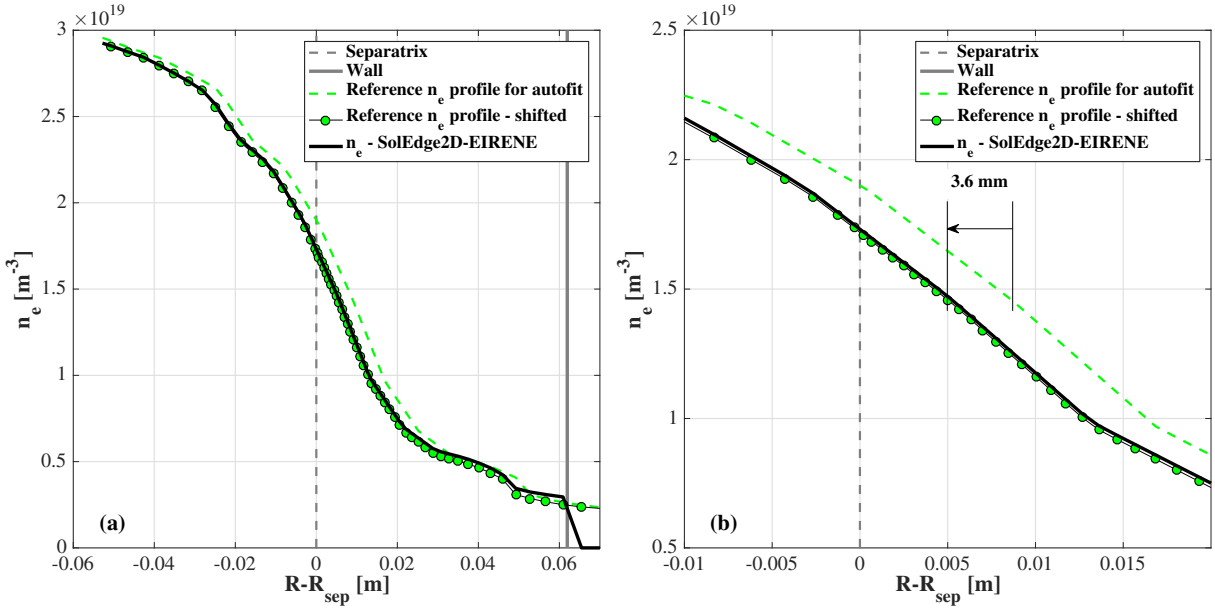

Figure 3.27: SolEdge2D-EIRENE steady-state outer midplane profiles of the electronic density n_e (black solid line) in the full simulated domain (a) and zoomed in the separatrix vicinity (b) for the L-mode phase simulation. The shifted autofit reference profiles (green circle markers) and the initial autofit profiles (green dashed line) are also plotted.

Eventually, the steady-state OMP profiles of the diffusion coefficients $D_\perp$, $\chi_{\perp,e}$ and $\chi_{\perp,i}$ for the L-mode phase are displayed in figure 3.29. Unlike for the H-mode phase, the profiles of the three diffusion coefficients are monotonic, increasing from the core to the SOL region (indicating a better confinement in the core). One can observe that $D_\perp$ is

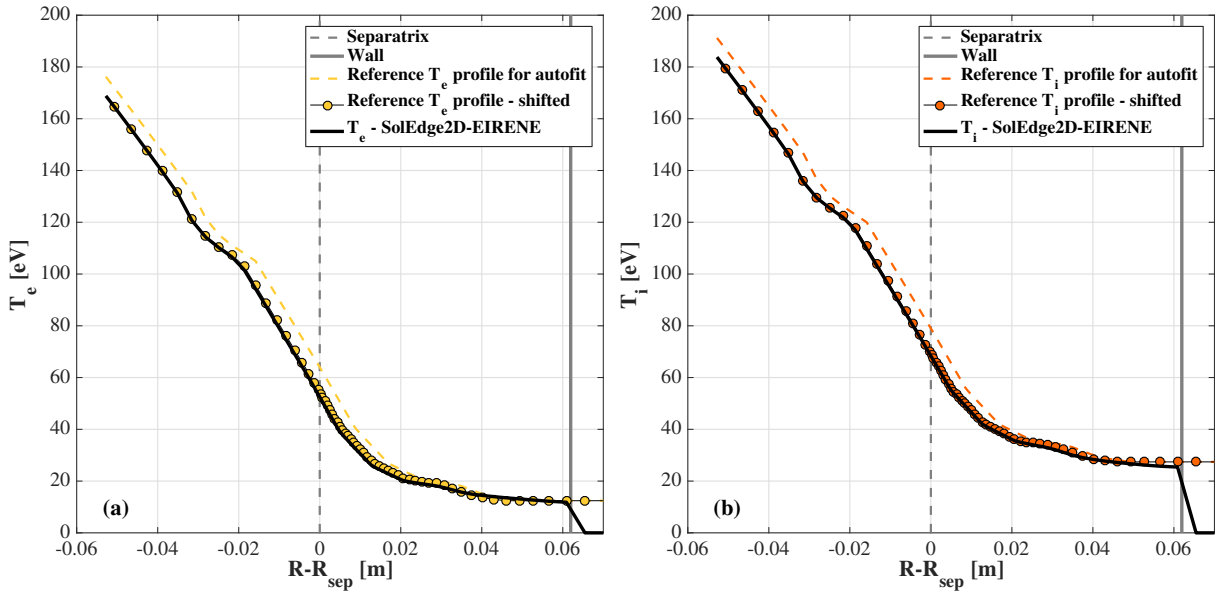

Figure 3.28: SolEdge2D-EIRENE steady-state outer midplane profiles (black solid lines) of (a) the electronic temperature T_e and (b) the ion temperature T_i for the L-mode phase simulation. The respective shifted autofit reference profiles (circle markers) and initial autofit profiles (dashed line) are also plotted.

lower than both $\chi_{\perp,e}$ and $\chi_{\perp,i}$ in all the simulated domain and that the two temperature diffusion coefficients remain similar. With respect to the H-mode phase, one can make the following observations:

- in the core region (for $R - R_{sep} \leq -0.02$ m), $D_\perp$ is one order of magnitude lower and $\chi_{\perp,e}$ is lower by a factor of ~ 3. On the contrary, $\chi_{\perp,i}$ is higher by a factor of ~ 3.

- in the separatrix vicinity (for -0.02 m $\leq R - R_{sep} \leq 0.02$ m), all the diffusion coefficients are higher which indicates the absence of a transport barrier in the L-mode phase. The difference between both phases is constant for $D_\perp$ and $\chi_{\perp,i}$ (factor of ~ 5 higher), while for $\chi_{\perp,e}$ the difference is lower in the core than in the SOL (factor of ~ 2 higher in the core, factor of 5 to 30 higher in the SOL).

- in the far-SOL region (for $R - R_{sep} \geq 0.02$ m), a similar value of $\chi_{\perp,e}$ and $\chi_{\perp,i}$ can be observed. A similar observation can be done for $D_\perp$ except for 0.03 m $\leq R - R_{sep} \leq 0.04$ m and in the wall vicinity where $D_\perp$ is one order of magnitude smaller.

However, a deep understanding of the profiles of these diffusion coefficients would require a more complete analysis of the simulation results. Such analysis is out of the scope of this PhD.

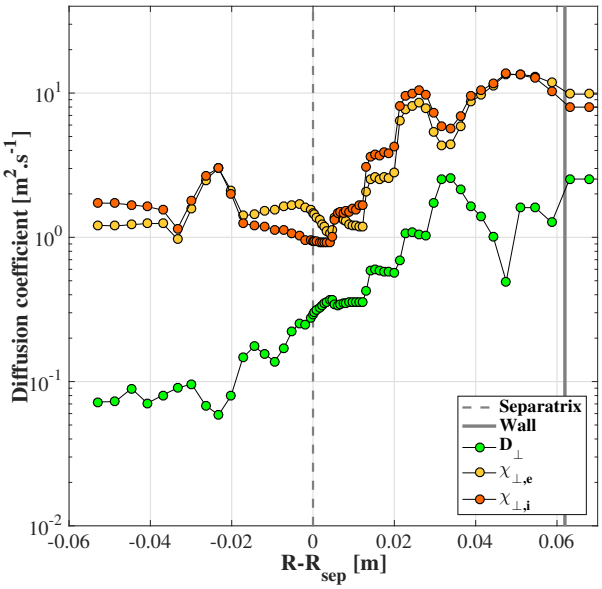

Figure 3.29: Steady-state outer midplane profiles of the perpendicular anomalous diffusion coefficients $D_\perp$, $\chi_{\perp,e}$ and $\chi_{\perp,i}$ given by the autofit procedure for the L-mode phase.

3.3 Analysis of the SolEdge2D-EIRENE steady-state plasma.

The following subsection is dedicated to a brief analysis of the steady-state plasma obtained for the L-mode phase simulation.

In figure 3.30.a-b, the 2D poloidal maps of the ion density n_i are respectively displayed in regular and logarithmic scales. A zoom in the divertor is shown in the lower part of the figure. Unlike for the H-mode phase, the divertor region is clearly much denser than the edge region. A difference of more than one order of magnitude exists between the edge density and the two divertor targets densities (cf. figure 3.30.b). The OMP separatrix density is 1.7×10^{19} m^{-3} while the maximum densities are 4.0×10^{20} m^{-3} and 3.2×10^{20} m^{-3} for the inner divertor and the outer divertor respectively. Such peaks of density are encountered few centimeters away from both targets but also away from the separatrix. The divertor is operating in detached regime [116] (which will be confirmed by the subsequent observations). The 2D poloidal map of the parallel ion flux density $\Gamma_{\parallel,i}$ is plotted in figure 3.30.c. The ion flow is of course bipolar but seems to be more symmetric in the divertor: unlike in the H-mode case, no negative flow can be seen close to the tile 8 in the outer divertor. In the main chamber, most of the SOL parallel flow is directed towards the inner divertor.

The 2D maps of the electronic temperature and of the ionic temperature (T_e and T_i respectively) are shown in figure 3.31. From the upper figures, one can note that both temperatures are lower than for the H-mode phase in all the simulated domain (below 150 eV in the edge region, OMP separatrix T_e and T_i of 68 eV and 52 eV respectively). Both sides of the divertor exhibit very low temperatures, below 10 eV. Therefore, a high plasma recombination can be expected in both targets which is a new indication of a divertor operating in detached regime during this phase.

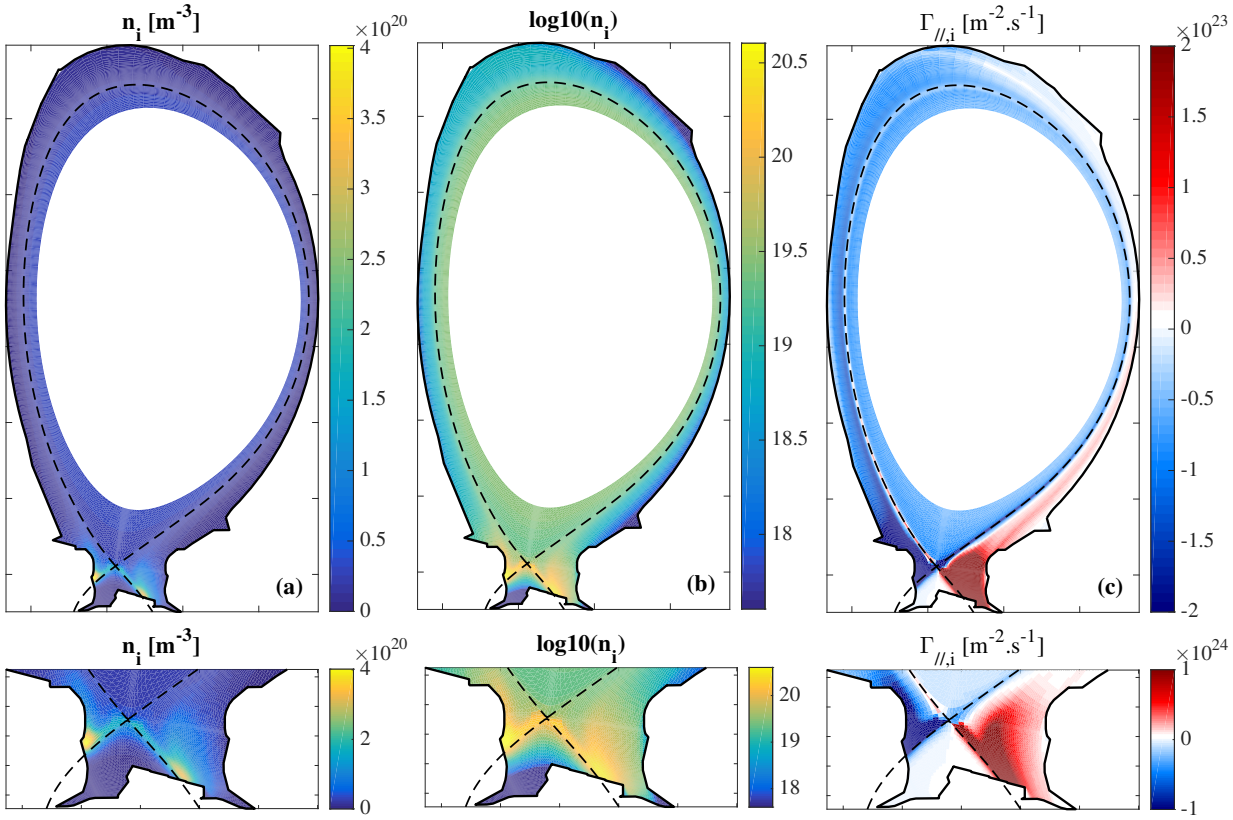

Figure 3.30: SolEdge2D-EIRENE 2D maps of the ion density n_i (a) and of the parallel ion flux density $\Gamma_{\parallel,i}$ (b) for the L-mode phase. The upper figures represent the full JET poloidal cross-section while the lower figures represent a zoom in the divertor region.

The detached operation is finally confirmed by the 2D maps of the total neutral pressure P_{tot}, of the positive ion source (from ionisation) S_{ion} and of the negative ion source (from recombination) S_{rec}:

- The divertor operates at a pressure above 1 Pa in all the outer divertor and in most of the inner divertor (cf. figure 3.32.a).
- An ionisation front expands away from the target, in the direction of the X-point (cf. figure 3.32.b).
- A volume of plasma recombination appears in both targets (cf. figure 3.32.c).

One can also note the presence of two ionisation zones on top of the machine and in the OMP where the two gas puffs are situated (cf. upper part of figure 3.32.b).

In conclusion, the L-mode phase simulation exhibits a divertor operating in detached regime. Such regime goes hand in hand with low temperature and high plasma density at the targets. Therefore, one can expect a strong evolution of the quantities related to the implantation process w.r.t. the ones observed during the H-mode phase.

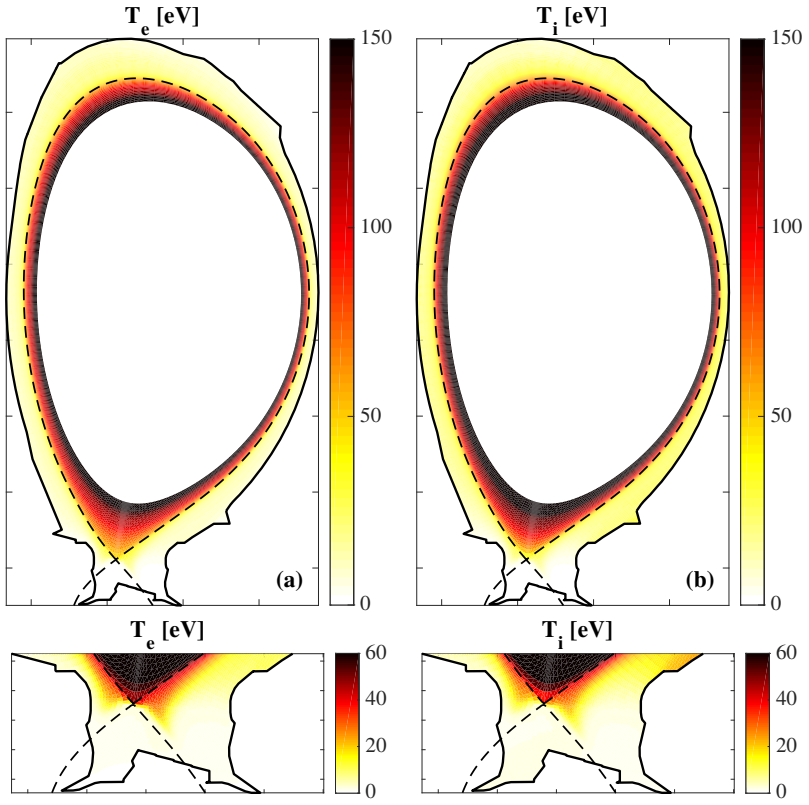

Figure 3.31: SolEdge2D-EIRENE 2D maps of the electronic temperature T_e (a) and of the ionic temperature T_i (b) for the L-mode phase. The upper figures represent the full JET poloidal cross-section while the lower figures represent a zoom in the divertor region.

3.4 Plasma conditions at the targets.

One is interested in verifying the consistency of the plasma conditions at both divertor targets. The L-mode phase simulation results can be confronted to Langmuir probe experimental measurements. As for the H-mode phase, only the J_{sat} measurements are available and the magnetic reconstruction exhibits the same shift of the strike-point locations. Therefore, the LP locations are shifted in the same fashion as for the H-mode phase (by 1.5 cm for the inner LPs, by 3.7 cm for the outer LPs) to allow a direct confrontation between the simulation and the experiment. The results are presented in figure 3.33 where the inner target J_{sat} profile (left figures) and the outer target J_{sat} profile (right figures) are plotted for each divertor module. In the inner divertor, the peak J_{sat} value is underestimated by ~ 20 % in the divertor module A (cf. figure 3.33.a, 3.5×10^5 A.m^{-2} for the simulation, 4.2×10^5 A.m^{-2} for the LP) and by ~ 40 % in the divertor module B (5.6×10^5 A.m^{-2} for the LP). Both probed peak values are measured at the same wall position which indicates a possible toroidal asymmetry of the flow pattern. In the far-SOL, only three probes are available. The simulation globally underestimates J_{sat}, with an error ranging between -20 % and -40 % (cf. figures 3.33.a-b). In the outer divertor, the results are more complicated to compare. At first sight, the J_{sat} decay is well caught by the simulation (cf. figures 3.33.e-f for 2.9 m $\leq s \leq$ 3.1 m). However, the

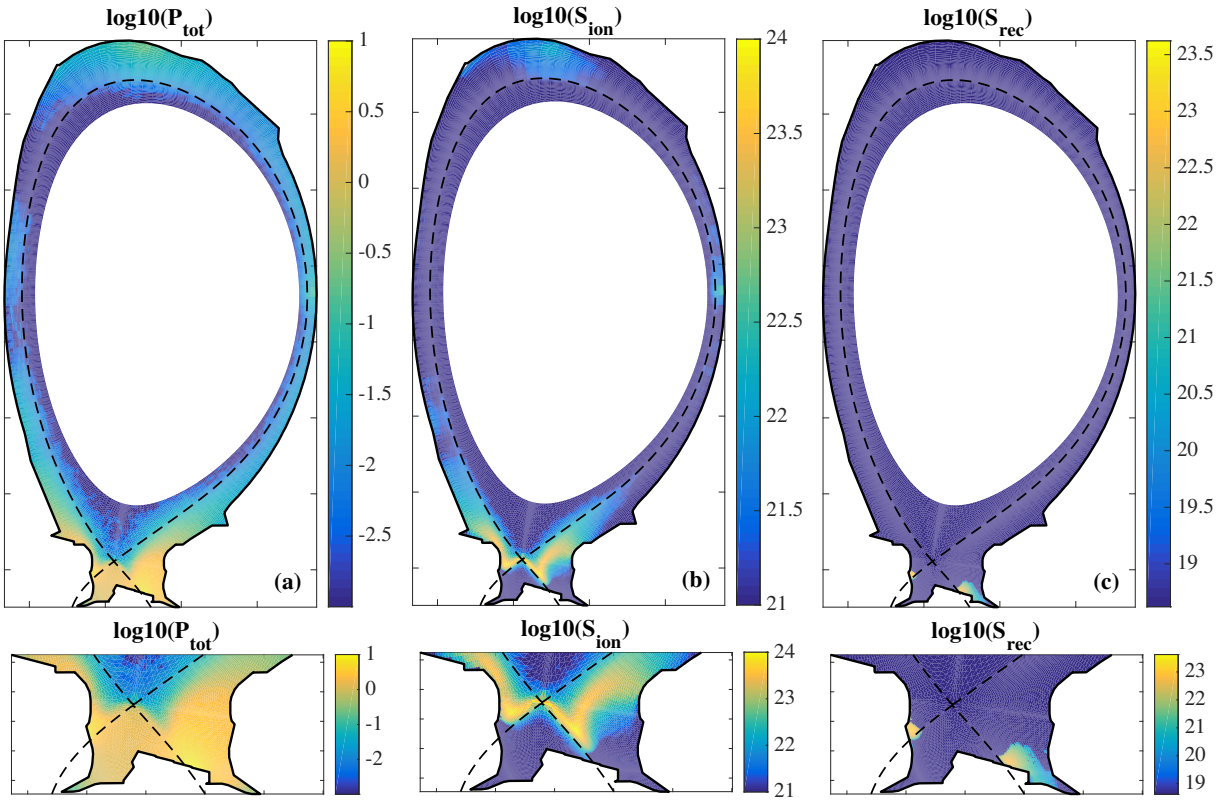

Figure 3.32: SolEdge2D-EIRENE 2D maps of the total pressure P_{tot} [Pa] (a), of the ionisation source S_{ion} [$m^{-3}.s^{-1}$] (b), and of the recombination source S_{rec} [$m^{-3}.s^{-1}$] (c) for the L-mode phase. The three quantities are plotted in logarithmic scale. The upper figures represent the full JET poloidal cross-section while the lower figures represent a zoom in the divertor region.

simulated peak value (3.4×10^5 A.m^{-2}) does not match the maximum probed value in each module. In the divertor modules A and B, this maximum value is measured at the same wall position ($s = 2.89$ m) and is equal to $\sim 5.0 \times 10^5$ A.m^{-2}. A similar value is also probed at this location in the module C (4.6×10^5 A.m^{-2}). However, a higher peak value is measured in the same module (7.7×10^5 A.m^{-2}) at a location which seems to be more consistent with the strike-point position ($s = 2.88$ m). Therefore the simulation could underestimate the peak of J_{sat} by ~ 50 %. Still some uncertainties exist (e.g. a probed value of 6.0×10^5 A.m^{-2} at $s = 2.865$ m in the module C, two times lower at the same location in module A) and no clear conclusion can be drawn on the peak value of J_{sat}. In any case, the interaction surface remains very small w.r.t. the divertor surface and no strong impact of this disagreement can be expected in the wall dynamics simulation.
In figure 3.34 the same plots are displayed in logarithmic scale to highlight the PFR and the far-SOL measurements. In both inner and outer PFRs, one can observe a quantitative agreement between the simulated and the probed values of J_{sat}: the J_{sat} decay is very well matched by the code. In the outer far-SOL, a good agreement can also be observed and the shadowing effect of tile 8 on tile 7 (for 3.3 m $< s <$ 3.6 m) is very well caught.
As it was explained in subsection 3.2, the L-mode phase simulation did not converged

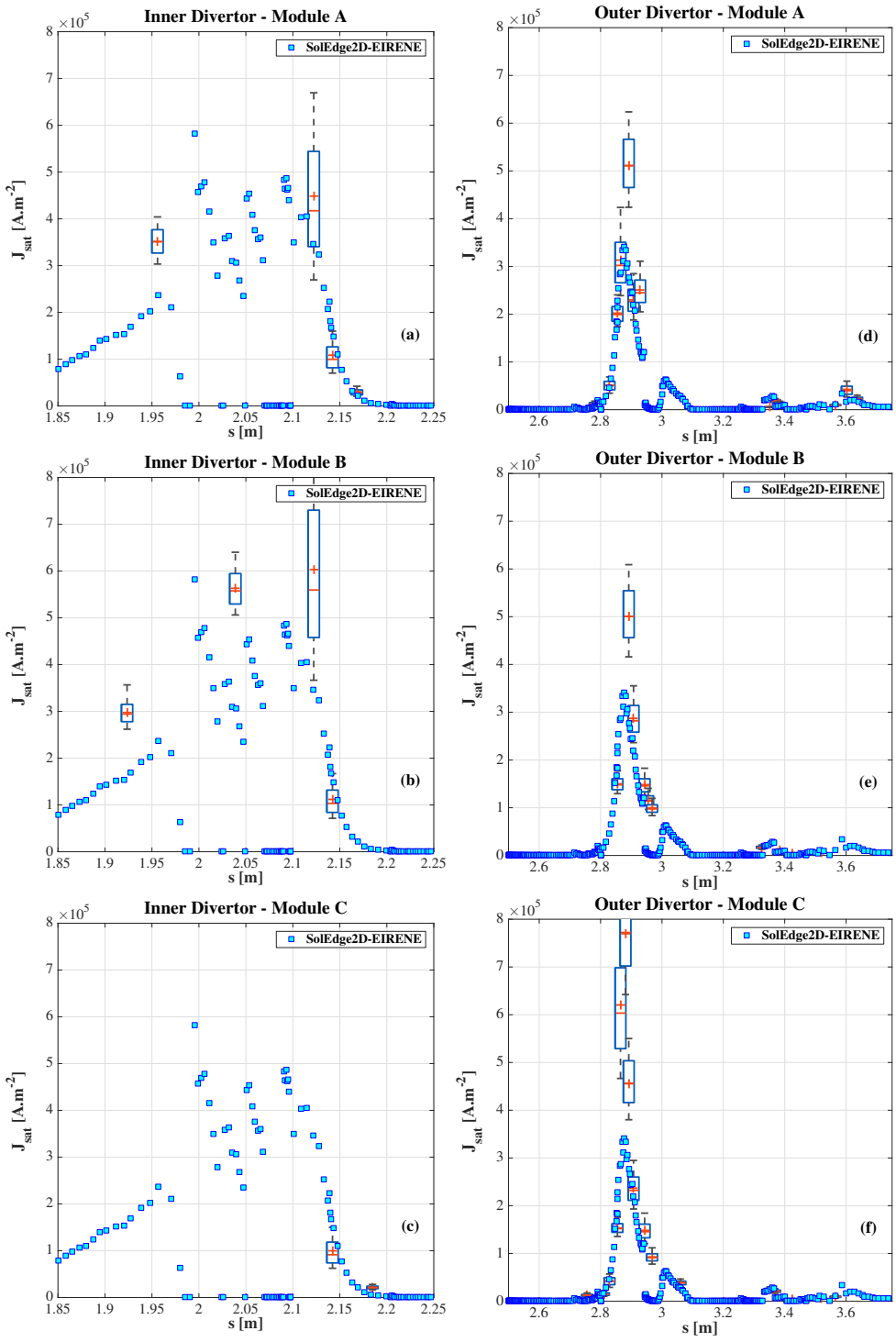

Figure 3.33: Inner target profile (left figures) and outer target profile (right figures) of J_{sat} for the L-mode phase (regular scale). The LP measurements are displayed using the boxplot representation while the simulated J_{sat} profile is displayed with blue filled squares. The experimental data are shifted by 1.5 cm for the inner target and by 3.7 cm for the outer target.

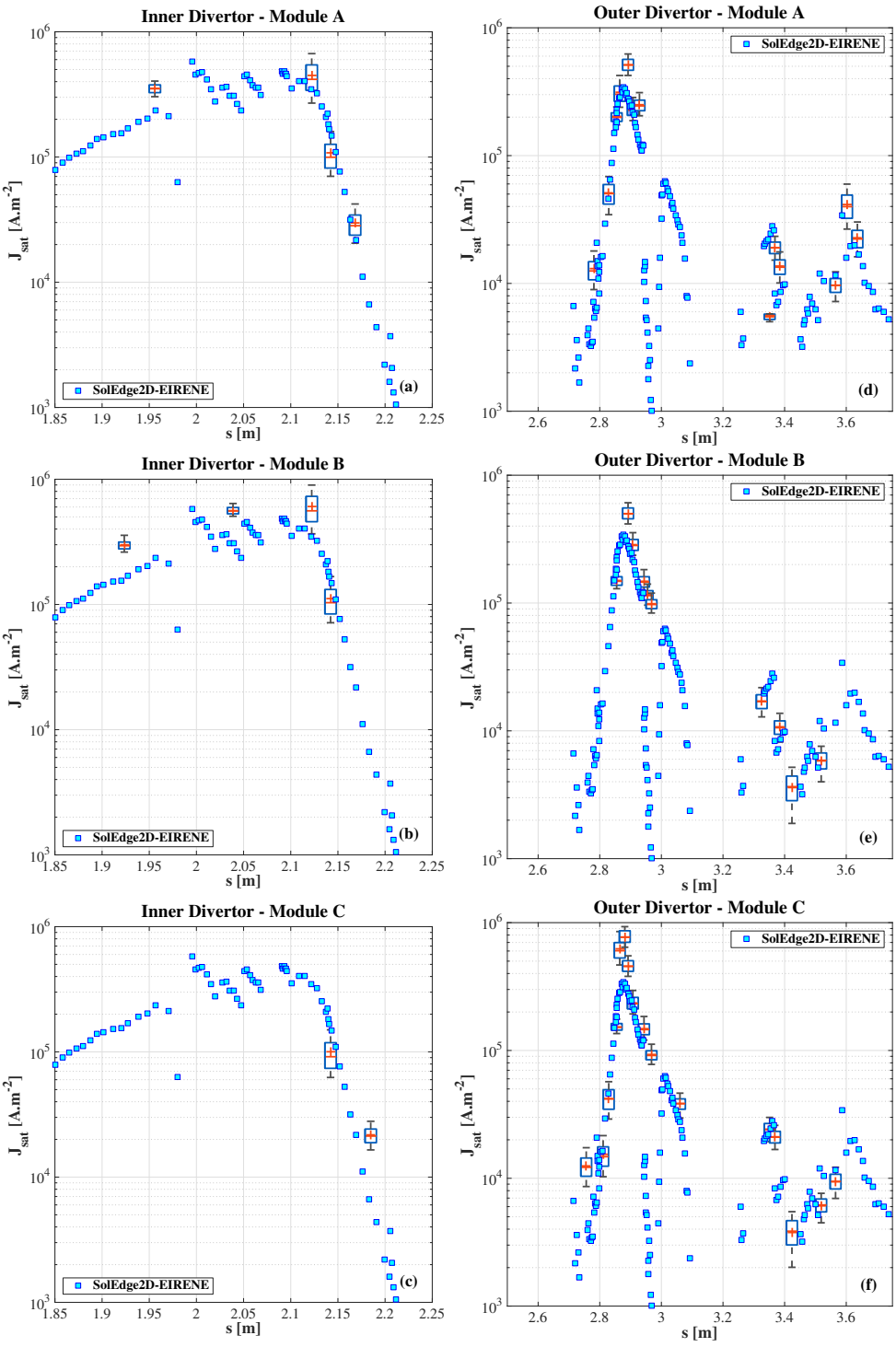

Figure 3.34: Inner target profile (left figures) and outer target profile (right figures) of J_{sat} for the L-mode phase (logarithmic scale). The LP measurements are displayed using the boxplot representation while the simulated J_{sat} profile is displayed with blue filled squares. The experimental data are shifted by 1.5 cm for the inner target and by 3.7 cm for the outer target.

to the experimental value of the power flowing in the simulated domain $P^{\{D^+ + e^-\}}_{CORE \rightarrow EDGE}$ (2.38 MW in the considered simulation, 2.5 MW estimated in the experiment). The simulation was run up to full convergence of this power. One can see the effect of this very little power increase in figure 3.35. The LP measurements of the divertor module A are also plotted. First of all, no clear impact can be observed in the far-SOL and in the PFR at both targets. However, an increase in the J_{sat} peak can be observed in both targets. In the inner target, J_{sat} increased from 3.5×10^5 A.m^{-2} to 4.3×10^5 A.m^{-2} at $s = 2.12$ m and now match perfectly the measured value. In the outer target, an increase of 0.4×10^5 A.m^{-2} is noticed, but the peak still remains distant to the probed value. A higher value of $P^{\{D^+ + e^-\}}_{CORE \rightarrow EDGE}$ could have further enhanced this peak value. Indeed, this power is estimated from the steady-state power balance equation 3.10. A huge uncertainty resides in the evaluation of the core radiative power from bolometry measurements. In JET, this power is estimated from the vertical bolometer situated on top of the machine. Therefore, its line of sight embeds the divertor region. In the L-mode phase, the divertor is highly radiative due to the detached target conditions. An overestimation of the core radiation is possible due to this highly localised radiative source in the divertor.
In conclusion, the saturation current density distribution given by SolEdge2D-EIRENE for the L-mode phase matches the experimental measurements in the whole divertor. Only the estimation of the peak J_{sat} value at the outer strike-point is questionable. In any case, the surface of interaction is very small and one does not expect a strong impact on the wall dynamics simulation.

3.5 SolEdge2D-EIRENE results used as inputs in D-WEE.

The SolEdge2D-EIRENE results which are required as inputs for D-WEE appear in figure 3.36. On the first-wall, no change can be seen for the implantation flux density and for the mean angle of incidence w.r.t. their values in phase 1 for both ions and atoms. The same observation is made for the net energy flux density. Two peaks can be seen for Γ^{at}_{imp} in the outer limiter (6.0×10^{20} m^{-2}.s^{-1} at $s = 5.7$ m) and in the dump plate (1.2×10^{21} m^{-2}.s^{-1} at $s = 7.9$ m). Both peaks are linked to the two operating gas puffs. However, a clear decrease of the impact energy is observed for both particles (decrease by a factor of ~ 2 w.r.t. the H-mode phase), with values ranging between 20 and 50 eV for the atoms and between 30 and 100 eV for the ions.
In the divertor region, tremendous differences w.r.t. phase 1 arise due to the decrease of the injected power and to the plasma going from attached to detached conditions. The implanted atom flux density increases by one order of magnitude from the inner strike-point vicinity ($s = 2$ m) up to the tile 8 ($s = 3.6$ m), reaching a value of 2.9×10^{22} and 4.3×10^{22} m^{-2}.s^{-1} at the inner and outer strike-points respectively. A factor of 2 increase is also noticed on top of the tile 1 and on the HFGC tile. The strongest change is seen on the impact energy, which collapses below 10 eV for 2 m $\leq s \leq$ 3.6 m for both types of particles. No evolution of this quantity is seen on the inner far-SOL ($s \leq 2$ m), while it decreases to ~ 30 eV in the outer far-SOL ($s \geq 3.6$ m). Concerning the energy

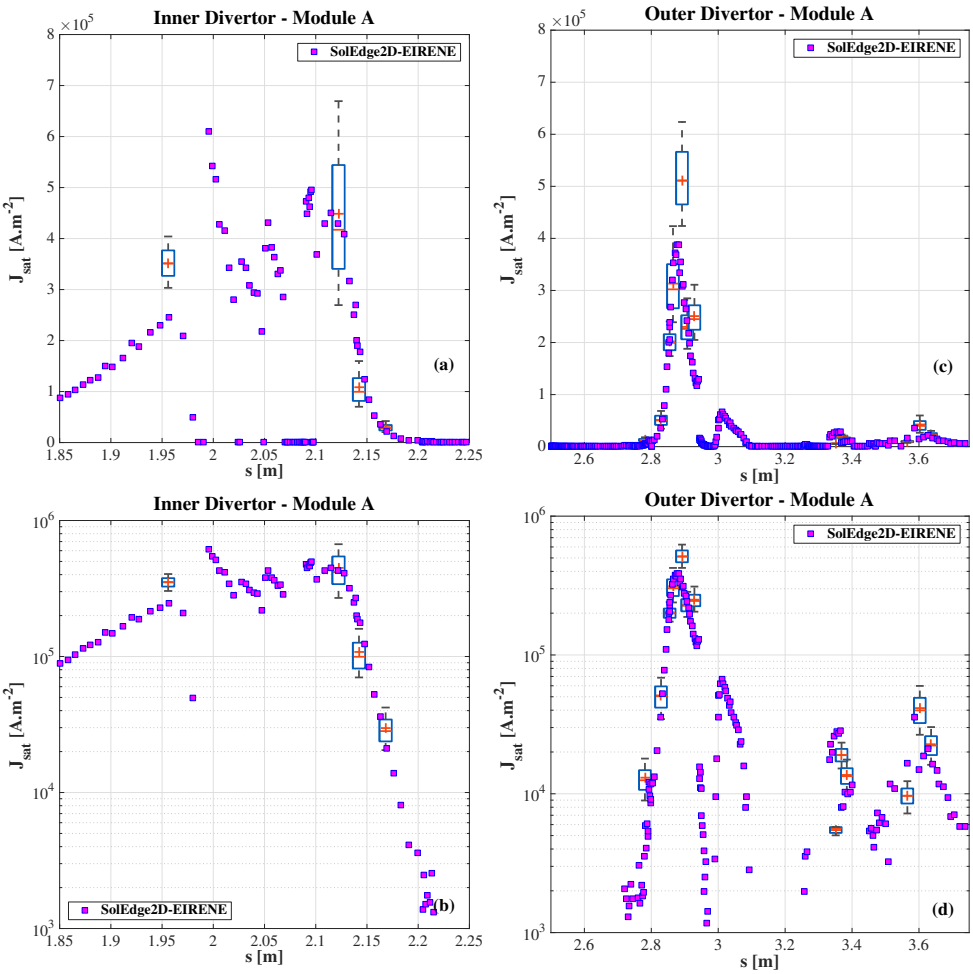

Figure 3.35: Inner target profile (left figures) and outer target profile (right figures) of J_{sat} for the converged L-mode phase simulation. The upper figures are plotted in regular scale and the lower figures are plotted in logarithmic scale. The LP measurements are displayed using the boxplot representation while the simulated J_{sat} profile is displayed with purple filled squares. The experimental data are shifted by 1.5 cm for the inner target and by 3.7 cm for the outer target.

flux density, its value at both strike-points collapses below 0.2 MW.m^{-2}. It decreases by a factor of 3 in the inner far-SOL and by a factor of 5 in the outer far-SOL, overall remaining below 0.2 MW.m^{-2}. No difference is seen in the PFR. Still no clear change is seen for the mean angle of incidence of ions and for their implantation flux density. Only the values of Γ^{i+}_{imp} at both strike-points decrease by a factor of ~ 2 (1×10^{22} m^{-2}.s^{-1}). The same reduction can be noted on top of tile 1 and on the HFGC tile.

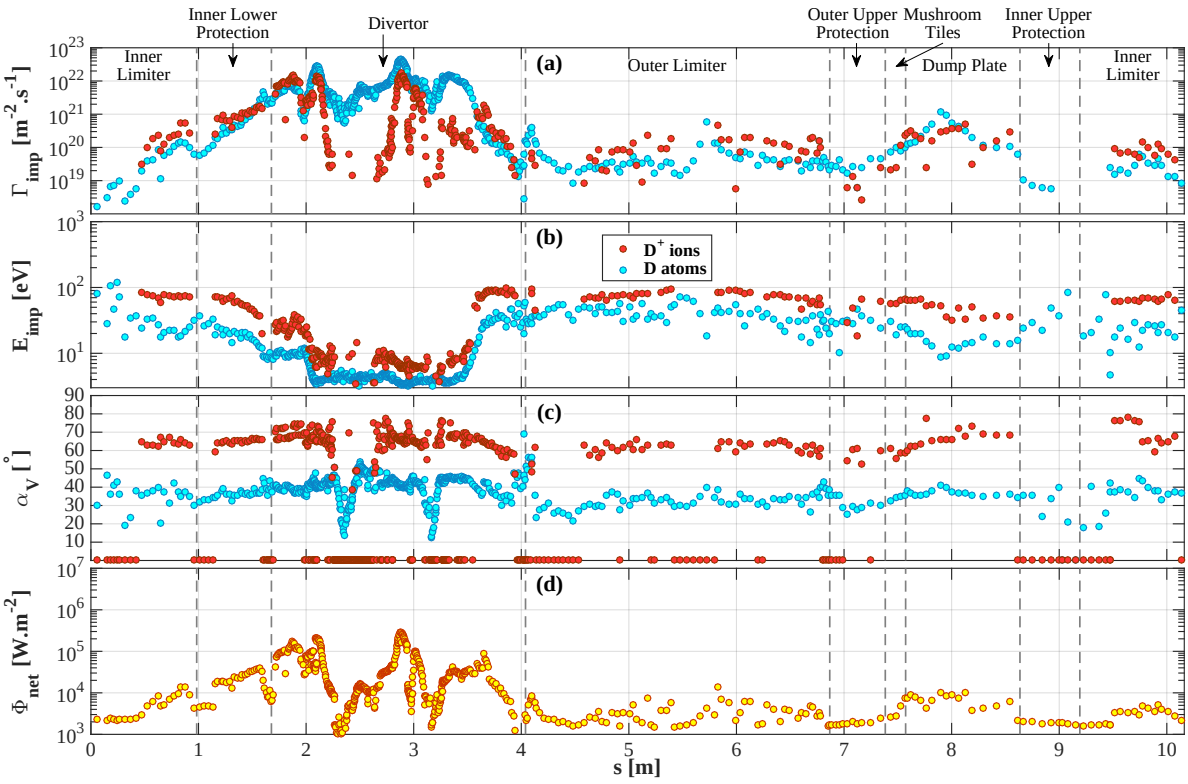

Figure 3.36: SolEdge2D-EIRENE simulation results for plasma phase 2 (L-mode): distribution along the wall of (a) the implanted particle flux density Γ_{imp}, of (b) the impact energy E_{imp}, of (c) the mean angle of incidence α_V and of (d) the net energy flux density Φ_{net}. These quantities are required as inputs for the D-WEE module. The first three quantities are plotted for both ions and atoms. The definition of the s curvilinear coordinate can be found in figure 3.8.b.

4 Evolution of fuel recycling and implantation conditions between plasma phase 1 and plasma phase 2.

As one has seen in subsections 2.5 and 3.5, the H-mode and the L-mode phases exhibit several differences in the plasma-wall interaction. However, due to the numerous quantities involved and due to their spatial variability, a clear picture of these differences is still required as they will strongly impact the results of the wall dynamics simulation presented in the next chapter. In this section, one will intend to disentangle the change in the recycling and implantation quantities between the two phases. The ion and atom contributions to the different quantities will be analysed while their spatial distributions will be tackled by arbitrarily dividing the JET wall in six different zones (cf. figure 3.37). These zones will be used to calculate integrated or mean simulation results.

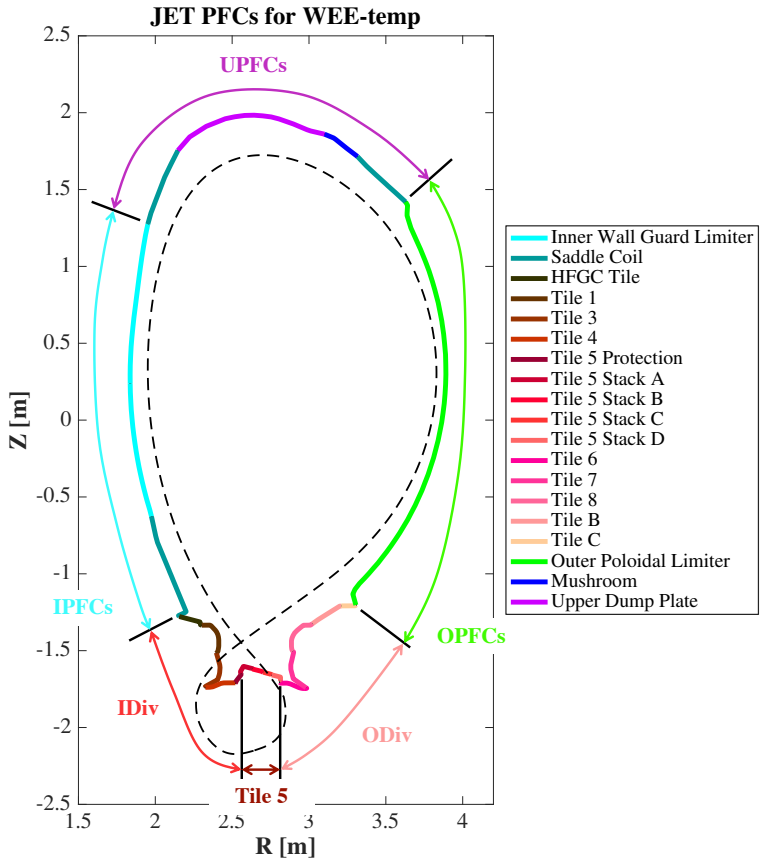

Figure 3.37: JET poloidal cross-section with the different PFCs considered in the thermal model WEE-temp. Six zones in the wall are also defined: the Inner Divertor zone (IDiv), the Tile 5 zone, the Outer Divertor zone (ODiv), the Outer PFCs (OPFCs), the Upper PFCs (UPFCs) and the Inner PFCs (IPFCs). In the following, these zones will be used to display integrated or mean simulation results.

4.1 Evolution of the incident fluxes and of the parameters of incidence.

In the following, one will focus on the evolution of the incident fluxes and the recycling quantities (i.e. the impact energy, the mean angle of incidence and the reflection coefficient) in the six zones of the JET wall.
First, the particle flux quantity has to be introduced. Assuming toroidal symmetry of the plasma-wall interaction, a given wall particle flux Q_* ($*$ being either incident, implanted or outgassed) at a given time t can be calculated using the following expression:

$$Q_*(t) = \int_{s_1}^{s_2} \int_0^{2\pi} \Gamma_*(s,t) R(s)\, ds\, d\varphi = 2\pi \int_{s_1}^{s_2} \Gamma_*(s,t) R(s)\, ds \tag{3.11}$$

where $\Gamma_*(s,t)$ is the respective particle flux density [$\mathrm{m}^{-2}.\mathrm{s}^{-1}$], $R(s)$ the wall major radius [m], s the curvilinear coordinate along the wall defined in figure 3.8.b [m] and φ the toroidal angle [rad]. s_1 and s_2 are the curvilinear coordinates of the boundaries of the considered zone. As an example, the total incident flux on the tile 5 zone $Q^{tile5}_{inc,tot}$ can be

expressed from the incident ion flux density Γ_{inc}^{i+} and the incident atom flux density Γ_{inc}^{at} as follows:

$$Q_{inc,tot}^{tile5}(t) = 2\pi \int_{s_1^{tile5}}^{s_2^{tile5}} \int_0^{2\pi} \left(\Gamma_{inc}^{i+}(s,t) + \Gamma_{inc}^{at}(s,t)\right) R(s)\, ds \tag{3.12}$$

The total incident flux on the JET wall $Q_{inc,tot}$ [at.s^{-1}] has been calculated using equation 3.11 and the incident ion and atom flux densities (Γ_{inc}^{i+} and Γ_{inc}^{at}) of the respective phases given by SolEdge2D-EIRENE. The time evolution of this flux during the two phases is displayed in figure 3.38. The different zone contributions are also plotted. First, one can notice that $Q_{inc,tot}$ increases between the two phases. Such increase can be observed in all the wall zones. Of course, due to the diverted magnetic topology, $Q_{inc,tot}$ is greater by almost one order of magnitude in the divertor zones than in the first-wall zones in both phases. Moreover, one can note that $Q_{inc,tot}$ on the outer divertor is at the same level as on the two other divertor zones hosting the strike-points in both phases.

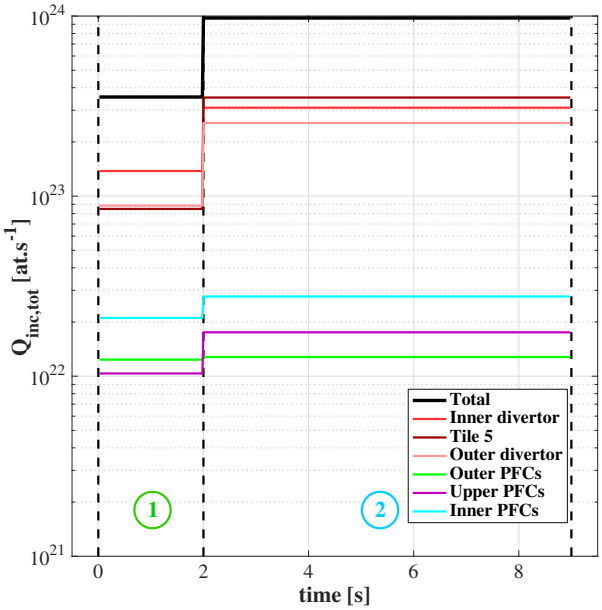

Figure 3.38: Time evolution of the total (ions and atoms) incident flux on the JET wall $Q_{inc,tot}$ during the discharge (black solid line). The contribution of the different zones of the wall (cf. figure 3.37) are also plotted. The plasma phases 1 (H-mode) and 2 (L-mode) are delimited by the dashed vertical lines.

Furthermore, the time evolutions of the incident ion flux $Q_{inc,ion}$ and of the incident atom flux $Q_{inc,at}$ on the JET wall are displayed in figure 3.39.a and in figure 3.39.b respectively. The different zone contributions are also plotted. Overall, the two fluxes are of the same order of magnitude in all the zones. Again, they are both greater in the divertor zones than in the first-wall zones. However, the ion flux clearly supersedes the atom flux during the H-mode phase whereas the reverse situation occurs during the L-mode phase. On the divertor, only the ion flux on tile 5 strongly increases between the two phases while it remains almost constant on the other zones. On the contrary, this flux decreases in

all the first-wall zones. Concerning the atom flux, it strongly increases in all the zones between the two phases (the strongest rise, by a factor of ~ 10, occurs on tile 5). The transition of both strike-points from attached condition during the H-mode phase to detached condition during the L-mode phase probably plays a role in this phenomenon.

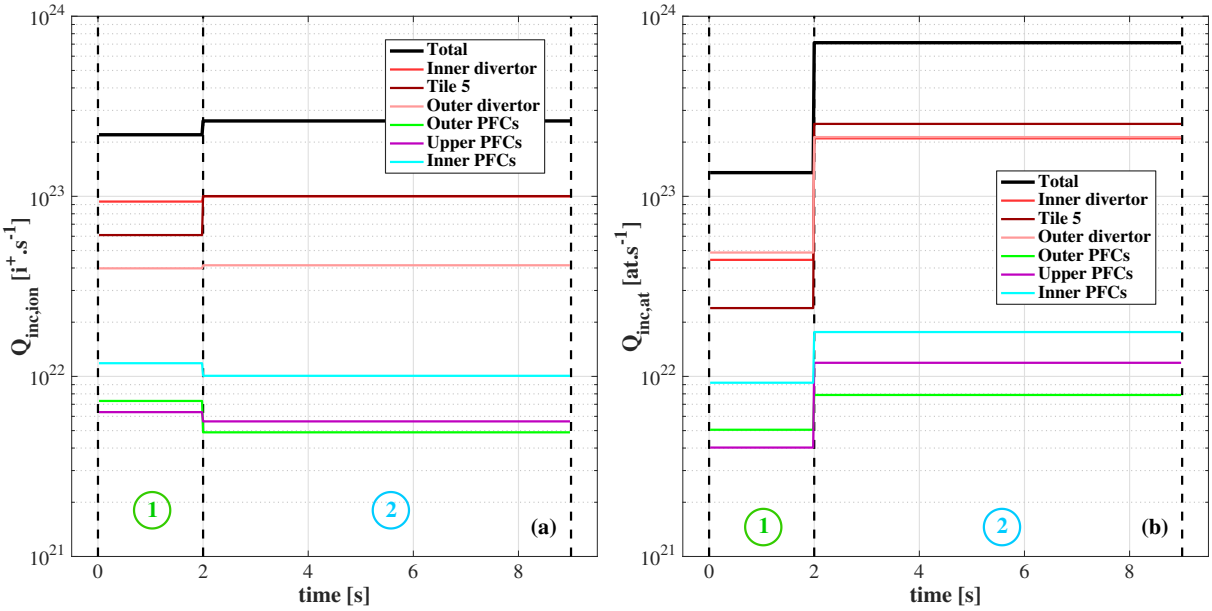

Figure 3.39: Time evolution of the incident ion flux $Q_{inc,ion}$ (a) and of the incident atom flux $Q_{inc,at}$ (b) on the JET wall during the discharge (black solid lines). The contribution of the different zones of the wall (cf. figure 3.37) are also plotted. The plasma phases 1 (H-mode) and 2 (L-mode) are delimited by the dashed vertical lines.

The value of Q_{inc} for both phases are summed up in table 3.1 for the divertor zones and in table 3.2 for the first-wall zones. The contribution of ions and atoms to the total incident flux is also reported. In the divertor, no clear evolution of the ion flux can be seen between the two phases except on tile 5 where it increases by a factor of 1.6. However the sharp increase of the atom flux by a factor of 4.4 on the outer divertor to 11 on tile 5 can be noted. On the first-wall, the moderate decrease of the incident ion flux (by a factor of 0.67 to 0.86) is compensated by a sharp increase of the incident atom flux by a factor of 1.6 to 3.0. Concerning the asymmetry between the inner divertor and the outer divertor, if one sums the contribution on the tile 5 zone and the outer divertor zone, the ion flux on the outer side is always stronger than on the inner side of the divertor.
The means of the impact energy (E_{imp}^{mean}) and of the mean angle of incidence (α_V^{mean}) in the different zones of the divertor and of the first-wall are also reported in table 3.3 and table 3.4 respectively. As it was noticed in figures 3.23.c and 3.36.c, α_V^{mean} does not clearly change between the two phases. It remains between 62° and 73° for the ions and between 32° and 43° for the atoms in all the zones. No clear impact of this quantity can be expected on the wall evolution between the two phases. On the contrary, a strong effect can be expected from the evolution of the impact energy. Indeed, E_{imp}^{mean} decreases by a factor of ~ 2 in the first-wall region for both ions and atoms. In the outer

		Inner Divertor			Tile 5			Outer Divertor		
		Total	Ions	Atoms	Total	Ions	Atoms	Total	Ions	Atoms
Q_{inc} [10^{22} s^{-1}]	H-mode	13.8	9.35	4.44	8.49	6.09	2.40	8.86	3.98	4.87
	L-mode	31.0	9.99	21.0	35.3	10.0	25.2	25.5	4.14	21.3
$\frac{Q_{inc}^{L-mode}}{Q_{inc}^{H-mode}}$		2.3	1.1	4.7	4.2	1.6	11.	2.9	1.0	4.4

Table 3.1: Incident flux (Q_{inc}) value in the different zones of the divertor (defined in figure 3.37) during both H-mode and L-mode phases. The ions and atoms contribution to the total incident flux is reported. The ratio between the L-mode and the H-mode fluxes, $Q_{inc}^{L-mode}/Q_{inc}^{H-mode}$, is also indicated.

		Outer PFCs			Upper PFCs			Inner PFCs		
		Total	Ions	Atoms	Total	Ions	Atoms	Total	Ions	Atoms
Q_{inc} [10^{22} s^{-1}]	H-mode	1.24	0.731	0.505	1.04	0.633	0.402	2.11	1.18	0.922
	L-mode	1.28	0.489	0.788	1.75	0.563	1.19	2.77	1.01	1.76
$\frac{Q_{inc}^{L-mode}}{Q_{inc}^{H-mode}}$		1.0	0.67	1.6	1.7	0.89	3.0	1.3	0.86	1.9

Table 3.2: Incident flux (Q_{inc}) value in the different zones of the first-wall (defined in figure 3.37) during both H-mode and L-mode phases. The ions and atoms contribution to the total incident flux is reported. The ratio between the L-mode and the H-mode fluxes, $Q_{inc}^{L-mode}/Q_{inc}^{H-mode}$, is also indicated.

divertor, a decrease of this energy by a factor of ~ 3 is observed for the ions and by a factor of ~ 6 for the atoms. This decrease is even more tremendous in the two other divertor zones (by a factor of 8 to 30 for both type of particles in the two zones hosting the strike-points). Again, the lower input power in L-mode phase and the transition from attached to detached conditions between the two phases have a strong impact on this quantity. Such evolution of the impact energy will have a strong influence on the deuterium reflection and implantation processes.

		Inner Divertor		Tile 5		Outer Divertor	
		Ions	Atoms	Ions	Atoms	Ions	Atoms
E_{imp}^{mean} [eV]	H-mode	164	52.6	247	77.4	136	114
	L-mode	18.6	6.46	7.55	4.04	50.3	19.5
α_V^{mean} [°]	H-mode	72.7	41.4	66.9	40.0	63.0	40.0
	L-mode	67.8	42.0	66.3	42.6	63.8	41.0

Table 3.3: Mean impact energy (E_{imp}^{mean}) and mean angle of incidence (α_V^{mean}) in the different zones of the divertor (defined in figure 3.37) during both H-mode and L-mode phases.

		Outer PFCs		Upper PFCs		Inner PFCs	
		Ions	Atoms	Ions	Atoms	Ions	Atoms
E_{imp}^{mean} [eV]	H-mode	133	107	115	68.4	115	62.6
	L-mode	76.2	41.1	50.5	24.6	65.8	28.5
α_V^{mean} [°]	H-mode	69.4	36.1	64.8	38.1	68.2	38.0
	L-mode	62.3	32.8	63.8	33.8	66.6	35.1

Table 3.4: Mean impact energy (E_{imp}^{mean}) and mean angle of incidence (α_V^{mean}) in the different zones of the first-wall (defined in figure 3.37) during both H-mode and L-mode phases.

4.2 Evolution of the reflection coefficient.

As it was observed above, a clear decrease of the impact energy between the two phases occurs in all the zones. Such decrease will affect the deuterium reflection on the wall. In table 3.5 and table 3.6, the mean value of the reflection coefficient, R_n^{mean}, is reported for the different zones of the JET wall. This coefficient is calculated from the ratio of the reemitted atom flux given by EIRENE to the considered incident flux (cf. tables 3.1 and 3.2). Such coefficient has been calculated for incident ions and for incident atoms. The reflection coefficient for the total particles is also reported to spotlight the type of particles (reflected atoms or desorbed molecules) which dominates the recycling flux in the simulation.

		Inner Divertor			Tile 5			Outer Divertor		
		Total	Ions	Atoms	Total	Ions	Atoms	Total	Ions	Atoms
R_n^{mean}	H-mode	0.46	0.38	0.63	0.65	0.59	0.79	0.72	0.65	0.77
	L-mode	0.60	0.56	0.62	0.67	0.80	0.61	0.68	0.77	0.66

Table 3.5: Mean reflection coefficient (R_n^{mean}) in the different zones of the divertor (defined in figure 3.37) during both H-mode and L-mode phases. The values for ions and atoms are also reported.

In the divertor zones, the total reflection coefficient is between 0.65 and 0.72 in tile 5 and in the outer divertor during both phases. The recycling is therefore dominated by deuterium atoms. In the inner divertor, this coefficient has a lower value of 0.46 for the H-mode phase and 0.60 for the L-mode phase. The difference is likely due to the Be surface considered on top of tile 1 and on top of the HFGC tile (cf. figure 3.8.a), as Be has a lower reflection coefficient w.r.t. W in the range of energy and angle of incidence at play here. Moreover, for the ions, R_n^{mean} increases between the two phases in all the divertor zones. This increase is linked to the reduction of their impact energy (cf. table 3.3). On the contrary, R_n^{mean} decreases for the atoms between the two phases. The reason for such evolution is still unclear as their impact energy also declines. A possible explanation could be the steep reduction of the reflection coefficient at energy below 10 eV which is estimated by TRIM for D interaction with W and Be (cf. reference [35]). From figure

3.36.b, one can see that in the divertor zone the impact energy for atoms is below 10 eV and is lower than the one for ions.

		Outer PFCs			Upper PFCs			Inner PFCs		
		Total	Ions	Atoms	Total	Ions	Atoms	Total	Ions	Atoms
R_n^{mean}	H-mode	0.29	0.17	0.47	0.29	0.18	0.47	0.30	0.17	0.46
	L-mode	0.39	0.22	0.49	0.40	0.24	0.47	0.40	0.24	0.50

Table 3.6: Mean reflection coefficient (R_n^{mean}) value in the different zones of the first-wall (defined in figure 3.37) during both H-mode and L-mode phases. The values for ions and atoms are also reported.

In the first-wall, the results are more simple to analyse as the evolution of the implantation parameters are not as abrupt as in the divertor zones. Due to the reduction of E_{imp}, R_n^{mean} increases in all the zones between the two phases (cf. table 3.6). Moreover, its value is higher for atoms than for ions due to their smaller angle of incidence. Eventually, due to the presence of Be at the surface, the total reflection coefficient in all the first-wall zones is below 0.50 (equal to ~ 0.30 for the H-mode phase and to ~ 0.40 for the L-mode phase): deuterium recycling in the JET-ILW first-wall predominately occurs in the form of desorbing molecules.

4.3 Evolution of the implantation fluxes.

The aforementioned evolutions of the incident flux and of the reflection coefficient indicate that the implantation flux will vary between the two phases. In order to quantify this change, an approach similar to the one carried out for the incident particle flux will be applied to the implantation flux.
The total implantation flux in the JET wall $Q_{imp,tot}$ [at.s^{-1}] has been calculated using equation 3.11 and the ion and atom implantation flux densities (Γ_{imp}^{i+} and Γ_{imp}^{at}) of the respective phases given by SolEdge2D-EIRENE (cf. figures 3.23.a and 3.36.a). The time evolution of this flux and of its contributions in the different wall zones are displayed in figure 3.40. First, as it was noticed for $Q_{inc,tot}$, $Q_{imp,tot}$ increases between the two phases. Such increase can be observed in all the wall zones, with the exception of the Outer PFCs zone (while the total incident flux slightly increases in this zone).
The time evolutions of the ion implantation flux $Q_{imp,ion}$ and of the atom implantation flux $Q_{imp,at}$ are displayed in figure 3.41.a and in figure 3.41.b respectively. Overall, the two fluxes are of the same order of magnitude in all the zones. Again, they are both greater in the divertor zones than in the first-wall zones. However, they exhibit a different time evolution: $Q_{imp,ion}$ slightly decreases between the two phases in all the zones while $Q_{imp,at}$ strongly increases. A sharp raise of $Q_{imp,at}$ by a factor of 20 can be noticed in the tile 5 zone (cf. table 3.7). Such behaviour can be explained by the increase by one order of magnitude of Γ_{imp}^{at} in the PFR and in the outer strike-point vicinity between both phases (cf. figures 3.23.a and 3.36.a).

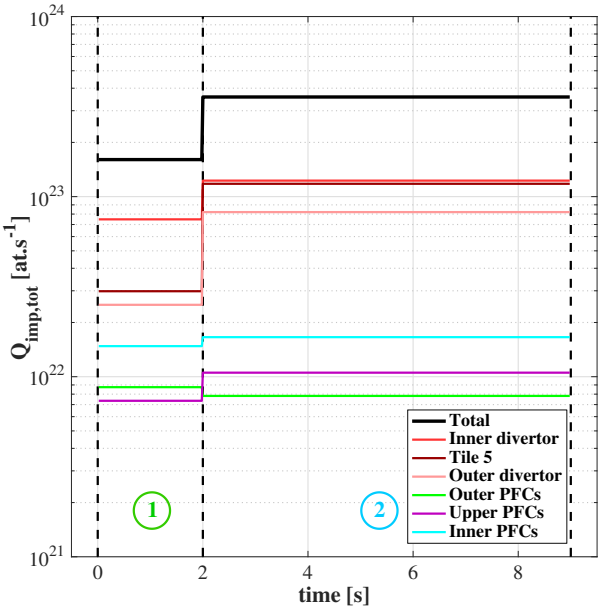

Figure 3.40: Time evolution of the total (ions and atoms) implantation flux in the JET wall $Q_{imp,tot}$ during the discharge (black solid line). The contribution of the different zones of the wall (cf. figure 3.37) are also plotted. The plasma phases 1 (H-mode) and 2 (L-mode) are delimited by the dashed vertical lines.

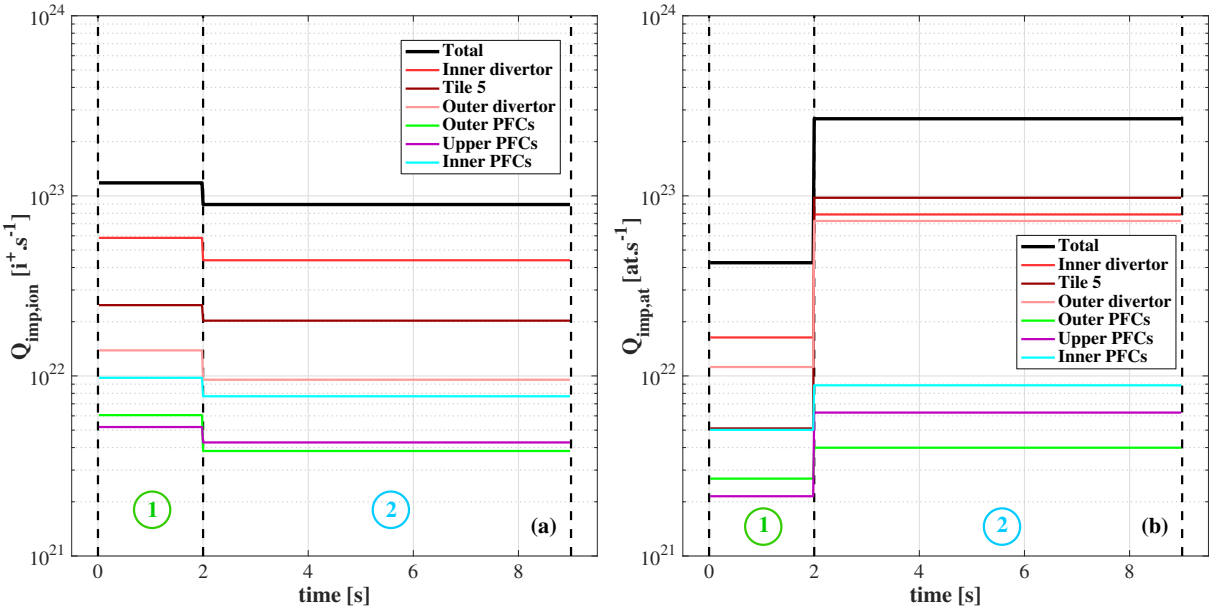

Figure 3.41: Time evolution of the ion implantation flux $Q_{imp,ion}$ (a) and of the atom implantation flux $Q_{imp,at}$ (b) in the JET wall during the discharge (black solid lines). The contribution of the different zones of the wall (cf. figure 3.37) are also plotted. The plasma phases 1 (H-mode) and 2 (L-mode) are delimited by the dashed vertical lines.

The value of Q_{imp} for both phases are summed up in table 3.7 for the divertor zones and in table 3.8 for the first-wall zones. The contribution of ions and atoms to the total

implantation flux is also reported. As it was noticed previously, the total implantation flux increases between the two phases in all the zones with the exception of the Outer PFCs zone. A striking results is that everywhere the ion flux prevails over the atom flux during the H-mode phase ($Q_{imp,ion}^{H-mode} > Q_{imp,at}^{H-mode}$) while the reverse situation occurs during the L-mode phase ($Q_{imp,at}^{L-mode} > Q_{imp,ion}^{L-mode}$). The ratio between the L-mode and the H-mode fluxes, $Q_{imp}^{L-mode}/Q_{imp}^{H-mode}$, is also indicated in both tables. Again, this ratio for the total flux is greater than one in all the zones except in the Outer PFCs zone. In these zones, the moderate decrease of the implanted ion flux is compensated by a sharp increase of the implanted atom flux.

		Inner Divertor			Tile 5			Outer Divertor		
		Total	Ions	Atoms	Total	Ions	Atoms	Total	Ions	Atoms
Q_{imp} [10^{22} s^{-1}]	H-mode	7.48	5.84	1.64	2.98	2.47	0.511	2.51	1.39	1.12
	L-mode	12.3	4.39	7.88	11.8	2.03	9.76	8.20	0.952	7.25
$\frac{Q_{imp}^{L-mode}}{Q_{imp}^{H-mode}}$		1.6	0.75	4.8	4.0	0.82	19	3.3	0.69	6.5

Table 3.7: Implantation flux (Q_{imp}) value in the different zones of the divertor (defined in figure 3.37) during both H-mode and L-mode phases. The ions and atoms contribution to the total implantation flux is reported. The ratio between the L-mode and the H-mode fluxes, $Q_{imp}^{L-mode}/Q_{imp}^{H-mode}$, is also indicated.

		Outer PFCs			Upper PFCs			Inner PFCs		
		Total	Ions	Atoms	Total	Ions	Atoms	Total	Ions	Atoms
Q_{imp} [10^{22} s^{-1}]	H-mode	0.875	0.606	0.269	0.735	0.520	0.215	1.48	0.976	0.502
	L-mode	0.782	0.383	0.399	1.05	0.427	0.626	1.66	0.771	0.887
$\frac{Q_{imp}^{L-mode}}{Q_{imp}^{H-mode}}$		0.89	0.63	1.5	1.4	0.82	2.9	1.1	0.79	1.8

Table 3.8: Implantation flux (Q_{imp}) value in the different zones of the first-wall (defined in figure 3.37) during both H-mode and L-mode phases. The ions and atoms contribution to the total implantation flux is reported. The ratio between the L-mode and the H-mode fluxes, $Q_{imp}^{L-mode}/Q_{imp}^{H-mode}$, is also indicated.

4.4 Evolution of the experimental incident ion fluxes on the divertor.

In the following, one will briefly present the evolution the incident ion fluxes on the divertor between the two phases. A full experimental assessment of the evolution of the recycling flux between the two phases would have required a careful analysis and post-treatment of passive spectroscopy of the so-called Balmer lines (to determine the atomic hydrogen particle flux) and the Fulcher-α line (to determine the molecular flux). However, spectroscopy measures photon fluxes of the different rays and these photon

fluxes are then converted to particle fluxes through inverse photon-efficiency coefficients (often called S/XB coefficient for the atomic flux and D/XB for the molecular flux) [120]. These coefficients depend strongly on the electron density and temperature [116]. Due to the lack of estimation of both quantities from Langmuir probes, such analysis was unfortunately not possible during this PhD.

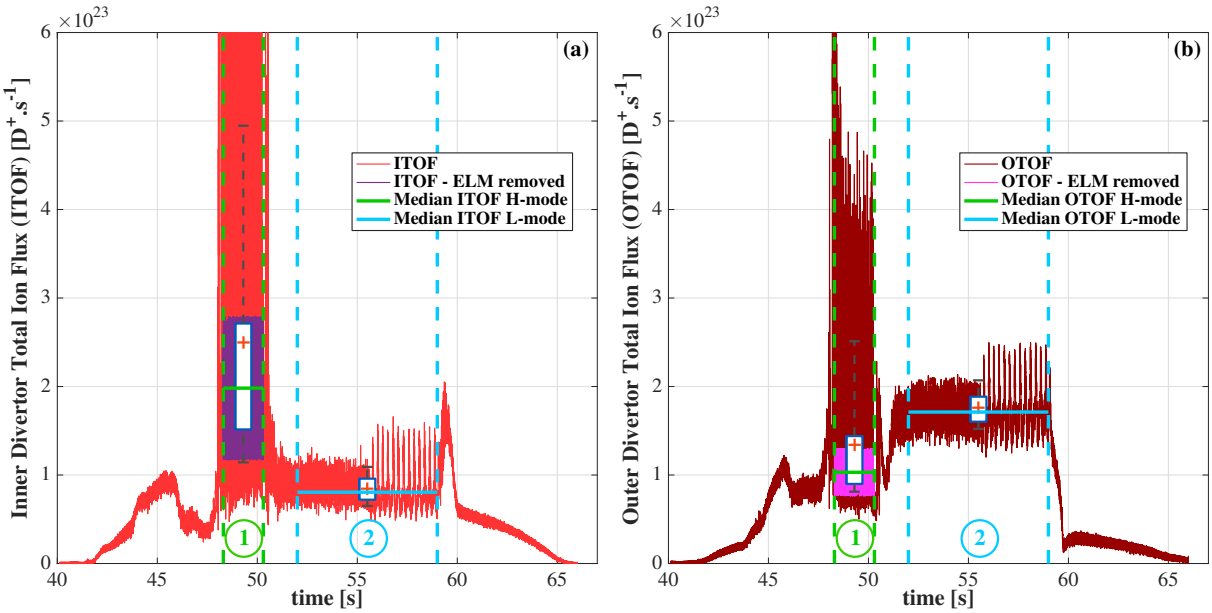

Figure 3.42: Total incident ion flux in the inner divertor ITOF (a) and in the outer divertor OTOF (b) measured by the Langmuir probes during #JPN89044. The two steady-state plasma phases are delimited by dashed lines. For the phase 1 (H-mode), the inter-ELM signal is also plotted. The statistics of the data sample during each phase are depicted using the boxplot.

The time evolution of the total ion flux in the inner divertor (ITOF in the JET nomenclature) and in the outer divertor (OTOF) obtained from the divertor Langmuir probes measurements are displayed in figure 3.42.a and in figure 3.42.b respectively. For the H-mode phase, the inter-ELM signals are also plotted. The statistics of the data in the time interval of each phase are depicted using the boxplot representation defined in subsection 2.1. The median of the data during each phase is also plotted. Both LP signals are highly scattered during the H-mode phase, with a skewness toward higher values due to the ELMs. On the contrary, the L-mode data seems to follow a normal distribution. Some ion flux peaks are observed at the end of this phase (for 55 s $\leq t \leq$ 59 s). These peaks are due to sawtooth oscillations of the core plasma reaching the SOL. During the H-mode phase, the inner flux is stronger than the outer signal while the reverse situation occurs during the L-mode phase. If one compares the evolution between the H-mode and the L-mode phase, the inner flux decreases while the outer flux increases.
The median values of both signals are reported in table 3.9 as well as the ratio of the L-mode flux to the H-mode flux. Such values can directly be confronted to the incident ion flux on the divertor zones given by SolEdge2D-EIRENE ($Q_{inc,ion}$, reported in

		Inner Divertor (ITOF)	Outer Divertor (OTOF)
$Q_{ion,LP}$ [10^{22} s^{-1}]	H-mode	19.8	10.3
	L-mode	8.06	17.1
$\frac{Q_{ion,LP}^{L-mode}}{Q_{ion,LP}^{H-mode}}$		0.41	1.7

Table 3.9: Total incident ion flux measured by the Langmuir probes ($Q_{ion,LP}$) in the inner divertor and in the outer divertor during both H-mode and L-mode phases (median values). The ratio between the L-mode and the H-mode fluxes, $Q_{ion,LP}^{L-mode}/Q_{ion,LP}^{H-mode}$, is also indicated.

table 3.1). For the inner divertor, $Q_{inc,ion}$ remains constant between the two phases ($Q_{inc,ion}^{L-mode}/Q_{inc,ion}^{H-mode} = 1.1$) in contradiction with the experimental ion flux which decreases ($Q_{ion,LP}^{L-mode}/Q_{ion,LP}^{H-mode} = 0.41$). If one compares the flux values, $Q_{inc,ion}$ is underestimated by 50 % for the H-mode phase (9.35×10^{22} D$^+$.s^{-1} in the simulation, 19.8×10^{22} D$^+$.s^{-1} in the experiment) while for the L-mode phase $Q_{inc,ion}$ is overestimated by 25 % (9.99×10^{22} D$^+$.s^{-1} in the simulation, 8.06×10^{22} D$^+$.s^{-1} in the experiment). For the outer divertor, the values of $Q_{inc,ion}$ in the tile 5 zone and in the outer divertor zone are added to allow the confrontation with the measurements. First, a qualitative agreement can be observed in the evolution between the two phases as the simulation predicts an increase of $Q_{inc,ion}$ by a factor of 1.4, while an increase by a factor of 1.7 is observed in the experiment. Likewise, a direct comparison of the fluxes can be done: for the H-mode phase $Q_{inc,ion}$ is very well estimated (10.1×10^{22} D$^+$.s^{-1} in the simulation, 10.3×10^{22} D$^+$.s^{-1} in the experiment) while for the L-mode phase $Q_{inc,ion}$ is underestimated by 17 % (14.1×10^{22} D$^+$.s^{-1} in the simulation, 17.1×10^{22} D$^+$.s^{-1} in the experiment). All these observations are in line with the confrontation of the J_{sat} profiles presented in subsections 2.4 and 3.4: a very good agreement of the outer profiles for both phases, a lower simulated inner profile for the H-mode phase and a relative agreement of the inner profiles for the L-mode phase. For the latter profiles, it must be pointed out that only five Langmuir probes are available in the inner SOL to calculate this flux (cf. figure 3.33). Moreover, from figure 3.42.a, one can see that the simulated value of $Q_{inc,ion}$ lies in the upper quartile of the experimental measurements. Last but not least, the error bars of the Langmuir probe measurements ($\sim$ 30 %) were not accounted. To conclude, except on the inner divertor during the H-mode phase, the incident ion flux on the divertor obtained in the simulation is in good agreement with the one measured by Langmuir probes: the ion integrated fluence that will be deposited on the divertor during the simulation of the sequence of discharges presented in the next chapter can be considered as representative of the experimental integrated fluence deposited during the plasma current flat-top phase of #JPN89044.

Conclusion of chapter 3:

– The two steady-state plasma phases of #JPN89044 have successfully been simulated with the SolEdge2D-EIRENE code. These two phases, which are assumed to be representative of the complete plasma discharge, can now be used as plasma backgrounds for simulations with the D-WEE code to initialise the wall.

– The simulation results have been confronted to the experimental measurements available during this discharge. The J_{sat} profiles on the divertor are consistent with the experimental profiles measured by Langmuir probes except for the H-mode phase where the inner experimental profile is higher. It results a good estimation of the incident ion flux on the divertor and therefore of the integrated ion fluence deposited during the plasma current flat-top phase of #JPN89044. However, no conclusion can be drawn on the resulting implantation flux density in the experiment due to the lack of estimation of T_e from Langmuir probes data.

– The simulations show the following evolutions in terms of implantation conditions between plasma phase 1 (H-mode) and plasma phase 2 (L-mode):

(1) the implanted ion flux decreases while the implanted atom flux sharply increases in all the JET zones defined in figure 3.37. It results a global increase of the implantation flux by a factor of 2 to 4 in the divertor zones while this flux remains almost constant in the first-wall zones.

(2) the ion and atom mean angles of incidence do not change in all the zones. It remains between 62° and 73° for the ions and between 32° and 43° for the atoms.

(3) the mean impact energy decreases for both ions and atoms by a factor of ~ 2 in all the first-wall, by a factor of ~ 8 in the inner divertor, by a factor of ~ 30 for the ions and of ~ 20 for the atoms in the tile 5, by a factor of ~ 3 for ions and of ~ 6 for the atoms in the outer divertor.

As indicated in chapter 2 subsection 2.8, one can expect that such sudden changes of the implantation conditions will impact the equilibrium filling ratio of the different traps (equation 2.46) and therefore the D inventory in the wall.

Chapter 4

Dynamic modelling of local fuel inventory and desorption in the whole tokamak vacuum vessel: application to the JET tokamak.

Contents

In chapter 2, the dynamic thermal desorption module D-WEE has been presented. This module is meant to be coupled with edge plasma transport code, like SolEdge2D-EIRENE, to study the feedback of the wall on the plasma. However, before launching coupled simulations, one has to define a realistic initial wall state (local fuel inventory and desorption flux density), ideally representative of the experimental one during a pulse. It is fundamental to determine this local wall state as it sets the wall behaviour w.r.t the fuel (pumping or fuelling areas) and the available fuel reservoir (retention). Such wall state cannot be fully evaluated experimentally. Indeed, post-mortem analysis are mostly performed weeks after tile removal, and therefore are representative of long-term fuel retention. In JET-ILW diverted discharges, a ratio of dynamic retention to long-term retention of 10 has been measured [15]. This indicates the prevailing role of dynamic retention during a discharge in this machine, mainly due to the time scale of the experimental discharges in this reactor (tens of seconds). Only gas balance analysis gives a global idea of this dynamic retention as it was seen in chapter 1 section 4. Still the local wall state cannot be extracted from this kind of experimental studies.
In the present chapter, a modelling approach is proposed to define this local wall state and is applied to a JET tokamak discharge. This approach was presented in chapter 2 section 5 and corresponds to the step 2 of our methodology of the modelling of an ELM – inter-ELM phase with SolEdge2D-EIRENE.

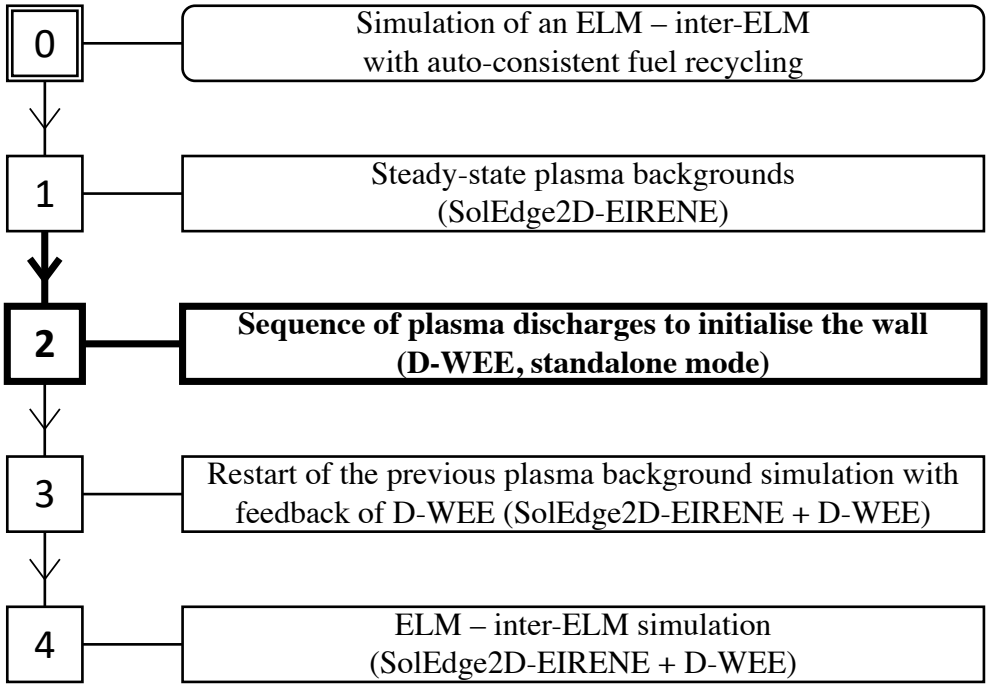

In this chapter, the simulation to initialise the wall is applied to the JET discharge number #89044 presented in the previous chapter whose different steady-state phases were modelled with SolEdge2D-EIRENE (cf. chapter 3 sections 2 and 3 for the H-mode phase and the L-mode phase respectively). A synthetic discharge is built from this

successive simulations and is used as a plasma background imposed to the D-WEE module to simulate a sequence of several discharges. The D-WEE inputs for each plasma phase (cf. figures 3.23 and 3.36) are imposed during the duration of the respective phase (cf. chapter 3 section 1), i.e. during 2 s for the H-mode phase and during 7 s for the L-mode phase. At this stage, due to computational reasons, only four successive pulses followed by 30 min of resting time have been simulated. The figure 4.1 exhibits the time evolution of the total implantation flux on the JET wall, $Q_{imp,tot}$ (cf. equation 3.11 and chapter 3 subsection 4.3 for its complete definition), which is considered in the following simulation. The four peaks indicate the plasma discharges. A zoom on the first discharge is also shown in the graphic window where one can see the increase of $Q_{imp,tot}$ between phase 1 (H-mode) and phase 2 (L-mode).

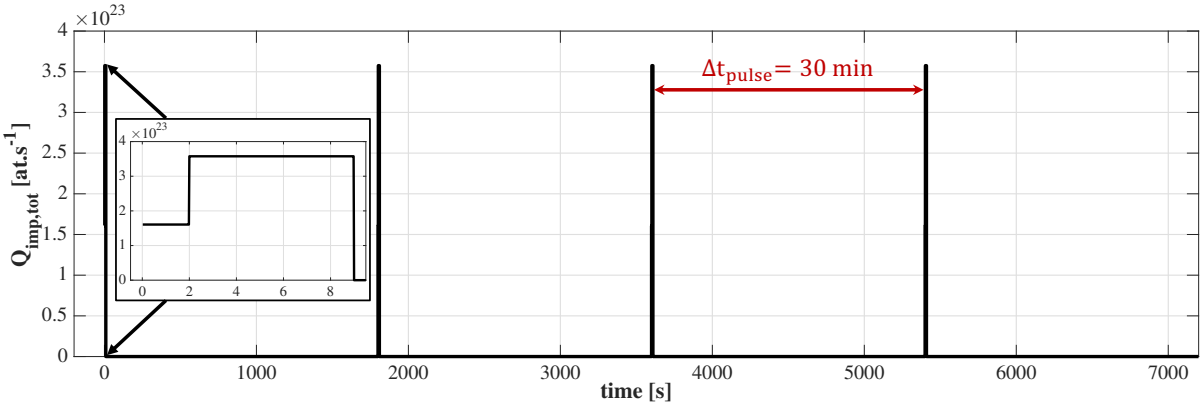

Figure 4.1: Time evolution of the total implantation flux $Q_{imp,tot}$ considered in the following simulation. The four consecutive peaks represent the different discharges. A 30 min resting time is considered in between each pulse. A zoom on the first pulse is shown in the graphic window.

In the following, the simulation of this four discharges will be presented and the results in terms of wall dynamics will be studied. For this simulation, the initial D density in the wall was taken equal to zero. Moreover, due to the lack in the literature of model of HI–Be interaction and of parameterisation of the R-D equations for the temperature of the Be first-wall in JET-ILW (cf. chapter 2 subsection 2.7), a full massive W wall configuration is considered in this simulation. The resulting local wall state at the end of the H-mode phase of the last discharge will also be presented. This local wall state will be used as initial condition for future plasma-wall interaction simulations with D-WEE coupled to SolEdge2D-EIRENE.

1 D-WEE simulation setup.

In this section, one will enumerate the different setups of the D-WEE module which were chosen for the simulation of sequence of discharges with D-WEE.

1.1 MHIMS: wall material setup.

For the MHIMS code, the main difficulty is to define a material distribution on the wall. Indeed, after two campaigns, JET-ILW exhibits a complex pattern of surface materials, with a mix of bulk materials in the net erosion zones and Be co-deposit layers in remote areas [78] (in the divertor but also on the edges of limiters). Moreover, as it was seen in chapter 2 subsection 2.7, no model of HI–Be interaction and/or parameterisation of the R-D equations are available in the literature for the temperature of the Be first-wall in JET-ILW (473 K / 200 °C). Therefore, as an initial simplified approach, a full massive W wall configuration has been assumed in the simulation. This choice of the materials composing the wall is purely arbitrary and the simulation presented here must be seen as a proof of principle of the initialisation of the wall with D-WEE.
Two types of massive W are considered on the wall: one in the divertor region and one in the first-wall region. The difference between the two types of massive W lies in the definition of the trap parameters and will be presented in the following. This wall configuration is displayed in figure 4.2. The zones where the pumping ducts are situated are also displayed in red solid line. D-WEE does not perform calculation in those two zones.

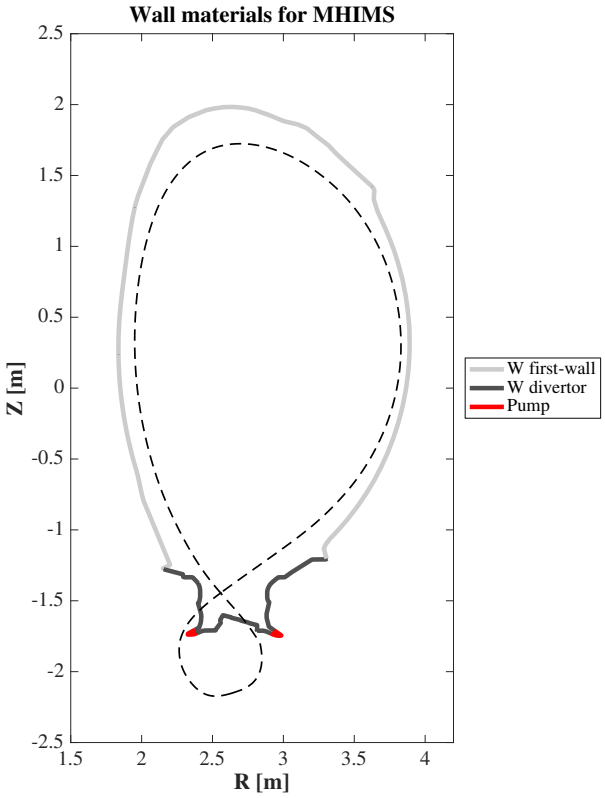

Figure 4.2: Distribution of materials of the JET tokamak considered in the D-WEE simulation. A full-W configuration of the JET wall is considered. The wall is composed of two types of W: one in the divertor region and one in the first-wall region. Their trap parameters are summed up in table 4.1.

Concerning MHIMS parameterisation, the parameters obtained by Hodille et al. for the interaction of D with PCW are used (cf. chapter 2 subsection 2.6). The parameters set by Hodille et al. are summed up in table 2.2. The diffusion coefficient from DFT is taken in [54]: $D(T) = 1.9\times10^{-7}\exp\left(-0.2/(k_BT)\right)$ m^2.s^{-1}. This diffusion coefficient was calculated for hydrogen. To take into account the isotope effect, the diffusion pre-exponential factor is divided by $\sim\sqrt{2}$, the square root of the mass ratio between D and H. For the traps, the free-parameters (detrapping energies and trap density profiles) obtained by Hodille et al. through fitting of TDS experiments (cf. chapter 2 subsection 2.6) are used. Three traps are considered: two intrinsic traps and one trap induced by plasma irradiation. The parameters of these traps are reported in table 4.1. The intrinsic traps have a flat depth profile (type "a" profile, cf. figure 2.3). Their density is equal to the value reported in the table. The plasma-induced trap presents two damaged zones like the ones reported in chapter 2 subsection 2.6: a highly damaged zone at the surface (in the implantation zone, with profile of type "c") and a damaged zone extending in the bulk of the material (with profile of type "b"). The densities reported in table 4.1 for trap 3 (n_3^i) are the maximum trap densities of each profile (at the surface of the material). The characteristic depths of each profile (X_3^i) are also reported in the table. The reader is referred to chapter 2 subsection 2.4 and figure 2.3 for more information about the different profiles of trap and their parameterisation. The trap parameters defined in table 4.1 are considered to be representative of a W wall which has experienced several hours of operation.

	Divertor	First-wall
Trap 1 (intrinsic)	$E_{dt,1} = 0.85$ eV	
Type a	$n_1^a = 0.13$ at.%	
Trap 2 (intrinsic)	$E_{dt,2} = 1.00$ eV	
Type a	$n_2^a = 0.035$ at.%	
Trap 3 (ion induced)	$E_{dt,3} = 1.5$ eV	
	$n_3^b(x=0) = 1$ at.%, $X_3^b = 11$ μm	$n_3^b(x=0) = 1$ at.%, $X_3^c = 2.7$ μm
Type b and c	$n_3^c(x=0) = 15$ at.%, $X_3^c = 30$ nm	$n_3^c(x=0) = 15$ at.%, $X_3^c = 20$ nm

Table 4.1: Trap parameters used in the simulation of sequence of plasma discharges with D-WEE. The trap densities are given in at.% of W. For intrinsic traps (type "a" profile), the trap densities are expected to be constant in all the depth of the material and equal to the values presented in this table (n_1^a and n_2^a respectively). The plasma-induced trap presents two damaged zones: a highly damaged zone at the surface (with profile of type "c") and a damaged zone extending in the depth of the material (with profile of type "b"). The densities reported for trap 3 (n_3^i) are the densities of trap at the surface of the material. The characteristic depths of each profile (X_3^i) are also reported. The reader is referred to chapter 2 subsection 2.4 and figure 2.3 for more information about the different profiles of trap.

As it can be seen in table 4.1, the difference between the two types of massive W in the divertor and in the first-wall lies in the definition of the trap 3. For both wall regions, one considers that the damaged implantation zone has reached its saturation value defined by Hodille et al., i.e. 15 at.% of W (cf. chapter 2 subsection 2.6). However, the extent of

this damaged zones differs in the two regions of the wall. In the divertor, it is considered that the implantation zone extends up to 30 nm which corresponds to the maximum implantation range of 1 keV D in W. Such implantation conditions can be found in the divertor during ELM events. For the first-wall region, this damaged region extends up to 20 nm which corresponds to the maximum implantation range of 0.5 keV D in W. One can expect that, during H-mode plasma, charge exchange neutrals with such energy escape from the pedestal region and hit the first-wall. Concerning the damaged zone in the bulk of the material, the penetration depth of this trap, related to diffusion of light impurities in the tungsten, can be estimated using the diffusion coefficient of this impurities D_{LI} calculated by Hodille et al. [60] and presented in chapter 2 subsection 2.6: $x_{diff} = 2\sqrt{D_{LI}(T)t}$. It was assumed that the divertor had experienced a working temperature of 1000 K during $\sim$ 1000 s of plasma operation while the first-wall was maintained at its base temperature of 473 K (200 °C) during the same time. This yields to respective values of the characteristic depth of the type "b" profile X_3^b of 11 μm for the divertor and 2.7 μm for the first-wall. In reality, the diffusion coefficient D_{LI} was calculated for the case of divertor-like implantation conditions, and in particular an incident flux density of 1×10^{21} D.m^{-2}.s^{-1} (cf. chapter 2 subsection 2.6). According to the SolEdge2-EIRENE simulations presented in the preceding chapter, the incident flux density on the first-wall is one order of magnitude lower. The effective operation time of the first-wall can therefore be considered as being ten times higher (i.e. $\sim$ 3 h).
To illustrate more concretely the difference between the different traps, their depth profiles are plotted in figure 4.3. Traps number 1 and 2 are similar for both first-wall and divertor regions. However, one can clearly see the different profiles for the trap 3 defined in the first-wall region and in the divertor region. Moreover, this figure exhibits the strong reservoir capability of the trap 3 in the implantation zone.
In order to compare the dynamics of both materials, synthetic TDS experiments have been simulated with MHIMS for both types of W. A slow heating rate (0.25 K.s^{-1}) has been considered in order to differentiate the different peaks, which are signs of detrapping from the different traps. As an initial condition, the 3 traps are considered saturated up to a depth of 15 μm and the sample is at 300 K. The two TDS spectra are displayed in figure 4.4). The spectra present two similar low-temperature peaks: one around 400 K and another one around 600 K that can be attributed to trap 1 and trap 2 respectively. However, the two spectra differ for the trap 3 due to its deeper density profile in the divertor region. The peak is much higher in the case of the divertor region which indicates a higher retention in this trap. Moreover, a shift of the peak position towards high temperature can be observed ($\sim$ 720 K for the first-wall, 800 K for the divertor). This shift is attributed to multiple *diffusion – trapping – detrapping* cycles of a single D atom during its transport up to the surface, phenomenon often referred to as *retrapping*, and which is known to delay the D desorption [121, 71]. The retrapping effect is higher in the case of the W in the divertor due to the extended depth of the trap 3. Overall, the total D inventory is almost twice higher in the divertor W than in the first-wall W (5.3×10^{21} D.m^{-2} and 2.6×10^{21} D.m^{-2} respectively).
In the following, an arbitrary differentiation of the traps is used, which is defined to

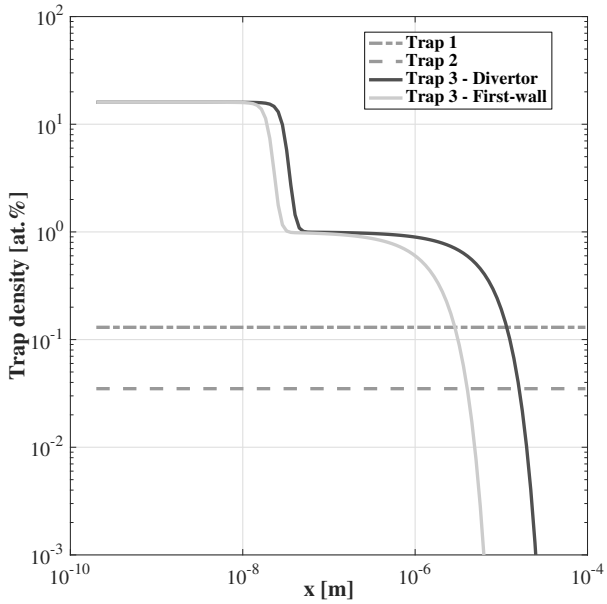

Figure 4.3: Density profile for the three types of trap of the W materials considered in the D-WEE simulation. Trap 1 and trap 2 (intrinsic traps) have a constant density and are similar for the W in the first-wall and for the W in the divertor. The profile of trap 3 differs for the two regions of the wall and is more extended for the divertor region.

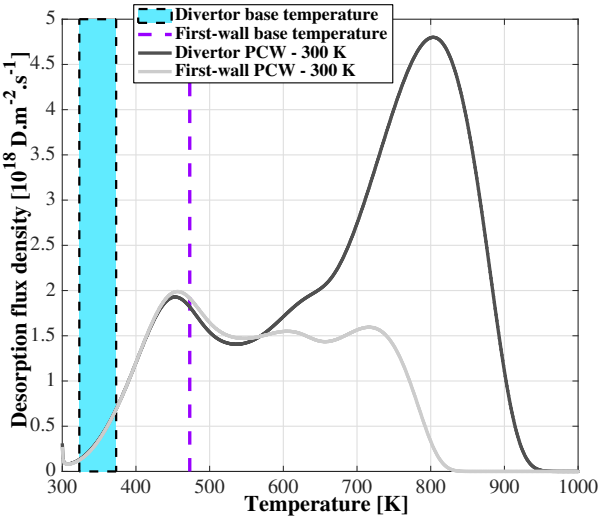

Figure 4.4: Synthetic TDS spectra of the two types of tungsten (PCW) considered in the D-WEE simulation: in dark grey the W in the divertor, in light grey the W in the first-wall. As initial condition, traps are considered saturated up to a depth of 15 μm. A heating rate of 0.25 K.s^{-1} has been considered. The base temperatures of the divertor zone and the first-wall zone in JET-ILW are also indicated.

highlight their dynamic retention capability in the following simulation. For the first-wall, traps 1 and 2 are gathered and labelled as *low-energy traps* (with $E_{dt,i} \leqslant 1$ eV) while trap 3 is labelled as *high-energy trap*. For the divertor, the *low-energy trap* refers to trap 1 while the *high-energy traps* (with $E_{dt,i} \geqslant 1$ eV) refer to traps 2 and 3. The

difference of merging of traps between the divertor and the first-wall, especially for the trap 2, is due to the difference of base temperature of these two zones. This temperature difference entails a different dynamical behaviour of the traps that will be highlighted and explained later in this report.

1.2 WEE-temp: JET PFCs setup.

JET-ILW tokamak is composed of inertially-cooled PFCs. As it was presented in chapter 2 subsection 3.3, in WEE-temp, such PFCs are simulated like actively-cooled PFCs with a very low heat convection coefficient (100 $W.m^{-2}.°C^{-1}$). This enables the model to mimic the cooling of the PFCs by radiation and by heat conduction into the tokamak structure between the pulses, while keeping their inertial behaviour during plasma exposure. JET-ILW has 19 different PFCs which are distributed in 22 different zones in the VV (cf. figure 3.22). Each PFC is defined by its material layers:

- The first-wall PFCs are made of massive Be.
- The inner and outer divertor tiles are made of a thick layer of CFC with on top of it a W-coating layer of 15 μm.
- The different stacks of tile 5 are made of massive W.

The adjustment procedure defined in chapter 2 subsection 3.3 for inertial PFCs is applied to each PFC of the JET-ILW to define the thickness of the main material layer e_{eff} (Be for first-wall PFCs, CFC for inner and outer divertor tiles and W for the tile 5 stacks). An equivalent slab geometry of the PFC is set by defining an effective thickness, $e_{eff} = V_{tile}/A_{wetted}$, where V_{tile} is the tile volume and A_{wetted} is the wetted surface of the tile. For each PFC, V_{tile} and A_{wetted} are taken from CAD drawings. Those two geometrical parameters as well as the resulting e_{eff} for the JET-ILW are summed up in tables 4.2, 4.3, 4.4 and 4.5. The values of e_{eff} range from 2 to 5 cm. As shown by equation 2.73, this procedure enables the different zones where the heat flux density is uniform to experience a good inter-pulse temperature increase plasma after plasma (provided that the energy accumulated by the tile, given by the SolEdge2D-EIRENE simulation, is correct).
However, such procedure is not working in regions where the heat flux density is peaked and reaches a high value, i.e. in the tiles hosting the strike-points (tile 3 and tile 5 Stack C in our present case). As an example, if a 10 $MW.m^{-2}$ heat flux density is applied during 5 s on both tiles, i.e. an energy fluence of 50 MJ, the resulting inter-pulse temperature increases, ΔT, can be estimated using equation 2.71 and considering the effective thicknesses reported in tables 4.3 for tile 3 and in table 4.4 for tile 5 Stack C):

- for tile 3:

$$\Delta T(x) \approx \frac{\mathscr{F}_E}{\rho_{CFC} \cdot c_{p_{CFC}} \cdot e_{CFC}}$$
$$\Delta T(x) \approx \frac{10 \times 10^6 \cdot 5}{1900 \cdot 1031 \cdot 41 \times 10^{-3}}$$
$$\Delta T(x) \approx 750 \text{ °C}$$

– for tile 5 Stack C:

$$\Delta T(x) \approx \frac{\mathscr{F}_E}{\rho_W \cdot c_{p_W} \cdot e_W}$$
$$\Delta T(x) \approx \frac{10 \times 10^6 \cdot 5}{132 \cdot 19279 \cdot 34 \times 10^{-3}}$$
$$\Delta T(x) \approx 600 \text{ °C}$$

This temperature increase will add pulse after pulse, leading to an extremely high temperature at both strike-points. The convection at the rear side of the PFC is not high enough to remove the energy stored by the tile. In reality, such high temperatures are not reached in the tokamak. Indeed, the temperature of those tiles homogenises between discharges due to transverse heat conduction. Such homogenisation cannot be simulated by WEE-temp as the heat equation solved by the code is 1D. In order to avoid inter-pulse over-heating, the two PFCs hosting the strike-points, i.e. tile 3 for inner strike-point and tile 5 Stack C for outer strike-point, have seen their effective thickness increased to 200 mm for the CFC layer and for the W layer respectively. Such thickness will give a temperature increase of ~ 100 °C for the heat load conditions described above (10 MW.m^{-2} during 5 s).
Eventually, the base temperature of the different PFCs (at the start of a day of operation) is taken from thermocouple measurements at the beginning of the session for the divertor region, leading to temperatures ranging between 50 and 70 °C. Such measurements are not available for the first-wall PFCs. They are considered at the minimum working temperature of the JET-ILW first-wall (i.e. 200 °C, cf. chapter 1 section 2) at the start of the simulation. Moreover, the value of the material thermal properties (thermal conductivity, specific heat and material density) have been considered at the closest temperature to the base temperature of the different regions of the vacuum vessel [84].

	Inner Limiter	Saddle Coil	Outer Limiter	Mushroom	Dump Plate
V_{tile} [m^3]	4.37×10^{-4}	3.09×10^{-5}	6.13×10^{-4}	1.93×10^{-4}	3.54×10^{-4}
A_{wetted} [m^2]	1.15×10^{-2}	1.90×10^{-3}	1.36×10^{-2}	8.72×10^{-3}	1.08×10^{-2}
e_i [mm] Be	**38**	**16**	**45**	**22**	**33**
h_{eff} [W.m^{-2}.°C^{-1}]	100	100	100	100	100
T_0 [°C]	200	200	200	200	200

Table 4.2: WEE-temp parameters of the PFCs composing the first-wall considered in the D-WEE simulation. The effective thickness of the main material of each PFC, e_{eff}, are indicated in bold (cf. chapter 2 subsection 3.3 for the calculation procedure of e_{eff}).

To conclude on the simulation inputs, it must be noticed that all the parameters related to the wall materials in SolEdge2D-EIRENE (to calculate the reflection coefficient) and in WEE-temp (thermal parameters) are consistent with the JET-ILW materials. This means that not only the implantation conditions but also the thermal dynamics of the

		HFGC tile	Tile 1	Tile 3	Tile 4	Tile 5 Protec
V_{tile} [m^3]		5.57×10^{-4}	1.44×10^{-3}	2.19×10^{-3}	1.20×10^{-3}	1.87×10^{-4}
A_{wetted} [m^2]		1.90×10^{-2}	3.74×10^{-2}	5.40×10^{-2}	3.24×10^{-2}	8.98×10^{-3}
e_i [mm]	W	15×10^{-3}	15×10^{-3}	15×10^{-3}	15×10^{-3}	15×10^{-3}
	CFC	**29**	**39**	41 $\Rightarrow$ **200**	**37**	**21**
h_{eff} [W.m^{-2}.°C^{-1}]		100	100	100	100	100
T_0 [°C]		70	70	75	40	50

Table 4.3: WEE-temp parameters of the PFCs composing the inner divertor considered in the D-WEE simulation. The effective thickness of the main material of each PFC, e_{eff}, are indicated in bold (cf. chapter 2 subsection 3.3 for the calculation procedure of e_{eff}).

		Tile 5 Stack A	Tile 5 Stack B	Tile 5 Stack C	Tile 5 Stack D
V_{tile} [m^3]		1.07×10^{-5}	1.08×10^{-5}	1.26×10^{-5}	1.16×10^{-5}
A_{wetted} [m^2]		5.09×10^{-4}	3.55×10^{-4}	3.68×10^{-4}	5.55×10^{-4}
e_i [mm]	W	**21**	**30**	34 $\Rightarrow$ **200**	**21**
h_{eff} [W.m^{-2}.°C^{-1}]		100	100	100	100
T_0 [°C]		50	50	50	50

Table 4.4: WEE-temp parameters of the PFCs composing the tile 5 of the divertor considered in the D-WEE simulation. The effective thickness of the main material of each PFC, e_{eff}, are indicated in bold (cf. chapter 2 subsection 3.3 for the calculation procedure of e_{eff}).

		Tile 6	Tile 7	Tile 8	Tile B	Tile C
V_{tile} [m^3]		1.03×10^{-3}	2.60×10^{-3}	1.77×10^{-3}	6.30×10^{-4}	4.21×10^{-4}
A_{wetted} [m^2]		3.42×10^{-2}	6.42×10^{-2}	4.33×10^{-2}	2.59×10^{-2}	1.89×10^{-2}
e_i [mm]	W	15×10^{-3}	15×10^{-3}	15×10^{-3}	15×10^{-3}	15×10^{-3}
	CFC	**30**	**40**	**41**	**24**	**22**
h_{eff} [W.m^{-2}.°C^{-1}]		100	100	100	100	100
T_0 [°C]		35	50	50	50	50

Table 4.5: WEE-temp parameters of the PFCs composing the outer divertor considered in the D-WEE simulation. The effective thickness of the main material of each PFC, e_{eff}, are indicated in bold (cf. chapter 2 subsection 3.3 for the calculation procedure of e_{eff}).

wall obtained from the simulation are representative of the JET-ILW. Only the input parameters considered for MHIMS are not consistent with the JET-ILW.

2 Simulation of four consecutive discharges with D-WEE.

In the following, the wall dynamics during the four discharges and in between discharges will be investigated.
Prior to that, some physical quantities must be introduced before presenting the simulation results. The outgassing flux Q_{out} [at.s^{-1}] is calculated using equation 3.11 and considering the desorption/outgassing flux density Γ_{out} calculated by D-WEE. It has to be remembered that the deuterium desorbs in the form of D_2 molecules so that the real molecular flux is half the value of Q_{out}. For conveniency, one will keep on expressing this flux in atomic form [D.s^{-1}].
Moreover, the wall particle inventory given by the simulation will be presented. Such inventory can be calculated from D-WEE results through the following integral:

$$N_{wall,*}(t) = \int_{s_1}^{s_2} \int_0^{L(s)} \int_0^{2\pi} n_*(s,x,t) R(s)\, ds\, dx\, d\varphi \tag{4.1}$$

where $N_{wall,*}$ is the considered wall inventory [at] related to the wall particle density n_* [at.m^{-3}] ($*$ being either mobile or trapped particles) and L is the maximum depth of the material [m]. Again s_1 and s_2 are the curvilinear coordinates of the considered zone boundaries. D-WEE directly provides the integral of n_* with respect to x. Such integral, which was introduced in chapter 2 subsection 2.8 (in the LHS of equation 2.35), is the areal inventory Inv_*:

$$Inv_*(s,t) = \int_0^{L(s)} n_*(s,x,t)\, dx \tag{4.2}$$

Therefore equation 4.1 yields:

$$N_{wall,*}(t) = 2\pi \int_{s_1}^{s_2} Inv_*(s,t) R(s)\, ds \tag{4.3}$$

As examples, the total D inventory in the JET wall, N_{wall}, and the D inventory of trap 1 in the tile 5 zone, $N^{tile5}_{wall,t,1}$, can be expressed as follows:

$$N_{wall}(t) = 2\pi \int_0^{s_{max}} \left(Inv_m(s,t) + \sum_{i=1}^{N_{trap}} Inv_{t,i}(s,t) \right) R(s)\, ds$$

$$N^{tile5}_{wall,t,1}(t) = 2\pi \int_{s_1^{tile5}}^{s_2^{tile5}} Inv_{t,1}(s,t) R(s)\, ds$$

where Inv_m is the mobile areal inventory and $Inv_{t,i}$ is the trapped particle areal inventory in the trap of kind i. All these quantities will be used in the following to illustrate the wall dynamics during the simulation.

2.1 Overview of the wall dynamics during the sequence of discharges.

In this subsection, the overall wall dynamics during the sequence of four discharges is investigated.

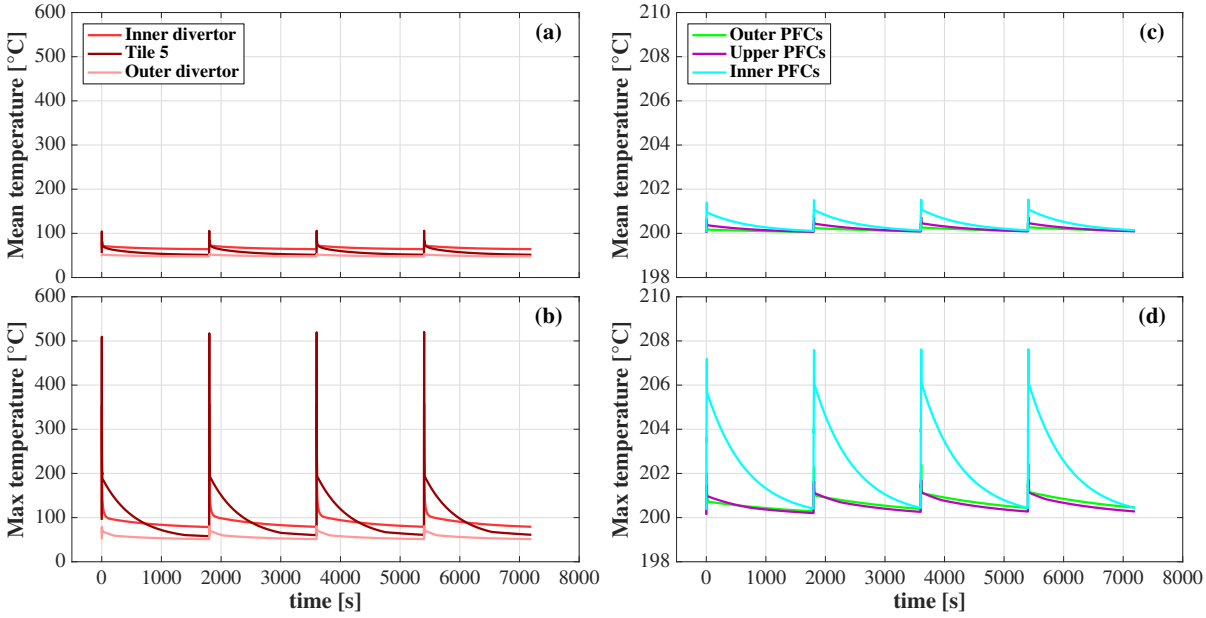

Figure 4.5: Time evolution of the mean and maximum PFC surface temperatures in the divertor zones ((a) and (b) respectively), and in the first-wall zones ((c) and (d) respectively) calculated by the thermal model WEE-temp during the sequence of four plasma discharges. The considered zones of the JET wall are displayed in figure 3.37.

The time evolution of the mean and maximum surface temperatures for each zone of the JET wall defined in figure 3.37 are displayed in figure 4.5. Each temperature peak indicates a plasma discharge. The first-wall zones do not exhibit a strong temperature excursion during the different discharges, with a mean temperature around their base temperature of 200 °C and a maximum temperature which does not exceed 208 °C. The same observation can be made for the outer divertor zone which remains around its base temperature of $\sim$ 50 °C. This is due to the fact that the heat flux density does not exceed 0.1 MW.m^{-2} in all these zones during both phases (cf. figures 3.23.d and 3.36.d). It must be pointed out that the radiative energy source from the core has not be accounted in the D-WEE simulation as the core plasma is not simulated in SolEdge2D-EIRENE. Therefore, the heat flux density in the first-wall is underestimated in the simulation. The two divertor zones hosting the strike-points undergo stronger temperature excursions during the pulses. The maximum temperature rises from 75 °C to $\sim$ 500 °C in the tile 5 zone (vicinity of outer strike-point) and from 50 °C to $\sim$ 350 °C in the inner divertor zone (vicinity of inner strike-point). These increases are due to the strong net heat flux density during the H-mode in these two locations, respectively of 5.9 MW.m^{-2} and 4.2 MW.m^{-2}. However the mean temperature remains below 100 °C in both zones which may indicate that the strong temperature increase is limited to the tiles hosting the two strike-points.

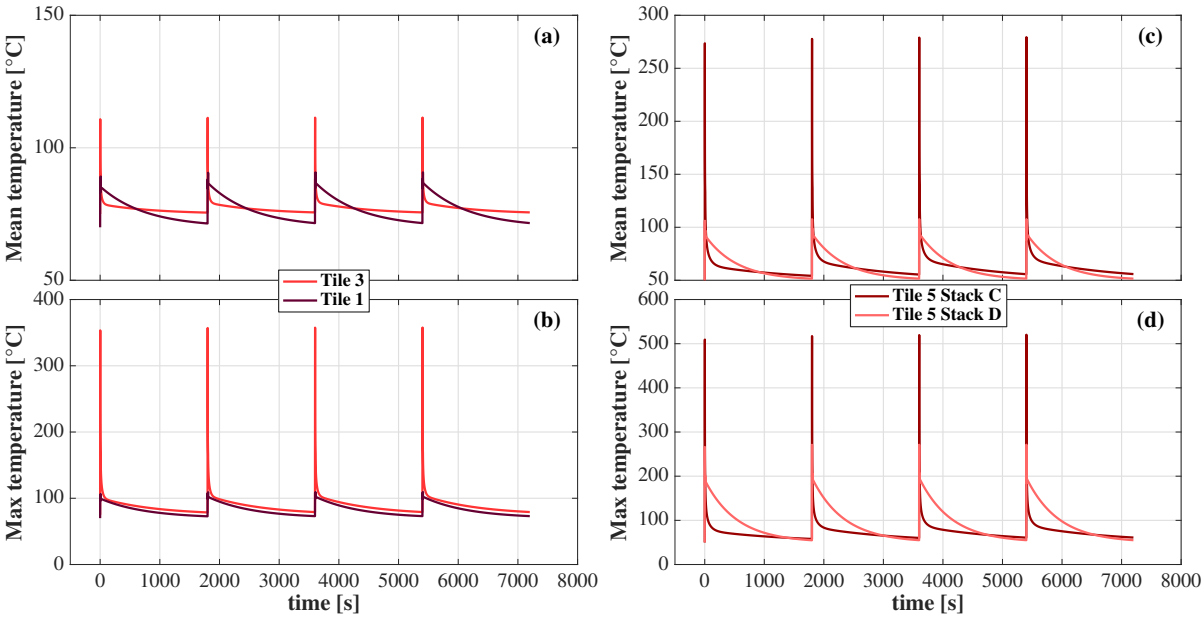

Figure 4.6: Time evolution of the mean and maximum surface temperatures of the tile 1 (inner far-SOL) and tile 3 (inner strike-point) in (a) and (b) respectively, and of the tile 5 stack C (outer strike-point) and tile 5 stack D (outer far-SOL) in (c) and (d) respectively.

In figure 4.6, the time evolution of the mean and maximum surface temperatures in the tile 3 (inner strike-point, figures (a) and (b) respectively) and in the tile 5 Stack C (outer strike-point, figure (c) and (d) respectively) are displayed. The temperature of the neighbouring tiles in the inner far-SOL (tile 1) and in the outer far-SOL (tile 5 stack D) are also plotted. These plots confirm that the strong temperature excursions during plasmas occur in tile 3 and in tile 5 stack C which host the strike-points. The tile 1 undergoes lower temperature excursions during plasmas with a maximum temperature of 109°C (cf. figure 4.6.b) and a mean temperature of 91 °C (cf. figure 4.6.a) due to very low heat flux densities on this tile (lower than 0.5 MW.m^{-2}). In tile 5 stack D, the temperature excursions are higher, with a maximum temperature of 270 °C and a mean temperature of up to 108 °C which are both reached at the end of the H-mode phase. Indeed, this tile is submitted to stronger heat flux density during the H-mode, with a maximum value of $\sim$ 3 MW.m^{-2} calculated by SolEdge2-EIRENE.
These temperature evolutions can be qualitatively confronted to experimental temperature measurements. In JET-ILW, four thermocouples are embedded at 1 cm depth in the divertor tiles 1 and 3 (cf. figure 4.7.a). These thermocouples give access to the temperature during discharges but also between discharges. Unfortunately, no thermocouples are available in the different stacks of tile 5. The temperatures measured by the thermocouples of tile 1 and tile 3 during the discharge 89044 and during the following resting time are respectively plotted in figure 4.7.b and figure 4.7.c. The discharge can be identified by the increase of the temperature measured by all the thermocouples. The highest temperatures during the discharge are measured by the thermocouple T1L on tile 1 (90 °C) and T3U on tile 3 (106 °C) as they are closer to the inner strike-point (cf. figure

4.7.a for the reference of each thermocouple). These values cannot be directly compared to the simulated values as they are not representative of the surface temperature of the tiles. However, one can note that the mean surface temperatures given by the thermal model during the discharge on tile 1 (90 °C) and on tile 3 (111 °C) are consistent with the measured values. The confrontation of the simulated temperatures to the temperatures measured by thermocouples enables to verify if the cooling process of inertial tiles that occurs between discharges is qualitatively reproduce by the thermal model. From the experimental temperature measurements, two time intervals can be identified after the discharge, each one highlighting characteristic thermal dynamics of inertial tiles between discharges. These intervals are denoted A and B for tile 1 (cf. figure 4.7.b), A' and B' for tile 3 (cf. figure 4.7.c). At the end of the time intervals A and A', the temperatures measured by the two thermocouples of each tile, which were different at the end of the discharge, tend to equalise: the temperature in the two tiles homogenises due to heat conduction in the respective tiles. The homogenisation lasts $\sim$ 350 s in tile 1 and $\sim$ 450 s in tile 3. During the time intervals B and B', the temperatures measured by the thermocouples of each tile are equal and decrease. This temperature drop, due to the cooling of the tile by surface radiation and by heat diffusion into the tokamak structure, is progressive and lasts during all the resting time of the reactor. One can note a similar

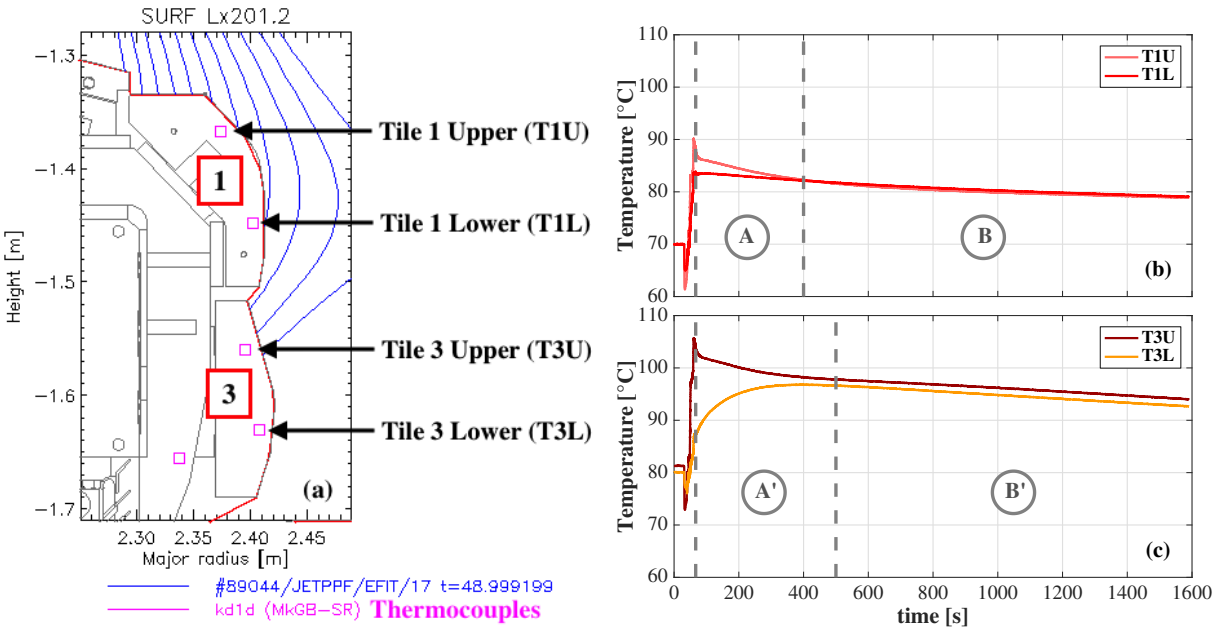

Figure 4.7: (a) Locations of the thermocouples (magenta squares) embedded at 1 cm depth in the divertor tiles 1 and 3. The #JPN89044 H-mode phase magnetic equilibrium is also displayed (blue lines). Time evolution of the temperatures measured by the different thermocouples in tile 1 (b) and in tile 3 (c) after the pulse #JPN89044. Two time intervals are identified (named A and B for tile 1, A' and B' for tile 3) which correspond respectively to the homogenisation of the temperature in the tiles after the pulse (A and A') and to the cooling of the tiles by surface radiation and by heat conduction into the tokamak structure (B and B').

behaviour for tile 1 and tile 5 stack C in figure 4.6: the mean and maximum surface temperatures from the simulation exhibit a continuous decrease between two discharges. 400 s after the end of a discharge, the mean and maximum surface temperatures in tile 1 are already below 90 °C as in the experiment. However this is not the case on tile 5 stack D as the maximum surface temperature is still around 120 °C, while the mean surface temperature is already around 70 °C. Indeed, the homogenisation of the temperature in the tiles cannot be modelled by WEE-temp as this code solves the 1D heat equation. For the two tiles hosting the strike-points, the temperature dynamics is more abrupt and the temperature of the tiles decreases rapidly at the end of a discharge. This dynamics is due to the effective thickness of the tiles which has been artificially increased (cf. subsection 1.2). Indeed, the heat conduction in the depth of the thick material (CFC for tile 3, W for tile 5 stack C) leads to an artificial cooling of the tile surface. In the 400 s after the end of the discharge n°4, the maximum temperature on tile 3 decreases from 167 °C to 94 °C which is in good agreement with the temperature given by the thermocouples (cf. figure 4.7.c). However, the mean surface temperature of tile 3 is already around 75 °C which indicates that the cooling of the tile is overestimated by the increase of the tile depth. As a conclusion, the adjustment procedure of inertial tiles described in chapter 2 subsection 3.3 seems to be sufficient for tiles which are submitted to low heat flux densities (< 1 MW.m^{-2}) like tile 1. However, this procedure is not sufficient for tiles with non-homogeneous high heat flux densities (≥ 1 MW.m^{-2}) like tile 3, tile 5 stack C and tile 5 stack D. The addition of transverse heat transport seems to be required to avoid an underestimation (in tile 3 and tile 5 stack C) or an overestimation (in tile 5 stack D) of the tile temperature between the discharges.
Concerning the thermal dynamics discharge after discharge, the maximum temperature given by the thermal model before and during each simulated discharge are summed up in table 4.6. The temperatures are similar from the second discharge which indicates that an equilibrium has been reached between the energy accumulated by the tiles during the discharge and the energy evacuated between discharges. However, the temperature increase between two discharges is underestimated for both tile 1 and tile 3. Indeed, 25 min after the end of #JPN89044, the thermocouples indicate a temperature increase of +9 °C for tile 1 and of +14 °C for tile 3 (cf. figure 4.7) while the simulation gives +3 °C and +4 °C for the respective tiles. The heat convection coefficient considered to cool down the tiles is probably too high.

Now one will focus on the dynamics of outgassing and retention during the sequence of discharges. The time evolutions of the total D outgassing flux $Q_{out,tot}$ [at.s^{-1}] and of the total D wall inventory $N_{wall,tot}$ [at] were calculated from the D-WEE simulation results of the sequence of discharges. These time evolutions are shown in figure 4.8. $Q_{out,tot}$ undergoes a steep increase (five orders of magnitude) during each pulse (due to plasma exposure), followed by a sharp decrease at the plasma shutdown. This decrease is then weaker up to the next pulse. The outgassing flux from the different zones of the wall (cf. figure 3.37) is also displayed. The first-wall PFCs are clearly dominating the outgassing in between pulses. The time evolution of the D trap inventory N_{wall} is also

	Discharge n°		1	2	3	4
Max temperature	Tile 1	Before discharge	70	73	73	73
		During discharge	106	109	109	109
	Tile 3	Before discharge	75	79	79	79
		During discharge	353	357	358	358
	Tile 5 C	Before discharge	50	58	60	61
		During discharge	509	517	520	520
	Tile 5 D	Before discharge	50	55	55	55
		During discharge	266	271	271	271

Table 4.6: Maximum temperature given by the thermal model WEE-temp before and during each simulated discharge on tile 1 (inner far-SOL), tile 3 (inner strike-point), tile 5 stack C (outer strike-point) and tile 5 stack D (outer far-SOL). The temperatures are similar from the second discharge which indicates that an equilibrium has been reached between the energy accumulated by the tiles during the discharge and the energy evacuated between discharges.

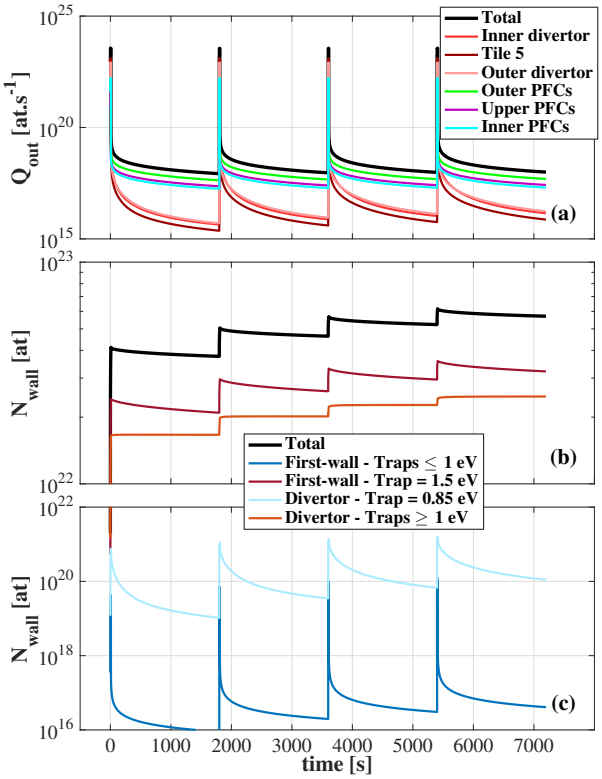

Figure 4.8: Time evolution of D outgassing flux Q_{out} (a) and D wall inventory N_{wall} (b-c). Each peak of outgassing indicates a plasma discharge. The outgassing fluxes from the different zones of the JET wall (cf. figure 3.37) are also displayed in (a). The inventories of the first-wall and divertor traps (b-c) are arbitrarily differentiated according to their detrapping energies (cf. subsection 1.1).

plotted for the first-wall and for the divertor (cf. figure 4.8.b-c), with the differentiation for the low-energy and high-energy traps defined in subsection 1.1. Most of the total wall inventory is found in the high-energy traps (cf. figure 4.8.b), mainly in trap 3 due to the combination of its high detrapping energy with its high density. However, the inventories of the high-energy traps do not share the same temporal evolution in between pulses: the divertor inventory tends to increase slightly (+2 % in the 30 min after the 4^{th} pulse) while the first-wall one decreases (−10 % in the same time period). This can be explained by the different base temperatures of the two VV regions. Indeed, the first-wall remains at 200 °C leading to detrapping from trap 3 in between pulses (while trap 1 and 2 do not seem to retain D during the pulses, cf. figure 4.8.c). As indicated earlier in this subsection, the divertor mean temperature remains between 50 and 80 °C between discharges. In this temperature interval, the detrapping characteristic time $1/\nu_{dt,i}$ ranges between 50 and 400 s for trap 2 and between 10^8 and 10^{10} s for trap 3. Therefore, D is efficiently retained in those two traps, even between the pulses. The low-energy trap 1 also retains D during plasma exposure, but releases its population in between pulses. Indeed, its detrapping characteristic time $1/\nu_{dt,1}$ ranges between 0.1 and 2 s in the range of temperature of the divertor between discharges. These detrapped particles diffuse in the material, partly up to the surface (leading to outgassing), but also in the bulk material where they fill the empty high-energy traps 2 and 3. This phenomenon has been exposed in [36] and will be highlighted in section 4. However, this effect is only transitory and will decrease plasma after plasma as the bulk high-energy traps get more and more filled in the depth of the material.

2.2 Wall dynamics during the four discharges.

This subsection focuses on the wall dynamics during the four discharges. First, the evolution of the surface temperature of the PFCs, which has been extensively studied in the previous subsection, will be briefly discussed. The time evolution of the mean and maximum surface temperatures for each zone of the JET wall defined in figure 3.37 are displayed in figure 4.9 for each of the four discharges. As indicated previously, the first-wall zones exhibit a very limited temperature increase during the discharge, with a maximum temperature reaching $\sim$ 208 °C at the end of the 4^{th} discharge (cf. figure 4.9.d). One can note that the maximum temperature increases during both plasma phases and exhibits a linear increase during plasma phase 2 (for $t > 2$ s) which is characteristic of inertial PFCs (as seen in chapter 2 section 3.3 and in appendix C). This anedoctal temperature is found in the inner lower protection zone where the maximum heat flux density of the first-wall is found during both phases (between 0.04 and 0.05 MW.m^{-2}. On the contrary, the evolution of the surface temperature in the divertor zones is similar and present an increase of the temperature during the plasma phase 1 followed by a decrease during plasma phase 2. This evolution is explained by the stronger heat flux densities found during the H-mode which induce this strong temperature increase. During the L-mode phase, the heat flux densities drop as the plasma is detached in both divertor targets. The heat accumulated at the surface of the material during the H-mode is conducted in the depth of the material, yielding to a cooling of the surface. As indicated

in the previous subsection, the two divertor zones hosting the strike-points undergo the strongest temperature excursions during the discharges, reaching during the 4$^{\text{th}}$ discharge 358 °C in the tile 3 (inner strike-point) and 520 °C in the tile 5 stack C (outer strike-point) at the end of the H-mode phase (cf. figure 4.9.b). During the L-mode phase, the maximum temperatures decrease up to $\sim$ 167 °C at the outer strike-point and up to 207 °C at the inner strike-point.

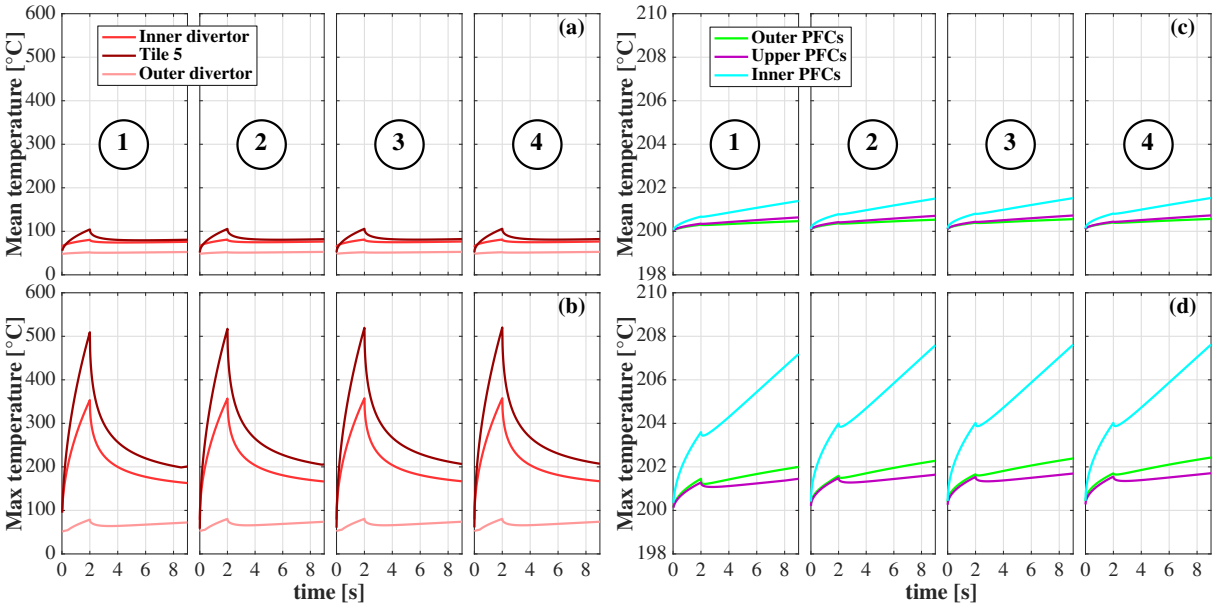

Figure 4.9: Time evolution of the mean and maximum PFC surface temperatures in the divertor zones ((a) and (b) respectively), and in the first-wall zones ((c) and (d) respectively) calculated by the thermal model WEE-temp during each of the four plasma discharges (indicated by their number). The considered zones of the JET wall are displayed in figure 3.37. Plasma phase 1 (H-mode) occurs for 0 s $\leq t \leq$ 2 s while plasma phase 2 (L-mode) occurs for 2 s $< t \leq$ 9 s.

The time evolution of the total outgassing flux $Q_{out,tot}$ during the plasma phase 1 and plasma phase 2 of the four consecutive discharges are displayed in figure 4.10.a and figure 4.10.b respectively. The total implantation flux $Q_{imp,tot}$ during each phase, which were extensively studied in chapter 3 subsection 4.3, is also plotted in both figures. As expected, $Q_{out,tot}$ tends to $Q_{imp,tot}$, which is a sign of the wall surface saturation. Its time evolution is very similar plasma after plasma and shows from the second plasma an apparent quick saturation in less than a second during the plasma phase 1 (cf. figure 4.10.a). During plasma phase 2, $Q_{out,tot}$ tends to $Q_{imp,tot}$ from the first plasma (cf. figure 4.10.b).
The lower part of figure 4.10 shows the time evolution of different retention fluxes: the total retention flux, $Q_{ret,tot} = Q_{imp,tot} - Q_{out,tot}$, and the retention fluxes related to the traps, defined as the positive time derivative of their respective inventory $dN_{wall,t,i}/dt$. As introduced in subsection 1.1, the trap retention fluxes are arbitrarily gathered according to the detrapping energies of the traps. First, one will focus on the evolution during the

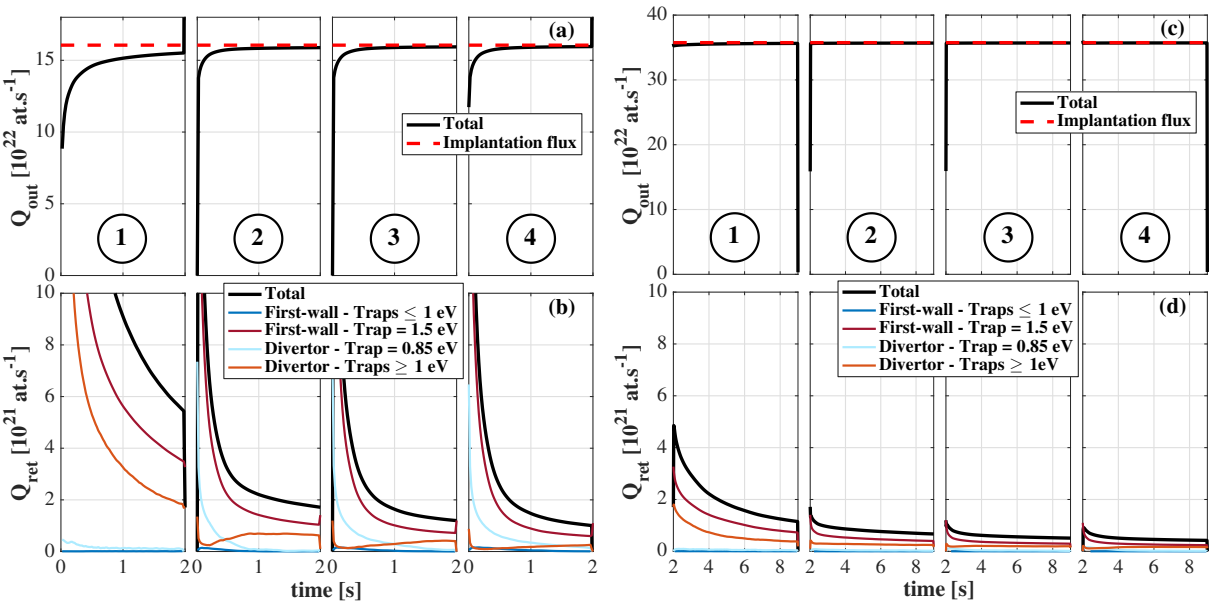

Figure 4.10: Time evolution of total outgassing flux $Q_{out,tot}$ and of the total retention flux $Q_{ret,tot}$ during the plasma phase 1 (H-mode, figures (a) and (b) respectively) and during the plasma phase 2 (L-mode, figures (c) and (d) respectively) of each of the four discharges (indicated by their number). The total implantation fluxes are also displayed in (a) and (c). The first-wall and divertor retention fluxes in traps, defined as the time derivative of their respective inventory $dN_{wall,t,i}/dt$, are arbitrarily differentiated according to their detrapping energies (cf. subsection 1.1) in figures (b) and (d).

plasma phase 1 of each discharge (figure 4.10.b). If one omits the first discharge, which exhibits a transitory behaviour with a filling of high-energy traps in both the divertor and the first-wall region, the following discharges present a similar retention behaviour. At the beginning of these discharges, the retention flux is clearly dominated by the first-wall high-energy trap and by the divertor low-energy trap. The latter one tends to see its contribution collapsing within a second while the retention flux in the divertor high-energy traps increases. Indeed, once the surface low-energy traps have reached saturation, D can diffuse in the bulk material and populate the high-energy traps. This phenomenon declines plasma after plasma, as these traps get more and more saturated in the bulk, and will vanish after a series of discharges. This saturation benefits to trap 1 which sees its dynamic retention slightly increasing plasma after plasma. However, even for the 4^{th} discharge, the dynamic retention in this trap still collapses within a second and the overall retention flux is mostly dominated by trapping in the first-wall trap 3. It probably results from a combination of a low implantation flux density in this region with the high density of trap 3 at the surface, which induces a slower trap filling. For the 4^{th} plasma, after two seconds of H-mode phase, the simulated total retention flux is $\sim 1 \times 10^{21}$ D.s^{-1} and keeps on decreasing. During the plasma phase 2 of each discharge, a slightly stronger decrease of $Q_{ret,tot}$ can be seen during the first second of this phase (cf. figure 4.10.d, for 2 s $< t <$ 3 s). This stronger decrease is attributed to the high-energy trap in the first-wall. In contrast to the plasma phase 1, the low-energy trap in the divertor has a

negligible contribution to the overall retention. From the 3rd discharge, one can note an almost constant retention flux at the end of the discharge. In reality, $Q_{ret,tot}$ exhibits a very low decrease of ~ -17 % from 4 to 9 s (e.g. 0.51×10^{21} to 0.42×10^{21} D.s^{-1} for the 4th discharge). To conclude, one can note that the order of magnitude of the obtained retention flux and its time evolution are consistent with what is experimentally observed in the JET-ILW [112]: a retention flux on the order of 10^{21} D.s^{-1} which decays within several seconds.

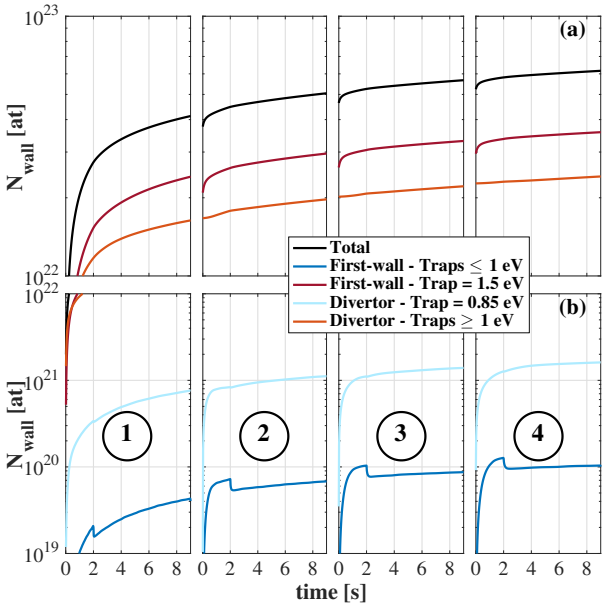

Figure 4.11: Time evolution of the D wall inventory N_{wall} during each of the four plasma discharges (indicated by their number). The inventories of the first-wall and divertor traps are arbitrarily differentiated according to their detrapping energies (cf. subsection 1.1). The figure (a) focuses on the inventory of the high-energy traps in the first-wall and in the divertor (where the majority of the inventory is found), while figure (b) focuses on the inventory of the low-energy traps.

In figure 4.11, the time evolution of the total D wall inventory $N_{wall,tot}$ during each of the four plasma discharges is displayed. The figure 4.11.a focuses on the inventory of the high-energy traps in the divertor and in the first-wall while the figure 4.11.b focuses on the inventory of the low-energy traps. $N_{wall,tot}$ increases discharge after discharge and the majority of the inventory is found in the high-energy traps. Such behaviour is characteristic of D diffusion and filling of traps in the bulk material. The inventory in the low-energy traps are one or even two orders of magnitude lower than the one in the high-energy traps. This is due to the higher density of trap 3 in both the divertor and in the first-wall (16 at.% in the implantation zone, ≤ 1 at.% in the bulk). The inventory is higher in the first-wall than in the divertor even though the reservoir capacity of the W considered in the divertor is higher (cf. trap 3 profiles in figure 4.3). This is due to the first-wall surface which is a factor of 3 higher than the divertor surface (137 m^2 for the first-wall, 40 m^2 for the divertor). Even though the inventories in the low-energy traps are anecdotal w.r.t. to the ones in the high-energy traps, one can notice a sharp

dynamical behaviour of these traps at the transition between the plasma phase 1 and the plasma phase 2 (cf. figure 4.11.b, at $t = 2$ s). In all the four discharges, the inventory of the low-energy traps in the first-wall (dark blue line) exhibits a sharp fall between the two phases. For the 4$^{\text{th}}$ discharge, these traps loose 25 % of their inventory. In the divertor, the trap 1 inventory (light blue line) seems to stabilise at the end of the phase 1 and increases again during plasma phase 2. This dynamical behaviour is more obvious during the 2$^{\text{nd}}$ discharge.

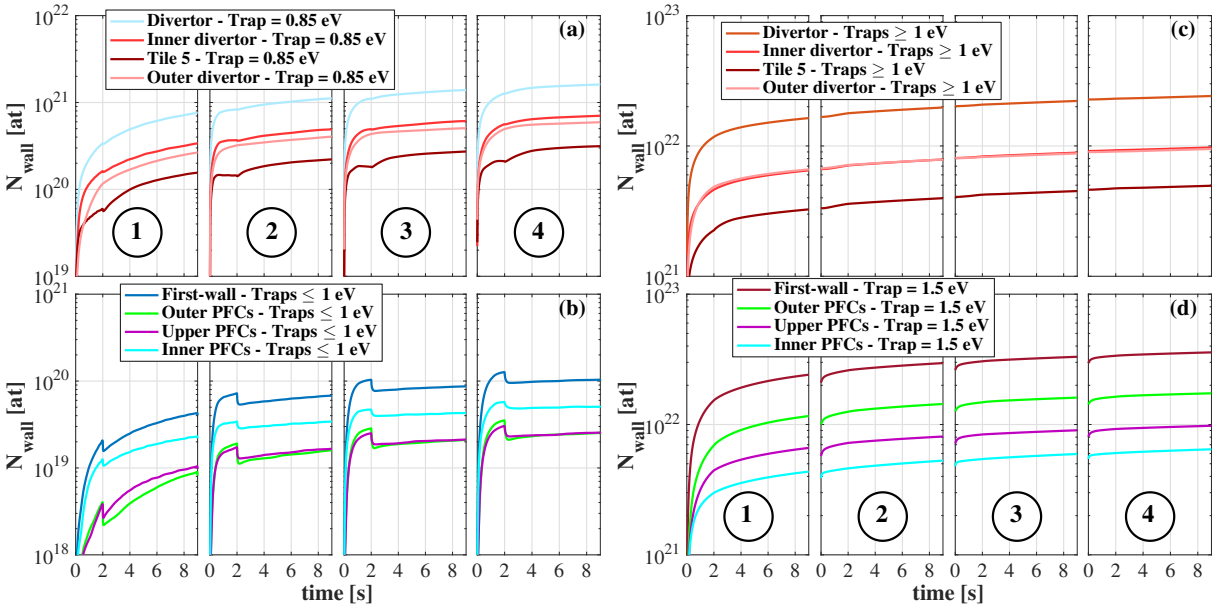

Figure 4.12: Time evolution of the D wall inventory N_{wall} during each of the four plasma discharges (indicated by their number). The inventories of the first-wall and divertor traps are arbitrarily differentiated according to their detrapping energies (cf. subsection 1.1) but also according to their location on the JET wall (cf. the different zones of the JET wall defined in figure 3.37). The inventories of the low-energy traps in the divertor and in the first-wall are displayed in figures (a) and (b) respectively. The inventories of the high-energy traps are displayed in figures (c) and (d) respectively.

To localise more precisely the areas where these dynamical behaviours occur, the same quantities are plotted in figure 4.12 for the different zones of the JET wall defined in figure 3.37. In figure 4.12.b, one can see that the sharp decrease of the inventory of the low-energy traps between the two phases happens in the three zones of the first-wall. In the two zones hosting the strike-points (tile 5 and inner divertor), the inventory of trap 1 increases at the beginning of the discharges and then drops during the plasma phase 1 (cf. figure 4.12.a). Its inventory increases again during phase 2. No sharp dynamics is seen in the high-energy traps in both the divertor and the first-wall and the inventory in those traps continuously increases during each discharge.

2.3 Dynamics of the fuel inventory during discharge n°4.

In this subsection, a more detailed analysis of the wall inventory during the last discharge will enable to understand the dynamics shown in figure 4.12.

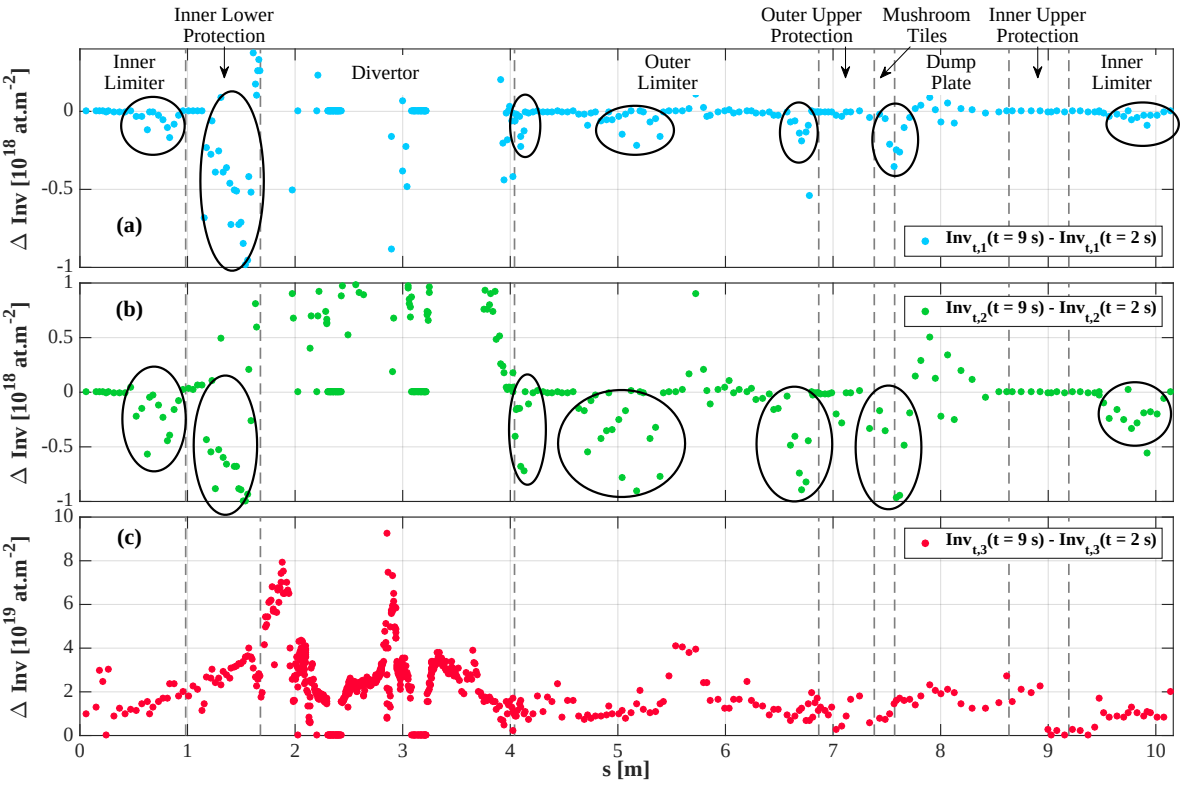

Figure 4.13: Distribution along the JET wall of the variation of the areal inventories of trap 1 (a), trap 2 (b) and trap 3 (c) between $t = 2$ s (end of phase 1) and $t = 9$ s (end of phase 2) for the 4$^{\text{th}}$ plasma discharge. The black ellipses indicate locations where the areal inventory of traps decreases between the end of phase 1 and the end of phase 2.

In figure 4.13 is shown the distribution along the JET wall of the variation of the areal inventory ($Inv_{t,i}$) of trap 1, trap 2 and trap 3 between $t = 2$ s (end of phase 1) and $t = 9$ s (end of phase 2) for the 4$^{\text{th}}$ plasma discharge. A negative variation of the areal inventory indicates that the corresponding trap have emptied in the considered time period while a positive variation indicates a filling of the traps. The areal inventory of the three traps increases everywhere in the divertor, which results in the increase of the inventories that was observed in figure 4.12.a and in figure 4.12.c for the considered discharge. In the first-wall, the trap 3 sees also its areal inventory increasing between the two selected times. On the contrary, the traps 1 and 2 exhibit a depletion of their areal inventory. The black ellipses in figure 4.13.a-b indicate the locations where such depletion occur. These drops of the local areal inventory result in an overall decrease of the inventory in the first-wall zones as it was observed in figure 4.12.b.
To explain this phenomenon, the maximum equilibrium filling ratio of the traps $R_{eq,i}^{MAX}$, introduced in chapter 2 subsection 2.8, will be used. As explained in that subsection, this parameter indicates how the D inventory builds up in traps as a function of the material

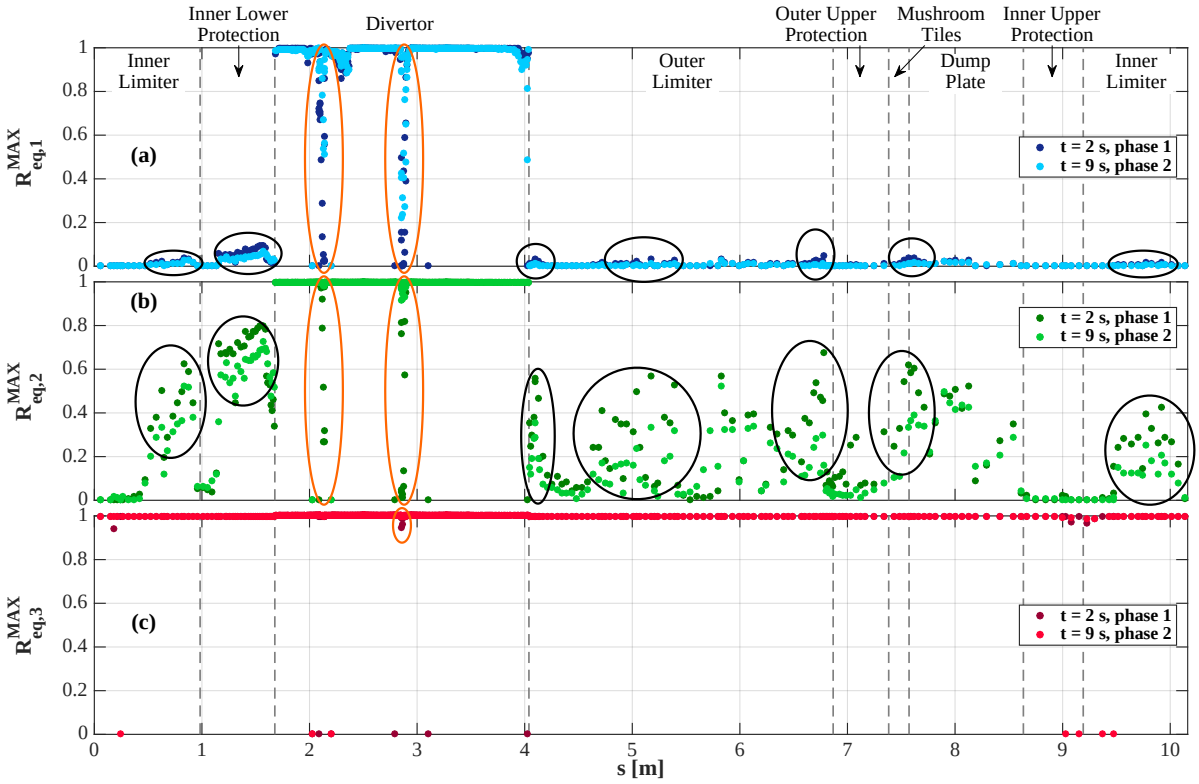

Figure 4.14: Distribution along the JET wall of the maximum equilibrium filling ratio, $R_{eq,i}^{MAX}$, of trap 1 (a), trap 2 (b) and trap 3 (c) calculated at $t = 2$ s (end of phase 1) and at $t = 9$ s (end of phase 2) for the 4$^{\text{th}}$ plasma discharge. The black ellipses indicate locations where $R_{eq,i}^{MAX}$ decreases between the end of phase 1 and the end of phase 2, leading to a release of D from the corresponding traps. The orange ellipses highlight two spots in the divertor (the vicinity of both strike-points) where $R_{eq,i}^{MAX}$ increases between the two selected times, which implies a filling of traps.

temperature and of the implantation conditions (implantation flux densities and mean implantation ranges). For $R_{eq,i}^{MAX} = 1$, the traps will tend to full saturation while for $R_{eq,i}^{MAX} = 0$ the traps will remain empty. In figure 4.14, the distribution along the JET wall of $R_{eq,i}^{MAX}$ is plotted for trap 1, trap 2 and trap 3. The values of $R_{eq,i}^{MAX}$ are calculated at $t = 2$ s (end of phase 1) and $t = 9$ s (end of phase 2) for the 4$^{\text{th}}$ plasma discharge. One can notice that the locations where the areal inventory of trap 1 and trap 2 decreases between the two selected times (identified in figure 4.13) correspond to locations where $R_{eq,1}^{MAX}$ and $R_{eq,2}^{MAX}$ decrease (cf. black ellipses in figure 4.14). For example, in the Inner Lower Protection, $R_{eq,2}^{MAX}$ exhibits a decrease of ~ 10 %. This reduction of $R_{eq,i}^{MAX}$ in the first-wall only concerns trap 1 and trap 2. $R_{eq,1}^{MAX}$ ranges between 0 and 0.1 in all the first-wall which means that this trap is almost empty. For trap 2, $R_{eq,2}^{MAX}$ ranges from 0 to 0.8 which indicates that this trap is partly filled. One can note that the decline of $R_{eq,i}^{MAX}$ between the two times, which is more pronounced for trap 2 than for trap 1, results in the same decrease of the areal inventory of the respective traps ($\sim 0.5 \times 10^{18}$ D.m^{-2}, cf. figure 4.13.a-b). This is due to the trap density which is a factor of 4 higher for trap 1

than for trap 2 (cf. table 4.1). Concerning trap 3, it remains saturated in the time period with a filling ratio of 1 everywhere in the wall (cf. figure 4.13.c). In the divertor, the traps 1 and 2 are fully saturated for the two considered times, with $R_{eq,i}^{MAX} = 1$, except in the vicinity of the two strike-points (orange ellipses in figure 4.14.a-b) where the filling ratio of both traps is higher at the end of phase 1 than at the end of phase 2. This results in the increase of the inventory in the zones hosting the strike-points which was previously observed for trap 1 in figure 4.12.a. The variation is more pronounced for $R_{eq,2}^{MAX}$ than for $R_{eq,1}^{MAX}$. For example, the trap 2 at the outer strike-point is almost empty at the end of plasma phase 1 ($R_{eq,2}^{MAX} \approx 0$) and is saturated at the end of plasma phase 2 ($R_{eq,2}^{MAX} \approx 1$). For trap 1, $R_{eq,1}^{MAX}$ goes from 0 to ~ 0.2 in the same location. One can notice a little increase of $R_{eq,3}^{MAX}$ for trap 3 at the outer strike-point (cf. orange ellipse in figure 4.14.c). The expression of $R_{eq,i}^{MAX}$, derived in chapter 2 subsection 2.8 and applied to our present study, is recalled in the following:

$$\begin{aligned} R_{eq,i}^{MAX}(s,t) &= \frac{1}{1 + \dfrac{\nu_{dt,i}\left(\overline{T_1}(s,0,t)\right)\lambda^2 n_{IS}}{\Gamma_{imp}^{i+}(s,t)X_{imp}^{i+}(s,t) + \Gamma_{imp}^{at}(s,t)X_{imp}^{at}(s,t)}} \\ R_{eq,i}^{MAX}(s,t) &= \frac{1}{1 + \dfrac{\nu_{dt,i}\left(\overline{T_1}(s,0,t)\right)}{\nu_t^{MAX}(\Gamma_{imp}^{i+}(s,t), X_{imp}^{i+}(s,t), \Gamma_{imp}^{at}(s,t), X_{imp}^{at}(s,t))}} \end{aligned} \tag{4.4}$$

where $\overline{T_1}(s,0,t)$ is the surface temperature calculated by WEE-temp, $\Gamma_{imp}^{i+}(s,t)$ and $\Gamma_{imp}^{at}(s,t)$ are the implantation flux density of ions and atoms respectively (calculated by EIRENE) and $X_{imp}^{i+}(s,t)$ and $X_{imp}^{at}(s,t)$ are the mean implantation ranges of ions and atoms respectively (calculated by SRIM). The expression exhibits a ratio between the detrapping frequency of the considered trap $\nu_{dt,i}$, which only depends on the material temperature, and another frequency that one will call ν_t^{MAX}, which only depends on the implantation conditions (flux densities and mean implantation ranges). The latter frequency can be regarded as the maximum trapping frequency. The comparison between those two frequencies enables to highlight the process that dominates the interaction between D and traps:

- when $\nu_{dt,i} \gg \nu_t^{MAX}$, detrapping is more efficient than trapping, $R_{eq,i}^{MAX}$ is equal to 0 and the considered trap remains empty.
- when $\nu_{dt,i} = \nu_t^{MAX}$, $R_{eq,i}^{MAX}$ is equal to 0.5 and the considered trap will tends to be half filled with D.
- when $\nu_{dt,i} \ll \nu_t^{MAX}$, trapping is more efficient than detrapping, $R_{eq,i}^{MAX}$ is equal to 1 and the considered trap will saturate.

In figure 4.15, the distribution along the JET wall of the detrapping frequency $\nu_{dt,i}$ for trap 1, trap 2 and trap 3 are plotted for the two considered times ($t = 2$ s and $t = 9$ s) during the 4$^{\text{th}}$ plasma discharge. As it could be expected, $\nu_{dt,i}$ does not evolve between the two times for the three traps in most of the vacuum vessel. Indeed, as it was seen

in figure 4.9, a great part of the vacuum vessel does not exhibit strong temperature excursion during the discharge due to the low heat flux density. One can note that the detrapping frequencies are higher in the first-wall than in the divertor due to the higher base temperature of the first-wall (200 °C, 50 – 70 °C for the divertor). In the divertor, only the temperature in the vicinity of both strike-points raises, reaching $\sim$ 350 °C in the tile 3 (inner strike-point) and $\sim$ 500 °C. Thus, the detrapping frequency raises for the three traps as it can be seen in figures 4.15.(a-c), respectively for 2.0 m $\leq s \leq$ 2.2 m and for 2.8 m $\leq s \leq$ 3. m. In those regions of the divertor, $\nu_{dt,i}$ is higher at the end of the plasma phase 1 than at the end of plasma phase 2 due to the cooling of the surface during plasma phase 2 (cf. figure 4.9.b). This decrease of $\nu_{dt,i}$ between the two considered times is tremendous, from three orders of magnitude for trap 1 up to six orders of magnitude for trap 3 at the outer strike-point (where the highest surface temperature is found).

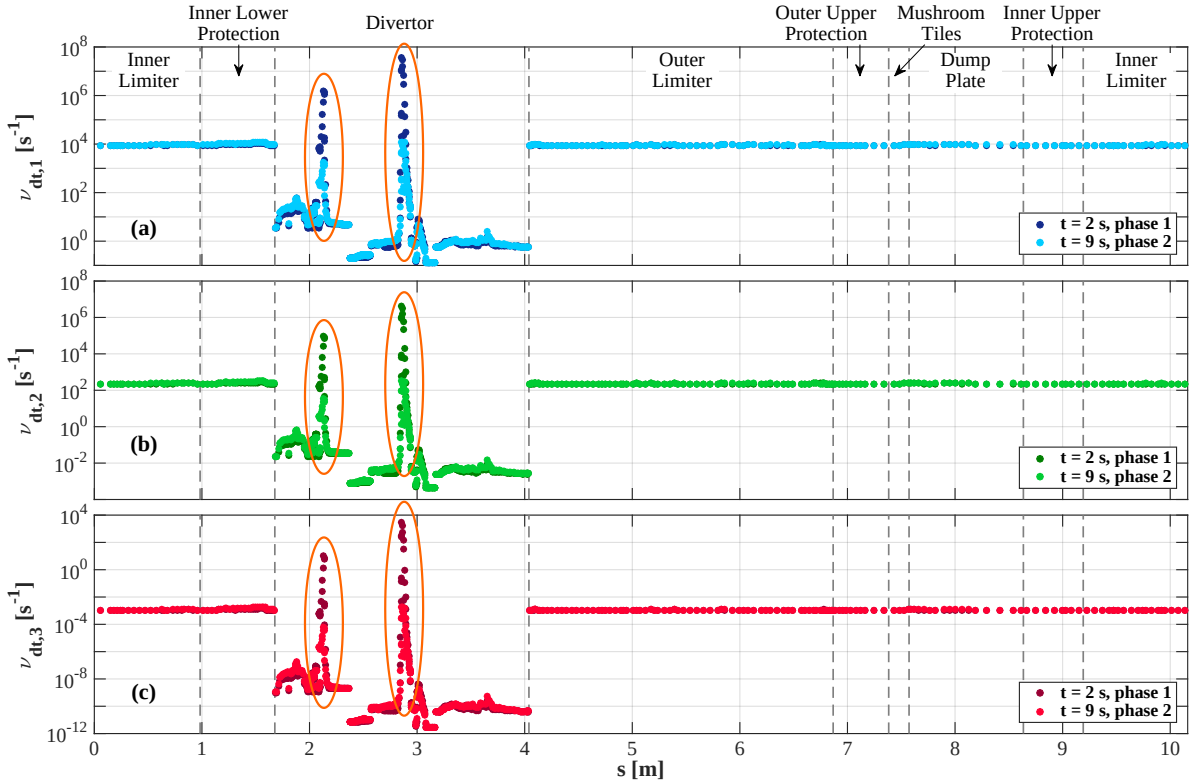

Figure 4.15: Distribution along the JET wall of the detrapping frequency $\nu_{dt,i}$ for trap 1 (a), trap 2 (b) and trap 3 (c) calculated at $t = 2$ s (end of phase 1) and at $t = 9$ s (end of phase 2) for the 4$^{\text{th}}$ plasma discharge.

The local value of $\nu_{dt,i}$ must be compared to the local value of ν_t^{MAX} to understand the resulting retention dynamics in traps induced by the change of plasma phases. The distribution of this quantity along the JET wall for the two considered times is displayed in figure 4.16. Everywhere in the vacuum vessel, ν_t^{MAX} decreases between the two phases, except in some shadowed region of the divertor and in the PFR.
Comparing the detrapping frequencies $\nu_{dt,i}$ in figure 4.15 and the maximum trapping frequency ν_t^{MAX} in figure 4.16, the following conclusions can be drawn:

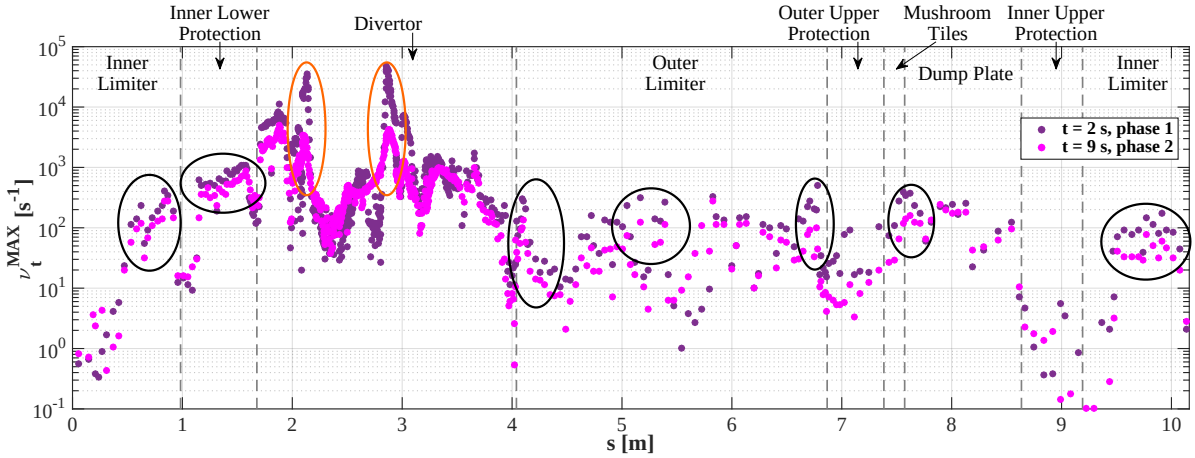

Figure 4.16: Distribution along the JET wall of the maximum trapping frequency ν_t^{MAX} calculated at $t = 2$ s (end of phase 1) and at $t = 9$ s (end of phase 2) for the 4$^{\text{th}}$ plasma discharge. This characteristic frequency is similar for the three traps and only depends on the implantation conditions. The expression of ν_t^{MAX} is reported in equation 4.4. The black ellipses indicate locations, identified in figure 4.13, where the areal inventory of trap 1 and trap 2 has decreased between the end of phase 1 and the end of phase 2, leading to a release of D from the corresponding traps. The orange ellipses highlight two spots in the divertor (the vicinity of both strike-points) where $R_{eq,i}^{MAX}$ increases between the two selected times as indicated in figure 4.15.

– <u>In the first-wall:</u> The detrapping frequency of the three traps remains constant during the two plasma phases as the temperature variation is moderate during the discharge. On the contrary, ν_t^{MAX} varies between the two phases. One can note that it predominantly decreases in all the PFCs of the first-wall. It was seen in chapter 3 subsection 4.3 that the implantation flux in the three zones (and therefore the mean implantation flux density) remains almost constant between the two phases (with variation by a factor of 0.89 to 1.4 depending on the zone). Thus, the drop of ν_t^{MAX} is attributed to the decrease of the impact energy of both ions and atoms between the two phases (by a factor of 1.7 to 2.8) which entails a decrease of their mean implantation range. For trap 3, the drop of ν_t^{MAX} has not impact as its detrapping frequency $\nu_{dt,3}$ is three to six orders of magnitude lower than ν_t^{MAX}: the filling ratio of this trap $R_{eq,3}^{MAX}$ is equal to 1 during the two phases and the trap remains saturated. This is not the case for trap 1 and trap 2 as their detrapping energy is lower and therefore their corresponding detrapping frequency is higher than for trap 3. ν_t^{MAX} is of the same order of magnitude as $\nu_{dt,1}$ and $\nu_{dt,2}$ in most of the first-wall. In the areas indicated with black ellipses in figure 4.16, a decrease of ν_t^{MAX} between the two phases is noted, which entails the decrease of the filling ratios of trap 1 and trap 2 that has been observed in figure 4.14.c. The inventory in those two traps drops between the two phases. The change of implantation conditions has caused a release of D from those two traps. Those detrapped D mainly refuelled the plasma.

– In the divertor, for the regions away from the two strike-points: One can note that $\nu_{dt,i}$ for the three traps is two to fourteen orders of magnitude below ν_t^{MAX}. $R_{eq,i}^{MAX}$ is equal to 1 for the two phases even though the implantation conditions evolve (leading to a decrease of ν_t^{MAX}): the three traps remains saturated and the wall keeps on pumping D from the plasma through diffusion of D in the depth of the material and filling of the three traps.

– In the divertor, in the vicinity of the two strike-points: The surface temperature is high enough at the end of plasma phase 1 (cf. figure 4.9.b, 350 °C at the inner strike-point, 500 °C at the outer strike-point) to have high detrapping frequencies $\nu_{dt,i}$ for the three traps. In those two locations, ν_t^{MAX} is also high during this phase ($\sim 10^4$ s^{-1}, cf. orange ellipses in figure 4.16) due to high implantation flux densities and high impact energies for both ions and atoms (cf. figure 3.23). Still, $\nu_{dt,i}$ of traps 1 and 2 are higher than ν_t^{MAX} at both strike-points at the end of the H-mode which explains the low values of $R_{eq,i}^{MAX}$ observed for those traps in figure 4.14.a-b. At the beginning of the discharge, the temperature at the strike-points is low and the traps 1 and 2 are filled with D atoms. Then the temperature at both strike-points increases due to high heat flux densities, the detrapping frequencies also increase leading to a release of particles from trap 1 as it was observed in figure 4.12.a. The trap 2 also releases D but this release is not detected in figure 4.12.c due to the lower density of this trap. At the end of the H-mode phase, these traps tend to empty completely. One can notice that, at the same moment, the value of $\nu_{dt,3}$ for trap 3 is of same order of magnitude as ν_t^{MAX} at the outer strike-point (2.8×10^3 s^{-1} as against 4.7×10^4 s^{-1}). The corresponding $R_{eq,3}^{MAX}$ in this location decreases to 0.95 (cf. orange ellipse in figure 4.14.c): the trap 3 starts to release D that refuels the plasma. This tiny decrease of the filling ratio of trap 3 is limited to a very small area of tile 5 which explains why the decrease of this trap in all tile 5 was undetected in figure 4.12.c. However, one can note that the stronger positive variation of the trap 3 areal inventory between $t = 2$ s and $t = 9$ s exactly occurs at the position of maximum temperature on tile 5 stack C (cf. figure 4.13.c, 9.2×10^{19} D.m^{-2} at $s = 2.86$ m). This indicates that the trap 3 at this location, which started to empty at the end the H-mode phase, got refilled during the L-mode phase. A longer H-mode phase would have induced higher temperatures at both strike-points and therefore a complete release of D trapped in trap 3. During the L-mode phase, the heat flux densities decrease strongly and the surface of the tiles hosting the strike-points is cooled by heat conduction in the depth of the tiles at it was observed in figure 4.9.b: the detrapping frequencies decrease for the three traps. ν_t^{MAX} also collapses by one order of magnitude at both strike-point. As mentioned in chapter 3 subsection 4.3, the mean implantation flux density increases by a factor of 1.6 on tile 3 and by a factor of 4.0 on tile 5. This increase is not consistent with an increase of ν_t^{MAX}. However, the impact energy declines by a factor of 8 to 30 in both tiles: the mean implantation range X_{imp} of both ions and atoms strongly drops between the two phases which explains the decrease of ν_t^{MAX}. For trap 2 and trap 3, the detrapping frequency is 1 to 6 orders of magnitude lower than ν_t^{MAX} at

the end of phase 2: $R_{eq,2}^{MAX}$ and $R_{eq,3}^{MAX}$ are equal to 1. The trap 2, which was empty in the vicinity of both strike-points at the end of the phase 1, got completely refilled during the phase 2 leading to a pumping of D from the plasma. For trap 1, the detrapping frequency is of same order of magnitude as ν_t^{MAX} at both strike-points. Its filling ratio increases from 0 at the end of plasma phase 1 (empty traps) up to 0.5 and 0.2 at the inner and outer strike-points respectively: the trap 1 pumps D during phase 2 as it was seen in figure 4.12.a.

To conclude, these results have exemplified some retention dynamics of the traps (pumping and fuelling of D) linked to the variation of temperature of the wall and to the variation of the implantation conditions. These dynamics have been successfully explained via the maximum equilibrium filling ratio of the traps $R_{eq,i}^{MAX}$. When $R_{eq,i}^{MAX}$ decreases, the traps release D that refuels the plasma. On the contrary, the increase of $R_{eq,i}^{MAX}$ indicates a more efficient trapping and therefore a pumping of D by traps. However, it must be noticed that the amplitude of those dynamics shown in the present simulation are very weak and did not affect the overall retention dynamics of the wall (cf. figures 4.10 and 4.11). The reason for this is simple: in the present case, the reported dynamics are mostly related to trap 1 and trap 2, which have a very low density in the depth of the material (0.13 at.% and 0.035 at.% respectively). Indeed, the D inventory is dominated by trapping in trap 3 which has a much higher density (16 at.% in the implantation zone, ≤ 1 at.% in the bulk material). Due to its high detrapping energy, the equilibrium filling ratio of trap 3 is equal to 1: the trap is saturated and its inventory increases due to D diffusion and trapping in the depth of the material. However, it must be stated that the parameter $R_{eq,i}^{MAX}$ does not depend on the trap density. As a consequence, the trap retention dynamics (pumping or fuelling of D) are independent of the trap density. However, the amplitude of these dynamics as well as their temporal rate strongly depend on that density.

3 Discharge n°4: local inventory and desorption flux density for auto-consistent plasma-wall interaction simulations.

As it was stated at the beginning of this chapter, the purpose of the simulation of sequence of discharges is to define a local wall state prior to launching auto-consistent simulation of SolEdge2D-EIRENE coupled to D-WEE. From the simulation results presented in the preceding section, one can note a reproducibility of the discharges from the third discharge in terms of thermal excursions (cf. figure 4.9) and in terms of dynamic retention (cf. figure 4.10). For the dynamic retention, additional discharges would have been necessary to fill the deep high-energy traps in the divertor that are responsible for a part of the retention flux even during the 4^{th} discharge (orange line in figure 4.10.b-d). These traps do not release their content between discharges and are therefore responsible for the long-term retention. Anyhow, the impact of these traps is negligible during the H-mode phase.

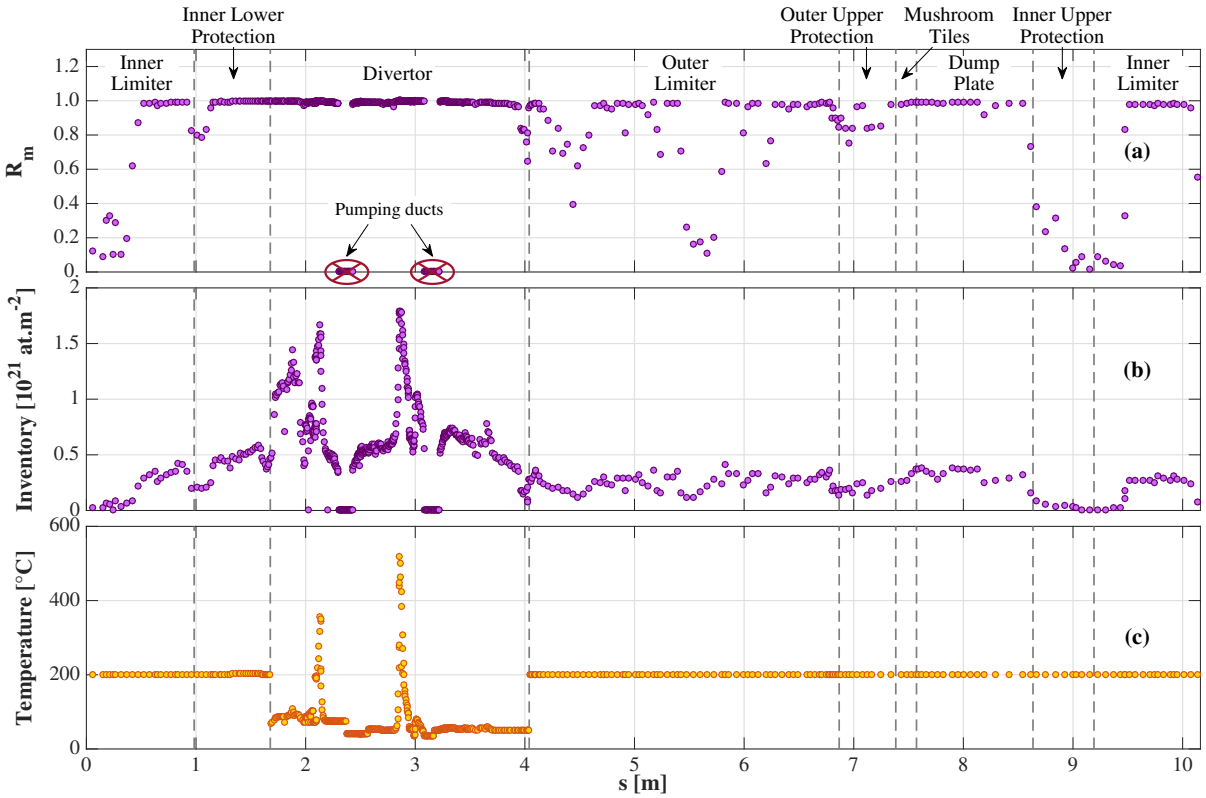

Figure 4.17: Distribution along the JET wall of the molecular recycling coefficient R_m (a), of the total D areal inventory (b) and of the surface temperature (c) calculated by D-WEE after 2 s of H-mode plasma during the 4$^{\text{th}}$ discharge. The positions of both pumping ducts, where R_m is not calculated by D-WEE but is directly forced in the SolEdge2D-EIRENE simulation, are also indicated.

The wall state during the 4$^{\text{th}}$ discharge can be extracted from the simulation, e.g. after two seconds of H-mode phase. The distribution along the JET-wall of the molecular recycling coefficient R_m is displayed in figure 4.17.a. The divertor seems to be completely saturated, with R_m around 1, while the first-wall is partly saturated, with some points where R_m ranges between 0 and 0.8. These points match with locations where only neutrals are striking (cf. figure 3.23) and therefore where the total particle flux density is smaller. A low value of R_m does not necessarily mean a high pumping of D in terms of amplitude. The time derivative of the areal inventory $dInv/dt$, defined as $(1 - R_m)(\Gamma^{i+}_{imp} + \Gamma^{at}_{imp})$ according to equation 2.36, is indeed of same order of magnitude everywhere in the first-wall with values ranging between 2×10^{18} and 10×10^{18} D.m^{-2}.s^{-1}. In the divertor, this time derivative is one order of magnitude higher in the inner SOL (HFGC tile, tile 1 and tile 3) and in the outer SOL (tile 5 Stack C, Stack D and tile 6) ranging between 2×10^{19} to 7×10^{19} D.m^{-2}.s^{-1}. In the PFR and in the far SOL, $dInv/dt$ is of same order of magnitude as in the first-wall. Due to the very large surface of the first-wall (134 m^2) w.r.t. the surface of the divertor (40 m^2, the resulting retention flux is higher in the first-wall than in the divertor at the end of the H-mode phase (cf. figure 4.10.b). The total areal inventory is displayed in figure 4.17.b. More than 90 % of this inventory

is found in the trap 3. The D areal inventory is higher in the divertor region than in the first-wall region by a factor of 2 in the remote areas to 7 in the vicinity of both strike-points. In most of the first-wall, the areal inventory is above its saturation value in the implantation zone (2×10^{20} D.m^{-2}) which indicates that the retention in the first-wall is due to diffusion of D and trapping in the bulk material trap 3. In the locations where low values of R_m are found, the areal inventory is below the saturation value: the atom flux density is not sufficient to saturate trap 3 in the implantation zone. Concerning the temperature (figure 4.17.c), the first-wall and the remote areas of the divertor remain at their base temperature (200 °C and 50 – 70 °C respectively) due to the low heat flux density to which they are exposed. The highest temperature excursions are found in the vicinity of both strike-points as it was seen in subsection 2.2.

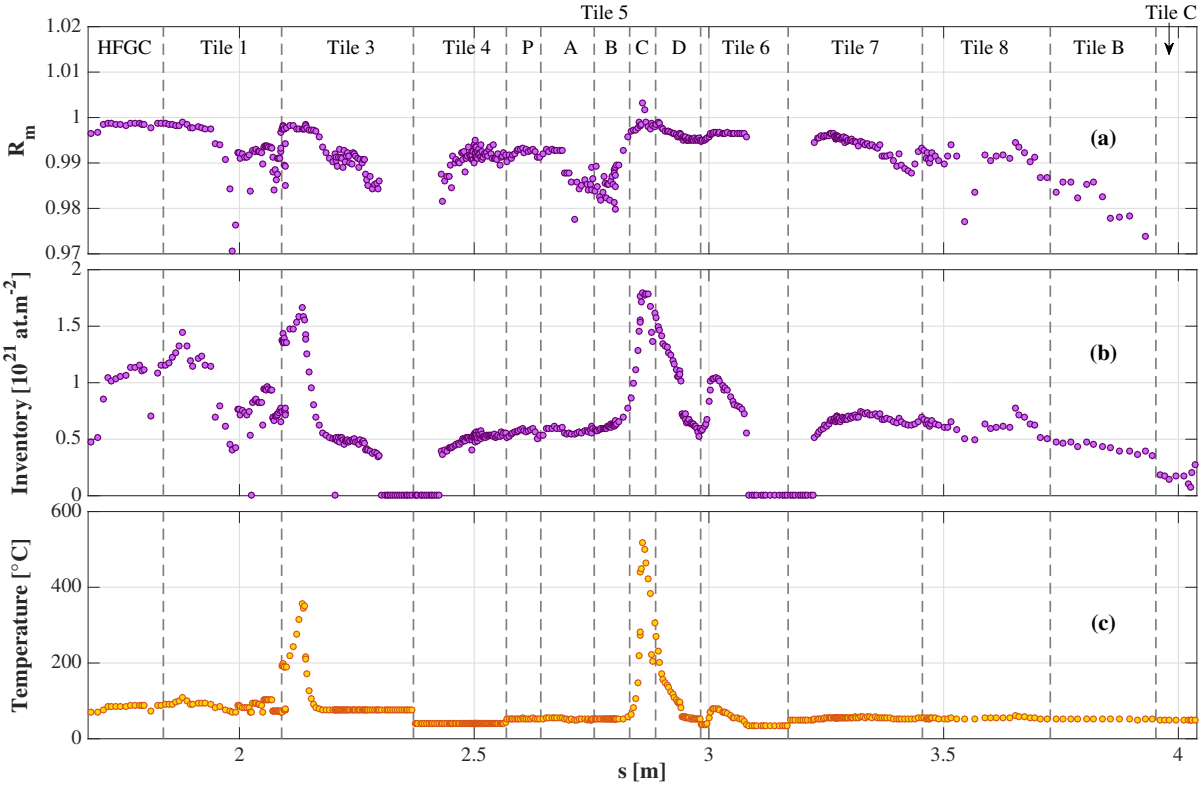

Figure 4.18: Distribution along the JET divertor of the molecular recycling coefficient R_m (a), of the total D areal inventory (b) and of the surface temperature (c) calculated by D-WEE after 2 s of H-mode plasma during the 4$^{\text{th}}$ discharge.

Figure 4.18 shows a zoom on the divertor region. The divertor is completely saturated, with R_m ranging between 0.97 and 1. The higher the implantation flux density is, the more R_m tends to 1. One can note that two points on Tile 5 Stack C have a R_m coefficient slightly above 1: the wall fuels the plasma. These points correspond to the highest heat flux densities found in the outer divertor, and therefore to the highest surface temperatures (500 °C). The detrapping frequency of trap 3 is high enough so that trap 3 releases its trapped D as it was seen in subsection 2.3 and in figure 4.14.c. In figure 4.18.b one can see that the areal inventory in Tile 5 Stack C is no depleted. This fuelling effect

can therefore be expected to increase with higher temperatures reached during longer H-mode phase.

4 Short and long term outgassing between discharges: confrontation of the simulation results to experimental pressure measurements.

As it was stated in subsection 2.2, the dynamic retention obtained in the simulation of sequence of discharges is consistent with what is observed experimentally in the JET-ILW [112]: a retention flux on the order of 10^{21} D.s^{-1} which decays within several seconds. However, a quantitative confrontation of the simulated retention flux with the experimental retention flux obtained from gas balance analysis is not conceivable as retention through Be-D co-deposition process is not modelled by D-WEE. Moreover, the quantitative evaluation of the experimental retention flux during divertor discharges with active pumping from the subdivertor (cryopumps), like the discharge #JPN89044, remains difficult due to the uncertainties on the effective pumping speed of the cryopump during such type of discharges. Cryopumps are known to have their pumping speed increasing with the inlet pressure for pressures above 10^{-2} Pa [122]. Such pressures are found in the subdivertor during diverted discharge, with as an example a subdivertor pressure ranging between 5.0×10^{-2} and 1.2×10^{-1} Pa during the flat-top phase of the discharge 89044. According to Philipps et al. [15], almost 80 % of the injected D is pumped by the cryopumps and the remaining 20 % is dynamically pumped by the wall during diverted discharge. However, the evaluation of the D flux pumped by the cryopumps has only an accuracy of ±10 % [15]: the uncertainty on the exhausted flux is of same order as the retention flux.

Nevertheless, outgassing of particles from the wall occurs after a plasma discharge and is the signature of dynamic retention in the wall during the discharge. In JET-ILW, such outgassing leads almost to a complete recovery of the trapped particles during the discharge [15]. Moreover, one of the interesting feature of the JET-ILW is the high reproducibility of the plasma discharges with similar plasma conditions and magnetic configurations. This feature has been demonstrated at the end of the first campaign of the JET-ILW: 151 identical deuterium discharges (JPN 83621 – 83791, $B_t = 2.0$ T, $I_p = 2.0$ MA, $Z_{eff} = 1.2$, $\delta = 0.2$, $P_{aux} = 12.0$ MW of NBI heating) have been performed at the end of this campaign, representing 2500 s of total plasma duration in divertor configuration [16]. The high reproducibility of the discharges can be seen in figure 4 of reference [16] where the plasma parameters for 9 consecutive discharges overlap perfectly. The outgassing flux between those consecutive discharges is also similar which tells that the reservoir of dynamic retention and its dynamics do not evolve discharge after discharge. The outgassing flux after a JET-ILW discharge is therefore characteristic of the dynamic retention that occured during that specific discharge. This outgassing flux can be evaluated through gas balance method with a higher accuracy than the retention flux during discharge due to the lower pressure found in the vacuum vessel after

the discharge ($\leq 10^{-2}$ Pa). In the following, a method is proposed to compare the time evolution of the simulated pressure with experimental pressure measurements after the discharge [123]. Such confrontation will indicate whether the dynamic retention during the discharge estimated in the simulation with D-WEE is consistent with the one of the JET-ILW. One hypothesises that the fluence obtained from the background discharge modelled with SolEdge2D-EIRENE, which is representative of the experimental fluence deposited in the divertor during the plasma current flat-top phase of #JPN89044 (cf. chapter 3 subsection 4.4), is sufficient to saturate the dynamic retention reservoir during the discharge.

First, the general particle balance equation for the tokamak system, introduced in appendix D, is remembered:

$$\frac{d}{dt}\left(N_{TOK}\right) = \frac{d}{dt}\left(N_{VV}^{D^+} + N_{VV}^{D} + N_{wall,tot}\right) = Q_{inj,tot} - Q_{pump,tot} \quad [\text{at.s}^{-1}] \tag{4.5}$$

where N_{TOK} is the total number of D particles in the tokamak, $N_{VV}^{D^+}$ the number of D ions in the VV, N_{VV}^{D} the number of D neutrals in the VV (atoms and molecules), $N_{wall,tot}$ the total number of D particles in the wall, $Q_{inj,tot}$ the total external D injection flux and $Q_{pump,tot}$ the total D pumping flux. The time variation of the wall inventory is obtained by writing the global flux balance at the wall surface, $dN_{wall,tot}/dt = Q_{imp,tot} - Q_{out,tot}$, where $Q_{imp,tot}$ is the total implanted particle flux and $Q_{out,tot}$ is the total outgassing flux. In between discharges, plasma is shut down and no external injection is operating: $N_{VV}^{D^+} = 0$, $Q_{imp,tot} = 0$ and $Q_{inj,tot} = 0$. The VV pressure P can be obtained using the ideal gas law $PV = 0.5 N_{atoms} k_B T$, where V is the VV volume [m^{-3}], k_B the Boltzmann constant [J.K^{-1}] and T the gas temperature in the VV [K]. Deuterium in the VV is in the form of D_2 molecules which explains the 0.5 factor. Moreover, the pumping flux can be expressed as $Q_{pump,tot} = 2PS_{VV}^{eff}/(k_B T)$ [122], where S_{VV}^{eff} is the total effective D_2 pumping speed related to the VV pressure P. This pumping speed embeds all the contributions from the external active VV pumps (in JET-ILW, the subdivertor cryopumps, the NBI box cryopumps and the turbo-molecular pumps [16]) and the impact of the conductances of the pipes connecting the pumps with the VV. In this situation, equation 4.5 yields:

$$\frac{V}{k_B T}\frac{dP}{dt} = -\frac{PS_{VV}^{eff}}{k_B T} + 0.5 Q_{out,tot} \tag{4.6}$$

The experimental outgassing flux $Q_{out,tot}$ can be obtained from equation 4.6 using the VV pressure measured by penning gauges. However, the penning gauge signal exhibits some noise that makes its time derivation unpractical. One has instead considered the simulated $Q_{out,tot}$ and has obtained the VV pressure by integrating numerically equation 4.6. The resulting simulated VV pressure is confronted to the pressure measured after the discharge [123].
After the 4^{th} discharges, a 100 h resting time is simulated to study the short and long term outgassing behaviour of the JET wall in full-W configuration. The VV pressure is calculated using equation 4.6. S_{VV}^{eff} has been estimated through a calibrated gas injection

(dry-run) performed at the beginning of the experimental session (S_{VV}^{eff} = 135 m^3.s^{-1}). The JET VV volume is used (V = 185 m^3) and the gas temperature in the VV is considered at the first-wall temperature (T = 200 °C). In figure 4.19, the time evolution of the experimental post-pulse VV pressure and of the simulated one is displayed. The simulation clearly underestimates the VV pressure, by a factor $\sim$ 7 right after the plasma shutdown. This factor decreases to a value $\sim$ 3 13 min later (end of pressure measurement). However, the simulated pressure follows a $t^{-0.74}$ trend during 100 h, close to the experimental trend ($t^{-0.89}$). Such trends have also been observed experimentally in carbon machines [124], in JET with Be first-wall [125] as well as in other JET-ILW experiment [16].

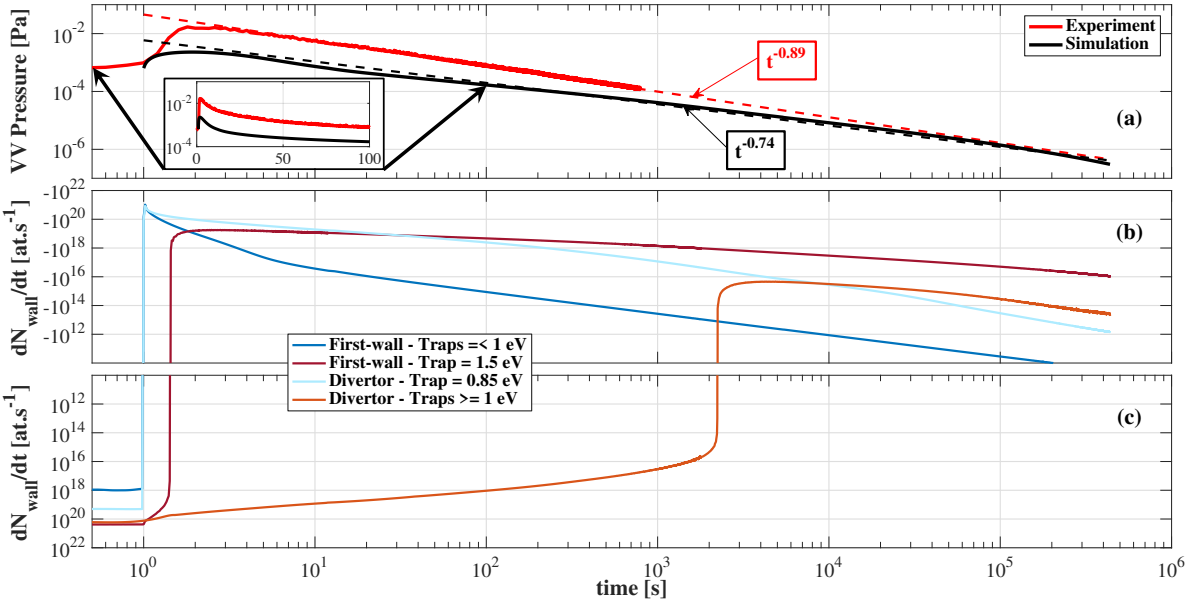

Figure 4.19: Time evolution of the simulated and experimental vacuum vessel pressures (a) and of the time variation of trap inventories (dN_{wall}/dt, negative in (b) and positive in (c)). The first-wall and divertor trap inventories are arbitrarily differentiated according to their detrapping energies (cf. subsection 1.1).

The time variation of the wall trap inventories are also displayed in figure 4.19, with the traps differentiation defined in subsection 1.1. A positive time variation indicates a filling of the traps while a negative one indicates that the traps are emptying, leading predominantly to outgassing. As explained in subsection 2.1, after the plasma shutdown, the low-energy traps are emptying and a part of these detrapped particles are repopulating the high-energy traps. This phenonemon lasts longer in the divertor region (up to 2000 s after the plasma shutdown) because the low-energy trap retains more D during plasma (due to the lower base temperature in this region). The short and long term outgassing are dominated by detrapping from trap 1 in the divertor, followed by detrapping from trap 3 in the first-wall. These traps are thus responsible for the dynamic retention of the wall. However, the quantity of desorbed D in between the pulse is clearly underestimated in the simulation (a difference of 1.3×10^{22} D atoms between the simulation and the experiment after 13 min). This difference is likely due to the consideration of a tungsten

first-wall in the simulation. However, the inventory of the first-wall trap 3 at the end of the 4^{th} plasma is high enough to entail such amount of outgassed particles between pulses (cf. figure 4.8.b). This indicates that the dynamics of this trap is incorrect, probably due to a too high detrapping activation energy. Thus, one can suppose that the beryllium in the JET-ILW first-wall has one or several traps with detrapping energy lower than the detrapping energy of the trap 3.

Conclusion of chapter 4:

– A sequence of plasma discharges has been successfully simulated with D-WEE to initialise the wall in terms of desorption flux density, areal inventory and wall temperature. Due to the lack of suitable retention model and parameters for HI-Be interaction, this simulation has been performed in the JET tokamak with full-W configuration. A reproducibility of the third and fourth discharges is observed in terms of thermal excursions and of dynamic retention (amplitude and dynamics). For the retention, additional discharges would have been necessary to fill the deep high-energy traps in the divertor as these traps are responsible for the long term retention (they do not release their D content between discharges). However, the impact of these traps is negligible during the H-mode phase of the 4^{th} discharge. The local wall state during this phase (e.g. at $t = 2$ s) can therefore be considered as initial condition for coupled plasma-wall interaction simulation with feedback of D-WEE on SolEdge2D-EIRENE.

– The wall dynamics during the sequence of discharges have been studied. For the thermal dynamics, the first-wall and the remote areas of the divertor remain at their base temperature (200 °C and 50 – 70 °C respectively) due to the low heat flux density to which they are exposed. The highest temperature excursions are found in the vicinity of both strike-points during the H-mode phase: 350 °C at the inner strike-point, 500 °C at the outer strike-point. During the L-mode phase, these temperatures decrease up to 167 °C at the outer strike-point and up to 207 °C at the inner strike-point due to the drop of the heat flux density in both regions. Between discharges, the cooling process of inertial tiles is qualitatively reproduce by the thermal model. The confrontation of the temperature measured by thermocouples and the temperature from the simulation reveals a good agreement between both temperature evolutions in tile 1 (inner far-SOL): the adjustment procedure of the depth of inertial tiles described in chapter 2 subsection 3.3 seems to be sufficient for tiles which are submitted to low heat flux densities (< 1 MW.m^{-2}) like tile 1. However, this procedure is not sufficient for tiles with non-homogeneous high heat flux densities (≥ 1 MW.m^{-2}). For tile 5 stack D, the temperature is probably overestimated with a maximum temperature above 100 °C 400 s after the end of the pulse. For the two tiles hosting the strike-points, the temperature of the tiles decrease rapidly at the end of the discharge due to heat conduction in the artificially increased depth of the tiles. 400 s after the end of a discharge, the mean temperature of tile 3 is almost equal to the temperature prior to the discharge while the thermocouples measure a temperature variation of +17 °C. This indicates that the cooling of the tile is overestimated by the increase of the tile depth. Thus, the addition of transverse heat transport seems to be required to avoid an underestimation (in tile 3 and tile 5 stack C) or an overestimation (in tile 5 stack D) of the tile temperature between the discharges.

– Concerning the retention dynamics, the simulation results reveal that D-WEE is able to qualitatively reproduce the decay of the retention flux experimentally observed in JET-ILW during plasma discharge (a retention flux on the order of 10^{21} D.s^{-1} which decays within several seconds [112]). The study of the retention flux during discharge and between discharges has shown that the traps responsible for the dynamic retention are the trap 1 in the divertor and the trap 3 in the first-wall. At the end of the H-mode phase, the retention flux is due to diffusion and trapping of D in the depth of the materials. A confrontation of the simulation with experimental pressure measurements between the discharge revealed a qualitative agreement between the pressure drop calculated by D-WEE (with a $t^{-0.74}$ trend) and the experimental pressure drop (with a $t^{-0.89}$ trend). However, the quantity of desorbed D between discharges (and therefore the dynamic retention reservoir available for the following discharge) is clearly underestimated in the simulation (1.3×10^{22} at difference between the simulation and the experiment after 13 min). This difference is likely due to the consideration of a tungsten first-wall in the simulation. However, the inventory of the first-wall trap 3 at the end of the 4$^{\text{th}}$ discharge is high enough to entail such amount of outgassed particles between pulses. This indicates that the dynamics of this trap is incorrect, probably due to a too high detrapping energy. Thus, one can suppose that the beryllium in the JET-ILW first-wall has one or several traps with detrapping energy lower than the one of the trap 3.

– The analysis of the results during the 4$^{\text{th}}$ discharge has shown some retention dynamics of the traps (pumping and fuelling of D) linked to the variation of temperature of the wall and to the variation of the implantation conditions. These dynamics have been explained via the maximum equilibrium filling ratio of the traps $R_{eq,i}^{MAX}$. When $R_{eq,i}^{MAX}$ decreases, the traps release D that refuels the plasma. This effect is observed in the vicinity of both strike-points during the H-mode phase: the high surface temperature reached at the end of this phase leads to a highly efficient detrapping of D from trap 1 and 2. A similar release of D is observed in the first-wall after the transition from the H-mode phase to the L-mode phase while the first-wall temperature variation remains moderate during all the discharge. This release of D is attributed to the decrease of the impact energy of both ions and atoms between the two phases (by a factor of 1.7 to 2.8) which entails a decrease of their mean implantation range and consequently a decrease of $R_{eq,i}^{MAX}$. On the contrary, the increase of $R_{eq,i}^{MAX}$ indicates a more efficient trapping and therefore a pumping of D by traps. This effect is observed in the vicinity of both strike-points during the L-mode phase: the decrease of the surface temperature during this phase leads to a lower detrapping frequency from trap 1 and trap 2 resulting in an increase of their local inventory.

Conclusion

The present work represents the first step towards the implementation in edge plasma transport codes of a module able to describe the dynamics of hydrogen isotopes (from now on referred to as *fuel*) in materials and the resulting desorption into the vacuum vessel of nuclear fusion reactors. This module, called D-WEE, enables to complete the physical description of the fuel recycling in those transport codes which, up to now, only treat the atomic reflection of fuel self-consistently. The purpose of this module is to study the dynamical pumping or release of fuel by the wall and its potential effect on plasma operation (density control) and performance (confinement time). The ultimate goal of this endeavour is to model an ELM-like event followed by its subsequent inter-ELM phase to study the potential effect of the interaction fuel-material on the reduction of the confinement observed in the JET-ILW tokamak (tungsten + beryllium configuration) w.r.t. the one observed in its previous JET-C wall configuration (full carbon). The module has been developed bearing this in mind.

The D-WEE module is made of two internal codes: MHIMS and WEE-temp. MHIMS describes the interaction between hydrogen isotopes and the material of the wall through the so-called reaction-diffusion system of equations. It simulates implantation of both hydrogen isotope ions and atoms, their subsequent diffusion and trapping in the bulk material, and eventually their desorption from the material surface. MHIMS has been strongly improved from a numerical point of view to decrease its computational time while preserving its computational accuracy. It is now able to simulate the whole vacuum vessel with different materials. Currently, the MHIMS version used in D-WEE does not take into account surface processes. The models available in the literature to treat those effects as well as the parameters required in those models have shown some inconsistencies under tokamak relevant implantation conditions which would lead to a large overestimation of the pumping effect by the wall. The modelling of hydrogen–beryllium interaction requires the treatment of those surface processes as almost 75 % of the total fuel inventory found in beryllium is possibly adsorbed at the surface of interconnected cavities within the implantation zone. Moreover, a clear change of the hydrogen–beryllium interaction with the implantation temperature can be seen from the experimental results compiled in the review paper by Anderl et al. [68]. This change of retention mechanism has been highlighted by Reinelt et al. [85]: the TDS spectra obtained after deuterium implantation in beryllium at 320 K (approximately the base temperature of the ITER beryllium first-wall) and at 530 K (approximately the temperature of the JET-ILW beryllium first-wall)

exhibit highly different patterns. No modelling effort has been undertaken in the fusion community to simulate and to understand this change of interaction. As a consequence, the present knowledge does not permit the modelling of hydrogen–beryllium interaction. For hydrogen–tungsten interaction, the parameterisation proposed by Hodille et al. through fitting of the implantation experiment and subsequent TDS analysis performed by Ogorodnikova et al. [47] has been selected. The strength of this parameterisation was confirmed by further simulations and confrontations to experimental results. With these parameters, Hodille et al. were able to reproduce with a relatively good agreement the evolution of retention with fluence measured by Ogorodnikova et al. [47] for two implantation temperatures on three orders of magnitude of D fluence. Moreover, these parameters were successfully used to reproduce the evolution of D retention with the implantation temperature experimentally obtained by Tian et al. [77] for reactor relevant implantation conditions. This parameterisation was considered in the D-WEE simulations presented in this PhD.
The diffusion, trapping and detrapping processes simulated by MHIMS are thermally-activated processes. A thermal model is therefore required to complete the description of the wall dynamics. The WEE-temp code calculates the temperature depth profile in the surface material of PFCs (the zone simulated by MHIMS). It has the capability to model actively-cooled PFCs and inertial PFCs, in both steady-state and transient conditions like ELMs, assuming that PFCs have a slab geometry made of a superposition of material layers. A special attention has been paid to the modelling of actively-cooled PFCs in the perspective of the WEST and ITER projects. Adjustments of the model have been proposed in order to reproduce the thermal behaviour of the real actively-cooled PFCs. For inertial PFCs, an adjustment of the model has been suggested to mimic the cooling of the PFCs between discharges (due to heat dissipation into the tokamak structure) while preserving their inertial behaviour during the discharges.

A methodology in four steps has been proposed to simulate an ELM – inter-ELM phase with SolEdge2D-EIRENE coupled to D-WEE. For step 1, the two steady-state plasma phases of the JET discharge 89044 have successfully been simulated with the SolEdge2D-EIRENE code. The simulation results have been confronted to the experimental measurements available during this discharge. The J_{sat} profiles on the divertor obtained in both simulations are consistent with the experimental profiles measured by Langmuir probes except for the H-mode phase where the inner experimental profile is higher. It results a good estimate of the incident ion flux on the divertor and therefore of the integrated ion fluence deposited during the plasma current flat-top phase of discharge 89044. However, no conclusion can be drawn on the resulting implantation flux density and on the impact energy during the experiment due to the lack of estimation of T_e from Langmuir probes data. These two phases, which are assumed to be representative of the complete plasma discharge, are then used as plasma backgrounds for simulations with the D-WEE code. For the step 2 of the methodology, a sequence of plasma discharges has been simulated with D-WEE to initialise the wall in terms of desorption flux density, areal inventory and wall temperature. This simulation has been performed in the JET tokamak with a

full tungsten wall configuration due to the aforementioned lack of model for simulating the hydrogen–beryllium interaction. At this stage, four successive discharges followed by 30 min of resting time were simulated. A reproducibility of the 3$^{\text{rd}}$ and 4$^{\text{th}}$ discharges is observed in terms of thermal excursions and of dynamic retention (amplitude and dynamics). One concludes that the dynamic retention of the wall would experience a periodic behaviour for subsequent discharges: the dynamic retention has been initialised. Thus the local wall state can be retrieved from this simulation like, for example, during the H-mode phase of the 4$^{\text{th}}$ discharge (e.g. at $t = 2$ s). This wall state can be considered as an initial condition for coupled plasma-wall interaction simulation with feedback of D-WEE on SolEdge2D-EIRENE, i.e. the step 3 of the methodology. This step is a restart of the SolEdge2D-EIRENE simulation of step 1 and aims to calculate a new steady-state plasma with SolEdge2D-EIRENE due to the modification of the recycling introduced by the feedback of D-WEE. The step 4 is the ELM – inter-ELM simulation. Due to numerical issues, related to the step decomposition of the heat flux density performed in the thermal model WEE-temp, steps 3 and 4 could not be achieved in the time scale of this PhD and will be addressed in future work.

The simulated wall dynamics during the sequence of discharges have been studied. The exhaustive conclusions of this study can be found in the conclusions of chapter 4. In a nutshell, the simulation results reveal that D-WEE is able to qualitatively reproduce the decay of the retention flux experimentally observed in JET-ILW during plasma discharge (a retention flux on the order of 10^{21} D.s^{-1} which decays within several seconds [112]). The study of the retention flux during discharge and between discharges has shown that the traps responsible for the dynamic retention are the trap 1 (with detrapping energy $E_{dt,1} = 0.85$ eV) in the divertor and the trap 3 (with detrapping energy $E_{dt,3} = 1.5$ eV) in the first-wall. This difference of traps involved in the dynamic retention is due to the different base temperature of the two zones (50 – 70 °C for the divertor, 200 °C for the first-wall). At the end of the H-mode phase, the retention flux is due to diffusion and trapping of D in the depth of the materials. It is dominated by the retention in trap 3 in the first-wall due to a combination of high trap density and a high surface of exposition of the first-wall (134 m^2 for the first-wall, 40 m^2 for the divertor). A confrontation of the simulation with experimental pressure measurements between the discharge revealed a qualitative agreement between the pressure drop calculated by D-WEE (with a $t^{-0.74}$ trend) and the experimental pressure drop (with a $t^{-0.89}$ trend). However, the quantity of desorbed D between discharges (and therefore the dynamic retention reservoir) is clearly underestimated in the simulation (1.3×10^{22} D difference between the simulation and the experiment after 13 min). This difference is likely due to the consideration of a tungsten first-wall in the simulation. However, the inventory of the first-wall trap 3 at the end of the 4$^{\text{th}}$ discharge is high enough to entail such amount of outgassed particles between pulses. This indicates that the dynamics of this trap is incorrect, probably due to a too high detrapping energy. Thus, one can suppose that the beryllium in the JET-ILW first-wall has one or several traps with detrapping energy lower than the one of the trap 3. Nevertheless, this simulation shows that D-WEE is able to reproduce qualitatively

experimental trends (order of magnitude of the dynamic retention flux during pulses and time evolution of post-pulse outgassing) if the required trapping parameters and the overall wall condition (distribution of particle flux density, impact energy, etc.) are considered. It also suggests that the dynamic retention can be related to the beryllium first-wall in JET-ILW. This suggestion is in line with experimental findings that have shown the high hydrogen storage capacity of beryllium in the implantation zone (with a hydrogen density up to 35 at.% of beryllium, a factor of ~ 4 higher than the capacity of the tungsten considered in this PhD). Moreover, a stronger deuterium pumping during discharge with a simultaneous increase of fuel release after discharge were observed in the JET tokamak after the replacement of graphite limiter tiles with beryllium tiles at the end of the 1980's [14, 126]. No direct comparison of the hydrogen pumping between the JET-C and the JET-ILW is available in the literature. However, the similar retention fluxes during discharge ($\sim 10^{21}$ s^{-1}) observed in JET with beryllium limiters [14] and in JET-ILW [15] reinforce our belief that the beryllium first-wall is responsible for the hydrogen pumping during discharge in the JET-ILW tokamak. However, one can wonder whether the JET-ILW first-wall is representative of the ITER first-wall in terms of pumping. Indeed, the base temperature of the JET-ILW is 473 K (200 °C) while the ITER first-wall will have a base temperature of 343 K (70 °C due to the active cooling). The results of Reinelt et al. [85] exhibit a change of the hydrogen–beryllium interaction as a function of the temperature of exposure and suggest that the ITER first-wall will not behave like the JET-ILW first-wall in particular during the start-up phase of the discharge. Experiments in the JET-ILW with a first-wall temperature similar to the cooling temperature of the ITER first-wall could provide a quick answer to that question. Simulations of a discharge with a beryllium first-wall in D-WEE and confrontation to the post-pulse pressure measurement (as exemplified in this PhD) could provide an indication of the binding states responsible for the high pumping effect seen in JET-ILW. However, this would require an extensive theoretical work to develop a model able to properly describe the hydrogen–beryllium interaction at different temperatures of exposure.

The analysis of the simulation results during the 4$^{\text{th}}$ discharge has also exemplified some retention dynamics of the traps (pumping and fuelling of D) linked to the variation of temperature of the wall and to the variation of the implantation conditions. These dynamics have been successfully explained via the maximum equilibrium filling ratio of the traps $R_{eq,i}^{MAX}$ recalled hereafter:

$$R_{eq,i}^{MAX} = \frac{n_{t,i}^{MAX}(x)}{n_i(x)}$$

$$R_{eq,i}^{MAX} = \frac{1}{1 + \dfrac{\nu_{dt,i}(T)\lambda^2 n_{IS}}{\Gamma_{imp}^{i+} X_{imp}^{i+} + \Gamma_{imp}^{at} X_{imp}^{at}}}$$

$$R_{eq,i}^{MAX} = \frac{1}{1 + \dfrac{\nu_{dt,i}(T)}{\nu_t^{MAX}}}$$

where $n_{t,i}^{MAX}$ is the maximum density of hydrogen isotopes trapped in the trap of kind i [m^{-3}], n_i is the density of the trap of kind i [m^{-3}], x is the material depth [m], $\nu_{dt,i}$ is the detrapping frequency of the trap of kind i [s^{-1}], T is the material temperature [K], λ is the distance between two interstitial sites for hydrogen isotopes [m], n_{IS} is the interstitial site density [m^{-3}], Γ_{imp}^{i+} and Γ_{imp}^{at} are the implantation flux densities of ions and atoms respectively [$m^{-2}.s^{-1}$], X_{imp}^{i+} and X_{imp}^{at} are the mean implantation depths of ions and atoms respectively [m]. The parameter $R_{eq,i}^{MAX}$ indicates the equilibrium inventory of traps, and therefore the total equilibrium inventory in the material that builds up during plasma operation for constant material temperature and implantation conditions. It gives an indication on the retention dynamics that occur during plasma operation. When $R_{eq,i}^{MAX}$ increases during plasma operation, the traps will tend to fill with hydrogen leading to a pumping effect from the plasma point of view, while when $R_{eq,i}^{MAX}$ decreases, the traps will tend to release hydrogen leading to a fuelling of the plasma. However, it is remembered that the amplitude of these dynamics as well as their temporal rate strongly depend on the trap density. Only simulations with D-WEE can give an idea of both amplitude and rate of these dynamics. The expression of $R_{eq,i}^{MAX}$ exhibits a ratio between the detrapping frequency of the considered trap $\nu_{dt,i}$, which depends on the material temperature during the discharge (the detrapping energy is fixed), and the maximum trapping frequency ν_t^{MAX}, which only depends on the implantation conditions (flux densities and mean implantation ranges).
The retention dynamics resulting from variation of temperature for constant implantation conditions are summed up in table 5.1.

At constant implantation conditions	$\nearrow T$	$\searrow T$
Detrapping frequency $\nu_{dt,i}(T)$ [s^{-1}]	$\nearrow$	$\searrow$
Filling ratio of traps $R_{eq,i}^{MAX}$	$\searrow$	$\nearrow$
Traps areal inventory $Inv_{t,i}$ [HI.m^{-2}]	$\searrow$	$\nearrow$
Retention dynamics	Fuelling	Pumping

Table 5.1: Retention dynamics as a function of temperature for constant implantation conditions (implantation flux densities, impact energy and angle of incidence).

The fuelling effect at constant implantation conditions is observed in the simulation of sequence of discharges in the vicinity of both strike-points during the H-mode phase: the high surface temperature reached at the end of this phase leads to a detrapping of D from traps with low detrapping energy. During the L-mode phase, the decrease of the surface temperature at both strike-points leads to decrease of the detrapping frequency of traps resulting in an increase of the local inventory and therefore a pumping effect.
The retention dynamics resulting from variation of implantation conditions at fixed temperature are summed up in table 5.2.
Such retention dynamics is also observed in the D-WEE simulation presented in this PhD. A release of D is observed in the first-wall after the transition from the H-mode phase to the L-mode phase while the first-wall temperature variation remains moderate during all the discharge. This release of D is attributed to the decrease of the impact

At constant temperature	$\nearrow (\Gamma_{imp}^{i+} X_{imp}^{i+} + \Gamma_{imp}^{at} X_{imp}^{at})$	$\searrow (\Gamma_{imp}^{i+} X_{imp}^{i+} + \Gamma_{imp}^{at} X_{imp}^{at})$
Max trapping frequency ν_t^{MAX} [s^{-1}]	$\nearrow$	$\searrow$
Filling ratio of traps $R_{eq,i}^{MAX}$	$\nearrow$	$\searrow$
Traps areal inventory $Inv_{t,i}$ [HI.m^{-2}]	$\nearrow$	$\searrow$
Retention dynamics	Pumping	Fuelling

Table 5.2: Retention dynamics as a function of implantation conditions for constant surface temperature.

energy of both ions and atoms between the two phases (by a factor of 1.7 to 2.8) which entails a decrease of their mean implantation range and consequently a decrease of the equilibrium filling ratio of traps $R_{eq,i}^{MAX}$.
Tables 5.1 and 5.2 can give an idea of the wall dynamics during ELMs. During such events, the heat flux density sharply increases, leading to a quick variation of the surface temperature (up to $\sim +100$ °C at the outer strike-point in JET-ILW). This temperature increase leads to an increase of the detrapping frequency of the traps. According to table 5.1 the traps inventory can deplete leading to a fuelling of the plasma. This fuelling effect could explain the strong D_α emission seen on tile 1 after the ELM event (cf. figure 1.12): the increase of the surface temperature leads to a desorption of D from the beryllium deposits situated on that tile. However, ELMs also induce a strong increase of the ion implantation flux density Γ_{imp}^{i+} by a factor of ~ 5 and a strong increase of the ion impact energy E_{imp}^{i+} from ~ 100 eV in steady-state to ~ 1 keV during ELMs. This higher impact energy entails a deeper implantation source, i.e. an increase of the mean implantation range X_{imp}^{i+} by a factor of ~ 4 in tungsten to ~ 8 in beryllium (deposit) according to the SRIM code. Hence the product $\Gamma_{imp}^{i+} X_{imp}^{i+}$ can increase by a factor of 20 to 40 during ELMs. The maximum trapping frequency ν_t^{MAX} increases by the same factor which could lead to a transient filling of traps if the surface temperature increase is moderate (cf. table 5.2). The retained particles during ELMs are then re-emitted into the plasma during the inter-ELM phase when the steady-state plasma conditions are recovered. The rate of re-emission depends on the detrapping frequency of the traps dynamically filled. This rate could cause a delay in the recovery of the density pedestal as seen in chapter 1 section 5. Experimentally, this hypothesis could be tested by increasing the base temperature of the JET-ILW divertor which would lead to an increase of the detrapping frequency of the traps during all the discharge. Then the wall pumping effect during ELMs would be diminished and the pedestal recovery possibly accelerated.

Appendix A

Numerical improvements of the MHIMS code.

The version of MHIMS used in D-WEE is relatively simple in terms of description of HI–material interaction. However, the addition of a second dimension to the model ($\vec{s}$) leads to a tremendous increase of the computational time required to solve the system of Partial Differential Equations (PDE) 2.28. In this appendix, one will intend to briefly explain the reason of this increase. To solve the system, its space differential operator must be discretised. Originally, this discretisation was done using a finite difference method. This space discretisation transforms the system of PDE equations 2.28 into a new system of Ordinary Differential Equations (ODE). The number of equations of this ODE system, N_{eq}^{MHIMS}, is given by the following expression:

$$N_{eq}^{MHIMS} = \sum_{i=1}^{N_s} N_x(i)(1 + N_{trap}(i)) \tag{A.1}$$

where N_s is the number of cells along the wall (defined by the SolEdge2D-EIRENE grid) and $N_x(s)$ is the number of cells in the depth of the material. N_x is set by the user and can be different for a different type of materials, hence explaining its s dependency. The number between brackets in equation A.1 indicates the number of ODE/unknowns of the system 2.28: one for the mobile particle (n_m) and one for each trap ($n_{t,i}$). Concerning the time integration of the ODE system, one must be aware that, depending on the temperature, the trap density and the filling level of the traps (given by the term $n_i(s,x) - n_{t,i}$), the characteristic time for the trapping process $1/\nu_{t,i}$ can range from picoseconds to almost infinity while the characteristic time for the detrapping process $1/\nu_{dt,i}$ can range from nanoseconds to almost infinity. These characteristic times can vary on orders of magnitude which indicates that the R-D equations are stiff. Hence, the use of an implicit time discretisation scheme called Backward Differentiation Formula (BDF) is necessary to avoid excessively small time step sizes. In MHIMS, the time integration of the ODE system is done by the LSODE solver [65] using the BDF. Moreover, as the system 2.28 is non-linear, the use of a predictor-corrector process for its resolution is required. In LSODE, the prediction is performed using an explicit method to estimate

an initial guess of the solution while the correction of this initial guess is performed through a Newton-Raphson iteration on the BDF [65]. This iteration process involves the resolution of a secondary system of equations involving the Jacobian matrix of the ODE system. This secondary system is solved using the LU method [65]. However, much computational work is required to form the Jacobian matrix and to perform the linear algebra necessary to solve this secondary system. The size of this system is equal to the size of the MHIMS ODE system (N_{eq}^{MHIMS}). The higher N_{eq}^{MHIMS} is, the more time-consuming the resolution is. One can try to estimate this number. Regular simulations of implantation experiments with subsequent TDS with MHIMS (like in references [36, 60]) were performed with $N_x = 1000$ points to discretise 1 mm of material. The number of cells along the wall for regular SolEdge2D-EIRENE simulations is $N_s \sim 1000$. Considering a number of traps N_{trap} equal to 3 and similar N_{trap} and N_x for all the elements of the wall, the size of the system to be solved A.1 becomes:

$$N_{eq}^{MHIMS} = N_s N_x (1 + N_{trap}) = 10^3 \cdot 10^3 \cdot (1 + 3) = 4 \times 10^6 \tag{A.2}$$

This number can be compared with the number of equations solved by SolEdge:

$$N_{eq}^{SolEdge} = N_{fields} N_{cells} \sim 4 \times 10^5 \tag{A.3}$$

where N_{fields} is the number of fields solved by SolEdge, i.e. 4 (n, $u_\parallel$, T_i and T_e) and N_{cells} is the number of cells of the SolEdge mesh. Even though the SolEdge equations are much more complex than the MHIMS equations, the direct comparison of both numbers can give an idea of the increase of the computational time due to the integration of MHIMS in the wall model of SolEdge2D-EIRENE. In reality, some improvements of MHIMS were necessary to envisage this integration. The following improvements have been implemented in the code:

- A new mesh in the depth of the materials has been developed. This new mesh enables a highly refined grid in the implantation zone in order to catch the implantation sources while keeping a low number of points N_x. According to equation A.1, dropping this quantity decreases the size of the system and hence increases computational efficiency.

- The decrease of the number of points has highlighted some issues of conservation of particles of the code. This was due to the finite difference scheme used for the diffusion operator. Thus, a new spatial discretisation scheme has been developed, based on the finite volume method intrinsically conservative. This has made possible a decrease up to a factor of 10 of the number of points N_x without impacting the calculation accuracy.

- The Jacobian matrix of the ODE system required in the correction process was previously estimated numerically by the LSODE solver. An analytical expression of this Jacobian matrix has been derived and coded in MHIMS, resulting in a decrease of the number of iteration required in the correction process and therefore a strong decrease of the computation time.

– The addition of the $\vec{s}$ dimension leads to an increase of the quantity of data handled by MHIMS. A more efficient handling of inputs and outputs of the code was therefore implemented.

Appendix B

PFC step response calculation through the quadrupole method.

This appendix focuses on the calculation of the PFC step response $T_i^{step}(s, x, t - t_k(s))$ in the general equation of WEE-temp 2.66. For the sake of clarity, the s coordinate will be omitted in the following derivation as it only refers to the considered PFC. To calculate it, the auxiliary system 2.57 needs to be solved.

First the heat equation in one given material layer i, equation 2.57a, is solved. To simplify the calculation, the following change of coordinate $X_i = x - x_{i-1}$, which depend on the considered material layer, is used:

$$\rho_i c_{p_i} \frac{\partial T_i^{step}(X_i, t)}{\partial t} = \lambda_i \frac{\partial^2 T_i^{step}}{\partial {X_i}^2} \tag{B.1}$$

One can now apply the Laplace transform to that equation:

$$\begin{aligned} \frac{\partial^2 \theta_i^{step}}{\partial {X_i}^2}(X_i, p) &= \frac{1}{a_i}\left(p\theta_i^{step}(X_i, p) - \cancel{T_i^{step}(X_i, 0)}\right) \\ \frac{\partial^2 \theta_i^{step}}{\partial {X_i}^2}(X_i, p) &= \frac{p}{a_i}\theta_i^{step}(X_i, p) \end{aligned} \tag{B.2}$$

where θ_i^{step} is the Laplace transform of T_i^{step} and $a_i = \lambda_i/(\rho_i c_{p_i})$ is the material heat diffusivity. The initial condition 2.57e has also been accounted. Such differential equation has the following solution:

$$\theta_i^{step}(X_i, p) = k_1(p)\cosh(\alpha_i X_i) + k_2(p)\sinh(\alpha_i X_i) \tag{B.3}$$

where $\alpha_i = \sqrt{p/a_i}$ and k_1 and k_2 are two functions of p. Now one will remember the Fourier law of heat conduction, implicitly used in the derivation of the heat equation B.1,

which relates the mean heat flux density in the material ϕ_i with the temperature:

$$\phi_i(X_i,t) = -\lambda_i \frac{\partial T_i^{step}}{\partial X_i}(X_i,p) \tag{B.4}$$

The Laplace transform can also be applied to that law:

$$\Phi_i(X_i,p) = -\lambda_i \frac{\partial \theta_i^{step}}{\partial X_i} = -\lambda_i\alpha_i k_1(p)\sinh(\alpha_i X_i) - \lambda_i\alpha_i k_2(p)\cosh(\alpha_i X_i) \tag{B.5}$$

where Φ_i is the Laplace transform of ϕ_i. Both equations B.3 and B.5 can be written at $X_i = 0$ ($x = x_{i-1}$) and $X_i = e_i$ ($x = x_i$):

$$\begin{cases} \theta_i^{step}(0,p) = k_1(p) \\ \Phi_i(0,p) = -\lambda_i\alpha_i k_2(p) \\ \theta_i^{step}(e_i,p) = k_1(p)\cosh(\alpha_i e_i) + k_2(p)\sinh(\alpha_i e_i) \\ \Phi_i(e_i,p) = -\lambda_i\alpha_i k_1(p)\sinh(\alpha_i e_i) - \lambda_i\alpha_i k_2(p)\cosh(\alpha_i e_i) \end{cases} \tag{B.6}$$

After some algebra, one can eliminate k_1 and k_2 to obtain the following expression relating θ_i^{step} and Φ_i at the boundaries of the material layer (at $x = x_{i-1}$ and $x = x_i$):

$$\begin{pmatrix} \theta_i^{step}(x_{i-1},p) \\ \Phi_i(x_{i-1},p) \end{pmatrix} = \underbrace{\begin{pmatrix} \cosh(\alpha_i e_i) & \dfrac{1}{\lambda_i\alpha_i}\sinh(\alpha_i e_i) \\ \lambda_i\alpha_i\sinh(\alpha_i e_i) & \cosh(\alpha_i e_i) \end{pmatrix}}_{M_{mat,i}} \begin{pmatrix} \theta_i^{step}(x_i,p) \\ \Phi_i(x_i,p) \end{pmatrix} \tag{B.7}$$

$M_{mat,i}$ is called the quadrupole matrix of the material layer [92].

The same method can be used to treat the interface boundary condition between two adjacent layers (equation 2.57c). Applying Laplace transform, this equation becomes:

$$\begin{cases} \theta_i^{step}(x_i,p) = \theta_{i+1}^{step}(x_i,p) + R_{c_i}\Phi_{i+1}(x_i,p) \\ \Phi_i(x_i,p) = \Phi_{i+1}(x_i,p) \end{cases} \tag{B.8}$$

which can be written in the following matrix form:

$$\begin{pmatrix} \theta_i^{step}(x_i,p) \\ \Phi_i(x_i,p) \end{pmatrix} = \underbrace{\begin{pmatrix} 1 & R_{c_i} \\ 0 & 1 \end{pmatrix}}_{M_{interf,i}} \begin{pmatrix} \theta_{i+1}^{step}(x_i,p) \\ \Phi_{i+1}(x_i,p) \end{pmatrix} \tag{B.9}$$

$M_{interf,i}$ is the quadrupole matrix of the interface [92].

Now the N successive material layers of the PFC will be addressed. First the equation

B.9 can be inserted in equation B.7:

$$\begin{aligned}\begin{pmatrix}\theta_i^{step}(x_{i-1},p)\\ \Phi_i(x_{i-1},p)\end{pmatrix} &= M_{mat,i}\ M_{interf,i}\ \begin{pmatrix}\theta_{i+1}^{step}(x_i,p)\\ \Phi_{i+1}(x_i,p)\end{pmatrix}\\ \begin{pmatrix}\theta_i^{step}(x_{i-1},p)\\ \Phi_i(x_{i-1},p)\end{pmatrix} &= \quad M_{lay,i}\quad\ \begin{pmatrix}\theta_{i+1}^{step}(x_i,p)\\ \Phi_{i+1}(x_i,p)\end{pmatrix}\end{aligned} \tag{B.10}$$

$M_{lay,i}$ is the generalised quadrupole matrix of a given material layer:

$$M_{lay,i}(p) = \begin{pmatrix}\cosh(\alpha_i e_i) & \dfrac{1}{\lambda_i\alpha_i}\sinh(\alpha_i e_i) + R_{c_i}\cosh(\alpha_i e_i)\\ \lambda_i\alpha_i\sinh(\alpha_i e_i) & \cosh(\alpha_i e_i) + R_{c_i}\lambda_i\alpha_i\sinh(\alpha_i e_i)\end{pmatrix},\ \alpha_i = \sqrt{\frac{p}{a_i}} \tag{B.11}$$

One can note that if $R_{c_i} = 0$, $M_{lay,i}$ is equivalent to $M_{mat,i}$. Therefore, if one sets $R_{c_N} = 0$, an expression between θ_i^{step} and Φ_i at the boundaries of the PFC (at $x = 0$ and $x = L_x$) is obtained through matrix multiplication of the N matrices $M_{lay,i}$:

$$\begin{pmatrix}\theta_1^{step}(0,p)\\ \Phi_1(0,p)\end{pmatrix} = M_{lay,1}\ M_{lay,2}\ ...\ M_{lay,i}\ ...\ M_{lay,N-1}\ M_{lay,N}\begin{pmatrix}\theta_N^{step}(L_x,p)\\ \Phi_N(L_x,p)\end{pmatrix} \tag{B.12}$$

Equation B.12 is a general expression stating the heat transfer through the whole PFC. It does not depend on the type of heat exchange with the surrounding. To do so, one needs to address the B.C. at the top and rear surfaces of the PFC. First the rear B.C (at $x = L_x$) for an inertial PFC is addressed by applying Laplace transform to equation 2.57d:

$$\Phi_N(L_x,p) = 0 \text{ for inertial PFCs} \tag{B.13}$$

For actively-cooled PFC, equation 2.57d needs to be precised. If one notes ϕ_{cool} the heat flux density evacuated in the cooling system, this equations becomes:

$$\phi_N(L_x,t) = \phi_{cool}(t) = hT_N^{step}(L_x,t) \text{ for actively-cooled PFCs} \tag{B.14}$$

By applying Laplace transform and considering Φ_{cool} as the Laplace transform of ϕ_{cool}, equation B.14 becomes:

$$\begin{cases}\theta_N^{step}(L_x,p) = \dfrac{1}{h}\Phi_{cool}(p)\\ \Phi_N(L_x,p) = \Phi_{cool}(p)\end{cases} \tag{B.15}$$

which can be written in the following matrix form:

$$\begin{pmatrix}\theta_N^{step}(L_x,p)\\ \Phi_N(L_x,p)\end{pmatrix} = \underbrace{\begin{pmatrix}1 & \dfrac{1}{h}\\ 0 & 1\end{pmatrix}}_{M_{cool}}\begin{pmatrix}0\\ \Phi_{cool}(p)\end{pmatrix} \tag{B.16}$$

where M_{cool} is the quadrupole matrix of convective B.C. [92]. One can note that M_{cool} is equivalent to $M_{interf,N}$ by setting $R_{c_N} = 1/h$. Therefore a quadrupole matrix of the whole PFC with N layers can be defined which is valid for both inertially-cooled and actively-cooled PFCs:

$$M_{PFC}^{N}(p) = \begin{pmatrix} A_{PFC}^{N}(p) & B_{PFC}^{N}(p) \\ C_{PFC}^{N}(p) & D_{PFC}^{N}(p) \end{pmatrix} = \overset{\curvearrowright}{\prod_{i=1}^{N}} M_{lay,i}, \quad \begin{vmatrix} R_{c_N} = 0 \text{ for inertial PFCs} \\ \text{or} \\ R_{c_N} = \frac{1}{h} \text{ for actively-cooled PFCs} \end{vmatrix} \tag{B.17}$$

For inertial PFCs, M_{PFC}^{N} links the Laplace temperature and heat flux density at the boundaries of the PFC. By considering equations B.12, B.17 and B.13, this yields to:

$$\begin{pmatrix} \theta_1^{step}(0,p) \\ \Phi_1(0,p) \end{pmatrix} = M_{PFC}^{N} \begin{pmatrix} \theta_N^{step}(L_x,p) \\ 0 \end{pmatrix} = \begin{pmatrix} A_{PFC}^{N}(p) & B_{PFC}^{N}(p) \\ C_{PFC}^{N}(p) & D_{PFC}^{N}(p) \end{pmatrix} \begin{pmatrix} \theta_N^{step}(L_x,p) \\ 0 \end{pmatrix} \tag{B.18}$$

By developing equation B.18 and eliminating $\theta_N^{step}(L_x,p)$, one obtains a direct relation between the Laplace temperature and the heat flux density at the PFC top surface:

$$\theta_1^{step}(0,p) = \frac{A_{PFC}^{N}(p)}{C_{PFC}^{N}(p)} \Phi_1(0,p) \text{ for inertial PFCs} \tag{B.19}$$

Concerning actively-cooled PFCs, M_{PFC}^{N} links the Laplace temperature and heat flux density at the top surface of the PFC with the Laplace temperature and heat flux density of the cooling system. By considering equations B.12, B.17 and B.16, this yields to:

$$\begin{pmatrix} \theta_1^{step}(0,p) \\ \Phi_1(0,p) \end{pmatrix} = M_{PFC}^{N} \begin{pmatrix} 0 \\ \Phi_{cool}(p) \end{pmatrix} = \begin{pmatrix} A_{PFC}^{N}(p) & B_{PFC}^{N}(p) \\ C_{PFC}^{N}(p) & D_{PFC}^{N}(p) \end{pmatrix} \begin{pmatrix} 0 \\ \Phi_{cool}(p) \end{pmatrix} \tag{B.20}$$

By developing equation B.20 and eliminating $\Phi_{cool}(p)$, one also obtains a direct relation between the Laplace temperature and heat flux density at the PFC top surface:

$$\theta_1^{step}(0,p) = \frac{B_{PFC}^{N}(p)}{D_{PFC}^{N}(p)} \Phi_1(0,p) \text{ for actively-cooled PFCs} \tag{B.21}$$

Eventually, $\Phi_1(0,p)$ can be obtained from the B.C. at the PFC top surface (equation 2.57b) and Laplace transform tables [91]:

$$\Phi_1(0,p) = \frac{1}{p} \tag{B.22}$$

which can be substituted in both equations B.19 and B.21:

$$\left|\begin{array}{l}\theta_1^{step}(0,p) = \dfrac{1}{p}\dfrac{A_{PFC}^N(p)}{C_{PFC}^N(p)} \text{ for inertial PFCs} \\ \text{or} \\ \theta_1^{step}(0,p) = \dfrac{1}{p}\dfrac{B_{PFC}^N(p)}{D_{PFC}^N(p)} \text{ for actively-cooled PFCs}\end{array}\right. \tag{B.23}$$

Therefore, to obtain the temperature at the PFC surface, the values of the step response at the PFC top surface in the general equation of WEE-temp (equations 2.66), $T_1^{step}(s, 0, t - t_k(s))$, can be calculated by inverting equation B.23 using the inversion formula 2.59. This integral cannot be calculated analytically but can be estimated numerically using an appropriate algorithm. In WEE-temp, such inversion is done using the De Hoog's algorithm [93].

The previous analytical development was focused on the calculation of the surface temperature. To obtain the temperature profile in the first material layer (one remembers here that at present MHIMS only handles one material layer), one only has to consider a first material layer with a thickness $e_1'(x) = e_1 - x$. In that case, the quadrupole matrix of the first material layer is:

for $0 \leqslant x \leqslant e_1$:

$$M_{lay,1}'(x,p) = \begin{pmatrix} \cosh\left(\alpha_1 e_1'(x)\right) & \dfrac{1}{\lambda_1\alpha_1}\sinh\left(\alpha_1 e_1'(x)\right) + R_{c_1}\cosh\left(\alpha_1 e_1'(x)\right) \\ \lambda_1\alpha_1\sinh\left(e_1'(x)\right) & \cosh\left(\alpha_1 e_1'(x)\right) + R_{c_1}\lambda_1\alpha_1\sinh\left(\alpha_1 e_1'(x)\right) \end{pmatrix} \tag{B.24}$$

and a quadrupole matrix of the whole PFC can be defined which is also valid for both inertially-cooled and actively-cooled PFCs:

for $0 \leqslant x \leqslant e_1$:

$$M_{PFC,1}^N(x,p) = M_{lay,1}'(x,p) + \overset{\curvearrowright N}{\prod_{i=2}} M_{lay,i} \ , \quad \left|\begin{array}{l} R_{c_N} = 0 \text{ for inertial PFCs} \\ \text{or} \\ R_{c_N} = \dfrac{1}{h} \text{ for actively-cooled PFCs}\end{array}\right.$$

$$M_{PFC,1}^N(x,p) = \begin{pmatrix} A_{PFC,1}^N(x,p) & B_{PFC,1}^N(x,p) \\ C_{PFC,1}^N(x,p) & D_{PFC,1}^N(x,p) \end{pmatrix} \tag{B.25}$$

One can note that this quadrupole matrix is equivalent to the one of the full PFC, M_{PFC}^N, when x is set to 0.

Now the Laplace temperature at a depth x, $\theta_1^{step}(x,p)$, will be obtained by analogy with the analytical study for the Laplace surface temperature $\theta_1^{step}(0,p)$. First, for inertial PFCs, $M_{PFC,1}^N(x,p)$ links the Laplace temperature and heat flux density at the depth x

with the ones at the rear boundary of the PFC ($x = L_x$):

$$\begin{aligned}\begin{pmatrix}\theta_1^{step}(x,p)\\ \Phi_1(x,p)\end{pmatrix} &= M^N_{PFC,1}(x,p)\begin{pmatrix}\theta_N^{step}(L_x,p)\\ 0\end{pmatrix}\\ \begin{pmatrix}\theta_1^{step}(x,p)\\ \Phi_1(x,p)\end{pmatrix} &= \begin{pmatrix}A^N_{PFC,1}(x,p) & B^N_{PFC,1}(x,p)\\ C^N_{PFC,1}(x,p) & D^N_{PFC,1}(x,p)\end{pmatrix}\begin{pmatrix}\theta_N^{step}(L_x,p)\\ 0\end{pmatrix}\end{aligned} \tag{B.26}$$

By developing equation B.26 and eliminating $\theta_N^{step}(L_x,p)$ using equation B.18, one obtains a direct relation between $\theta_1^{step}(x,p)$ and the Laplace heat flux density at the PFC top surface $\Phi_1(0,p)$:

$$\theta_1^{step}(x,p) = \frac{A^N_{PFC,1}(x,p)}{C^N_{PFC}(p)}\Phi_1(0,p) \text{ for inertial PFCs} \tag{B.27}$$

Likewise, for actively-cooled PFCs, $M^N_{PFC,1}(x,p)$ links the Laplace temperature and heat flux density at the depth x with the ones of the cooling system:

$$\begin{aligned}\begin{pmatrix}\theta_1^{step}(x,p)\\ \Phi_1(x,p)\end{pmatrix} &= M^N_{PFC,1}(x,p)\begin{pmatrix}0\\ \Phi_{cool}(p)\end{pmatrix}\\ \begin{pmatrix}\theta_1^{step}(x,p)\\ \Phi_1(x,p)\end{pmatrix} &= \begin{pmatrix}A^N_{PFC,1}(x,p) & B^N_{PFC,1}(x,p)\\ D^N_{PFC,1}(x,p) & D^N_{PFC,1}(x,p)\end{pmatrix}\begin{pmatrix}0\\ \Phi_{cool}(p)\end{pmatrix}\end{aligned} \tag{B.28}$$

By developing equation B.28 and eliminating $\Phi_{cool}(p)$ using equation B.20, one also obtains a direct relation between $\theta_1^{step}(x,p)$ and the Laplace heat flux density at the PFC top surface $\Phi_1(0,p)$:

$$\theta_1^{step}(x,p) = \frac{B^N_{PFC,1}(x,p)}{D^N_{PFC}(p)}\Phi_1(0,p) \text{ for actively-cooled PFCs} \tag{B.29}$$

One can substitute the expression of $\Phi_1(0,p)$ (equation B.22) in both equations B.27 and B.29 to obtain the general expression for $\theta_1^{step}(x,p)$:

$$\begin{aligned}&\underline{\text{for } 0 \leqslant x \leqslant e_1\text{:}}\\ &\left|\begin{aligned}&\theta_1^{step}(x,p) = \frac{1}{p}\frac{A^N_{PFC,1}(x,p)}{C^N_{PFC}(p)} \text{ for inertial PFCs}\\ &\qquad\qquad\text{or}\\ &\theta_1^{step}(x,p) = \frac{1}{p}\frac{B^N_{PFC,1}(x,p)}{D^N_{PFC}(p)} \text{ for actively-cooled PFCs}\end{aligned}\right.\end{aligned} \tag{B.30}$$

Again, to obtain the temperature at a depth x, the values of the step response at a depth x in the general equation of WEE-temp (equations 2.66), $T_1^{step}(s,x,t-t_k(s))$, are calculated by inverting numerically equation B.30 using the inversion formula 2.59. As in the case of the surface temperature, theses inversions are done using the De Hoog's algorithm [93].

Appendix C

PFC step response calculation through an analytical treatment.

In this appendix, one will use the properties of the Laplace transform to calculate analytical asymptotic expressions of the step response which are valid for a limited interval of the time domain. These analytical expressions are used in their interval of validity to calculate the value of the step response in the general equation of WEE-temp 2.66 instead of the time-consuming numerical inversion of equation B.30.

First, one will focus on the inversion for short time ($t \to 0$). The initial value theorem for a function $f(t)$ says that [91]:

$$\lim_{t\to 0} f(t) = f(0^+) = \lim_{p\to+\infty} pF(p) \tag{C.1}$$

This relation indicates that the large values of p in the Laplace domain correspond to small values of t in the time domain. Therefore it is possible to obtain an approximation of $T_1^{step}(x,t)$ valid for short time from the knowledge of an approximation of $\theta_1^{step}(x,p)$ for large values of p [91, 92]. First the Taylor expansion of the quadrupole matrix $M_{lay,i}$ when p goes to infinity is calculated:

$$M_{lay,i}(p) \underset{p\to+\infty}{=} \frac{1}{2}\lambda_i\alpha_i e^{\alpha_i e_i} \begin{pmatrix} \frac{1}{\lambda_i\alpha_i} + o(e^{-\sqrt{p}}) & \frac{1}{\lambda_i\alpha_i}\left(R_{c_i} + \frac{1}{\lambda_i\alpha_i}\right) + o(e^{-\sqrt{p}}) \\ 1 + o(e^{-\sqrt{p}}) & R_{c_i} + \frac{1}{\lambda_i\alpha_i} + o(e^{-\sqrt{p}}) \end{pmatrix} \tag{C.2}$$

This equation holds also for the quadrupole matrix of the first material layer $M'_{lay,1}(x,p)$

with thickness $e'_1(x) = e_1 - x$:

for $0 \leqslant x \leqslant e_1$:

$$M'_{lay,1}(x,p) \underset{p\to+\infty}{=} \frac{1}{2}\lambda_i\alpha_i e^{\alpha_i e'_1(x)} \begin{pmatrix} \frac{1}{\lambda_i\alpha_i} + o(e^{-\sqrt{p}}) & \frac{1}{\lambda_i\alpha_i}\left(R_{c_i} + \frac{1}{\lambda_i\alpha_i}\right) + o(e^{-\sqrt{p}}) \\ 1 + o(e^{-\sqrt{p}}) & R_{c_i} + \frac{1}{\lambda_i\alpha_i} + o(e^{-\sqrt{p}}) \end{pmatrix} \tag{C.3}$$

For the specific case of a PFC with $N = 1$ material layer, the following equalities hold:

$$\begin{gathered} M^N_{PFC}(p) = M^1_{PFC}(p) = M_{lay,1}(p) \\ \text{and} \\ M^N_{PFC,1}(x,p) = M^1_{PFC,1}(x,p) = M'_{lay,1}(x,p) \end{gathered} \tag{C.4}$$

Then, if one defines the following expression for M^1_{PFC}:

$$M^1_{PFC}(p) \underset{p\to+\infty}{=} \frac{1}{2}\lambda_1\alpha_1 e^{\alpha_1 e_1} \begin{pmatrix} A^{1,\infty}_{PFC}\left(\frac{1}{\sqrt{p}}\right) + o(e^{-\sqrt{p}}) & B^{1,\infty}_{PFC}\left(\frac{1}{\sqrt{p}}\right) + o(e^{-\sqrt{p}}) \\ C^{1,\infty}_{PFC}\left(\frac{1}{\sqrt{p}}\right) + o(e^{-\sqrt{p}}) & D^{1,\infty}_{PFC}\left(\frac{1}{\sqrt{p}}\right) + o(e^{-\sqrt{p}}) \end{pmatrix} \tag{C.5}$$

the value of the complex function $A^{1,\infty}_{PFC}$, $B^{1,\infty}_{PFC}$, $C^{1,\infty}_{PFC}$ and $D^{1,\infty}_{PFC}$ can be identified in equation C.2:

$$\begin{cases} A^{1,\infty}_{PFC}\left(\frac{1}{\sqrt{p}}\right) = C^{1,\infty}_{PFC}\left(\frac{1}{\sqrt{p}}\right)/(\lambda_1\alpha_1) \\ B^{1,\infty}_{PFC}\left(\frac{1}{\sqrt{p}}\right) = D^{1,\infty}_{PFC}\left(\frac{1}{\sqrt{p}}\right)/(\lambda_1\alpha_1) \\ C^{1,\infty}_{PFC}\left(\frac{1}{\sqrt{p}}\right) = 1 \\ D^{1,\infty}_{PFC}\left(\frac{1}{\sqrt{p}}\right) = R_{c_1} + \frac{1}{\lambda_1\alpha_1} = R_{c_1} + \sqrt{\frac{a_1}{\lambda_1}}\frac{1}{\sqrt{p}} \end{cases} \tag{C.6}$$

Thus, from equations C.5 and C.3 respectively, the quadrupole matrices M^1_{PFC} and $M^1_{PFC,1}$ can be written as:

$$M^1_{PFC}(p) \underset{p\to+\infty}{=} \frac{1}{2}\lambda_1\alpha_1 e^{\alpha_1 e_1} \begin{pmatrix} \frac{C^{1,\infty}_{PFC}\left(\frac{1}{\sqrt{p}}\right)}{\lambda_1\alpha_1} + o(e^{-\sqrt{p}}) & \frac{D^{1,\infty}_{PFC}\left(\frac{1}{\sqrt{p}}\right)}{\lambda_1\alpha_1} + o(e^{-\sqrt{p}}) \\ C^{1,\infty}_{PFC}\left(\frac{1}{\sqrt{p}}\right) + o(e^{-\sqrt{p}}) & D^{1,\infty}_{PFC}(p) + o(e^{-\sqrt{p}}) \end{pmatrix} \tag{C.7}$$

for $0 \leqslant x \leqslant e_1$:

$$M^1_{PFC,1}(x,p) \underset{p\to+\infty}{=} \frac{1}{2}\lambda_1\alpha_1 e^{\alpha_1 e'_1(x)} \begin{pmatrix} \dfrac{C^{1,\infty}_{PFC}\left(\dfrac{1}{\sqrt{p}}\right)}{\lambda_1\alpha_1} + o(e^{-\sqrt{p}}) & \dfrac{D^{1,\infty}_{PFC}\left(\dfrac{1}{\sqrt{p}}\right)}{\lambda_1\alpha_1} + o(e^{-\sqrt{p}}) \\ C^{1,\infty}_{PFC}\left(\dfrac{1}{\sqrt{p}}\right) + o(e^{-\sqrt{p}}) & D^{1,\infty}_{PFC}(p) + o(e^{-\sqrt{p}}) \end{pmatrix} \tag{C.8}$$

Actually, it can be proven by recurrence that, for a PFC with N layers, the two quadrupole matrices M^N_{PFC} and $M^N_{PFC,1}$ (defined by equations B.17 and B.25 respectively) can be expressed as follows:

$$M^N_{PFC}(p) \underset{p\to+\infty}{=} \frac{1}{2^N}\left(\prod_{i=1}^{N}\lambda_i\alpha_i e^{\alpha_i e_i}\right) \times \begin{pmatrix} \dfrac{C^{N,\infty}_{PFC}\left(\dfrac{1}{\sqrt{p}}\right)}{\lambda_1\alpha_1} + o(e^{-\sqrt{p}}) & \dfrac{D^{N,\infty}_{PFC}\left(\dfrac{1}{\sqrt{p}}\right)}{\lambda_1\alpha_1} + o(e^{-\sqrt{p}}) \\ C^{N,\infty}_{PFC}\left(\dfrac{1}{\sqrt{p}}\right) + o(e^{-\sqrt{p}}) & D^{N,\infty}_{PFC}(p) + o(e^{-\sqrt{p}}) \end{pmatrix} \tag{C.9}$$

for $0 \leqslant x \leqslant e_1$:

$$M^N_{PFC,1}(x,p) \underset{p\to+\infty}{=} \frac{1}{2^N}\left(\lambda_1\alpha_1 e^{\alpha_1 e'_1(x)} \times \prod_{i=2}^{N}\lambda_i\alpha_i e^{\alpha_i e_i}\right) \times \begin{pmatrix} \dfrac{C^{N,\infty}_{PFC}\left(\dfrac{1}{\sqrt{p}}\right)}{\lambda_1\alpha_1} + o(e^{-\sqrt{p}}) & \dfrac{D^{N,\infty}_{PFC}\left(\dfrac{1}{\sqrt{p}}\right)}{\lambda_1\alpha_1} + o(e^{-\sqrt{p}}) \\ C^{N,\infty}_{PFC}\left(\dfrac{1}{\sqrt{p}}\right) + o(e^{-\sqrt{p}}) & D^{N,\infty}_{PFC}(p) + o(e^{-\sqrt{p}}) \end{pmatrix} \tag{C.10}$$

where $C^{N,\infty}_{PFC}$ and $D^{N,\infty}_{PFC}$ are two polynomials of degree $N-1$ and N respectively. Therefore, from equation B.30, one obtains the following expansion for $\theta_1^{step}(x,p)$ when p goes to infinity:

for $0 \leqslant x \leqslant e_1$:

$$\left|\begin{array}{l} \theta_1^{step}(x,p) = \dfrac{1}{p}\dfrac{A^N_{PFC,1}(x,p)}{C^N_{PFC}(p)} \underset{p\to+\infty}{=} \dfrac{1}{p}\dfrac{e^{-\alpha_1 x}}{\lambda_1\alpha_1} + o\left(\dfrac{e^{-\alpha_1 x-\sqrt{p}}}{p}\right) \text{ for inertial PFCs} \\ \qquad\qquad \text{or} \\ \theta_1^{step}(x,p) = \dfrac{1}{p}\dfrac{B^N_{PFC,1}(x,p)}{D^N_{PFC}(p)} \underset{p\to+\infty}{=} \dfrac{1}{p}\dfrac{e^{-\alpha_1 x}}{\lambda_1\alpha_1} + o\left(\dfrac{e^{-\alpha_1 x-\sqrt{p}}}{p}\right) \text{ for actively-cooled PFCs} \end{array}\right. \tag{C.11}$$

The formula is the same for both type of PFCs. Moreover, if one notes that:

$$\frac{e^{-\alpha_1 x-\sqrt{p}}}{p} = o\left(\frac{1}{p}\frac{e^{-\alpha_1 x}}{\lambda_1\alpha_1}\right) \tag{C.12}$$

equation C.11 becomes:

$$\begin{aligned}&\underline{\text{for } 0 \leqslant x \leqslant e_1\text{:}}\\ &\theta_1^{step}(x,p) \underset{p\to+\infty}{=} \frac{1}{p}\frac{e^{-\alpha_1 x}}{\lambda_1\alpha_1} + o\left(\frac{1}{p}\frac{e^{-\alpha_1 x}}{\lambda_1\alpha_1}\right)\end{aligned} \tag{C.13}$$

Therefore, the following approximation of $\theta_1^{step}(x,p)$ is obtained when p goes to infinity:

$$\begin{aligned}&\underline{\text{for } 0 \leqslant x \leqslant e_1\text{:}}\\ &\theta_1^{step}(x,p) \underset{p\to+\infty}{\approx} \frac{1}{p}\frac{e^{-\alpha_1 x}}{\lambda_1\alpha_1}\end{aligned} \tag{C.14}$$

The inverse Laplace transform of the RHS of equation C.14 is calculated using Laplace transform table [91]:

$$\mathscr{L}^{-1}\left[\frac{1}{p}\frac{e^{-\alpha_1 x}}{\lambda_1\alpha_1}\right] = \mathscr{L}^{-1}\left[\frac{\sqrt{a_1}}{\lambda_1}\frac{e^{-\sqrt{p/a_1}x}}{p\sqrt{p}}\right] = \frac{2\sqrt{t}}{\sqrt{\lambda_1\rho_1 c_{p_1}}}\,\text{ierfc}\left(\frac{x}{2\sqrt{a_1 t}}\right) \tag{C.15}$$

where ierfc is the integral of the complementary error function erfc defined as [90]:

$$\text{ierfc}\,(z) = \int_z^\infty \text{erfc}\,(z)dz = \frac{e^{-z^2}}{\sqrt{\pi}} - z\,\text{erfc}\,(z) \tag{C.16}$$

Thus the function C.15 is an asymptotic expression of $T_1^{step}(x,t)$ for short time:

$$\begin{aligned}&\underline{\text{for } 0 \leqslant x \leqslant e_1\text{:}}\\ &T_1^{step}(x,t) \underset{t\to 0}{\approx} \frac{2\sqrt{t}}{\sqrt{\lambda_1\rho_1 c_{p_1}}}\,\text{ierfc}\left(\frac{x}{2\sqrt{a_1 t}}\right) \text{ for } \begin{vmatrix}\text{inertial PFCs}\\ \text{actively-cooled PFCs}\end{vmatrix}\end{aligned} \tag{C.17}$$

One can recognise in equation C.17 the solution of the linear heat equation for a semi-infinite wall submitted to a heat flux density step of 1 W.m^{-2} at $t = 0$ s [91]. For the special case of the surface temperature ($x = 0$), the step response $T_1^{step}(0,t)$ for short time is:

$$T_1^{step}(0,t) \underset{t\to 0}{\approx} \frac{2\sqrt{t}}{\sqrt{\pi}\sqrt{\lambda_1\rho_1 c_{p_1}}} \tag{C.18}$$

Therefore, the surface temperature response for short time only depends on the effusivity of the surface material $E_1 = \sqrt{\lambda_1 c_{p_1}\rho_1}$.
A comparison between $T_1^{step}(0,t)$ and its short time approximation is displayed in figure C.1 in the case of the PFC defined in the previous subsection (PFC with three mate-

rial layers). The results are plotted for both types of cooling techniques, namely for an inertially-cooled PFC in figure C.1.a and an actively-cooled PFC in figure C.1.b. For a given relative error, one can numerically evaluate an interval of validity $[0, t_0^{max}]$ of the short time asymptotic expression where equation C.17 can be used to calculate $T_1^{step}(x,t)$ instead of the numerical inversion of equation B.30. As an example, for the aforementioned PFC and accepting a relative error of 0.1 %, the asymptotic approximation is valid up to $t_0^{max} = 0.73$ s for the inertial PFC case and up to $t_0^{max} = 0.51$ s for the actively-cooled PFC case. Thus, for a simulation of an ELM – inter-ELM period with an ELM frequency of 50 Hz, the simulated time is 0.02 s which means that all the values of $T_1^{step}(s, x, t - t_k(s))$ in the general equation of WEE-temp 2.66 will be treated analytically using the asymptotic expression C.17.

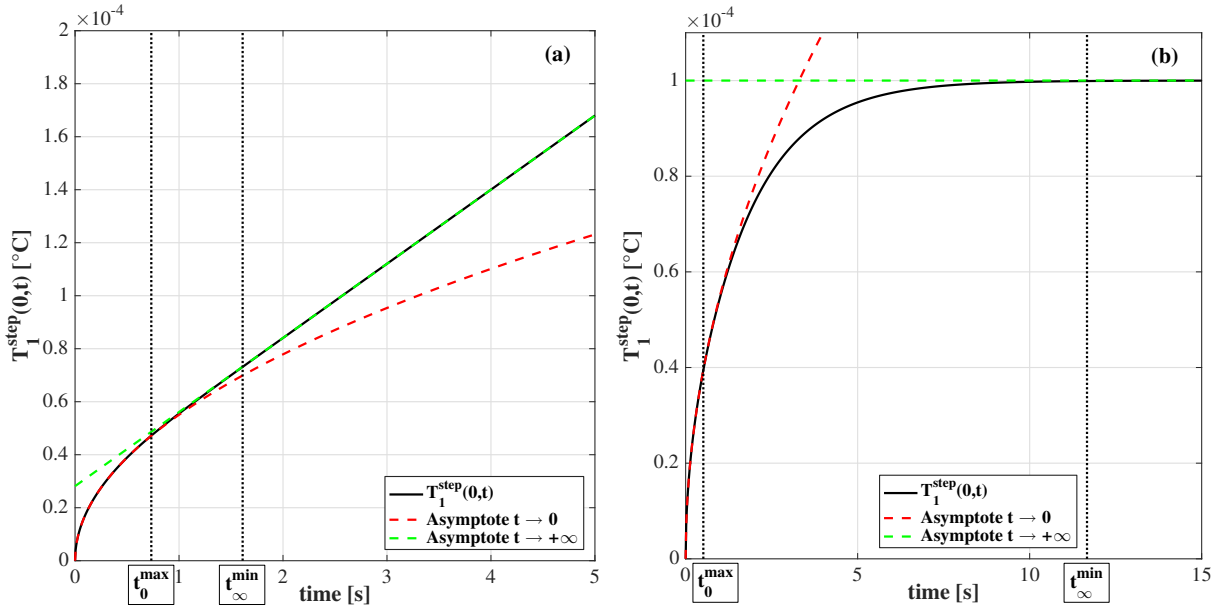

Figure C.1: Surface step response $T_1^{step}(0,t)$ of a PFC made of three material layers (cf. table 2.8 for the layer specifications) and its corresponding short time approximation (red dashed line) and long time asymptote (green dashed line) in the case of an inertially-cooled PFC (a) and and actively-cooled PFC (b). For a given relative error, the short time approximation is valid up to $t = t_0^{max}$ while the long time asymptote is valid from $t = t_\infty^{min}$.

Now, one will focus on the inversion for long time ($t \to +\infty$). The final value theorem for a function $f(t)$ says that [91]:

$$\lim_{t \to +\infty} f(t) = \lim_{p \to 0} pF(p) \tag{C.19}$$

This relation will be used to calculate an asymptote of $T_1^{step}(x,t)$ for long time. First the

Taylor expansion of the quadrupole matrix $M_{lay,i}$ when p goes to 0 is calculated:

$$M_{lay,i}(p) \underset{p\to 0}{=} \begin{pmatrix} A^0_{lay,i}(p) & B^0_{lay,i}(p) \\ C^0_{lay,i}(p) & D^0_{lay,i}(p) \end{pmatrix} \tag{C.20}$$

$$\begin{cases} A^0_{lay,i}(p) = 1 + \dfrac{e_i^2}{2a_i}p + \dfrac{e_i^4}{4!a_i^2}p^2 + o(p^2) \\ B^0_{lay,i}(p) = \left(\dfrac{e_i}{\lambda_i} + R_{c_i}\right) + \left(\dfrac{e_i^3}{3!\lambda_i a_i} + \dfrac{R_{c_i}e_i^2}{2a_i}\right)p + \left(\dfrac{e_i^5}{5!\lambda_i a_i^2} + \dfrac{R_{c_i}e_i^4}{4!a_i^2}\right) + o(p^2) \\ C^0_{lay,i}(p) = \dfrac{\lambda_i e_i}{a_i}p + \dfrac{\lambda_i e_i^3}{3!a_i^2}p^2 + o(p^2) \\ D^0_{lay,i}(p) = 1 + \left(\dfrac{e_i^2}{2a_i} + \dfrac{R_{c_i}\lambda_i e_i}{a_i}\right)p + \left(\dfrac{e_i^4}{4!a_i^2} + \dfrac{R_{c_i}\lambda_i e_i^3}{3!a_i^2}\right) + o(p^2) \end{cases}$$

This equation holds also for the quadrupole matrix of the first material layer $M'_{lay,1}(x,p)$ with thickness $e'_1(x) = e_1 - x$:

$$M'_{lay,1}(x,p) \underset{p\to 0}{=} \begin{pmatrix} A'^{,0}_{lay,1}(x,p) & B'^{,0}_{lay,i}(x,p) \\ C'^{,0}_{lay,1}(x,p) & D'^{,0}_{lay,1}(x,p) \end{pmatrix} \tag{C.21}$$

$$\begin{cases} A'^{,0}_{lay,1}(x,p) = 1 + \dfrac{e'_1(x)^2}{2a_1}p + \dfrac{e'_1(x)^4}{4!a_1^2}p^2 + o(p^2) \\ B'^{,0}_{lay,1}(x,p) = \left(\dfrac{e'_1(x)}{\lambda_1} + R_{c_1}\right) + \left(\dfrac{e'_1(x)^3}{3!\lambda_1 a_1} + \dfrac{R_{c_1}e'_1(x)^2}{2a_1}\right)p + \left(\dfrac{e'_1(x)^5}{5!\lambda_1 a_1^2} + \dfrac{R_{c_1}e'_1(x)^4}{4!a_1^2}\right) + o(p^2) \\ C'^{,0}_{lay,1}(x,p) = \dfrac{\lambda_1 e'_1(x)}{a_1}p + \dfrac{\lambda_1 e'_1(x)^3}{3!a_1^2}p^2 + o(p^2) \\ D'^{,0}_{lay,1}(x,p) = 1 + \left(\dfrac{e'_1(x)^2}{2a_1} + \dfrac{R_{c_1}\lambda_1 e'_1(x)}{a_1}\right)p + \left(\dfrac{e'_1(x)^4}{4!a_1^2} + \dfrac{R_{c_1}\lambda_1 e'_1(x)^3}{3!a_1^2}\right) + o(p^2) \end{cases}$$

Using the two matrices C.20 and C.21, one can show by recurrence that, for a PFC with N layers, the two quadrupole matrices M^N_{PFC} and $M^N_{PFC,1}$ (defined by equations B.17 and B.25 respectively) can be expressed as follows:

$$M^N_{PFC}(p) \underset{p\to 0}{=} \begin{pmatrix} A^{N,0}_{PFC,1}(0,p) & B^{N,0}_{PFC,1}(0,p) \\ C^{N,0}_{PFC,1}(0,p) & D^{N,0}_{PFC,1}(0,p) \end{pmatrix} \tag{C.22}$$

for $0 \leqslant x \leqslant e_1$:

$$M^N_{PFC,1}(x,p) \underset{p\to 0}{=} \begin{pmatrix} A^{N,0}_{PFC,1}(x,p) & B^{N,0}_{PFC,1}(x,p) \\ C^{N,0}_{PFC,1}(x,p) & D^{N,0}_{PFC,1}(x,p) \end{pmatrix} \tag{C.23}$$

for $0 \leqslant x \leqslant e_1$:

$$
\begin{cases}
A^{N,0}_{PFC,1}(x,p) = 1 + \left[\left(\dfrac{(e_1-x)^2}{2a_1} + \displaystyle\sum_{i=2}^{N} \dfrac{e_i^2}{2a_i} \right) \right. \\
\qquad\qquad \left. + \displaystyle\sum_{i=2}^{N} \left(\dfrac{\lambda_i e_i}{a_i} \left[\left(\dfrac{e_1-x}{\lambda_1} + R_{c_1} \right) + \displaystyle\sum_{j=2}^{i-1} \left(\dfrac{e_j}{\lambda_j} + R_{c_j} \right) \right] \right) \right] p + o(p) \\
B^{N,0}_{PFC,1}(x,p) = \left(\dfrac{e_1-x}{\lambda_1} + R_{c_1} \right) + \displaystyle\sum_{i=2}^{N} \left(\dfrac{e_i}{\lambda_i} + R_{c_i} \right) + o(1) \\
C^{N,0}_{PFC,1}(x,p) = \left[\left(\dfrac{\lambda_1(e_1-x)}{a_1} \right) + \displaystyle\sum_{i=2}^{N} \left(\dfrac{\lambda_i e_i}{a_i} \right) \right] p + \\
\qquad \left[\left(\dfrac{\lambda_1(e_1-x)^3}{3!a_1^2} + \displaystyle\sum_{i=2}^{N} \dfrac{\lambda_i e_i^3}{3!a_i^2} \right) \right. \\
\qquad + \displaystyle\sum_{i=2}^{N} \left(\dfrac{\lambda_i e_i}{a_i} \left[\left(\dfrac{(e_1-x)^2}{2a_1} + \dfrac{R_{c_1}\lambda_1(e_1-x)}{a_1} \right) + \displaystyle\sum_{j=2}^{i-1} \left(\dfrac{e_j^2}{2a_j} + \dfrac{R_{c_j}\lambda_j e_j}{a_j} \right) \right] \right) \\
\qquad + \displaystyle\sum_{i=2}^{N} \left(\dfrac{e_i^2}{2a_i} \left[\dfrac{\lambda_1(e_1-x)}{a_1} + \displaystyle\sum_{j=2}^{i-1} \dfrac{\lambda_i e_i}{a_i} \right] \right) \\
\qquad \left. + \displaystyle\sum_{i=2}^{N} \left(\dfrac{\lambda_i e_i}{a_i} \left[\displaystyle\sum_{j=2}^{N-1} \left(\left[\dfrac{e_j}{\lambda_j} + R_{c_j} \right] \left[\dfrac{\lambda_1(e_1-x)}{a_1} + \displaystyle\sum_{k=2}^{j-1} \dfrac{\lambda_k e_k}{a_k} \right] \right) \right] \right) \right] p^2 + o(p^2) \\
D^{N,0}_{PFC,1}(x,p) = 1 + \left[\left(\left[\dfrac{(e_1-x)^2}{2a_1} + \dfrac{R_{c_1}\lambda_1(e_1-x)}{a_1} \right] + \displaystyle\sum_{i=2}^{N} \left[\dfrac{e_i^2}{2a_i} + \dfrac{R_{c_i}\lambda_i e_i}{a_i} \right] \right) \right. \\
\qquad\qquad \left. + \displaystyle\sum_{i=2}^{N} \left(\left[\dfrac{e_i}{\lambda_i} + R_{c_i} \right] \left[\dfrac{\lambda_1(e_1-x)}{a_1} + \displaystyle\sum_{j=2}^{i-1} \dfrac{\lambda_j e_j}{a_j} \right] \right) \right] p + o(p)
\end{cases}
\tag{C.24}
$$

First one will focus on actively-cooled PFCs. From equation B.30, one obtains the following expansion for $\theta_1^{step}(x,p)$ when p goes to 0 for such type of PFCs:

$$
\begin{aligned}
\theta_1^{step}(x,p) &\underset{p\to 0}{=} \frac{1}{p} \frac{B^{N,0}_{PFC,1}(x,p)}{D^{N,0}_{PFC,1}(0,p)} \\
\theta_1^{step}(x,p) &\underset{p\to 0}{=} \left[\left(\frac{e_1-x}{\lambda_1} + R_{c_1} \right) + \sum_{i=2}^{N} \left(\frac{e_i}{\lambda_i} + R_{c_i} \right) \right] \frac{1}{p} + o\left(\frac{1}{p}\right)
\end{aligned}
\tag{C.25}
$$

From this expansion, one can note that:

$$p\left(\theta_1^{step}(x,p) - \left[\left(\frac{e_1-x}{\lambda_1}+R_{c_1}\right)+\sum_{i=2}^{N}\left(\frac{e_i}{\lambda_i}+R_{c_i}\right)\right]\frac{1}{p}\right) \underset{p\to 0}{=} o(1) \tag{C.26}$$

From Laplace transform table [91], one knows that:

$$\mathscr{L}^{-1}\left[\frac{1}{p}\right] = 1 \tag{C.27}$$

Therefore, by applying the final value theorem C.19 and the inverse Laplace transform C.27, one obtains the following limit from equation C.26:

$$\begin{aligned} K_{AC}^{\infty} &= \lim_{p\to 0} p\left(\theta_1^{step}(x,p) - \left[\left(\frac{e_1-x}{\lambda_1}+R_{c_1}\right)+\sum_{i=2}^{N}\left(\frac{e_i}{\lambda_i}+R_{c_i}\right)\right]\frac{1}{p}\right) \\ K_{AC}^{\infty} &= \lim_{t\to+\infty}\left(T_1^{step}(x,t) - \left[\left(\frac{e_1-x}{\lambda_1}+R_{c_1}\right)+\sum_{i=2}^{N}\left(\frac{e_i}{\lambda_i}+R_{c_i}\right)\right]\right) \\ K_{AC}^{\infty} &= 0 \end{aligned} \tag{C.28}$$

As a consequence, the step response of actively-cooled PFCs has a horizontal asymptote when t goes to infinity:

for $0 \leqslant x \leqslant e_1$:

$$T_1^{step}(x,t) \underset{t\to+\infty}{\approx} \left(\frac{e_1-x}{\lambda_1}+R_{c_1}\right)+\sum_{i=2}^{N}\left(\frac{e_i}{\lambda_i}+R_{c_i}\right) \text{ for actively-cooled PFCs} \tag{C.29}$$

From the general equation of WEE-temp 2.66, one can see that actively-cooled PFCs reach a steady-state temperature profile which is proportional to the steady-state net heat flux density ϕ_{net}^{steady}:

$$\begin{aligned} \overline{T_1}(s,x,t) &= T_{cool}(s) + \sum_{k=1}^{N_\phi(s,t)} \Delta\phi_k(s) T_1^{step}(s,x,t-t_k(s)) \\ \overline{T_1}(s,x,t) &\underset{t\to+\infty}{=} T_{cool}(s) + \left[\left(\frac{e_1(s)-x}{\lambda_1(s)}+R_{c_1}(s)\right)+\sum_{i=2}^{N}\left(\frac{e_i(s)}{\lambda_i(s)}+R_{c_i}(s)\right)\right]\sum_{k=1}^{N_\phi(s,t)}\Delta\phi_k(s) \\ \overline{T_1}(s,x,t) &\underset{t\to+\infty}{=} T_{cool}(s) + \left[\left(\frac{e_1(s)-x}{\lambda_1(s)}+R_{c_1}(s)\right)+\sum_{i=2}^{N}\left(\frac{e_i(s)}{\lambda_i(s)}+R_{c_i}(s)\right)\right]\phi_{net}^{steady}(s) \end{aligned} \tag{C.30}$$

The same reasoning will be applied to inertial PFCs. First, one defines more synthetic

expressions for the two functions $A^{N,0}_{PFC,1}(x,p)$ and $C^{N,0}_{PFC,1}(x,p)$ defined in equation C.24:

$$\begin{aligned} A^{N,0}_{PFC,1}(x,p) &= 1 + A_1(x)p + o(p) \\ C^{N,0}_{PFC,1}(x,p) &= C_1(x)p + C_2(x)p^2 + o(p^2) \end{aligned} \tag{C.31}$$

Where $A_1(x)$, $C_1(x)$ and $C_2(x)$ are three functions of the depth x. They can be identified in equation C.24 through the colored square brackets. Hence, from equation B.30, one obtains the following expansion for $\theta_1^{step}(x,p)$ when p goes to 0 for inertial PFCs:

$$\begin{aligned} \theta_1^{step}(x,p) &\underset{p\to 0}{=} \frac{1}{p}\frac{A^{N,0}_{PFC,1}(x,p)}{C^{N,0}_{PFC,1}(0,p)} \\ \theta_1^{step}(x,p) &\underset{p\to 0}{=} \frac{1}{p^2}\frac{1 + A_1(x)p + o(p)}{C_1(0) + C_2(0)p + o(p)} \\ \theta_1^{step}(x,p) &\underset{p\to 0}{=} \frac{1}{p^2}\left(\frac{1}{C_1(0)} + \frac{1}{C_1(0)}\left[A_1(x) - \frac{C_2(0)}{C_1(0)}\right]\frac{1}{p} + o(p)\right) \\ \theta_1^{step}(x,p) &\underset{p\to 0}{=} \frac{1}{C_1(0)}\frac{1}{p^2} + \frac{1}{C_1(0)}\left[A_1(x) - \frac{C_2(0)}{C_1(0)}\right]\frac{1}{p} + o\left(\frac{1}{p}\right) \end{aligned} \tag{C.32}$$

From this expansion, one can note that:

$$p\left(\theta_1^{step}(x,p) - \left(\frac{1}{C_1(0)}\frac{1}{p^2} + \frac{1}{C_1(0)}\left[A_1(x) - \frac{C_2(0)}{C_1(0)}\right]\frac{1}{p}\right)\right) \underset{p\to 0}{=} o(1) \tag{C.33}$$

From Laplace transform table [91], one knows that:

$$\mathscr{L}^{-1}\left[\frac{1}{p^2}\right] = t \tag{C.34}$$

Therefore, by applying the final value theorem C.19 and the inverse Laplace transforms C.27 and C.34, one obtains the following limit from equation C.33:

$$\begin{aligned} K^{\infty}_{IC} &= \lim_{p\to 0} p\left(\theta_1^{step}(x,p) - \left(\frac{1}{C_1(0)}\frac{1}{p^2} + \frac{1}{C_1(0)}\left[A_1(x) - \frac{C_2(0)}{C_1(0)}\right]\frac{1}{p}\right)\right) \\ K^{\infty}_{IC} &= \lim_{t\to +\infty}\left(T_1^{step}(x,t) - \left(\frac{1}{C_1(0)}t + \frac{1}{C_1(0)}\left[A_1(x) - \frac{C_2(0)}{C_1(0)}\right]\right)\right) \\ K^{\infty}_{IC} &= 0 \end{aligned} \tag{C.35}$$

As a consequence, the step response of inertially-cooled PFCs has an oblique asymptote when t goes to infinity:

$$\underline{\text{for } 0 \leqslant x \leqslant e_1\text{:}}$$
$$T_1^{step}(x,t) \underset{t\to+\infty}{\approx} \frac{1}{C_1(0)}t + \frac{1}{C_1(0)}\left[A_1(x) - \frac{C_2(0)}{C_1(0)}\right] \text{ for inertial PFCs} \tag{C.36}$$

In the same way as for the short time approximation, a comparison between the surface step response $T_1^{step}(0,t)$ and its long time asymptote is displayed in figure C.1 in the case of the PFC defined in the previous subsection. The results are plotted for both types of cooling techniques, namely for an inertially-cooled PFC in figure C.1.a and an actively-cooled PFC in figure C.1.b. Again, for a given relative error, one can numerically evaluate an interval of validity $[t_\infty^{min}, +\infty]$ of the long time asymptote where equation C.36 or equation C.29 can be used to calculate $T_1^{step}(x,t)$ instead of the numerical inversion of equation B.30. For the aforementioned PFC and accepting a relative error of 0.1 %, the asymptote is valid from $t_\infty^{min} = 1.61$ s for the inertial PFC case and from $t_\infty^{min} = 11.7$ s for the actively-cooled PFC case.

Appendix D

Particle and energy flux balances of a SolEdge2D-EIRENE simulation.

In this appendix, two convergence criteria, one for particle and one for energy, will be derived to determine if a SolEdge2D-EIRENE simulation has converged to a steady-state. These criteria are based on multi-system particle flux (herein referred to as *flux*) and power balances. The experimental steady-state plasma satisfies these criteria which entails that the SolEdge2D-EIRENE solution has to satisfy it as well. The overlapped systems used for the flux and power balances are displayed in figure D.1. The tokamak system encompasses the Vacuum Vessel (VV) and the wall. The VV itself is divided into the CORE domain and the EDGE+SOL domain which corresponds to the SolEdge2D-EIRENE simulated domain.

First, one will focus on the multi-system particle flux balances. These flux balances will be applied to deuterium (D) as it is the working gas of the discharge of interest #JPN89044. As a first step, the flux balance equation for the tokamak system has to be introduced:

$$\frac{d}{dt}\left(N_{TOK}\right) = \frac{d}{dt}\left(N_{VV}^{D^+} + N_{VV}^{D} + N_{wall,tot}\right) = Q_{inj,tot} - Q_{pump,tot} \quad [\text{at.s}^{-1}] \tag{D.1}$$

where N_{TOK} is the total number of deuterium particles in the tokamak, $N_{VV}^{D^+}$ the number of D ions in the VV, N_{VV}^{D} the number of D neutrals in the VV (atoms and molecules), $N_{wall,tot}$ the number of D particles in the wall (wall inventory), $Q_{inj,tot}$ the total external D injection flux and $Q_{pump,tot}$ the total D pumping flux. This equation is the particle balance equation introduced in chapter 1 section 5 to experimentally study the fuel retention of the reactor wall. The VV flux balance can easily be obtained from equation D.1:

$$\frac{d}{dt}\left(N_{VV}^{D^+} + N_{VV}^{D}\right) = Q_{inj,tot} - Q_{pump,tot} - \frac{dN_{wall,tot}}{dt} \tag{D.2}$$

Now, the LHS of equation D.2 can be developed to take into account the two VV regions

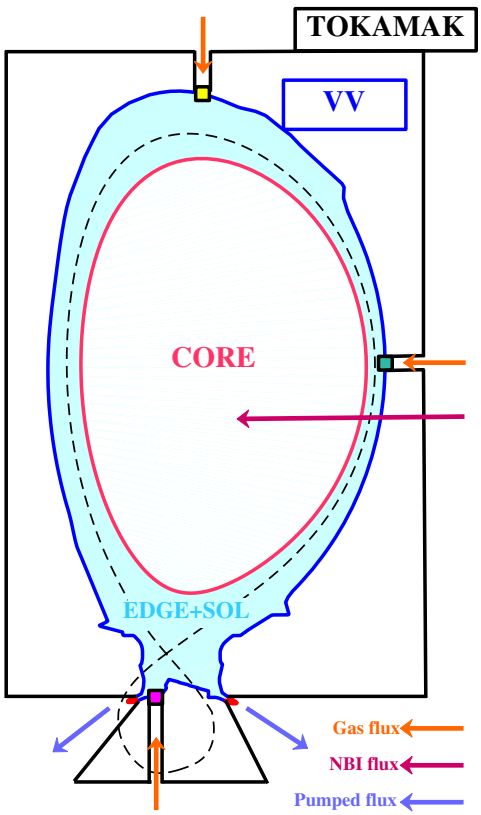

Figure D.1: Sketch of the different systems used in the particle and power balances: the tokamak (inside the black boundary), the vacuum vessel (VV, inside the blue boundary), and the core (inside the red boundary). The light blue area represents the SolEdge2D-EIRENE simulated domain (EDGE+SOL). The different external particle fluxes involved in #JPN89044 are also displayed.

defined in figure D.1. Then equation D.2 becomes:

$$\frac{dN^{D^+}_{EDGE+SOL}}{dt} + \frac{dN^{D}_{EDGE+SOL}}{dt} + \frac{dN_{CORE}}{dt} = Q_{inj,tot} - Q_{pump,tot} - \frac{dN_{wall,tot}}{dt} \tag{D.3}$$

where $N^{D^+}_{EDGE+SOL}$ and $N^{D}_{EDGE+SOL}$ are respectively the number of D ions and D neutrals in the EDGE+SOL domain, while N_{CORE} is the total number of D particles in the core. The types of particles in the core are deliberately not differentiated as this region is not simulated in SolEdge2D-EIRENE. Equation D.3 can be written to highlight the particle steady-state condition for a SolEdge2D-EIRENE simulation:

$$\frac{dN^{D^+}_{EDGE+SOL}}{dt} + \frac{dN^{D}_{EDGE+SOL}}{dt} = Q_{inj,tot} - Q_{pump,tot} - \frac{dN_{wall,tot}}{dt} - \frac{dN_{CORE}}{dt} \tag{D.4}$$

Indeed, the EDGE+SOL domain is in steady state when the D ions number and the D neutrals number in this domain do not evolve anymore:

$$\left(\frac{dN^{D^+}_{EDGE+SOL}}{dt} = 0\right) \quad \text{AND} \quad \left(\frac{dN^{D}_{EDGE+SOL}}{dt} = 0\right) \tag{D.5}$$

Using equation D.4, the steady-state condition D.5 is equivalent to:

$$(D.5) \underset{(D.4)}{\iff} \begin{cases} Q_{inj,tot} - Q_{pump,tot} - \dfrac{dN_{wall,tot}}{dt} - \dfrac{dN_{CORE}}{dt} = 0 \\ \dfrac{dN^{D^+}_{EDGE+SOL}}{dt} = 0 \end{cases} \tag{D.6}$$

In the experiment, the plasma core is also in steady state which implies that the condition $\frac{dN_{CORE}}{dt} = 0$ is satisfied. Then the system D.6 becomes:

$$\begin{cases} Q_{inj,tot} - Q_{pump,tot} - \dfrac{dN_{wall,tot}}{dt} = 0 \\ \dfrac{dN_{CORE}}{dt} = 0 \\ \dfrac{dN^{D^+}_{EDGE+SOL}}{dt} = 0 \end{cases} \tag{D.7}$$

It can be noticed that the first equation in the system D.7 is the steady-state condition of the VV flux balance equation D.2. Now, each equation of the system D.7 will be developed.

First the steady-state condition of the VV particle balance equation is developed taking into account the external D supplies (cf. figure D.1):

$$Q_{NBI} + Q_{inj} - Q_{pump,tot} - \frac{dN_{wall,tot}}{dt} = 0 \quad [\text{at.s}^{-1}] \tag{D.8}$$

where Q_{NBI} is the NBI injection rate and Q_{inj} the total gas puff injection rate.

Now, the core flux balance can be developed by doing the flux balance at the CORE-EDGE boundary (cf. figure D.1):

$$\frac{dN_{CORE}}{dt} = Q_{NBI} + Q^{D}_{EDGE\to CORE} - Q^{D^+}_{CORE\to EDGE} \quad [\text{at.s}^{-1}] \tag{D.9}$$

where $Q^{D}_{EDGE\to CORE}$ is the flux of unconfined D neutrals going from the edge to the core and $Q^{D^+}_{CORE\to EDGE}$ is the flux of deconfined D ions flowing from the core to the edge. In this equation, Q_{NBI} is assumed to directly fuel the plasma core.

Eventually, the ion flux balance in the EDGE+SOL region gives:

$$\frac{dN^{D^+}_{EDGE+SOL}}{dt} = Q^{D^+}_{CORE\to EDGE} + S^{D^+}_{EDGE+SOL} - Q^{D^+}_{SOL\to wall} \quad [\text{at.s}^{-1}] \tag{D.10}$$

where $S^{D^+}_{EDGE+SOL}$ is the net ion source in the EDGE+SOL domain, which is the sum of the positive ionisation source and the negative recombination source in the EDGE+SOL region. $Q^{D^+}_{SOL\rightarrow wall}$ is the ion flux flowing from the SOL to the wall. This equation states the recycling process in the EDGE+SOL region from the point of view of the ions.
Using equations D.8, D.9 and D.10, the system D.7 becomes:

$$\begin{cases} Q_{NBI} + Q_{inj} - Q_{pump,tot} - \dfrac{dN_{wall,tot}}{dt} = 0 \\ Q_{NBI} + Q^{D}_{EDGE\rightarrow CORE} - Q^{D^+}_{CORE\rightarrow EDGE} = 0 \\ Q^{D^+}_{CORE\rightarrow EDGE} + S^{D^+}_{EDGE+SOL} - Q^{D^+}_{SOL\rightarrow wall} = 0 \end{cases} \tag{D.11}$$

The system D.11 represents the steady-state criterion for particles in the EDGE+SOL domain. This criterion is valid for experimental discharges and has to be verified by any SolEdge2D-EIRENE converged simulation. One can notice that this criterion will still be valid when the D-WEE module will be fully coupled with SolEdge2D-EIRENE: the D-WEE contribution in the flux balances system D.11 will have to be accounted in the wall contribution $\dfrac{dN_{wall,tot}}{dt}$ in the first equation of the system.

Now one will focus on the power balances. In the following balances, no distinction will be done between ions and electrons for the sake of clarity. Moreover, the tokamak is assumed insulated in the time scale of a discharge (which is the case in JET as no heat exhaust system are installed). The power balance equation for the tokamak system can be introduced:

$$\frac{d}{dt}\left(U_{TOK}\right) = \frac{d}{dt}\left(U_{VV}^{\{D^+ + e^-\}} + U^{D}_{VV} + U_{wall}\right) = P_{inj,tot} \quad [\mathrm{W}] \tag{D.12}$$

where U_{TOK} is the internal energy of the tokamak [J], $U_{VV}^{\{D^+ + e^-\}}$ the internal energy of the system {D ions + electrons} in the VV [J], U_{wall} the internal energy of the wall [J] and $P_{inj,tot}$ the total injected power in the tokamak. The VV power balance can easily be obtained from equation D.12:

$$\frac{d}{dt}\left(U_{VV}^{\{D^+ + e^-\}} + U^{D}_{VV}\right) = P_{inj,tot} - \frac{dU_{wall}}{dt} \tag{D.13}$$

Again, the LHS of equation D.13 can be developed to take into account the two VV regions defined in figure D.1. Then equation D.13 becomes:

$$\frac{dU_{EDGE+SOL}^{\{D^+ + e^-\}}}{dt} + \frac{dU^{D}_{EDGE+SOL}}{dt} + \frac{dU_{CORE}}{dt} = P_{inj,tot} - \frac{dU_{wall}}{dt} \tag{D.14}$$

where $U_{EDGE+SOL}^{\{D^+ + e^-\}}$ and $U^{D}_{EDGE+SOL}$ are respectively the internal energy of the system {D ions+electrons} and D neutrals in the EDGE+SOL domain, while U_{CORE} is the internal energy of the core. Equation D.14 can be written to highlight the energy steady-state

condition for a SolEdge2D-EIRENE simulation:

$$\frac{dU^{\{D^+ + e^-\}}_{EDGE+SOL}}{dt} + \frac{dU^{D}_{EDGE+SOL}}{dt} = P_{inj,tot} - \frac{dU_{wall}}{dt} - \frac{dU_{CORE}}{dt} \tag{D.15}$$

Indeed, the EDGE+SOL domain is in steady state when the internal energy of {D ions+electrons} and the internal energy of D neutrals in this domain do not evolve anymore:

$$\left(\frac{dU^{\{D^+ + e^-\}}_{EDGE+SOL}}{dt} = 0\right) \quad \text{AND} \quad \left(\frac{dU^{D}_{EDGE+SOL}}{dt} = 0\right) \tag{D.16}$$

Using equation D.15, the steady-state condition D.16 is equivalent to:

$$(D.16) \quad \underset{(D.15)}{\Longleftrightarrow} \quad \begin{cases} P_{inj,tot} - \dfrac{dU_{wall}}{dt} - \dfrac{dU_{CORE}}{dt} = 0 \\ \dfrac{dU^{\{D^+ + e^-\}}_{EDGE+SOL}}{dt} = 0 \end{cases} \tag{D.17}$$

In the experiment, the plasma core is also stationnary which implies that the condition $\frac{dU_{CORE}}{dt} = 0$ is satisfied. Then the system D.17 becomes:

$$\begin{cases} P_{inj,tot} - \dfrac{dU_{wall}}{dt} = 0 \\ \dfrac{dU_{CORE}}{dt} = 0 \\ \dfrac{dU^{\{D^+ + e^-\}}_{EDGE+SOL}}{dt} = 0 \end{cases} \tag{D.18}$$

As for the flux balance, the first equation in the system D.18 is the steady-state condition of the VV power balance equation D.13. Each equation of the system D.18 will be developed.

First, the steady-state condition of the VV power balance equation is developed taking into account the external power supplies:

$$P_{NBI} + P_{ICRH} + P_{Ohm} - \frac{dU_{wall}}{dt} = 0 \quad \text{[W]} \tag{D.19}$$

where P_{NBI} is the NBI injected power, P_{ICRH} the ICRH injected power and P_{Ohm} the ohmic power.

The core power balance can also be developed:

$$\frac{dU_{CORE}}{dt} = P_{NBI} + P_{ICRH} + P_{Ohm} - S^{E,rad}_{CORE} - P^{\{D^+ + e^-\}}_{CORE \rightarrow EDGE} \quad \text{[W]} \tag{D.20}$$

where $S^{E,rad}_{CORE}$ is the core radiative energy source while $P^{\{D^+ + e^-\}}_{CORE \rightarrow EDGE}$ is the unconfined

power carried by ions and electrons going from the edge to the core. The power carried by neutrals flowing from the EDGE to the CORE is negligible w.r.t. the different terms in equation D.20 and therefore has not been accounted in the calculation.
Eventually, the {D ions+electrons} balance in the EDGE+SOL region gives:

$$\frac{dU_{EDGE+SOL}^{\{D^+ + e^-\}}}{dt} = P_{CORE\rightarrow EDGE}^{\{D^+ + e^-\}} + S_{EDGE+SOL}^{E,\{D^+ + e^-\}} - P_{SOL\rightarrow wall}^{\{D^+ + e^-\}} \quad [\mathrm{W}] \tag{D.21}$$

where $S_{EDGE+SOL}^{E,\{D^+ + e^-\}}$ is the net energy source due to interaction with neutrals in the EDGE+SOL domain and $P_{SOL\rightarrow wall}^{\{D^+ + e^-\}}$ is the energy flux going from the SOL to the wall. The latter does not have to be confused with the plasma net heat flux coupled to the wall. Indeed, the reflected energy flux on the wall surface would have to be accounted in the calculation of this heat flux.
Using equations D.19, D.20 and D.21, the system D.18 becomes:

$$\begin{cases} P_{NBI} + P_{ICRH} + P_{Ohm} - \dfrac{dU_{wall}}{dt} = 0 \\ P_{NBI} + P_{ICRH} + P_{Ohm} - S_{CORE}^{E,rad} - P_{CORE\rightarrow EDGE}^{\{D^+ + e^-\}} = 0 \\ P_{CORE\rightarrow EDGE}^{\{D^+ + e^-\}} + S_{EDGE+SOL}^{E,\{D^+ + e^-\}} - P_{SOL\rightarrow wall}^{\{D^+ + e^-\}} = 0 \end{cases} \tag{D.22}$$

The system D.22 represents the experimental steady-state criterion for energy in the EDGE+SOL domain. Equation 1 in this system can be rearranged using equation 2:

$$\begin{cases} S_{CORE}^{E,rad} + P_{CORE\rightarrow EDGE}^{\{D^+ + e^-\}} - \dfrac{dU_{wall}}{dt} = 0 \\ P_{NBI} + P_{ICRH} + P_{Ohm} - S_{CORE}^{E,rad} - P_{CORE\rightarrow EDGE}^{\{D^+ + e^-\}} = 0 \\ P_{CORE\rightarrow EDGE}^{\{D^+ + e^-\}} + S_{EDGE+SOL}^{E,\{D^+ + e^-\}} - P_{SOL\rightarrow wall}^{\{D^+ + e^-\}} = 0 \end{cases} \tag{D.23}$$

Indeed, now equation 1 and 2 reveal that the total injected power splits into the plasma power flowing into the EDGE region and the radiative energy source in the core and that the latter one, which is not simulated by SolEdge2D-EIRENE, is directly coupled to the wall. In the following, equation 1 will be omitted due to the difficulty in assessing the distribution of the radiative energy source on the JET wall. However this contribution to the net energy flux density given to the thermal model WEE-temp would have to be taken into account in future work as it can be non-negligible in the first-wall region w.r.t. the plasma energy flux density.

Bibliography

[1] J. Wesson. *Tokamaks - Third Edition*. 2004. (Cited in page 8.)

[2] EUROfusion website, "Tokamak principle". https://www.euro-fusion.org/news/detail/detail/News/tokamak-principle/. Accessed: 10 Nov, 2019. (Cited in page 9.)

[3] European Fusion Development Agreement, "Limiters and divertors". Accessed: 2011. (Cited in page 10.)

[4] L. Horton. Jet forward programme and opportunities for collaboration. Presentation, FESAC strategic planning panel, Maryland, July 2014. (Cited in page 11.)

[5] S. Carpentier-Chouchana et al. Status of the ITER full-tungsten divertor shaping and heat load distribution analysis. *Physica Scripta*, T159:014002, apr 2014. (Cited in page 11.)

[6] A. R. Raffray et al. The ITER blanket system design challenge. *Nuclear Fusion*, 54(3):033004, feb 2014. (Cited in pages 12, 19, and 54.)

[7] R. A. Causey. Hydrogen isotope retention and recycling in fusion reactor plasma-facing components. *Journal of Nuclear Materials*, 300(2):91 – 117, 2002. (Cited in pages 12, 32, 36, 37, and 45.)

[8] ITER newsline. https://www.iter.org/newsline/-/3172. Accessed: 10 Dec, 2018. (Cited in page 12.)

[9] Defects in crystals. https://www.tf.uni-kiel.de/matwis/amat/def_en/. (Cited in page 15.)

[10] H. Bufferand et al. Numerical modelling for divertor design of the WEST device with a focus on plasma–wall interactions. *Nuclear Fusion*, 55(5):053025, apr 2015. (Cited in pages 15, 26, 27, and 111.)

[11] W. Eckstein and H. Verbeek. Reflection of h, d, and he from c, ti, ni, mo, w, and au. *Journal of Nuclear Materials*, 76-77:365 – 369, 1978. (Cited in page 15.)

[12] W. Eckstein and D. B. Heifetz. Data sets for hydrogen reflection and their use in neutral transport calculations. *Journal of Nuclear Materials*, 145-147:332 – 338, 1987. (Cited in page 15.)

[13] T. Loarer et al. Gas balance and fuel retention in fusion devices. *Nuclear Fusion*, 47(9):1112–1120, aug 2007. (Cited in pages 16 and 17.)

[14] J. Ehrenberg et al. Analysis of deuterium recycling in jet under beryllium first wall conditions. *Journal of Nuclear Materials*, 176-177:226 – 230, 1990. (Cited in pages

17 and 194.)

[15] V. Philipps et al. Dynamic fuel retention and release under iter like wall conditions in jet. *Journal of Nuclear Materials*, 438:S1067 – S1071, 2013. Proceedings of the 20th International Conference on Plasma-Surface Interactions in Controlled Fusion Devices. (Cited in pages 17, 18, 19, 156, 185, and 194.)

[16] S. Brezinsek et al. Fuel retention studies with the iter-like wall in jet. *Nuclear Fusion*, 53(8):083023, 2013. (Cited in pages 19, 185, 186, and 187.)

[17] C. Grisolia. Plasma wall interaction during long pulse operation in tore supra. *Journal of Nuclear Materials*, 266-269:146 – 152, 1999. (Cited in page 19.)

[18] B. Pégourié and Tore Supra Team. Particle balance and fuel retention in tore supra. *Fusion Science and Technology*, 56(3):1334–1352, 2009. (Cited in pages 19 and 20.)

[19] F. Wagner et al. Development of an edge transport barrier at the h-mode transition of asdex. *Phys. Rev. Lett.*, 53:1453–1456, Oct 1984. (Cited in page 20.)

[20] F. Wagner. A quarter-century of h-mode studies. *Plasma Physics and Controlled Fusion*, 49(12B):B1–B33, nov 2007. (Cited in page 20.)

[21] E. J. Doyle et al. Chapter 2: Plasma confinement and transport. *Nuclear Fusion*, 47(6):S18–S127, jun 2007. (Cited in page 20.)

[22] E. Joffrin et al. Impact of divertor geometry on h-mode confinement in the JET metallic wall. *Nuclear Fusion*, 57(8):086025, jun 2017. (Cited in page 20.)

[23] S. Wiesen et al. Impact of the JET ITER-like wall on h-mode plasma fueling. *Nuclear Fusion*, 57(6):066024, apr 2017. (Cited in pages 20, 21, 22, and 23.)

[24] E. de la Luna et al. Comparative study of high triangularity h-mode plasma performance in jet with be/w wall and cfc wall. (Cited in page 22.)

[25] R. Bisson et al. Dynamic fuel retention in tokamak wall materials: An in situ laboratory study of deuterium release from polycrystalline tungsten at room temperature. *Journal of Nuclear Materials*, 467:432 – 438, 2015. (Cited in pages 23 and 52.)

[26] C. Linsmeier et al. ARTOSS – a new surface science experiment to study the hydrogen inventory in multi-component materials. *Physica Scripta*, T94(1):28, 2001. (Cited in page 23.)

[27] J. Scholten et al. Operational status of the magnum-psi linear plasma device. *Fusion Engineering and Design*, 88(9):1785 – 1788, 2013. Proceedings of the 27th Symposium On Fusion Technology (SOFT-27); Liège, Belgium, September 24-28, 2012. (Cited in page 23.)

[28] V. Kh. Alimov et al. Depth distribution of deuterium atoms and molecules in beryllium implanted with d ions. *Journal of Nuclear Materials*, 241-243:1047 – 1051, 1997. (Cited in pages 23, 24, and 38.)

[29] V. Kh. Alimov et al. Depth distribution of deuterium in single- and polycrystalline tungsten up to depths of several micrometers. *Journal of Nuclear Materials*, 337-339:619 – 623, 2005. PSI-16. (Cited in pages 24 and 50.)

[30] M. Mayer. *SIMNRA User's Guide*. Max-Planck-Institut für Plasmaphysik, Garching. (Cited in page 24.)

[31] A. A. Haasz and J. W. Davis. Deuterium retention in beryllium, molybdenum and tungsten at high fluences. *Journal of Nuclear Materials*, 241-243:1076 – 1081, 1997. (Cited in pages 25, 54, and 55.)

[32] S. Wiesen et al. The new solps-iter code package. *Journal of Nuclear Materials*, 463:480 – 484, 2015. PLASMA-SURFACE INTERACTIONS 21. (Cited in page 26.)

[33] R. Simonini et al. Models and numerics in the multi-fluid 2-d edge plasma code edge2d/u. *Contributions to Plasma Physics*, 34(2-3):368–373, 1994. (Cited in page 26.)

[34] Y. Feng et al. Recent improvements in the emc3-eirene code. *Contributions to Plasma Physics*, 54(4-6):426–431, 2014. (Cited in page 26.)

[35] D. Reiter. *The EIRENE Code User Manual*. Institut für Energie - und Klimaforschung Plasmaphysik, Forschungszentrum Jülich. (Cited in pages 27, 28, and 147.)

[36] E. A. Hodille et al. Macroscopic rate equation modeling of trapping/detrapping of hydrogen isotopes in tungsten materials. *Journal of Nuclear Materials*, 467:424 – 431, 2015. (Cited in pages 32, 36, 46, 171, and 198.)

[37] E. A. Hodille et al. Study of hydrogen isotopes behavior in tungsten by a multi trapping macroscopic rate equation model. *Physica Scripta*, T167:014011, jan 2016. (Cited in page 32.)

[38] J. Roth and K. Schmid. Hydrogen in tungsten as plasma-facing material. *Physica Scripta*, T145:014031, dec 2011. (Cited in pages 32 and 45.)

[39] M. A. Pick and K. Sonnenberg. A model for atomic hydrogen-metal interactions — application to recycling, recombination and permeation. *Journal of Nuclear Materials*, 131(2):208 – 220, 1985. (Cited in pages 32, 34, 35, 36, and 52.)

[40] A. A. Pisarev. 1 - hydrogen adsorption on the surface of metals. In R. P. Gangloff and B. P. Somerday, editors, *Gaseous Hydrogen Embrittlement of Materials in Energy Technologies*, volume 1 of *Woodhead Publishing Series in Metals and Surface Engineering*, pages 3 – 26. Woodhead Publishing, 2012. (Cited in pages 32 and 34.)

[41] J. W. Davis and A. A. Haasz. Reemission of deuterium atoms from mo, ta and w during d+-irradiation. *Journal of Nuclear Materials*, 223(3):312 – 315, 1995. (Cited in page 34.)

[42] A. McNabb and P. K. Foster. A new analysis of the diffusion of hydrogen in iron and ferritic steels. *Transactions of the Metallurgical Society of AIME*, 227(3):618, 1963. (Cited in page 36.)

[43] R. A. Oriani. The diffusion and trapping of hydrogen in steel. *Acta Metallurgica*, 18(1):147 – 157, 1970. (Cited in page 36.)

[44] A. H. M. Krom and Ad. Bakker. Hydrogen trapping models in steel. *Metallurgical and Materials Transactions B*, 31(6):1475–1482, Dec 2000. (Cited in page 36.)

[45] C. Quirós et al. Blister formation and hydrogen retention in aluminium and beryllium: A modeling and experimental approach. *Nuclear Materials and Energy*, 12:1178 – 1183, 2017. Proceedings of the 22nd International Conference on Plasma Surface Interactions 2016, 22nd PSI. (Cited in page 36.)

[46] C. García-Rosales et al. Re-emission and thermal desorption of deuterium from plasma sprayed tungsten coatings for application in asdex-upgrade. *Journal of Nuclear Materials*, 233-237:803 – 808, 1996. (Cited in page 36.)

[47] O. V. Ogorodnikova et al. Deuterium retention in tungsten in dependence of the surface conditions. *Journal of Nuclear Materials*, 313-316:469 – 477, 2003. Plasma-Surface Interactions in Controlled Fusion Devices 15. (Cited in pages 36, 46, 47, 48, 49, 50, 51, 99, and 192.)

[48] M. Poon et al. Modelling deuterium release during thermal desorption of d+-irradiated tungsten. *Journal of Nuclear Materials*, 374(3):390 – 402, 2008. (Cited in page 36.)

[49] K. Schmid et al. Comparison of hydrogen retention in w and w/ta alloys. *Journal of Nuclear Materials*, 426(1):247 – 253, 2012. (Cited in pages 36 and 52.)

[50] J. Guterl et al. Theoretical analysis of deuterium retention in tungsten plasma-facing components induced by various traps via thermal desorption spectroscopy. *Nuclear Fusion*, 55(9):093017, aug 2015. (Cited in pages 36 and 46.)

[51] M. Oberkofler et al. Retention and release mechanisms of deuterium implanted into beryllium. *Nuclear Instruments and Methods in Physics Research Section B: Beam Interactions with Materials and Atoms*, 269(11):1266 – 1270, 2011. INELASTIC ION-SURFACE COLLISIONS. (Cited in page 36.)

[52] R. Piechoczek et al. Deuterium trapping and release in be(0001), be(11–20) and polycrystalline beryllium. *Journal of Nuclear Materials*, 438:S1072 – S1075, 2013. Proceedings of the 20th International Conference on Plasma-Surface Interactions in Controlled Fusion Devices. (Cited in page 36.)

[53] H. Pastor. Propriétés du tungstène et de ses alliages. *Techniques de l'ingénieur Métaux et alliages non ferreux*, base documentaire : TIB357DUO.(ref. article : m570), 1985. fre. (Cited in pages 38, 47, and 48.)

[54] N. Fernandez et al. Hydrogen diffusion and vacancies formation in tungsten: Density functional theory calculations and statistical models. *Acta Materialia*, 94:307 – 318, 2015. (Cited in pages 38, 46, 47, 48, 52, 60, and 159.)

[55] K. Heinola and T. Ahlgren. Diffusion of hydrogen in bcc tungsten studied with first principle calculations. *Journal of Applied Physics*, 107(11):113531, 2010. (Cited in pages 38, 46, 47, and 48.)

[56] L. Ferry. *Contribution à l'étude du comportement du tritium dans le béryllium (contexte ITER)*. Theses, UNIVERSITE D'AIX-MARSEILLE, November 2017. (Cited in pages 38, 46, and 54.)

[57] M. G. Ganchenkova et al. Hydrogen in beryllium: Solubility, transport, and trapping. *Phys. Rev. B*, 79:134101, Apr 2009. (Cited in pages 38 and 54.)

[58] W. R. Wampler. Retention and thermal release of deuterium implanted in beryllium. *Journal of Nuclear Materials*, 123(1):1598 – 1602, 1984. (Cited in pages 38 and 54.)

[59] H. Kawamura et al. Retention of deuterium implanted in hot-pressed beryllium. *Journal of Nuclear Materials*, 176-177:661 – 665, 1990. (Cited in pages 38 and 54.)

[60] E. A. Hodille. *Study and modeling of the deuterium trapping in ITER relevant materials*. Theses, UNIVERSITE D'AIX-MARSEILLE, November 2016. (Cited in pages 40, 46, 47, 48, 49, 50, 51, 52, 63, 160, and 198.)

[61] D. Matveev et al. Reaction-diffusion modeling of hydrogen transport and surface effects in application to single-crystalline be. *Nuclear Instruments and Methods in Physics Research Section B: Beam Interactions with Materials and Atoms*, 430:23 – 30, 2018. (Cited in pages 40, 55, 56, and 58.)

[62] J. F. Ziegler, M. D. Ziegler, and J. P. Biersack. Srim – the stopping and range of ions in matter (2010). *Nuclear Instruments and Methods in Physics Research Section B: Beam Interactions with Materials and Atoms*, 268(11):1818 – 1823, 2010. 19th International Conference on Ion Beam Analysis. (Cited in page 40.)

[63] O. V. Ogorodnikova et al. Ion-induced deuterium retention in tungsten coatings on carbon substrate. *Journal of Nuclear Materials*, 419(1):194 – 200, 2011. (Cited in page 42.)

[64] J. Likonen et al. Deuterium trapping and release in JET ITER-like wall divertor tiles. *Physica Scripta*, T167:014074, feb 2016. (Cited in page 42.)

[65] K. Radhakrishnan and A. C. Hindmarsh. *Description and use of LSODE, the Livermore Solver for Ordinary Differential Equations*. Lawrence Livermore National Laboratory. (Cited in pages 45, 197, and 198.)

[66] T. Tanabe. Review of hydrogen retention in tungsten. *Physica Scripta*, T159:014044, apr 2014. (Cited in page 45.)

[67] K. Schmid et al. Recent progress in the understanding of h transport and trapping in w. *Physica Scripta*, T170:014037, oct 2017. (Cited in page 45.)

[68] R. A. Anderl et al. Hydrogen isotope retention in beryllium for tokamak plasma-facing applications. *Journal of Nuclear Materials*, 273(1):1 – 26, 1999. (Cited in pages 45, 54, 58, 108, and 191.)

[69] R. Frauenfelder. Solution and diffusion of hydrogen in tungsten. *Journal of Vacuum Science and Technology*, 6(3):388–397, 1969. (Cited in pages 45 and 47.)

[70] E. Abramov et al. Deuterium permeation and diffusion in high-purity beryllium. *Journal of Nuclear Materials*, 175(1):90 – 95, 1990. (Cited in pages 45 and 54.)

[71] M. Wensing. *Reaction-diffusion modelling of hydrogen retention and release mechanisms in beryllium*. Master thesis, Aachen University, 2016. (Cited in pages 46, 54, 55, 58, and 160.)

[72] V. T. Deshpande and R. Pawar. X-ray determination of the thermal expansion of tungsten. *Current Science*, 31(12):497–499, 1962. (Cited in page 48.)

[73] M. Poon et al. Flux dependence of deuterium retention in single crystal tungsten. *Journal of Nuclear Materials*, 307-311:723 – 728, 2002. (Cited in page 50.)

[74] M. Poon et al. Effects of background gas impurities during d+ irradiation on d trapping in single crystal tungsten. *Journal of Nuclear Materials*, 337-339:629 – 633, 2005. PSI-16. (Cited in page 50.)

[75] V. Kh. Alimov et al. Deuterium retention in tungsten exposed to low-energy, high-flux clean and carbon-seeded deuterium plasmas. *Journal of Nuclear Materials*, 375(2):192 – 201, 2008. (Cited in pages 50 and 51.)

[76] J. P. Roszell et al. Deuterium retention in single-crystal tungsten irradiated with 10–500 ev/d+. *Journal of Nuclear Materials*, 438:S1084 – S1087, 2013. Proceedings of the 20th International Conference on Plasma-Surface Interactions in Controlled Fusion Devices. (Cited in page 50.)

[77] Z. Tian et al. Deuterium retention in tungsten at fluences of up to 1026 d+/m2 using d+ ion beams. *Journal of Nuclear Materials*, 399(1):101 – 107, 2010. (Cited in pages 50, 51, and 192.)

[78] A. Widdowson et al. Overview of fuel inventory in jet with the iter-like wall. *Nuclear Fusion*, 57(8):086045, 2017. (Cited in pages 51 and 158.)

[79] K. Schmid. Diffusion-trapping modelling of hydrogen recycling in tungsten under ELM-like heat loads. *Physica Scripta*, T167:014025, jan 2016. (Cited in pages 52 and 63.)

[80] E. A. Hodille et al. Simulations of atomic deuterium exposure in self-damaged tungsten. *Nuclear Fusion*, 57(5):056002, mar 2017. (Cited in pages 52 and 53.)

[81] A. A. Pisarev and O. V. Ogorodnikova. Elementary processes near the interface between hydrogen gas and solid. *Journal of Nuclear Materials*, 248:52 – 59, 1997. (Cited in page 52.)

[82] S. Markelj et al. In situ nra study of hydrogen isotope exchange in self-ion damaged tungsten exposed to neutral atoms. *Journal of Nuclear Materials*, 469:133 – 144, 2016. (Cited in page 53.)

[83] L. Ferry et al. Theoretical investigation on the point defect formation energies in beryllium and comparison with experiments. *Nuclear Materials and Energy*, 12:453 – 457, 2017. Proceedings of the 22nd International Conference on Plasma Surface Interactions 2016, 22nd PSI. (Cited in page 55.)

[84] V. Barabash. *Summary of material properties for structural analysis of the ITER internal components*. ITER Organization. (Cited in pages 55, 72, 81, 83, and 163.)

[85] M. Reinelt et al. Retention mechanisms and binding states of deuterium implanted into beryllium. *New Journal of Physics*, 11(4):043023, apr 2009. (Cited in pages 55, 56, 57, 58, 59, 99, 191, and 194.)

[86] A. V. Markin et al. Thermal desorption of deuterium implanted into beryllium. *Journal of Nuclear Materials*, 233-237:865 – 869, 1996. (Cited in page 55.)

[87] V. N. Chernikov et al. Gas swelling and related phenomena in beryllium implanted with deuterium ions. *Journal of Nuclear Materials*, 228(1):47 – 60, 1996. (Cited in

page 55.)

[88] B. L. Doyle. A simple theory for maximum h inventory and release: A new transport parameter. *Journal of Nuclear Materials*, 111-112:628 – 635, 1982. (Cited in page 63.)

[89] S. Brezinsek et al. Characterisation of the deuterium recycling at the w divertor target plates in JET during steady-state plasma conditions and ELMs. *Physica Scripta*, T167:014076, feb 2016. (Cited in page 71.)

[90] H. S. Carslaw and J. C. Jaeger. *Conduction of Heat in Solids*. 1959. (Cited in pages 74 and 210.)

[91] N. Ozisik. *Heat Conduction - Second Edition*. 1980. (Cited in pages 74, 76, 77, 78, 204, 207, 210, 211, 214, and 215.)

[92] D. Maillet et al. *Thermal Quadrupoles: Solving the Heat Equation through Integral Transforms*. 2000. (Cited in pages 78, 202, 204, and 207.)

[93] F. R. de Hoog et al. An improved method for numerical inversion of laplace transforms. *SIAM Journal on Scientific and Statistical Computing*, 3(3):357–366, 1982. (Cited in pages 78, 205, and 206.)

[94] A. Gallo. *Impact of the plasma geometry on the divertor power exhaust in a magnetic fusion reactor*. PhD thesis, 2018. Thèse de doctorat dirigée par Ghendrih, Philippe et Fedorczak, Nicolas Energie, Rayonnement, Plasma Aix-Marseille 2018. (Cited in page 81.)

[95] A. Loarte et al. Chapter 4: Power and particle control. *Nuclear Fusion*, 47(6):S203–S263, jun 2007. (Cited in page 82.)

[96] J. Denis et al. Wall surface temperature calculation in the soledge2d-eirene transport code. *Physica Scripta*, 2016(T167):014073, 2016. (Cited in page 83.)

[97] E. Lefichoux. *Présentation et utilisation de CAST3M*. CEA. (Cited in page 83.)

[98] J. Gaspar. Private communication. (Cited in page 83.)

[99] J. Bucalossi et al. The west project: Testing iter divertor high heat flux component technology in a steady state tokamak environment. *Fusion Engineering and Design*, 89(7):907 – 912, 2014. Proceedings of the 11th International Symposium on Fusion Nuclear Technology-11 (ISFNT-11) Barcelona, Spain, 15-20 September, 2013. (Cited in page 89.)

[100] C. Bourdelle et al. WEST physics basis. *Nuclear Fusion*, 55(6):063017, may 2015. (Cited in page 89.)

[101] M. Lipa et al. Design of an improved vacuum vessel protection for very long pulse operation in tore supra. *Fusion Engineering and Design*, 56-57:855 – 859, 2001. (Cited in page 90.)

[102] A. Herrmann. Overview on stationary and transient divertor heat loads. *Plasma Physics and Controlled Fusion*, 44(6):883–903, may 2002. (Cited in page 93.)

[103] A. Herrmann et al. Power deposition outside the divertor in ASDEX upgrade. *Plasma Physics and Controlled Fusion*, 46(6):971–979, may 2004. (Cited in page 94.)

[104] T. Eich et al. Type-i elm power deposition profile width and temporal shape in jet. *Journal of Nuclear Materials*, 415(1, Supplement):S856 – S859, 2011. Proceedings of the 19th International Conference on Plasma-Surface Interactions in Controlled Fusion. (Cited in page 94.)

[105] T. Eich et al. Divertor power deposition and target current asymmetries during type-i elms in asdex upgrade and jet. *Journal of Nuclear Materials*, 363-365:989 – 993, 2007. Plasma-Surface Interactions-17. (Cited in page 94.)

[106] J. Sheffield et al. In *Plasma Scattering of Electromagnetic Radiation (Second Edition)*. Academic Press, second edition edition, 2011. (Cited in page 104.)

[107] A. Widdowson et al. Overview of the jet iter-like wall divertor. *Nuclear Materials and Energy*, 12:499 – 505, 2017. Proceedings of the 22nd International Conference on Plasma Surface Interactions 2016, 22nd PSI. (Cited in page 107.)

[108] N. Catarino et al. Assessment of erosion, deposition and fuel retention in the jet-ilw divertor from ion beam analysis data. *Nuclear Materials and Energy*, 12:559 – 563, 2017. Proceedings of the 22nd International Conference on Plasma Surface Interactions 2016, 22nd PSI. (Cited in page 108.)

[109] K. Heinola et al. Experience on divertor fuel retention after two ITER-like wall campaigns. *Physica Scripta*, T170:014063, nov 2017. (Cited in page 108.)

[110] M. Mayer et al. Erosion and deposition in the JET divertor during the second ITER-like wall campaign. *Physica Scripta*, T170:014058, nov 2017. (Cited in page 108.)

[111] C. Guillemaut et al. Influence of atomic physics on edge2d-eirene simulations of jet divertor detachment with carbon and beryllium/tungsten plasma-facing components. *Nuclear Fusion*, 54(9):093012, 2014. (Cited in page 108.)

[112] T. Loarer et al. Comparison of long term fuel retention in jet between carbon and the iter-like wall. *Journal of Nuclear Materials*, 438:S108 – S113, 2013. Proceedings of the 20th International Conference on Plasma-Surface Interactions in Controlled Fusion Devices. (Cited in pages 108, 174, 185, 190, and 193.)

[113] G. D. Porter et al. Characterization of the separatrix plasma parameters in diii-d. *Physics of Plasmas*, 5(5):1410–1422, 1998. (Cited in page 114.)

[114] H. Bufferand et al. Comparison on heat flux deposition between carbon and tungsten wall – investigations on energy recycling. *Journal of Nuclear Materials*, 463:420 – 423, 2015. PLASMA-SURFACE INTERACTIONS 21. (Cited in pages 117 and 119.)

[115] A. Wynn et al. Investigation into the formation of the scrape-off layer density shoulder in JET ITER-like wall l-mode and h-mode plasmas. *Nuclear Fusion*, 58(5):056001, feb 2018. (Cited in page 117.)

[116] P. C. Stangeby. *The Plasma Boundary of Magnetic Fusion Devices*. 2000. (Cited in pages 118, 121, 134, and 151.)

[117] H. M. Mott-Smith and I. Langmuir. The theory of collectors in gaseous discharges. *Phys. Rev.*, 28:727–763, Oct 1926. (Cited in page 121.)

[118] J. P. Gunn et al. Flush-mounted probes in the divertor plates of tokamak de varennes. *Review of Scientific Instruments*, 66(1):154–159, 1995. (Cited in page 121.)

[119] M. Brix et al. Accuracy of efit equilibrium reconstruction with internal diagnostic information at jet. *Review of Scientific Instruments*, 79(10):10F325, 2008. (Cited in page 121.)

[120] S. Brezinsek et al. Characterization of the deuterium recycling flux in front of a graphite surface in the TEXTOR tokamak. *Plasma Physics and Controlled Fusion*, 47(4):615–634, mar 2005. (Cited in page 151.)

[121] J. Guterl et al. Revisited reaction-diffusion model of thermal desorption spectroscopy experiments on hydrogen retention in material. *Journal of Applied Physics*, 118(4):043302, 2015. (Cited in page 160.)

[122] K. Jousten. John Wiley & Sons, Ltd, 2016. (Cited in pages 185 and 186.)

[123] J. Denis et al. Dynamic modelling of local fuel inventory and desorption in the whole tokamak vacuum vessel for auto-consistent plasma-wall interaction simulations. *Nuclear Materials and Energy*, 19:550 – 557, 2019. (Cited in page 186.)

[124] B. Pégourié et al. Deuterium inventory in tore supra: Coupled carbon–deuterium balance. *Journal of Nuclear Materials*, 438:S120 – S125, 2013. Proceedings of the 20th International Conference on Plasma-Surface Interactions in Controlled Fusion Devices. (Cited in page 187.)

[125] V. Philipps and J. Ehrenberg. Analysis of outgassing after joint european torus discharges under beryllium first wall conditions. *Journal of Vacuum Science & Technology A*, 11(2):437–445, 1993. (Cited in page 187.)

[126] The JET Team. Results of jet operation with beryllium. *Journal of Nuclear Materials*, 176-177:3 – 13, 1990. (Cited in page 194.)